Instituto de Física de Cantabria

CSIC Consejo Superior de Investigaciones Científicas

UC Universidad de Cantabria

Programa de Doctorado en Ciencia y Tecnología

Unveiling the polarization of the Cosmic Microwave Background: characterization of the synchrotron emission and methods for estimating the tensor-to-scalar ratio

Desvelando la polarización del Fondo Cósmico de Microondas: caracterización de la emisión sincrotrón y métodos de estimación de la razón tensor-escalar

Directores:
Rita Belén Barreiro Vilas
Enrique Martínez González

Autor:
Felice Antonio Martire

Tesis Doctoral 2024

Rita Belén Barreiro Vilas, Doctora en Ciencias Físicas e Investigadora Científica del Consejo Superior de Investigaciones Científicas

y

Enrique Martínez González, Doctor en Ciencias Físicas y Profesor de Investigación del Consejo Superior de Investigaciones Científicas

CERTIFICAN que la presente memoria

Desvelando la polarización del Fondo Cósmico de Microondas: caracterización de la emisión sincrotrón y métodos de estimación de la razón tensor-escalar

ha sido realizada, bajo su dirección, por Felice Antonio Martire, y constituye su tesis para optar al grado de doctor por la Universidad de Cantabria. Asimismo, emiten su conformidad para que la presente memoria sea depositada y se celebre, ulteriormente, la correspondiente lectura y defensa.

En Santander, a 8 de octubre de 2024,

Fdo.: Dr. Rita Belén Barreiro Vilas

Fdo.: Dr. Enrique Martínez González

Acknowledgement

Vorrei esprimere la mia profonda gratitudine ai miei genitori, che hanno sempre creduto in me, sostenendomi e offrendomi il loro aiuto in ogni momento. È grazie a loro se oggi sono la persona che sono e se ho potuto realizzare tutti i miei obiettivi. Desidero ringraziare mia sorella, anche se spesso siamo lontani, il tuo sostegno e il tuo affetto sono sempre presenti e non sono mai stati in dubbio.

Un grazie dal profondo del cuore a Ludovica, che è sempre stata al mio fianco, soprattutto nei momenti e nelle decisioni più difficili. Il tuo supporto e la tua comprensione mi hanno dato la forza di affrontare ogni sfida. Infine, desidero ringraziare il mio compagno di vita quotidiano, Frango, che mi ha isegnato l'amore incodizionato.

Deseo expresar mi sincera gratitud a Belén y Enrique, por sus valiosas enseñanzas y consejos. En todos estos años en Santander, habéis sido mis referentes académicos, profesionales y a veces personales.

Cuando pienso en los años de doctorado, solo puedo dar las gracias a todas las personas que me hicieron sentir como en casa en Santander. Los amigos del IFCA: Guille, Christian, Miguel, Maria, Miriam, Patricio y Matteo, entre otros; los amigos del IDIVAL: Sara, Nancy, Lolo, Rebeca, Isma, Angel y Emilio; y los amigos que el azar me unió: Alberto, Jhon y Vanessa.

Finally, I would like to acknowledge all the researchers with whom I collaborated. Special thanks to Tony and Paolo, whose contribution has been fundamental to the work presented in this thesis.

Abstract

The cosmic microwave background (CMB) is a diffuse electromagnetic radiation that permeates the entire universe. It originated about 380,000 years after the Big Bang, when the cosmos went from an opaque state to a transparent one. This remnant radiation plays a fundamental role in shaping our understanding of cosmology. All theories proposed to describe the universe have to reproduce the precise statistical characterisation we currently have of the CMB. Although we now have a good understanding of the CMB, some aspects concerning its polarisation remain unknown. B-modes are a distinctive polarization pattern that is assumed to have originated from the first gravitational waves produced at the beginning of the universe during cosmic inflation. However, this polarization mode has not yet been observed and its detection represents one of the main goals of observational cosmology.

Observing the polarized CMB presents formidable challenges. Part of these challenges stem from the fact that the signal is very weak and requires enormous control of systematic instrumental errors. Another part stems from the fact that Galactic and extragalactic astrophysical emissions overshadow this primordial signal. In the microwave spectrum, thermal dust dominates the short-wavelength polarized emission, synchrotron radiation the long-wavelength one. Most of the presented work focuses on characterising the latter. The thesis includes two published articles on this topic.

The first work focuses on the characterization of the power spectra (EE, BB and EB) of the polarized synchrotron emission at 23 and 30 GHz provided respectively by two space observatories: *WMAP* and *Planck*. We study six sky regions covering from 30% to 94% of the sky, masking the Galactic center and point sources. We analyze the angular distribution and the spectral energy distribution (SED) at angular scales between several tens of arcmin and several degrees. We prove that the polarized synchrotron emission is well described by the EE and BB power-law model with zero EB cross-correlation. In particular, we find that the EE and BB power spectra show steep decay as a function of the angular scale, $\ell^{\alpha_{EE,BB}}$, where $\alpha_{EE} = -2.95 \pm 0.04$ and $\alpha_{BB} = -2.85 \pm 0.14$. The amplitude ratio between BB and EE, at multipole $\ell = 80$, is 0.22 ± 0.02. The EB cross-spectrum is compatible with zero at 1σ. The spectral energy distribution is well described with a power-law, $\nu^{\beta_{EE,BB}}$, with indices $\beta_{EE} = -3.00 \pm 0.10$ and $\beta_{BB} = -3.05 \pm 0.36$, with a tendency for the SED to become steeper from low to high Galactic latitude. The results of this work are presented in [1].

The second work focuses on the characterization of some morphological and statistical properties of the polarized synchrotron emission. We implement a novel algorithm with which we identify 19 bright elongated structures, or filaments, in the polarized intensity sky. We use again maps at 23 and 30 GHz, provided by *WMAP* and *Planck*. For each filament we analyze the polarization fraction, finding values typically larger

than those from areas with more diffuse emission, and the polarization spectral index, typically compatible with the average across the sky. Making use of Minkowski tensors, we analyse the Gaussianity and statistical isotropy of the polarized synchrotron emission. We study the region of the sky corresponding to 80% and 60% of the faintest emission, for scales roughly between 6 and 1.5 degrees. For the larger region, the deviations from Gaussianity and isotropy exceed 3σ, while they slightly decrease for the smaller region. This work also presents a data-driven algorithm to generate non-Gaussian and anisotropic polarized synchrotron simulations, fitting the spectral and statistical properties of the real observations. The results of this work are presented in [2].

An in-depth knowledge of the foregrounds, such as the synchrotron radiation, allows us to decouple these emissions more precisely from the CMB. However, we will never be able to completely separate these contaminants from the cosmological signal. The cosmological parameter estimates must always take into account the presence of foreground residuals, as well as instrumental noise. The final work presented in this thesis is an analysis of different statistical approaches and likelihood estimators used to estimate a cosmological parameter, the tensor-to-scalar ratio (r). The particular case study involves estimating the uncertainty or upper-bound of r from partial sky, specifically for the case of null CMB tensor modes ($r = 0$). Since this work is a methodological analysis, we only take into account simulations that include white noise and CMB. We introduce four likelihood estimators, three of which operate in the spectral domain and one in real space. We describe the approximations and implementation challenges associated with each estimator. We test them using three statistical approaches: Maximum Likelihood Estimation (MLE), Maximum A Posteriori Estimation (MAP) and Bayesian Inference (BI). We demonstrate how each method provides different estimates depending on the fraction of sky observed. The Bayesian approach and pixel-based estimator yield the most reliable results, so they are considered as references. We demonstrate that spectral estimators that ignore the correlation between different multipoles, approximating the presence of the mask with the term $(f_{sky})^{-1}$, underestimate the uncertainty. Spectral estimators that are more complex and account for this correlation result in overestimates of the uncertainties when compared to pixel-based methods. These considerations are especially relevant for $r = 0$. For positive tensor-to-scalar ratios, the spectral approaches converge to similar estimates and become more accurate. The results of this work, although obtained under simpler conditions than real observations, highlights how crucial the choice of methods is for forecasting the results of future experiments.

Resumen

El fondo cósmico de microondas (CMB, por sus siglas en inglés) es una radiación electromagnética difusa que impregna todo el universo. Se originó aproximadamente 380,000 años después del Big Bang, cuando el cosmos pasó de un estado opaco a uno transparente. Esta radiación remanente desempeña un papel fundamental en nuestra forma de entender la cosmología. Aunque ahora tenemos una buena comprensión del CMB, algunos aspectos relacionados con su polarización siguen siendo desconocidos. Los modos B son un patrón de polarización distintivo que se supone originado por las primeras ondas gravitacionales producidas al principio del universo durante la inflación cósmica. Sin embargo, este patrón de polarización aún no se ha observado y su detección es uno de los principales objetivos de la cosmología observacional.

Observar el CMB polarizado presenta desafíos muy importantes. Parte de estos desafíos proviene del hecho de que la señal es muy débil y requiere un control enorme de los errores instrumentales sistemáticos. Otra parte proviene del hecho de que las emisiones astrofísicas galácticas y extragalácticas eclipsan esta señal primordial. En el espectro de microondas, el polvo térmico domina la emisión polarizada de longitud de onda corta, y la radiación sincrotrón la de longitud de onda larga. La mayor parte del trabajo presentado se centra en caracterizar esta última. La tesis incluye dos artículos publicados sobre este tema.

El primer trabajo se centra en la caracterización de los espectros de potencia (EE, BB y EB) de la emisión polarizada de sincrotrón a 23 y 30 GHz utilizando datos proporcionados, respectivamente, por dos observatorios espaciales: *WMAP* y *Planck*. Estudiamos seis regiones del cielo que cubren desde el 30 % hasta el 94 % del cielo, enmascarando el centro galáctico y las fuentes puntuales. Analizamos la distribución angular y la distribución espectral de energía (SED) a escalas entre varias decenas de minutos de arco y varios grados. Los resultados de referencia se obtienen para la máscara que permite el 50 % del cielo, utilizando el análisis cruzado de los experimentos. Encontramos que los espectros de potencia EE y BB muestran una caída pronunciada en función de la escala angular, $\ell^{\alpha_{EE,BB}}$, donde $\alpha_{EE} = -2{,}95 \pm 0{,}04$ y $\alpha_{BB} = -2{,}85 \pm 0{,}14$. La razón de amplitud entre BB y EE, en el multipolo $\ell = 80$, es 0.22 ± 0.02. El espectro EB es compatible con cero a 1σ. La distribución espectral de energía se ajusta bien a una ley de potencia, $\nu^{\beta_{EE,BB}}$, con índices $\beta_{EE} = -3{,}00 \pm 0{,}10$ y $\beta_{BB} = -3{,}05 \pm 0{,}36$, con una tendencia a que la SED sea más pronunciada a medida que aumenta la latitud galáctica. Además del análisis para el caso de correlación cruzada, hemos obtenido resultados de los análisis independientes de *Planck* y *WMAP* que son generalmente consistentes. Al mismo tiempo, también hemos realizado pruebas para validar la solidez de nuestros resultados: hemos ajustado nuestro modelo en un rango de multipolos mayor ($10 \leq \ell \leq 400$), hemos usado mapas de frecuencia del *Planck release 4* (PR4) publicados en

2020 y hemos estimado por separado los espectros de los dos hemisferios. En todos los casos, no se registraron diferencias importantes con respecto al caso de referencia. Los resultados de este trabajo se han presentado en [1].

El segundo trabajo se centra en la caracterización de algunas propiedades morfológicas y estadísticas de la emisión polarizada de sincrotrón. Implementamos un nuevo código basado en un algoritmo recursivo amigo-de-amigo, con el cual identificamos 19 filamentos polarizados. También en este caso utilizamos los mapas de 23 y 30 GHz proporcionados por *WMAP* y *Planck*. Algunos de los filamentos ya han sido documentados en la literatura como hallazgos de anteriores análisis de *WMAP* en el cielo de microondas, mientras que cinco de ellos se presentan por primera vez. Para cada filamento analizamos la fracción de polarización, encontrando valores típicamente mayores que los de áreas con emisión más difusa, con valores de hasta el 30 %. Además, analizamos el índice espectral de polarización, que típicamente es compatible con el promedio en todo el cielo. La mayoría de los filamentos tienen una fuerte componente de polarización E, pero no B, además, algunos de ellos no tienen una contrapartida brillante en intensidad. Haciendo uso de tensores de Minkowski, analizamos la gaussianidad y la isotropía estadística de la emisión polarizada de sincrotrón. Estudiamos la región del cielo que corresponde al 80 % y 60 % de la emisión más débil, en escalas de aproximadamente entre 6 y 1.5 grados. Los resultados obtenidos a partir de los datos se compararon con los obtenidos mediante un conjunto de simulaciones gaussianas e isótropas. Encontramos grandes desviaciones ($> 3\sigma$) de la gaussianidad y la isotropía en la escala de 6° para la fracción de cielo del 80 %. Aunque las desviaciones siguen siendo notablemente altas a 1.5 °, se reducen a medida que se avanza hacia escalas más pequeñas. Analizando la fracción de cielo del 60 %, encontramos resultados compatibles entre las simulaciones y los datos al nivel de 3σ. Nuestros resultados sugieren que, incluso a escalas pequeñas, los grandes filamentos son la principal fuente de no gaussianidad. Las simulaciones gaussianas e isótropas a la resolución de *WMAP* y *Planck* imitan fielmente la emisión difusa cuando se enmascaran esas estructuras filamentosas. En la parte final de este trabajo, presentamos un algoritmo basado en datos para generar simulaciones de sincrotrón polarizado no gaussianas y anisótropas. Las simulaciones se ajustan para que coincidan con las características estadísticas y espectrales de los datos para la cobertura del 80 % del cielo. Los resultados de este trabajo se han presentado en [2].

Un conocimiento profundo de los contaminantes, como la radiación sincrotrón, nos permite desacoplar estas emisiones del CMB con mayor precisión. Sin embargo, nunca seremos capaces de separar completamente estos contaminantes de la señal cosmológica. Las estimaciones de los parámetros cosmológicos siempre deben tener en cuenta la presencia de residuos de contaminantes, así como el ruido instrumental. El último trabajo presentado en esta tesis es un análisis de diferentes métodos estadísticos y estimadores de verosimilitud utilizados para estimar un parámetro cosmológico, la razón tensor-escalar (r). El caso de estudio consiste en estimar la incertidumbre o límite superior de r a partir de un cielo parcial, en particular para el caso de modos tensoriales nulos ($r = 0$). Dado que este trabajo es un análisis metodológico, solo se han considerado simulaciones que incluyen ruido blanco y CMB. Presentamos cuatro estimadores de verosimilitud, tres de los cuales operan en el espacio armónico y el cuarto en el espacio real, detallando las aproximaciones y los desafíos de implementación asociados con cada estimador. Utilizando tres métodos estadísticos: estimación de máxima verosimilitud, estimación de máxima probabilidad a posteriori e inferencia bayesiana, se muestra cómo

cada método proporciona estimaciones diferentes en función de la fracción de cielo observada. El método bayesiano y el estimador basado en píxeles ofrecen los resultados más fiables, por lo que se consideran los métodos de referencia. Mostramos que los estimadores espectrales que ignoran la correlación entre diferentes multipolos, aproximando la presencia de la máscara con el término $(f_{sky})^{-1}$, subestiman la incertidumbre. Los estimadores espectrales más complejos que tienen en cuenta esta correlación dan lugar a una sobreestimación de las incertidumbres en comparación con los métodos basados en píxeles. Estas consideraciones son especialmente relevantes para $r = 0$. Para valores de la razón tensor-escalar (r) progresivamente más grandes, los métodos espectrales convergen hacia estimaciones similares y se vuelven más precisos. En este trabajo se han probado varias combinaciones de estimadores y técnicas estadísticas. Sin embargo, todos los resultados se obtienen con condiciones menos complejas que las observaciones reales, es decir, con mapas que sólo contienen ruido blanco y CMB. La situación se complica considerablemente cuando las estimaciones se obtienen a partir de observaciones experimentales. Sin embargo, incluso a partir de este caso simplificado, la conclusión clave es que una elección incorrecta del método puede llevar a una sobreestimación o a una subestimación de las capacidades de un experimento dado para estimar la razón tensor-escalar. Estas consideraciones deben tenerse en cuenta especialmente a la hora de hacer previsiones sobre futuros experimentos.

Contents

Chapter 1

Introduction

1.1 Modern Cosmology

The scientific discipline of modern cosmology aims to understand the universe's beginnings, development, and ultimate fate. It bridges the fields of particle physics and astrophysics to express our quest for the most comprehensive understanding of the universe. The development of contemporary cosmology has been a journey that began in the early 20th century, with the development of large telescopes, ground-breaking theoretical models, and technical advancements.

The realization that the universe is expanding was one of the major turning points in contemporary cosmology. This awareness is the result of observations made by Edwin Hubble in the 1920s that showed galaxies are moving away from us [3]. On a theoretical level, it was Albert Einstein's revolutionary insights that brought enormous contributions to the understanding of the universe. He proposed that gravity was not a force, but rather an acceleration caused by the wrapping of spacetime, the so-called General Theory of Relativity [4]. Before the 1930s, several authors already derived a model from Einstein's theories of an expanding homogeneous isotropic universe. Finding a framework to explain Hubble's observations, and leading to the formulation of the Big Bang theory.

1.1.1 Big Bang theory

The Big Bang theory postulates that the universe had a definite beginning. In its initial state it was hot and dense, from which it expanded and is still evolving. The Cosmological Principle, on which the theory is based, states that today the universe is isotropic and homogeneous on large scale. An isotropic, homogeneous and expanding universe is described by the Friedmann-Lemaître-Robertson-Walker (FLRW) metric

$$\mathrm{d}s^2 = -\mathrm{d}t^2 + a(t)^2\Big(\frac{\mathrm{d}r^2}{1-kr^2} + r^2(\mathrm{d}\theta^2 + \sin^2\theta\,\mathrm{d}\phi^2)\Big) \tag{1.1}$$

where: t is the cosmological proper time, (r, θ, ϕ) are the comoving spatial variables, $a(t)$ is a dimensionless scalar function of time and k is the so-called curvature constant. Nominally, the universe is intended as flat when $k = 0$, but it could also have a positive or negative curvature, according to the sign of k. The dynamics of the universe is

determined by the Einstein Equation

$$G_{\mu\nu} - \Lambda g_{\mu\nu} = 8\pi G T_{\mu\nu}. \tag{1.2}$$

$G_{\mu\nu}$ is the Einstein tensor, and $g_{\mu\nu}$ is the metric. These quantities encapsulate information about the geometry of spacetime. $T_{\mu\nu}$ is the stress-energy tensor, which encapsulates the information of the components that constitute the universe. G is Newton's constant, and Λ is a cosmological constant.

The solutions of the Einstein Equation for the FLRW metric[1], are the so-called Friedmann Equations

$$H^2 = \left(\frac{\dot{a}}{a}\right)^2 = \frac{1}{3}\rho - \frac{k}{a^2} \tag{1.3}$$

$$\dot{H} + H^2 = \frac{\ddot{a}}{a} = -\frac{1}{6}(\rho + 3p) \tag{1.4}$$

which combine with the continuity equation

$$\dot{\rho} + 3H(\rho + p) = 0. \tag{1.5}$$

The quantity ρ and p are respectively the energy density and the pressure of the elements that make up the universe. $H = \dot{a}/a$ is the Hubble parameter. It is a fundamental cosmological parameter, and describes the rate of expansion of the universe. The value at present time, the Hubble constant (H_0), measures how quickly the distant galaxies are fading away from us.

Both the two Friedmann equations relate the expansion rate of the universe to its energy content. The first equation 1.3 also accounts for the curvature of the universe. The second equation 1.4 accounts for the pressure exerted by the different forms of energy presented in the universe. Solving the Friedmann equations we can determine the expansion history, age, and the abundance of different components in the universe. The model that best describes the experimental evidence found to date is the so called Lambda-Cold Dark Matter (ΛCDM).

1.1.2 ΛCDM

The creation of the ΛCDM (Lambda-Cold Dark Matter) model is the outcome of years of advances in the field of cosmology. The model, which developed from the earlier Hot Big Bang theory, has taken the lead in describing the universe's large-scale dynamics and structure. According to the ΛCDM model, the universe is flat and composed by four components which contribute to its energy density: radiation, baryonic matter, dark matter and dark energy.

The *Radiation* represents the contribution of relativistic particles, mainly photons. The energy density of radiation scales as the inverse of the universe expansion factor (a) raised to the fourth, that is $\rho_r = a^{-4}\rho_{0,r}$, where $\rho_{0,r}$ is the present-day energy density of photons. Due to this, radiation made a significant contribution to the overall density in the early stages of the universe. But its energy density decreased very quickly over time as the universe cooled and expanded.

[1]We assume that the universe is filled with the so-called perfect cosmic fluid, i.e. fluid with null viscosity and without heat flows, which fully constrains the stress-energy tensor.

The *Baryonic matter*, or ordinary matter, refers to the familiar matter which includes stars, galaxies, planets and everything we can observe. This matter is well-known and described by the Standard Model (SM) of particle physics. The energy density of baryonic matter is inversely proportional to the cube of the universe expansion factor, $\rho_m = a^{-3}\rho_{0,m}$, where $\rho_{0,m}$ is the present-day energy density. It strongly interacted with electromagnetic radiation, especially in the early stage of the universe. Ordinary matter plays a fundamental role in formation of galaxies, large-scale structures, and shaping the structure of the universe.

The *Dark matter*, or non-baryonic matter, represents the non-visible matter, which is not included in the Standard Model. Its possible interaction with electromagnetic radiation or any of the particles of the standard model is very weak or non-existent. It only manifests itself through gravitational interaction with visible matter. As baryonic matter, the energy density of dark matter scales as the cube of the inverse of the universe expansion factor, $\rho_m \propto a^{-3}$. The exact nature of dark matter is still unknown. Current cosmological observations tell us that the dark matter must be cold, that is, non-relativistic. A dominant contribution of hot, i.e., relativistic, dark matter would not explain the current structure of the universe [5]. Several potential cold dark matter particle candidates have been proposed, such as weakly interacting massive particles (WIMPs) and axions. However, the nature of this matter remains an open question in modern cosmology [6].

The *Dark energy* is a form of energy that permeates the entire universe and is what causes the universe to expand at an accelerated rate. It does not interact with radiation or any forms of matter. The energy density of dark energy remains nearly constant during the universe expansion, even if recent results indicate that it may be getting weaker [7]. It is typically expressed as $\rho_\Lambda = \Lambda/(8\pi G)$, where Λ is a positive cosmological constant. The cosmological constant is a measure of the uniform energy density of empty space, which produces a repulsive gravitational force that balances the gravitational attraction of ordinary and dark matter. The exact nature of this energy is still unknown and its understanding represents one of the greatest challenges in modern cosmology.

Considering all the components present in the ΛCDM model, the first Friedmann equation 1.3 can be written in terms of the present values of the density parameters

$$\frac{H^2}{H_0^2} = \Omega_{0,r}a^{-4} + \Omega_{0,m}a^{-3} + \Omega_{0,k}a^{-2} + \Omega_{0,\Lambda}. \tag{1.6}$$

$\Omega_{0,k} = -k/H_0^2$ is the contribution coming from the curvature of the spacetime. $\Omega_{i,0} = \rho_{i,0}/\rho_{crit,0}$ are the present-day density parameter of each component of the universe, where $\rho_{crit,0} = 3H_0^2/(8\pi G)$ is the so-called critical energy density[2].

The latest observational results give the best current values of each component

$$|\Omega_{0,k}| < 0.01, \quad \Omega_{0,r} = 9.4 \times 10^{-5}, \quad \Omega_{0,m} = 0.32, \quad \Omega_{0,\Lambda} = 0.68.$$

The actual dominant component is the dark energy, which causes the accelerated expansion of the Universe. The second most abundant element is matter. In particular, dark matter makes up a majority of the universe's total mass by a factor of about five,

[2]It represents the value of total energy density in case of a perfectly flat universe ($k = 0$).

compared to ordinary matter. Radiation is completely subdominant, as is curvature, suggesting that we live in an old flat universe. In addition, experimental evidence tells us that the universe is about 13.8 billion years, and the Hubble constant is $H_0 = 67.7$ km/s/Mpc [8].

Looking at the energy density dependency on the expansion factor (a) of the single components in equation 1.6; we can easily understand that the contribution of each element to total energy density has changed over time. Three different epochs can be determined: the radiation domination era, the matter domination era and the present dark energy domination era. The succession of these epochs led to the structure of the universe as we observe it today.

1.1.3 Universe timeline

In this section we briefly review the timeline of the universe, from the Big Bang to the present [9]. We will introduce concepts that will then be explained in detail in later sections. However, it is important first to describe the context and succession of events that led to the universe as we see it today.

- Everything begins from a singularity in time and space, with infinite density and temperature. After a tiny fraction of a second from the beginning and for the duration of another tiny fraction of a second, the universe underwent a rapid and exponential expansion, known as cosmic *inflation*. This spatial stretching unified and smoothed out the universe's irregularities, making the universe homogeneous and isotropic.

- In the period between about 10^{-36} and 10^{-12} seconds from its beginning, the *Electroweak* epoch occurred. During this epoch, because of the extremely high temperature, electromagnetism and weak nuclear force were unified into the electroweak force. Particles were massless and interacted through this force. The study of this epoch provides fundamental insights into the understanding of ultra-high energy particle interactions.

- As the universe expanded and cooled, the electromagnetic and weak forces separate, leading to the *Particle era*. It refers to the period which spans approximately from 10^{-12} seconds to around 380 000 years after the Big Bang. At that time, a hot dense plasma filled the universe. The high temperature provided the necessary conditions for nuclear reactions to occur, where lightest elements, such as hydrogen (H), helium (He), and lithium (Li), were formed. This phase is known as Big Bang *Nucleosynthesis* (BBN).

- Up to 47 000 years after the beginning, most of the energy in the universe was in the form of radiation. However, as the universe expands and cools, the energy density of matter becomes comparable to that of radiation, marking the transition from the radiation to the *Matter era*. From that moment, matter mainly drives the dynamics of the universe through gravitational interactions.

- Approximately 380 000 years after the Big Bang, the temperature of the universe dropped to a critical point. Electrons and protons were able to combine forming

neutral hydrogen atoms. This critical time is known as *Recombination*, which marked the transition from an ionized to a neutral universe. At this point, the universe becomes transparent to photons, which became free to travel through space. This phase is commonly called *Decoupling*.

- After the Recombination, the universe enters a period known as the *Dark Ages*. The name comes from the fact that the universe was filled with neutral atoms, with the absence of significant sources of light. During this period, gravity causes matter to form the first stars and galaxies. These celestial objects emitted intense ultraviolet radiation, which interacted with neutral hydrogen atoms ionizing them. This process, which ended the Dark Ages, is known as *Reionization*.

- With matter dominating, ordinary and dark matter density fluctuations lead to the formation of large-scale structures such as galaxy clusters and superclusters. As the universe continues to age and expand, the matter energy density dilutes, becoming comparable to the dark energy density. Dark energy remains close to a constant as the universe grows, and relatively recently it became the predominant component, marking the beginning of *Dark Energy era*, which is still going on today.

The timeline in Figure 1.1 shows the three dominant epochs: radiation, matter and dark energy, and some of the most important stages in the evolution of the universe from the Big Bang to the present.

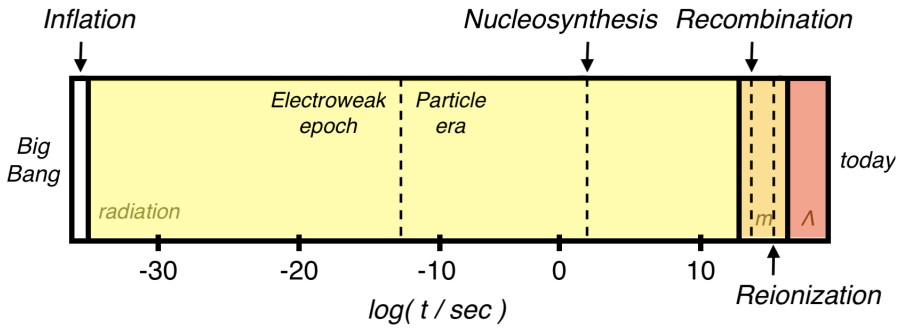

Figure 1.1: Timeline of the universe from the Big Bang to the present. The different colors represent the eras determined by the component that contributed most to the density energy. Yellow represents the Radiation era, orange the Matter era, and red the Dark Energy era. In white the very early period called cosmic inflation. The dashed lines represent some of the most important milestones in the history of the universe.

1.1.4 Observational Probes

The Big Bang theory, the ΛCDM model and the description of the universe timeline have been developed over time from observational evidence that years of research have revealed. This section reviews such observational probes, which represent cornerstones of knowledge in cosmology and astrophysics.

The most direct and well-known evidence for studying the origin and formation of the universe is the *Cosmic Microwave Background* (CMB). The CMB is a radiation that permeates the entire universe, generated at the time of photon decoupling, when the Universe was 380 000 years old. We will not go into details in this section, because it will be discussed extensively in the next sections.

An important branch of cosmology is devoted to the study of the *Large-Scale Structure* (LSS) of the universe. The term "large-scale" is commonly associated to structures on scales of tens of megaparsecs or larger, but it can vary based on the specific research question. This concept stems from the idea to separate it from the analysis of small-scales, approximately smaller than 100 Mpc, where the universe is strongly not homogeneous, and the main distribution of the matter is along filaments, clusters, and walls [10, 11]. Studying the statistical properties of the large-scale galaxies distribution, we can constrain cosmological parameters and test theoretical models. By analyzing growth and dynamics of cosmic structures, we can learn about the nature of dark matter and dark energy. By comparing observations and simulations, LSS studies provide a multifaceted approach to understanding the dynamics of structure formation, the evolution of galaxies, and the validity of gravitational theories.

There are a number of cosmological disciplines, as well as LSS, that benefit from galaxy surveys data. One of these is the analysis of *Baryon Acoustic Oscillations* (BAO). BAO refer to those acoustic oscillations generated by the photon-baryon plasma before recombination, which left a characteristic imprint in the distribution of galaxies. BAO measurements are a powerful instrument to study the expansion and evolution of the Universe [12]. Also in the context of galaxy surveys data, a further cosmological probe are *Weak gravitational lensing* measurements. Cosmological quantities can be inferred measuring the distortions in the shapes of distant galaxies due to the bending of light passing through the gravitational fields of closer massive structures. These studies provide important knowledge about dark matter distribution, the expansion of the universe, and gravitational theories [13].

An important cosmological probe is the *abundances of elements* in the universe. As mentioned in the previous section, few minutes after the Big Bang, the primordial nucleosynthesis (BBN) took place, which generated light nuclei. The comparison of predicted abundances with observations provides valuable constraints on the expansion of the early universe and on the density of the baryonic matter [14, 15].

Aside from those already mentioned, there are a number of independent cosmological evidences that contribute to the understanding of the universe. Here we mention a few of them: *Supernovae* observations, luminous astrophysical objects used for measuring cosmic distances [16]; *Gravitational Waves*, ripples in the spacetime carrying direct information about extreme astrophysical events [17]; *Neutrino* physics, subatomic particles enclosing information about astrophysical processes [18].

1.1.5 Cosmic Inflation

The Big Bang theory gives a very strong and accurate description of the Universe as we know it today and how it was in its very early times. However, the theory presented so far is a consequence of precisely such a fine-tuned set of initial conditions. Considering the Universe an improbable accident event leads cosmologists to question the meaning and reasons for these conditions. There are two conceptual issues with the standard

Hot Big Bang scenario, which form the so-called Cauchy problem [19, 20].

The first issue is the *Flatness* problem. Supernova observations and CMB measurements point out that, today, on large scale the spacetime geometry is consistent with a flat universe. This is equivalent to write the first Friedmann equation 1.3 as

$$|1 - \Omega_0| = \left| \frac{k}{(aH)_0^2} \right| \leq 0.2 \tag{1.7}$$

where Ω_0 is the density parameter of all components that fill the universe, k is the curvature constant, and the quantity $(aH)^{-1}$ is usually referred to as the comoving Hubble radius. The latter represents the maximum distance between particles in causal contact. This distance is proportional to the expansion of the universe, so it decreases going backwards in time. Roughly, at the Planck epoch $t_{pl} \sim 10^{-44}$, the quantity $|1 - \Omega_{pl}| \leq 10^{-60}$. In other words, at the very early stages the universe had to be extremely flat. A very unlikely casual initial condition.

The second issue is the *Horizon* problem. CMB observations and galaxy surveys show that the observable universe is nearly isotropic and homogeneous. This would imply that the entire observable sky, and by extension the entire universe, must have been causally connected to reach thermal equilibrium. The problem can be quantified by the comoving horizon distance, which represents the maximum distance that light could have traveled since the Big Bang. The comoving horizon can be expressed as an integral of the comoving Hubble radius

$$\tau = \int_0^t \frac{\mathrm{d}t'}{a(t')} = \int_0^a (aH)^{-1} \mathrm{d} \log a \ \propto a^{\frac{1}{2}(1+3w)} \tag{1.8}$$

where the last equality holds for a universe dominated by a fluid with equation of state $w = p/\rho$. Equation 1.8 is telling us that during the expansion ($w > 0$) the comoving horizon, thus the fraction of the universe in causal contact, increases with time. This suggests that comoving scales that are entering the horizon today were outside the horizon during the CMB decoupling. From this reasoning we infer that some region did not have time to reach thermal equilibrium, in disagreement with what we observe today.

A very logical answer to the Cauchy problem is given by the concept of a cosmic inflation. The Inflation theory was proposed for the first time in 1980 by Alan Guth [21] in order to explain the issue concerning the absence of magnetic monopoles in the universe. It assumes that everything was in causal contact very early on, and an exponential expansion of spacetime produced the initial conditions for the Hot Big Bang scenario [22]. Today, it is one of the most discussed topics of modern Cosmology. The basic paradigm is supported by a series of observational evidences, however, a definitive experimental probe is still lacking.

Back to the Cauchy problem, passing from complete causality of the universe to the condition of not causal contact, requires the existence of a period in which the comoving Hubble radius decreases

$$\frac{\mathrm{d}}{\mathrm{d}t}(aH)^{-1} = -\frac{\ddot{a}}{(aH)^2} < 0 \quad \text{so} \quad \ddot{a} > 0 \tag{1.9}$$

that is a period of accelerated expansion, for this the name inflation. By definition, this solves the Horizon problem. In addition, the same accelerated expansion can solve the

Flatness problem. From equation 1.7, we can infer

$$|1 - \Omega_f| = \frac{a_f}{a_i} |1 - \Omega_i| \tag{1.10}$$

where the suffixes i and f indicate respectively the initial and final time of the period of inflation. Equation 1.10 is telling us that whatever is the value of universe curvature before inflation, it is reduced by the factor a_f/a_i after inflation. Thus, the flatness of the universe at its early stages is not a coincidence, but a consequence of the exponential expansion.

Combining equation 1.9 with the second Friedmann equation 1.4

$$\frac{\ddot{a}}{a} = -\frac{1}{6}(\rho + 3p) > 0 \quad \Leftrightarrow \quad p < -\frac{1}{3}\rho \tag{1.11}$$

we obtain an equation of state incompatible with matter ($p = 0$) and radiation ($p = \rho/3$). The only component which satisfies this inequality is the cosmological constant ($p = -\rho$). In other words, the known particle physics is insufficient to explain this phenomenon, and an undiscovered physical field is needed for understanding the nature of this inflation.

1.2 Cosmic Microwave Background

While adjusting a microwave antenna in 1964 in order to study the reflection of radio waves from Echo balloon satellites, A. Penzias and B. Wilson found a background noise of unknown origin [23]. They discovered a homogeneous and uniform signal that was consistent with background noise of about 3.5 K; this signal was later recognized as the Cosmic Microwave Background radiation predicted by Dicke in 1965 [24].

Let's go back in time when, because of extreme temperature, the universe was filled with a dense hydrogenic plasma. Matter and free electrons strongly interacted with photon through Thomson scattering, i.e. elastic scatterings without any change in energy. When the universe was in this plasma state, it is commonly said it was opaque. As the expansion proceed and both plasma and radiation cooled down, electrons started to stably bound to nuclei. Atoms could not scatter the thermal radiation anymore. Thus, the universe became transparent, and the photons became free to propagate in space. The CMB is the thermal radiation left over from the so-called surface of last scattering. That is the set of photons we are receiving now from the time of photon decoupling, when the universe was 380 000 years old.

The history of CMB science is marked by a series of satellite and ground-based experiments that have shaped our knowledge of the universe.

1.2.1 Experiments History

A NASA satellite, the Cosmic Background Explorer (COBE), between 1989 and 1993, measured for the first time the CMB radiation at different wavelengths. It carried three instruments: Diffuse Infrared Background Experiment, or *DIRBE*, searching for cosmic infrared background radiation; Differential Microwave Radiometer, or *DMR*, mapping the cosmic radiation sensitively; and Far Infrared Absolute Spectrophotometer, or *FIRAS*, comparing the spectrum of the cosmic microwave background radiation with a precise black body. Among many remarkable achievements, we recall that it measured the blackbody spectrum of the CMB and detected temperature fluctuations, for the first time ever [25]. A milestone that earned a Nobel Prize for two of the principal investigators, George F. Smoot and John C. Mather.

The early 2000s were marked by a series of ground-based and balloon-borne experiments. *BOOMERanG* [26] was the first baloon microwave telescope to measure the first acoustic peak in the CMB power spectrum, inferring a flat universe. These measurements were confirmed soon after by other balloons like *MAXIMA* [27] and *ARCHEOPS* [28], which refined our knowledge of the universe's age and composition. The ground-based interferometers observing at frequencies around 30 GHz: Degree Angular Scale Interferometer (DASI) [29] at the South Pole, Cosmic Background Imager (CBI) [30] at the Chilean Andes, and Very Small Array (VSA) [31] at Tenerife, together with other direct maging experiments like Arcminute Cosmology Bolometer Array Receiver (ACBAR) [32] observing at 150 GHz, were able to measure higher-order peaks up to multipoles $\ell \approx 1500$. In 2002, DASI reported the discovery of the CMB polarization anisotropies [33].

A game changer in the CMB experimental history was the Wilkinson Microwave Anisotropy Probe (WMAP) mission. It was a NASA spacecraft operating from 2001 to 2010, observing the sky at five discrete radio frequency bands, from 23 to 94 GHz. It

was 45 times more sensitive than its satellite predecessor COBE, marking the beginning of the era of "precision cosmology". WMAP's measurements played a key role in establishing the ΛCDM model [34].

The benchmark for CMB science today is the Planck mission. It was a European Space Agency (ESA) spacecraft, operating from 2009 to 2013. It carried two instruments: the Low Frequency Instrument, or LFI, observing at 30, 44 and 70 GHz, and the High Frequency Instrument, or HFI, observing at 100, 143, 217, 353, 545 and 857 GHz, with resolution up to 5 arcmin. It improved and extended the results from its predecessor WMAP, providing the strongest constraints on the parameters of the ΛCDM cosmological model. Planck's data also provide strong evidence supporting the inflationary theory [8].

The future of cosmology is illuminated by a series of CMB experiments, on-going or proposed, that will bring more clarity to the early universe, digging down to the time of inflation. Remarkable ground-based experiments are: Simons Observatory (SO), a new-generation observatory in the Atacama Desert in Chile, observing around 40 percent of the sky at frequencies between 27 and 280 GHz [35]; *BICEP/Keck* array, a multi-generational series of CMB polarization experiments operating in the Antarctic Treaty area [36]; the third generation South Pole Telescope (*SPT-3G*) which will observe the southern sky at frequencies 95, 150 and 220 GHz with high angular resolution, about 1 arcmin [37]; and *CMB-S4*, a longstanding program of ground-based experiments in the Atacama Desert, covering 11 observing bands [38]. The most remarkable on-going space-based experiment is LiteBIRD [39], a satellite carrying three telescopes in 15 frequency bands between 34 and 448 GHz. The project is currently in the design and development phase, scheduled to launch in early 2030s, and will carry out its observations for about three years. Other ambitious space-based experiments are in the conceptual stage, such as *PICO*, an imaging polarimeter observing the sky in 21 frequency bands between 21 and 799 GHz [40].

1.2.2 Power Spectra

We know that today the CMB contributes about 10^{-5} to the whole energy density (Ω) of the Universe. It has a thermal black body spectrum at an average temperature of $\bar{T} = 2.725\ K$, and peaks at the frequency around 160 GHz, about 2 mm in wavelength units. It is extremely isotropic, with very small fluctuations, with typical value around 10^{-5}, equivalent to one part in 100 000 [8]. The full sky map of the temperature anisotropies as observed by Planck is showed in figure 1.2.

For a CMB observation, the temperature fluctuation in a specific direction in the sky $\hat{n} = (\theta, \psi)$, is typically written as

$$\Theta(\hat{n}) = \frac{\Delta T(\hat{n})}{\bar{T}} = \frac{T(\hat{n}) - \bar{T}}{\bar{T}}. \tag{1.12}$$

The temperature fluctuation is a two-dimensional scalar field, defined on the surface of a sphere. It can be expanded as a superposition of spherical harmonics

$$\Theta(\hat{n}) = \sum_{\ell=1}^{\infty} \sum_{m=-\ell}^{\ell} a_{\ell m} Y_{\ell m}(\hat{n}) \tag{1.13}$$

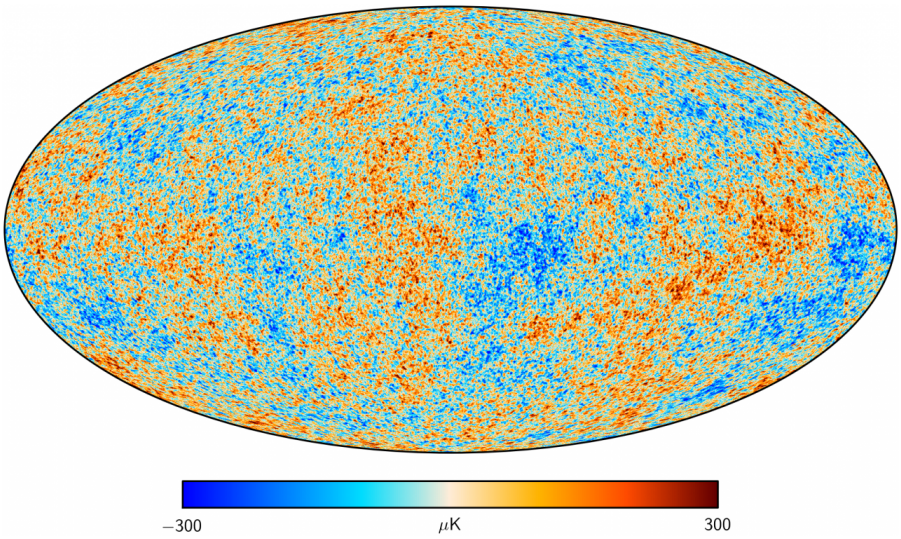

Figure 1.2: CMB temperature anisotropies map obtained with the Planck observations. [8]

where $Y_{\ell m}$ are the standard spherical harmonics on a sphere

$$Y_{\ell m}(\hat{n}) = \sqrt{\frac{2\ell+1}{4\pi}}\sqrt{\frac{(\ell-m)!}{(\ell+m)!}}P_\ell^m(\cos\theta)e^{im\phi}. \tag{1.14}$$

The multipole ℓ describes the angular size, with $\ell = 0$, $\ell = 1$ and $\ell = 2$ corresponding respectively to the monopole, dipole and quadrupole. The magnetic quantum number m, ranging between $-\ell$ and ℓ, describes the angular orientations. P_ℓ^m are the Legendre polynomials for a particular multipole ℓ and order m. All of the physical information, which is contained in the temperature field T, is also contained in the harmonic coefficients

$$a_{\ell m} = \int \mathrm{d}\Omega\; Y_{\ell m}(\hat{n})\Theta(\hat{n}). \tag{1.15}$$

By construction, the mean value of all the $a_{\ell m}$'s is zero, but with nonzero variance. The variance of the $a_{\ell m}$'s is a rotationally invariant quantity, called angular power spectrum

$$C_\ell^{TT} = \frac{1}{2\ell+1}\sum_m \langle a_{\ell m}^* a_{\ell m}\rangle \;\Leftrightarrow\; \langle a_{\ell m}^* a_{\ell' m'}\rangle = C_\ell^{TT}\delta_{\ell\ell'}\delta_{mm'}. \tag{1.16}$$

The power spectrum is a two-point function of the multipoles ℓ. It does not depend on the order m, reflecting the fact that for a given ℓ, each $a_{\ell m}$ has the same variance.

Temperature fluctuations we see in the CMB are reflections, in a complicated way that we will explore in the next sections, of primordial fluctuations. Nevertheless, we cannot make predictions about the specific value of each $a_{\ell m}$'s, we can only predict the distribution from which they are drawn. There is a fundamental statistical uncertainty in the knowledge we get from the power spectrum. This is related to the fact that we have only one realization of these distributions, which is the universe we observe. This

uncertainty is called cosmic variance

$$\sigma_{\rm cv} = \sqrt{\frac{2}{2\ell+1}} C_\ell. \tag{1.17}$$

and is most pronounced for low multipoles.

Very valuable information about the universe is encapsulated not only in the CMB temperature, but also in its polarization. Polarization is an expression of the orientation of the lines of electric flux in an electromagnetic field. The linear polarization state of the CMB radiation is usually described by two variables, Q and U, called the Stokes parameters. While the temperature T is a simple scalar field, Q and U are not rotational invariant quantities. To obviate this, linear polarization is typically described as a complex spin-2 field, $Q \pm iU$, on the sky. This quantity can be decomposed into the spin-2 spherical harmonics ${}_{\pm2}Y_{\ell m}$

$$Q(\hat{n}) \pm iU(\hat{n}) = \sum_{\ell=2}^{\infty} \sum_{m=-\ell}^{\ell} {}_{\pm2}a_{\ell m}\ {}_{\pm2}Y_{\ell m}(\hat{n}). \tag{1.18}$$

Conventionally, instead of the coefficient ${}_{\pm2}a_{\ell m}$, it is convenient to introduce the quantities

$$a^E_{\ell m} = -\frac{1}{2}({}_2a_{\ell m} + {}_{-2}a_{\ell m}), \quad a^B_{\ell m} = -\frac{1}{2i}({}_2a_{\ell m} - {}_{-2}a_{\ell m}) \tag{1.19}$$

which allow to define two scalar fields, E and B, instead of the spin-2 Stokes parameters Q and U. These fields can be expanded as a superposition of spin-0 spherical harmonics

$$E(\hat{n}) = \sum_{\ell m} a^E_{\ell m} Y_{\ell m}(\hat{n}), \quad B(\hat{n}) = \sum_{\ell m} a^B_{\ell m} Y_{\ell m}(\hat{n}). \tag{1.20}$$

This decomposition of the CMB polarization into modes has a particular geometrical interpretation. The E-mode and B-mode represent respectively the polarization orientations with electric $(-1)^\ell$ and magnetic $(-1)^{\ell+1}$ parity on the sphere. Thus, under parity transformation ($\hat{n} \to -\hat{n}$), the E-mode remains unchanged for even multipoles ℓ, whereas the B-mode changes sign.

The angular power spectra, including temperature and polarization, are defined as

$$C^{XY}_\ell = \frac{1}{2\ell+1} \sum_m \langle (a^X_{\ell m})^* a^Y_{\ell m} \rangle \quad \text{with } X, Y = T, E, B. \tag{1.21}$$

The symmetries of the anisotropies allow four types of correlations: the auto-correlations denoted by TT, EE, and BB, and the cross-correlation between temperature and E-modes denoted by TE. Under the assumption that CMB parity is conserved, the TB and EB cross-correlations vanish. In figure 1.3 are plotted the CMB temperature and polarization power spectra as observed by Planck, compared to the theoretical spectra obtained from the best ΛCDM parameter constraints.

1.2.3 CMB Temperature

The CMB temperature power spectrum, as showed in the top panel of figure 1.3, exhibits several features which provide valuable insights about properties and evolution

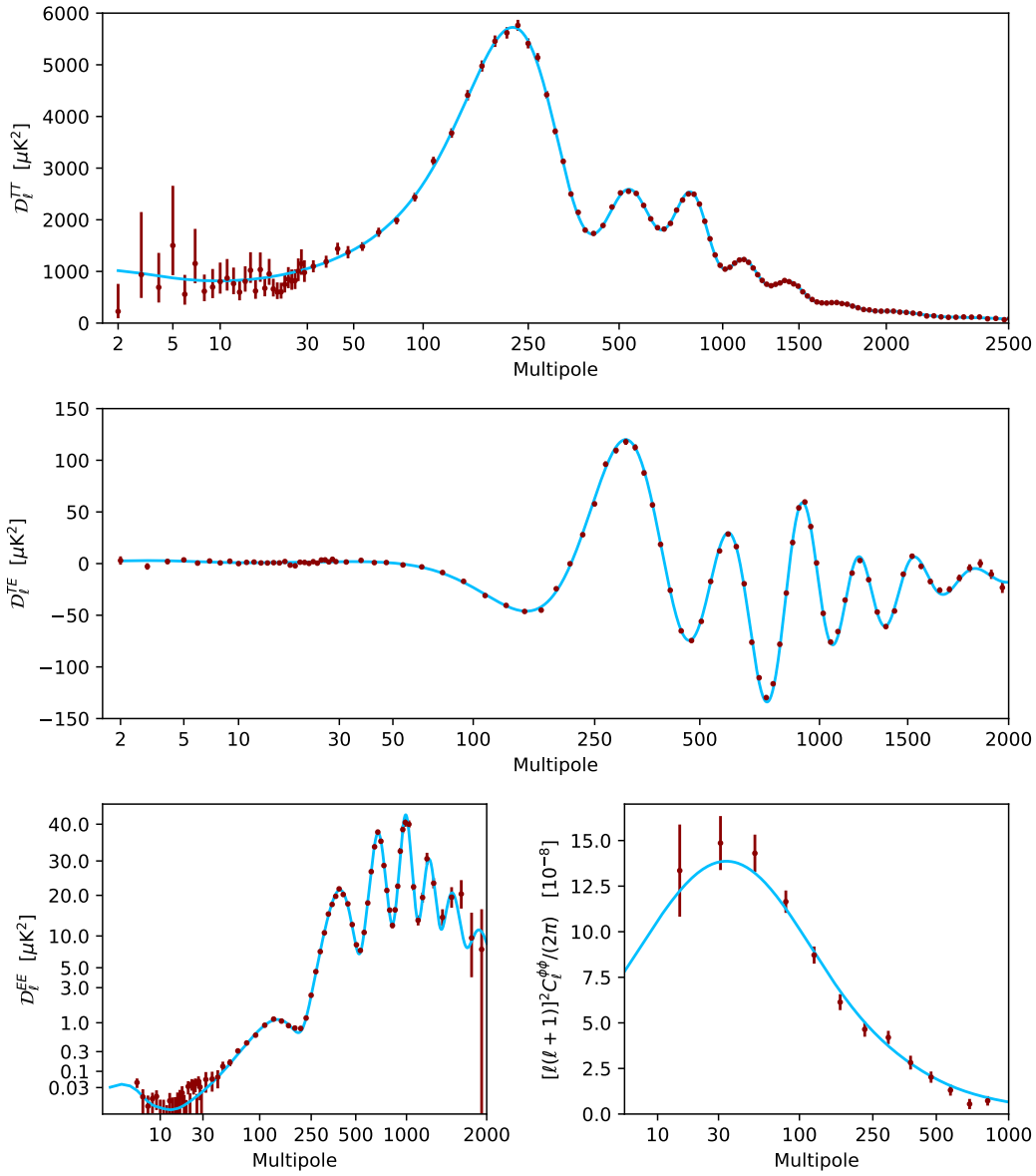

Figure 1.3: Planck 2018 CMB power spectra. Top: temperature auto-spectra; middle: temperature and polarization E-mode cross-spectra; bottom left: polarization E-mode auto-spectra; bottom right: lensing potential. Red dots are the Planck observational data, the blue line is the fitted best-fit base-ΛCDM model theoretical spectra. [8]

of the universe. Next we will describe some of those features, explaining the physical significance they contain.

The *Acoustic peaks* are the most obvious characteristics of the power spectrum. These peaks are oscillations in the density of the primordial plasma brought on by acoustic waves that were propagating through the early universe, and reached their maximum amplitude at the time of decoupling. The positions and amplitudes of these peaks play a fundamental role in the ΛCDM parameter constraints. The first peak ($\ell \sim 200$), i.e. the largest acoustic oscillations in the early universe, gives information about the spatial curvature of the universe. The second peak ($\ell \sim 500$) provides insights about the abundance of baryonic matter. Similarly, the third peak ($\ell \sim 900$) and beyond help in determining the energy content of the universe [41].

The second important feature is the *Diffusion damping* effect, appearing as a suppression of power at small angular scales ($\ell > 1000$). This phenomenon occurs because photons continue to scatter with electrons during recombination, smoothing out small-scale fluctuations. The damping provides information about the photon diffusion length at decoupling time. Moreover, the diffusion damping plays a role in shaping the characteristic scale of baryon acoustic oscilations (BAOs) [12].

At medium-to-large angular scale ($\ell < 100$), the CMB temperature spectrum is characterised by the *Sachs-Wolfe* (SW) effect, which describes the influence of gravitational fields on CMB photons. The *ordinary SW* effect occurs when CMB photons are redshifted or blueshifted while climbing out of or falling into gravitational wells at the surface of last scattering. This effect is responsible for the initial rise and nearly flat plateau around $\ell \lesssim 30$, known as the *Sachs-Wolfe plateau*. The *integrated SW* (ISW) arises from photons passing through time-varying gravitational potentials during the time of transitions to and from matter dominated eras, producing the so-called *Early* and *Late ISW* effects, respectively. The Early ISW affects the CMB spectrum from multipoles $\ell \approx 10$ up to 100, instead, the Late ISW is noticeable on very large scales ($\ell \lesssim 10$).

1.2.4 CMB Polarization

The CMB polarization information is encapsulated in the temperature-polarization cross power spectrum, namely the TE spectrum, and the auto-correlation of the two polarization modes, the EE and BB power spectra.

The correlation between temperature and polarization fluctuations in the CMB is showed in the middle panel of figure 1.3. The amplitude and shape of the TE spectrum contains information about the epoch of reionization, when energetic photons were emitted by the formation of the first galaxies. By studying the low multipoles, we learn about the matter-radiation coupling in this early stage of the universe.

As regards polarisation modes only, the EE spectrum is easier to measure compared to the BB spectrum. This is due to the fact that E-modes dominates over the B-mode in the CMB, making the BB spectrum measurement more challenging due to the relatively low amplitude. We will show in the next sections that the CMB polarization is closely tied to the primordial density and tensor perturbations of the universe. For now, we just need to know that the E-modes arise from scalars and tensor perturbations, and B-mode arise only from tensor perturbations; the difference between these types of perturbations will be explained later on.

The EE spectrum, showed in the bottom left panel of figure 1.3, is important for understanding the large-scale structure of the universe. At high multipoles ($\ell > 100$), similar to temperature, the spectrum shows Acoustic Peaks and a Silk Damping Tail. The peaks are due to the compression and rarefaction of baryons and photons in the primordial plasma. The damping is due to photon scattering during and shortly after recombination. At low multipoles, the EE spectrum shows a bump, called *Polarization Reionization Bump*. It is related to the reionization process that followed the creation of the first Galactic structures, and it offers important information about the timing and nature of that phase of the universe timeline.

Moreover, a precise measurement of the amplitude of the polarization bump, as expected from LiteBIRD [39], will allow a significant improvement in the determination of the sum of the neutrino masses. The reason is that massive neutrinos slow down structure formation and the sum of their masses can be inferred from the comparison of the amplitude of the density fluctuations at low-redshifts (given by e.g. galaxy surveys or CMB lensing) and at decoupling (given by the CMB anistropies). A good determination of the amplitude of the polarization bump will break the degeneracy between the optical depth and the amplitude of the density fluctuations at decoupling allowing an improvement in the determination of the latter.

BB spectrum measurement and characterization is the biggest challenge that modern cosmology is facing. Last experiments, including Planck, have accurately measured the contribution due to gravitation lensing. This comes from CMB photons encountering gravitational potentials while propagating through the universe. The path of the photons is then bent by gravity, leading to a distortion in the polarization patterns, generation additional B-mode polarization. This effect is important at all scales, and dominates completely at high multiples. In the bottom right panel of figure 1.3 is shown the lensing potential, i.e. a scalar field that quantifies the cumulative effect of these deflections over the entire line of sight from the surface of last scattering to the observer.

Future and ongoing experiments, such as SO and LiteBIRD, aim to shed light on another signal that it is expected to be measured in the BB spectrum, especially at large scales. This B-polarized signal would be generated by primordial gravitational waves (GW). The detection of this signal would be the ultimate proof of the inflationary theory, and the measurement of its amplitude and shape would provide crucial information about the energy scale and nature of the inflation. The relationship between the CMB B-signal, primordial GW and inflation will be explored in the following sections.

1.3 Primordial Perturbations

In the previous section we have seen how the CMB is characterized by small fluctuations in both temperature and polarization, which allow us to understand in depth the history of the universe. In this section we will show that these fluctuations we see today could be explained with primordial perturbations generated by quantum fluctuations during inflation. Finally, we will discuss how these primordial perturbations left a unique imprint on the CMB. We do not show all the details which can instead be found in [9, 20], to which we refer. We only present the key points necessary to understand this connection.

1.3.1 Scalar and Tensor

In section 1.2.2 we mentioned that the CMB is extremely isotropic, with very small fluctuations. It is therefore reasonable to assume that the universe was nearly homogeneous, with small inhomogeneities, at the time of decoupling, and even before. The small, random fluctuations in the energy density of the universe, generated during its early stages, are referred as *Primordial Perturbations*. According to this idea, we can describe the physical quantities involved in the Einstein Equations 1.2 as the sum of a homogeneous background and a perturbation

$$T_{\mu\nu}(t,x) = \bar{T}_{\mu\nu}(t) + \delta T_{\mu\nu}(t,x), \qquad g_{\mu\nu}(t,x) = \bar{g}_{\mu\nu}(t) + \delta g_{\mu\nu}(t,x). \tag{1.22}$$

The quantities with the bar at the top, $\bar{T}_{\mu\nu}(t)$ and $\bar{g}_{\mu\nu}(t)$, represent a spatially flat, homogeneous and isotropic universe. $\delta T_{\mu\nu}(t,x)$ and $\delta g_{\mu\nu}(t,x)$ are respectively the matter and metric perturbations, which are temporally and spatially dependent.

By the geometry of the background solutions, we can decompose the metric and matter perturbations into independent scalar (S), vector (V) and tensor (T) components. The importance of this SVT decomposition lies in the fact that perturbations of each type evolve independently.

Scalar perturbations are compression-like perturbations in the energy density of the cosmological fluid. This source leads to potential fluctuations that generate photons bulk flows, or dipole anisotropies, from hot to cold temperature regions. Vector perturbations are vortical motions of the matter, not associated to the energy density. This kind of perturbation decays with the expansion of the universe, for this reason we will ignore them. Tensor perturbations are transverse-traceless perturbations to the metric, representing a quadrupolar stretching of space in the plane of the perturbation.

In order to understand the nature of tensor perturbations, let us consider a metric composed of FLRW background, equation 1.1, plus a perturbation h_{ij}

$$ds^2 = -dt^2 + a(t)^2(\delta_{ij} + h_{ij}(t,x))dx^i dx^j \tag{1.23}$$

where we ignore scalar and vector contributions, according to the principle they evolve independently. Solving the Einstein Equation 1.2 at first perturbation order, we obtain the dynamic equation for the tensor perturbations

$$\ddot{h}_{ij} + 3\frac{\dot{a}}{a}\dot{h}_{ij} - \frac{\nabla^2}{a^2}h_{ij} = 0. \tag{1.24}$$

Equation 1.24 is a wave equation in an expanding universe. Therefore, primordial tensor perturbations are actually *primordial Gravitational Waves*.

1.3.2 Quantum Fluctuations

So far, we have described some features of the primordial perturbations, which now manifest themselves as CMB inhomogeneities. However, we have not explained how these perturbations were generated. The nature of this phenomenon arises from the concept of quantum field theory applied to the primordial universe. According to quantum field theory, particles and fields are subject to intrinsic quantum fluctuations, which result from the uncertainty principle. The universe dynamics was mostly subject to quantum mechanisms during its first stage, the inflationary period.

Today there are several models that try to explain the inflation mechanism, the simplest and most intuitive is the *single field slow-roll* model. This model involves a single scalar field ϕ, called *inflaton*. The single-field dynamics is determined by a self-interaction potential $V(\phi)$ which is coupled to gravity as

$$\ddot{\phi} + 3H\dot{\phi} - \frac{\nabla^2}{a^2}\phi = \frac{\partial V}{\partial \phi}. \tag{1.25}$$

The name *slow-roll* comes from the fact that to explain the accelerated expansion of the universe, the potential term must be much larger than the kinetic term $V(\phi) \gg \dot{\phi}^2$, thus causing a slow fall from the potential. Note that equation 1.25 has the same form of equation 1.24, the only crucial difference is that the inflaton dynamics has a source term $\partial_\phi V$. Instead, the equation of the metric perturbations does not.

The inflaton field is a quantum field so it is affected by quantum fluctuations, that can be expressed as

$$\phi(t, x) = \bar{\phi}(t) + \delta\phi(t, x), \tag{1.26}$$

where $\bar{\phi}$ is the homogeneous background and $\delta\phi(t, x)$ is a small quantum perturbation. In the single field model, the inflaton is the only component which filled the universe during inflation, thus it is the only contribute to the stress-energy tensor $T_{\mu\nu}$. According to the Einstein Equation 1.2, fluctuations of the field $\delta\phi$, which means fluctuations in the stress-energy tensor $\delta T_{\mu\nu}$, lead to fluctuations in the metric $\delta g_{\mu\nu}$. Fluctuations in the metric, as seen in the previous section, are nothing more than gravitational waves. Thus, quantum fluctuations during inflation are the cause of both scalar and tensor perturbations.

In a more general framework, we can divide the evolution of these quantum fluctuations into several stages. During inflation, quantum fluctuations of the primordial field at different scales, or *modes*, evolve independently. When a mode becomes larger than the horizon, because of the exponential expansion, causal physics cannot act and the fluctuations freeze out. The universe expansion proceeds, inflation ends and the radiation era starts. The expansion slows down and the modes starts to re-enter the horizon, not as quantum field fluctuations, but as physical energy density fluctuations. A diagram of this process is shown in figure 1.4. These fluctuations evolve in time and finally imprint a signature on the CMB.

1.3.3 Tensor-to-scalar ratio

Scalar perturbations are usually parameterized by the *curvature perturbation on uniform-density hypersurfaces*

$$\zeta = \Psi + \frac{H}{\dot{\bar{\rho}}}\delta\rho. \tag{1.27}$$

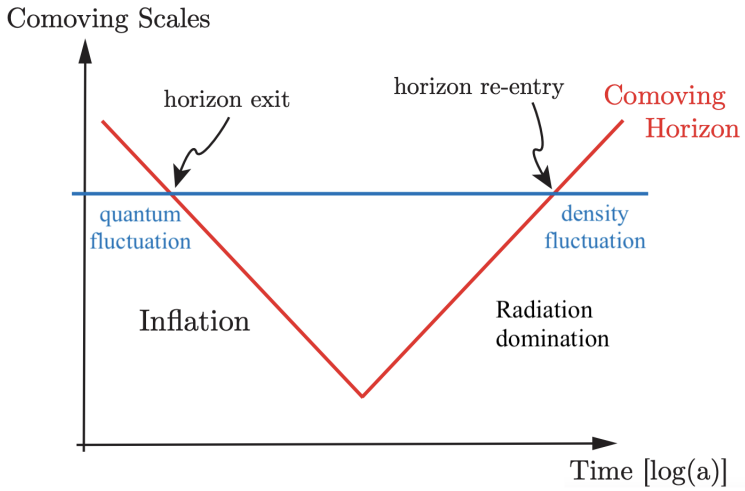

Figure 1.4: Quantum fluctuations are created on a specific sub-horizon scale. During inflation the comoving Hubble radius $(aH)^{-1}$ shrinks, and the fluctuations exit the horizon. When inflation ends and radiation domination era begins, the comoving Hubble increases. Eventually, the fluctuation re-enters the horizon, as density fluctuation. [20]

It is a combination of metric and matter perturbations, in particular, the spatial curvature perturbation Ψ and the energy density perturbations $\delta\rho$. Geometrically, ζ is a measure of the spatial curvature of hypersurfaces of constant density. It has two important features: it is gauge-invariant[3], and it remains constant for perturbation modes larger then the horizon. Tensor perturbations are gauge-invariant by construction, thus, they do not require any further definitions and are simply parameterized by the tensor perturbation h_{ij} in equation 1.23.

Primordial scalar and tensor fluctuations are conventionally treated with a statistical approach. Two important statistical measures of the primordial fluctuations are the power spectra

$$\begin{aligned} \langle \zeta_k \zeta_{k'} \rangle &= (2\pi)^3 \, \mathcal{P}_\zeta(k) \, \delta^{(3)}(k+k') \\ \langle h_k h_{k'} \rangle &= (2\pi)^3 \, \mathcal{P}_h(k) \, \delta^{(3)}(k+k'), \end{aligned} \tag{1.28}$$

which are nothing more that the Fourier transform of the perturbation two-point correlation functions. In cosmological context, the power spectra are commonly redefined as

$$\Delta^2_\zeta(k) = \frac{k^3}{2\pi^2}\mathcal{P}_\zeta(k), \qquad \Delta^2_h(k) = \frac{k^3}{2\pi^2}\mathcal{P}_h(k) \tag{1.29}$$

such that the scalar power spectrum is $\Delta_s = \Delta_\zeta$ and tensor power spectrum is $\Delta_t = 2\Delta_h$[4].

[3]In perturbation analysis, the split of quantities into background and perturbations is not unique, but it depends on the coordinates choice, or *gauge choice*. An approach to prevent such issue is to consider gauge-invariant combinations of perturbations, as fluctuations of gauge-invariant quantities cannot be eliminated by a coordinate transformation.

[4]The factor 2 accounts for the two polarization modes of h_{ij} , i.e. h^+, h^x.

An extremely important quantity in modern cosmology is the *tensor-to-scalar ratio*, which measures the ratio between the tensor over scalar power spectrum

$$r = \frac{\Delta_t^2(k)}{\Delta_s^2(k)}. \tag{1.30}$$

Detecting a nonzero tensor-to-scalar ratio would be a a direct evidence of primordial gravitational waves. Being tensor perturbations predicted by inflationary theory, the tensor-to-scalar ratio is considered the "smoking gun" of inflation. In addition, the value of r is directly related to the energy of the inflation, giving us important clues on the physics of fundamental interactions at very early times. To date, we still do not have an estimation of r, the current most stringent upper limit on the tensor-to-scalar ratio comes from the combined analysis of *Planck* and *BICEP2/KECK* data, yielding $r < 0.032$ at 95% *C.L.* [42]. Future experiments, such as LiteBIRD, aim to reach a sensitivity on r around 10^{-3}.

1.3.4 Primordial Imprint on CMB

To fully understand how primordial perturbations influenced the structure of the CMB we observe today, one would have to solve the *Radiation Transport* equation. It is the Boltzmann equation which describes the transport of photons under Thomson scattering with electrons, including gravitational effects. Following the formalism of [43], the equation can be written as

$$\frac{D}{D\eta}\mathbf{T}\ (\eta, x) = \mathbf{C}[\mathbf{T}] + \mathbf{G}[h_{\mu\nu}] \tag{1.31}$$

where η is the conformal time, $\mathbf{T} = (\Theta, Q + iU, Q - iU)$ includes both temperature and polarization, $\mathbf{C}$ is the Thomson collision term, which is functional of $\mathbf{T}$ itself, and $\mathbf{G}$ represents the gravitational effects in a perturbed metric $h_{\mu\nu}$.

The Thomson scattering is the elastic scattering of radiation by a charged particle, where both the kinetic energy of the particle and the photon frequency are conserved. Consider the simple case showed in figure 1.5, where an electron is hit by a radiation coming from the left and one coming from the top. The incident light shakes the electrons, which in turn re-radiates the outgoing light. If the incoming radiations are unpolarized but have different intensity, the scattered radiation is linearly polarized. In other words, the Thomson scattering introduces linear polarization if the initial photon distribution has a *quadrupole* pattern.

The gravitational contribution in equation 1.31 is the gravitational redshift

$$\mathbf{G}[h_{\mu\nu}] = \frac{1}{2}n^i n^j \dot{h}_{ij} + n^i \dot{h}_{0i} + \frac{1}{2}n^i \nabla_i h_{00} \tag{1.32}$$

where, for a particular direction $(\hat{n})$, the first term of the sum accounts for the stretching of the expanding spatial metric, the second for the frame dragging and the third term for the time dilation effects. These gravitational effects have an impact on freely streaming radiation, producing anisotropies in both temperature and polarisation.

The radiation transport equation is commonly evaluated in harmonic space, thus in terms of intensity I, and polarization E- and B-mode. The solution of the equation

has been reported in [44, 45], we only summarize the most remarkable result: scalar perturbations create only E-modes and no B-modes, tensor perturbations create both E-modes and B-modes. This is explained by the fact that Thomson scattering can only produce E-mode locally, B-mode cannot be generated by scattering, it arises from the photons free streaming in the pertubated metric. Therefore, detecting a cosmological signal in the CMB B-spectrum means having direct proof of the existence of primordial tensor perturbations, with a direct estimation of the tensor-to-scalar ratio.

In this section, we have come to the conclusion that the polarisation of the CMB, in particular of the B-mode, holds fundamental information to conclusively confirm the inflationary theory, while also giving us information on its nature. This turns the characterisation of the polarisation of the CMB into one of the main goals of modern cosmology. However, this goal is extremely challenging because it requires a precision in measurements and modelling of the sky that has never been achieved before.

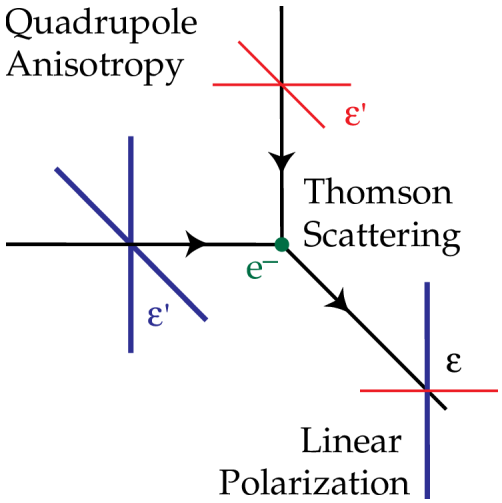

Figure 1.5: Simplified representation of Thomson scattering, showing how from two unpolarised radiations, a linearly polarised one could result. [46]

Chapter 2

CMB Detection Challenges

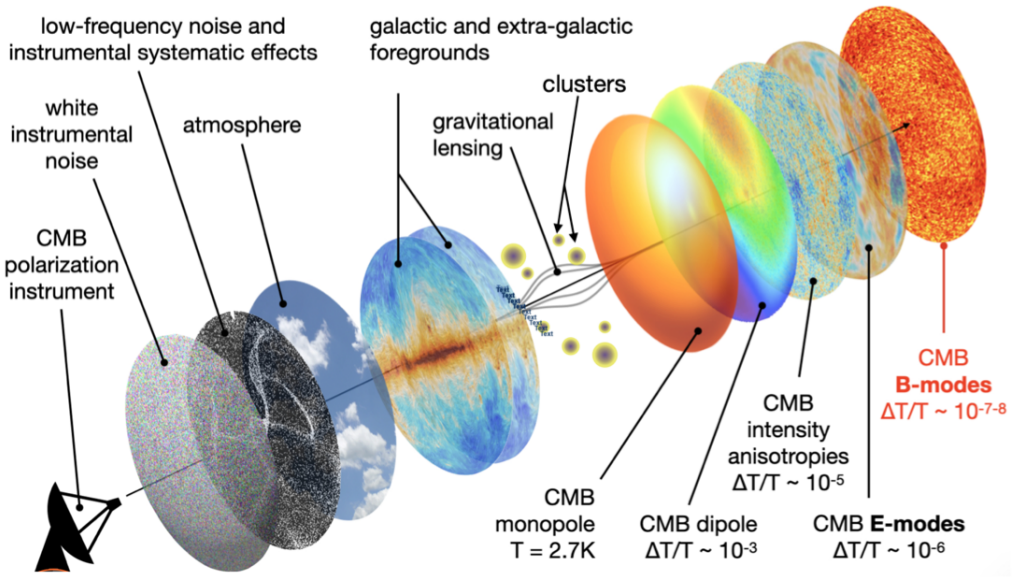

Figure 2.1: CMB experiment looking for B-modes through a maze of contaminants. Credit: *J. Errard*. https://claraverges.github.io/cmb_science.html

2.1 CMB foregrounds

The Cosmic Microwave Background radiation is an enormous source of information that allows us to discover the origin and evolution of the universe. The cosmological community has turned its efforts to the detection of the polarisation of the CMB, in particular the B-mode. The weakness of primordial B-modes makes their detection a complicated technological challenge, requiring highly sensitive experiments and sophisticated control of systematics. As showed in figure 2.1, even though we were able to control the instrumental effects, we need to make our way through a forest of contaminants.

Ground-based experiments, although easier to construct and control, have to deal with contamination from the atmosphere. Space-based experiments are much more

complex experimentally, but allow the barrier of the atmosphere to be bypassed. Past these local layers, at microwave frequencies what we observe is a complex radiation, where the contribution of the CMB is minimal. Most of the signal comes from astrophysical processes emitting in the microwave frequency range. Those Galactic and extragalactic emissions are called *CMB foregrounds*. To complete the journey to the B-modes, let us mention that even if we manage to overcome the huge barrier due to the foregrounds, there are other difficulties around the corner. Power leakage from intensity to polarisation, mainly produced by systematic effects, must be taken into account and corrected. Moreover, we should decouple the E-modes from B-modes, adjusting for possible leakage. One cause of leakage are gravitational lensing effects due to the large scale structure of the universe, such as distant galaxy clusters.

In this work, we mainly focus on the enormous difficulty we face in characterising and separating the different Galactic foreground emissions. Figure 2.2 shows the frequency dependence of those emissions in the microwave sky. In temperature, the CMB is sub-dominant everywhere except in the frequency range between 70 and 100 GHz. In polarization, the CMB is always sub-dominant. There is a minimum in the polarised foreground emissions in the 70-100 GHz range that is, however, stronger than the polarised primordial signal. For this reason, this range is typically used as a reference to separate the Galactic emissions in the so-called high and low frequency foregrounds. We will explore the physical origin of those emissions, and describe some of their features in intensity and polarisation.

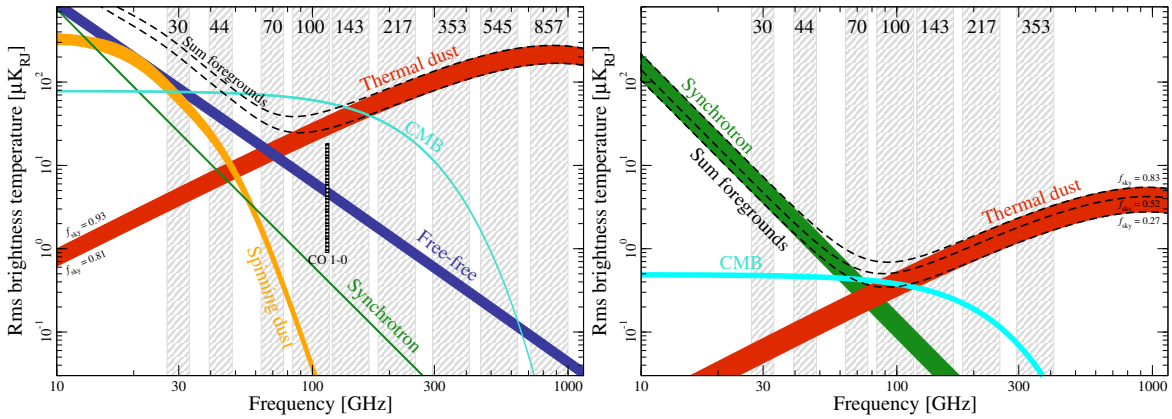

Figure 2.2: Main components of the microwave sky in temperature (left) and polarization (right) at different frequencies. The (vertical) grey bands show the Planck channels. [8]

2.1.1 Thermal dust

At high frequencies, indicatively greater than 100 GHz, the component that dominates the celestial signal is the *thermal dust radiation*. It is an electromagnetic radiation produced by interstellar dust grains in thermal motion. The spectral energy distribution (SED) is usually described by a modified black body spectrum

$$T(\nu) \propto \nu^{\beta_d} B(\nu, T_d), \tag{2.1}$$

where $B(\nu, T_d)$ is the standard black body spectrum, and $\beta_d \in [1, 2]$ is the opacity spectral index of the grains. The latest Planck observations seem to be consistent with this single black body model, although with a temperature not uniformly distributed over the entire sky [47]. A higher temperature, $T \approx 19\ K$, is measured in the Galactic centre than in the outer Galactic regions, $T \approx 15\ K$. This difference could be explained by the high number of active star formations in the inner regions of the Galaxy [48]. The latest measure of the spectral index by Planck is $\beta_d \approx 1.6$, slightly flatter compared to past measurements, suggesting more power in frequencies around 100 GHz [49]. Recent studies that include frequencies higher than those covered by Planck suggest that a two-component modified black body model fits the data better than a single modified black body model [50]. However, the analysis done with Planck alone find no significant difference between the two models.

The radiation emitted by aspherical dust grains aligned with the magnetic field has a polarized component. The net polarization fraction of thermal dust is about 5%, but can reach values up to about 20% in some regions at high Galactic latitude. As temperature, the polarized SED is well modelled by the modified black-body in equation 2.1 [51]. However, recent studies suggest that the presence of certain grains, silicate and carbonaceous, can generate spectral differences between intensity and polarization [52].

This characterisation of the thermal dust emission is based on the measurements we obtain at particular frequencies, for example the *Planck* channels, whose features are then extended to the entire frequency spectrum. This generalisation may fail in case of frequency decorrelation. Recent analyses have shown that the decorrelation can arise from the complex three-dimensional grain distribution which generates the dust emission [53]. Incorrect modelling of the emission can lead to an incorrect recovery of the CMB, and thus to an estimation of cosmological parameters, such as the tensor-to-scalar ratio, with large uncertainties and even bias [54, 55, 42].

2.1.2 Synchrotron

Relativistic cosmic ray (CR) electrons accelerated by the Galactic magnetic field emit photons, this radiation is called *Synchrotron emission*. The intensity of this radiation depends on the CR density distribution, the electrons' energy spectrum, and the strength of the Galactic magnetic field. The energy distribution of the electrons can be approximated by a power-law, $N(E) \propto E^{-p}$, with typical values close to $p = 3$ [56, 57]. Thus, the synchrotron spectrum can be described by $T \propto B^{(p+1)/2}\ \nu^{\beta}$, where B is the magnetic field strength, and $\beta = -(p + 3)/2$ is the synchrotron spectral index [58]. Typical values of β, obtained at frequencies above a few GHz, range between -2.5 and -3.5, with spatial variations of about ± 0.2 at the 1-σ level [59, 60].

The synchrotron radiation is highly polarised. In a uniform magnetic field, it can reach a polarization fractional of $\Pi = (p + 1)/(p + 7/3) \approx 75\%$. However, we observe much smaller values, because of a geometric depolarization due to tangled magnetic fields and superposition effects along the line-of-sight. In addition, at frequencies typically below 10 GHz, the synchrotron radiation is affected by the *Faraday rotation*. It is a rotation of the radiation polarization plane as photons propagates through a magnetized plasma [61]. This rotation can lead to a depolarisation of the radiation, and a mixing between the polarisation modes, E and B, most notably in the Galactic plane

region [62].

As for intensity, the polarized synchrotron emission is well described by a power law with typical spectral index β of about -3 [63]. Recent analyses seem to indicate spatial variations in the spectral index, with a tendency to steeper values from low to high Galactic latitudes [64, 65]. The spatial distribution of the polarised radiation is not uniform and extremely complicated. The emission is dominated by complex structures both local and widespread, such as loops and filaments [66]. The presence of such structures makes the statistics of the synchrotron emission strongly non-Gaussian and anisotropic.

The synchrotron emission plays an important role at frequencies below 100 GHz, becoming completely sub-dominant at higher frequencies. However, even when observed at such low frequencies the characterisation of the synchrotron intensity is complicated by degeneracy with other diffuse foreground emissions, as discussed in the next section. This degeneration is not present in polarisation, making the synchrotron radiation the most important source of CMB contamination at frequencies below 100 GHz. Some of the concepts introduced in this section will be explored in more detail in the two chapters following this one, devoted to presenting the work done to characterise the polarised synchrotron emission.

2.1.3 Free-free

At frequencies below 100 GHz, the microwave sky reveals another two important Galactic foregrounds: the free-free radiation and Anomalous Microwave Emission (AME). Despite their different nature, due to the lack of a sufficient number of observations available at these frequencies, the two emissions are still treated as degenerate.

The *free-free* emission, or thermal bremsstrahlung, is the product of free electrons interacting with ionised gas. These gases are typically composed of ionised hydrogen found in star-forming regions or in ionised bubbles around hot young stars, such as HII regions. Hence, Hα emission maps are good tracers of the diffuse free-free emission at radio wavelengths. [67]

The spectrum has a relatively flat spectral index β, with values of about -2.1, for frequencies between a few GHz and 100 GHz [67]. This feature makes the free-free radiation the dominant foreground near the foreground minimum, as showed in Figure 2.2. Free-free is intrinsically unpolarized, because electrons-ions interactions are random in orientation and present no significant alignment with the Galactic magnetic field. Thus, it is not expected to be a major concern for CMB polarization experiments.

2.1.4 AME

The *Anomalous Microwave Emission* (AME) refers to that excess of radiation that we observe at frequencies below 70 GHz, which cannot be explained by the mechanisms presented so far. Several sources have been proposed to explain its nature, the most accepted is the hypothesis of *spinning dust*. Radiation would then be emitted by rotating dust grains with irregular shapes and electric charges. Different observations, such as the measurements of the spectrum of the Perseus molecular cloud obtained by *Planck*, as shown in Figure 2.3, support the spinning dust model. An alternative hypothesis suggests that AME is the electric dipole emission from polycyclic aromatic hydrocarbon

(PAH) molecules [68]. A further hypothesis is that AME is generated by magnetic dust (MD) [69]. We do not exclude that these radiation sources may all contribute to AME, but with different amounts.

AME is expected to be very weakly polarized, less than 5%. This has been confirmed by recent studies on Galactic AME sources, such as molecular clouds [70, 71] and supernova remnants [72, 73]. Studies suggest that a polarisation of the AME, albeit small, could affect the observations of the CMB B-modes [55].

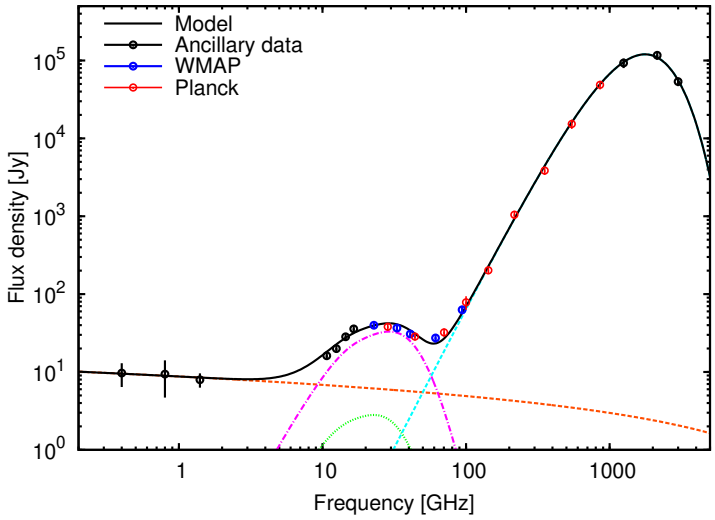

Figure 2.3: Spectrum of the Perseus molecular cloud. The emission is well fitted by free-free (orange), thermal dust (light blue), and two-component spinning dust: high density molecular gas (magenta) and low density atomic gas (green). [74]

2.1.5 Other Contaminants

The emissions described so far represent the foregrounds that contaminate the sky in a diffuse manner, however there are other emissions, mainly local, that play an important role in the CMB analysis.

Galactic and extragalactic *Point Sources* are compact astronomical objects, such as radio galaxies, quasars, active Galactic nucleus (AGN), and compact stellar remnants, that emit radiation at all microwave frequencies. The emission coming from point sources can be polarized due to the internal mechanisms of the sources. CMB analysis at small scales can be strongly affected by the presence of these sources, which therefore require special treatments such as masking or subtraction [75].

The *Sunyaev-Zel'dovich* (SZ) effect arises from the interaction of CMB photons with electrons in galaxy clusters. This phenomenon causes a distortion in the CMB intensity spectrum, but the effect is neglected in polarisation [76].

We also mention two foregrounds at frequencies higher than 100 GHz, which contaminate the sky intensity signal, but not polarisation. The *Cosmic Infrared Background* (CIB), that is an isotropic extragalactic emission coming from different sources, such as dusty star-forming galaxies, quasars and intergalactic stars. This emission is usually studied taking into account the Galactic HI emission [77]. The *CO* (carbon monoxide)

line emission, that arises from the excitation of CO molecules in Galactic or extragalactic molecular clouds. This emission occurs at specific frequencies, associated with the energy rotational transition of CO [78].

Finally we recall a source of contamination already mentioned in the previous sections, the *Gravitational Lensing*, which is not strictly speaking a foreground, but a physical effect that directly affects the CMB. In a nutshell, the gravitational potential of large-scale structures deflects the CMB photons, introducing changes in the power spectra and higher-order statistics of the CMB fluctuations. Thus, lensing generates small amounts of non-Gaussianity to the CMB and, most important, leaks power from E- to B-modes. This contribution acts like white noise to the B spectrum, becoming an enormous obstacle for the detection of primordial tensor modes.

2.2 Foreground Characterization

Observational results show that foreground signals, in particular from our Galaxy, are one of the major limiting factors of the observation of the CMB B-modes. Thus, the precise measurement of B-modes involves the analysis of those contaminants. When talking about foregrounds characterization, we usually refer to the investigation of models that describe the Galactic signal we measure, both spatially and spectrally. Specifically, there are three aspects to be measured and modelled: angular power spectrum, spectral energy distribution and morphology.

In the following sections we will give an overview of the most accepted and used foregrounds models. We focus on the characterization of two Galactic polarised diffuse contaminants: thermal dust and synchrotron. The reasons why it is important to accurately study those Galactic emissions are presented in more detail in section 2.3.

2.2.1 Angular Power Spectrum

The angular power spectrum is a statistical measure that quantifies the amount of fluctuations in the signal as a function of angular scale. It plays an important role in the generation of realistic foreground simulations.

The angular power spectrum of the polarized thermal dust radiation has been characterized in detail with *Planck* data at high frequencies [51]. It is well-described by the power law

$$C_\ell^{XY} = A^{XY} \left(\frac{\ell}{80}\right)^{\alpha_{XY}} \quad \text{with} \quad XY = EE, BB, TE. \tag{2.2}$$

The parameter α_{XY} is called angular spectral index. In figure 2.4, the best-fit lines to the Planck observations at 353 GHz are displayed. The spectra are compatible with an index $\alpha \sim -2.4$, and a B-to-E ratio of about 0.5. It has been measured a weakly positive TB correlation, but the EB signal is consistent with zero, with the EB/EE ratio smaller than 3%. The latter result has gained significant importance in studies of cosmic birefringence, which involves the rotation of the CMB plane of linear polarization, a phenomenon that may indicate new physics beyond the standard cosmological model. It has been shown that the birefringence angle can be measured via CMB EB-spectrum [79]. However, this measurement could be strongly affected by the contamination of EB from foregrounds [80].

The characterisation of dust angular spectra was performed by analysing the regions of the sky far from the Galactic plane. However, this is not possible for the synchrotron polarized signal, because of the relatively low sensitivity of current space-based observations, *WMAP* and *Planck*. The most comprehensive study on synchrotron polarization prior to our work presented in chapter 3 were conducted using data obtained at 2.3 GHz with S-PASS, a frequency quite distant from that of interest to cosmology [81]. This motivated our work in characterising the diffuse synchrotron polarization analyzing the observations of *WMAP* K-band and *Planck* 30 GHz frequency channels focusing on the intermediate and low Galactic latitudes. This is done by fitting the model in equation 2.2 also for the synchrotron, where spectra are estimated in the sky regions allowed by a set of customized masks, trying to maximise the diffuse synchrotron signal-to-noise ratio. Full details of the analysis, including methodologies and results, are given in chapter 3.

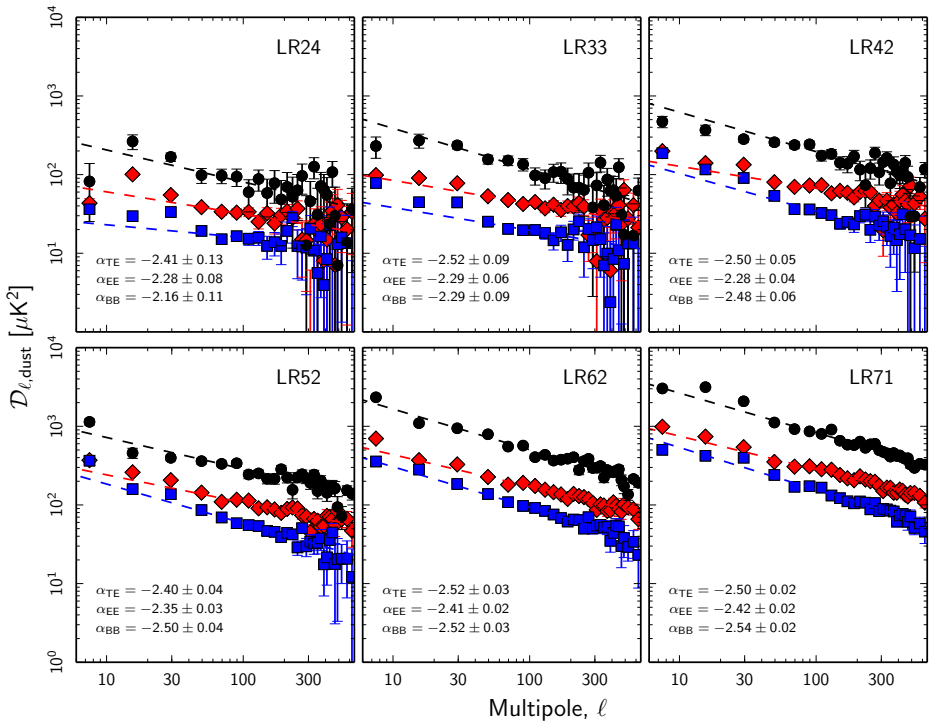

Figure 2.4: EE (red diamonds), BB (blue squares), and TE (black circles) thermal dust power spectra at 353 GHz. Each panel represents a different region of the sky, where the number in the name in the upper right corner recalls the fraction of sky. The dashed lines represent power-law fits to the data points. The obtained indices of these fits appear on the lower left corner of each panel. [51]

2.2.2 SED

The spectral energy distribution (SED) measures the dependence of the signal on the emission frequency. We have already anticipated concepts in the previous section, here we discuss them in more detail, focusing on polarisation.

The SED of the polarized thermal dust radiation is modelled by a modified blackbody with a power-law emissivity

$$\begin{pmatrix} Q(\hat{n}) \\ U(\hat{n}) \end{pmatrix} = \begin{pmatrix} A_Q(\hat{n}) \\ A_U(\hat{n}) \end{pmatrix} \left(\frac{\nu}{\nu_0}\right)^{\beta(\hat{n})} B_\nu(T(\hat{n})) \tag{2.3}$$

where $A_{Q,U}$ are the amplitudes of the dust in brightness temperature evaluated at the pivot frequency ν_0, and B_ν is the Planck function. Both spectral parameters $\beta(\hat{n})$ and $T(\hat{n})$ vary spatially. According to Planck data, the average polarized dust emissivity is $\beta = 1.55 \pm 0.05$, and the temperature $T(\hat{n})$ has values ranging between 14 and 26 K [63]. Some more complex models include the fact that dust comprises different types of materials, each with a different emissivity, however the model for each sub-species of dust remains the same [82].

The polarized synchrotron SED is usually modelled as a power law. Nevertheless, the hypothesis of a more complex model which includes a curvature factor is gaining ground

$$\begin{pmatrix} Q(\hat{n}) \\ U(\hat{n}) \end{pmatrix} = \begin{pmatrix} A_Q(\hat{n}) \\ A_U(\hat{n}) \end{pmatrix} \left(\frac{\nu}{\nu_0}\right)^{\beta(\hat{n})+c(\hat{n})\log(\nu/\nu_0)} . \tag{2.4}$$

In this equation $\beta(\hat{n})$ is the usual spectral index, whereas $c(\hat{n})$ is a parameter that quantifies deviations from a simple power law, due to various physical effects such as synchrotron self-absorption, cosmic ray's aging effect, etc. In principle, both parameters could vary spatially. In practice, this model is commonly simplified by neglecting the curvature and using a constat value for β. This is due to the fact that polarisation data at frequencies where the synchrotron dominates have still low sensitivity. On this consideration, in chapter 3 we present our work done to fit the synchrotron spectral index β to the observations of *WMAP* K-band and *Planck* 30 GHz frequency channel.

2.2.3 Morphology

What makes the study of foregrounds even more complex is their morphology. The Planck maps of thermal dust emission, as showed in figure 2.5, are characterised by a dense and intricate filamentary structure distributed over the whole sky. *Planck* analysis of the diffuse interstellar medium (ISM) points out how the structures of interstellar matter tend to be aligned with the magnetic field projected onto the plane of the sky (B_{POS}) [83]. This feature makes dust emission an excellent candidate for studying the interplay between matter and magnetic fields in the ISM.

The estimated mean polarization fraction of the filaments is about 11%. Although small, the relationship between filaments and dust polarisation plays an important role. The preferential alignment between anisotropic density structures and the interstellar magnetic field could be the cause of the B/E asymmetry [84]. A recent study proposes that the misalignment of ISM structures with the B_{POS} can generate positive TB, implying a non-zero Galactic EB [85].

Regarding synchrotron emission, although we currently have less information compared to dust, an equally complex structure is expected. The all-sky map at 408 MHz [86, 87, 88], often referred as the *Haslam* map, shows that the synchrotron intensity is mainly generated by cosmic rays accelerated by shock fronts in supernova remnants (SNRs) and pulsar wind nebulae (PWN). Outside the Galactic plane, the strong emission originates mostly from filamentary structures. The North Polar Spur (NPS), or Loop I, is the most obvious feature, but others have been observed: the Cetus arc (or Loop II) [89], Loop III [90], and Loop IV [91]. Those filaments are even more visible in the polarized sky. Studying *WMAP* polarization maps, 11 filaments have been identified and studied [66]. The true origins of filaments are still poorly understood. The most widely accepted progenitors of these large structures are old and nearby supernova remnants [92].

The presence of complex structures makes the statistics of the synchrotron emission strongly non-Gaussian and anisotropic at large scales, even in the diffuse region. Studies of the 408 MHz intensity map show that the level of non-Gaussianity remains significantly high ($> 3\sigma$) on small angular scales, $\sim 1.5°$ [93, 94]. Nevertheless, several models simulating synchrotron emission assume that the small scale fluctuations are statistically isotropic and Gaussian [95, 96, 97, 98].

This lack of information regarding polarised synchrotron emission prompted our work in chapter 4. We have characterised some of its morphological and statistical features, analyzing the observations of the *WMAP* K-band and *Planck* 30 GHz frequency channels in a region of the sky where the emission is predominantly diffuse. Full details of the analysis, including methodologies and results, are given in chapter 4.

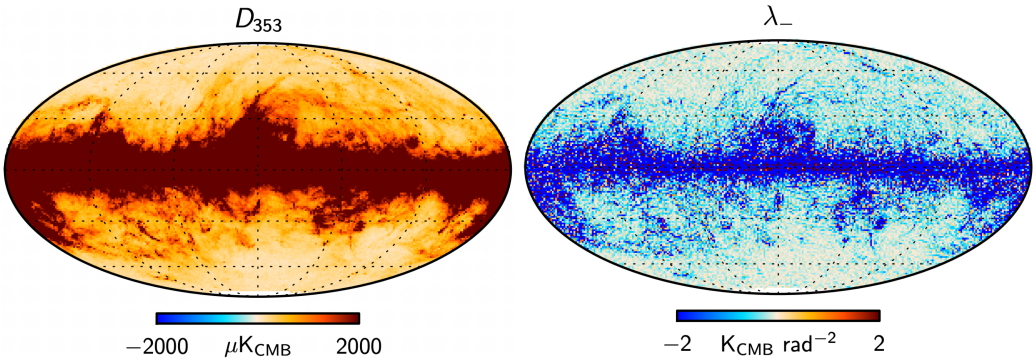

Figure 2.5: Left: Thermal dust model intensity map D_{353}, computed from a modified blackbody fit to the 353 GHz *Planck* data. Right: map of the lower eigenvalue λ_- of the Hessian matrix computed at each pixel. The map of λ_- highlights the filaments in the D_{353} map. See reference [84] for details.

2.3 Foreground Science

The microwave sky is a forest of emissions coming from different astrophysical processes. The study of these signals has always been of great interest to the astrophysical community. However, the need for accurate CMB B-mode measurements has increasingly led the cosmological community to also focus on these Galactic emissions. This has led to the design of experiments that look in greater detail at those frequencies where the cosmological signal is clearly sub-dominant, to complement cosmological observations.

In the following sections we present in more detail the motivations that lead cosmologists to study foregrounds. The same reasons that have motivated our work. In the final section we will provide a summary of experiments that aim to observe these Galactic emissions and their and their relevance for CMB studies.

2.3.1 Component Separation

The main purpose of foreground science is to extract the CMB from the sky signal. The different strategies that aim to separate the different components that make up the microwave emission are called *Component Separation* techniques. Yield at the simplest level, the observed data ($\mathbf{d}$) can be expressed as the sum of mixed sky signals ($\mathbf{s}$) and noise ($\mathbf{n}$)

$$\mathbf{d} = \mathbf{A}\ \mathbf{s} + \mathbf{n} \tag{2.5}$$

where $\mathbf{A}$ is the mixing matrix among sky components. Component Separation algorithms aim to solve the inverse problem, that is, to determine the sky components given the data. This is done by mainly combining observations of the sky at different frequencies, trying to resolve the degeneracy between the different emissions.

The Component Separation techniques are usually divided in two categories: *Blind* and *Parametric*. Blind methods make minimal assumptions about the components, such as the statistical independence of the sources or the knowledge of the spectral dependence of the CMB, but do not require a general physical modeling of the sky components. The Internal Linear Combination (ILC) [99] is the simplest blind method, which simply assumes that the CMB signal is constant, in units of thermodynamic temperature, and uncorrelated with the other signals. From the ILC, multiple extensions have been developed, such as `NILC` [100], `GNILC` [101] and `cMILC` [102]. More complex methods that are however based on linear combinations are `SMICA` [103] and `SEVEM` [104], which, together with `NILC`, played an important role in the *Planck* pipeline.

Parametric methods require modelling of the different components, including Galactic foregrounds. Those methods benefit from prior information, as the foregrounds SEDs, to disentangle signal sky components. There are many implementations of this technique in the literature, the one used in *Planck* is `Commander`, a Bayesian parametric method that allows the reconstruction of both CMB and foreground maps [105]. Other remarkable methods are *FGBuster* [106] and *B-SeCRET* [107].

In recent years, innovative techniques, such as clustering algorithms, have been developed in order to improve both blind, as `NILC` [108], and parametric, as *FGBuster* [109], methods. At the same time, new methods based on machine learning algorithms, such as neural networks [110], are emerging.

All these techniques agree that foregrounds represent a huge obstacle that needs to be mitigated in order to achieve the CMB. Among these, parametric methods di-

rectly require characterisation of these emissions, especially in polarisation, where our knowledge is still limited.

2.3.2 Models and Simulations

Having a good characterisation of foregrounds, and therefore models describing their features, allows us to generate accurate simulations of the sky microwave emission. Simulations are crucial in cosmology for several reasons. Here we describe some of the many advantages of having precise sky models and simulations, including those of Galactic emissions.

As discussed in the previous section, parametric Component Separation techniques require foregrounds models to extract the CMB. Nevertheless, even blind methods indirectly need accurate foreground information. This is because all Component Separation methods require simulations for validating and benchmarking pipelines and results. Simulations help to assess effectiveness, limitations, and potential biases of the different techniques. Apart from validation, precise simulations could also help the process of defining and optimising the separation technique.

Sky models and simulations play also a crucial role in the design and optimisation of instruments. Having examples of the sky they are going to measure, it is possible to better understand how different observational strategies, frequency coverage, and instrumental configurations could affect the CMB observations. For example, it is possible to self-calibrate instruments by forcing the observed EB angular power cross-spectra to be zero. However, this method necessarily depends on the contribution of the foregrounds to the EB spectrum [111].

Simulations are essential for parameter and error estimation for two reasons. First, they allow us to make accurate forecasts of cosmological parameters under certain experimental conditions. This is important when proposing future experiments. Second, when simulations are compared with data, they provide a framework for quantifying the contaminant impact on parameter estimation in terms of uncertainties. For example, it is possible to have a robust measure of the cosmic birefringence angle from CMB EB spectrum, only if realistic dust models are taken into account [80].

2.3.3 Current Observations of Foregrounds

There is a large effort within the CMB community in order to measure the tensor-to-scalar ratio, with a large number of currently on-going or planned experiments whose main goal is to reach a sensitivity on r down to 10^{-3}. As shown so far, the way to get to the CMB B-modes is through the complex foreground science.

Thanks to the advent of the new generation of ground and space-based telescopes, which we mentioned in section 1.2.1, we expect to obtain very relevant information about foreground emissions. However, a new class of experiments, observing frequencies far from the range where the foreground emission is minimum, is emerging and becoming increasingly decisive. These are characterised by the fact that the study of foregrounds is a fundamental part of their objectives, in order to pave the way for next-generation CMB-oriented experiments.

There are important experiments already observing the sky at frequencies below the minimum emission of foregrounds, some of which are listed below. The *QUIJOTE*

(*Q-U-I* JOint TEnerife) experiment consists of two telescopes observing the northern sky emission in the microwaves frequency range 10-42 GHz [112]. It provides unique information to characterize the Galactic and extragalactic physical processes such as synchrotron radiation and AME. Observations of the sky at even lower frequencies were obtained through the S-Band Polarization All Sky Survey (*S-PASS*), a survey of polarized radio emission taken with the Parkes radio telescope at 2.3 GHz [113]. The C-Band All Sky Survey (*C-BASS*), is an on-going project to map the whole sky both in temperature and polarization at 5 GHz, whose observations will be publicly released soon [114].

At frequencies above 100 GHz, there are several experiments that will bring great information about foregrounds and lensing, such as SO and SPT-3G, already mentioned in section 1.2.1. Additionally, other experiments include *Taurus*, a balloon-borne experiment that will measure over 70 per cent of the sky in four frequency bands within the range 150-350 GHz [115].

2.4 Parameter Estimation

A major challenge in modern cosmology is the determination of the cosmological parameters that together describe a model for the universe, such as the ΛCDM. Therefore, scientific advances require these parameters to be estimated with increasing precision. In the context of the CMB, this translates into the demand for progressively more precise measurements of the primordial radiation.

In the previous chapters, we have seen some of the challenges we face when measuring the CMB, and how the observational community seeks to address them. Experimentally, by building increasingly precise instruments. Analytically, by implementing increasingly sophisticated Component Separation algorithms. However, it is physically impossible to have a direct and uncontaminated measurement of the CMB. Even the best instrumentation and the most advanced Component Separation algorithms leave noise and foreground residuals. Therefore, parameter estimation must always take these contaminants into account, which makes the task non-trivial.

2.4.1 Probability notions

The estimation of parameters is based on probabilistic concepts. Probability represents a quantitative measure of the uncertainty associated with an event. In cosmology, it is used to assess the likelihood of a theory, against observed data. In this section we review some fundamental concepts of probability.

Given a certain theory, what we have is the probability of obtaining a data set ($\mathbf{d}$) given a set of parameters ($\boldsymbol{\theta}$) defining the theory. Introducing some notation, this probability is described by the function $P(\mathbf{d}|\boldsymbol{\theta})$, often referred to as *likelihood* function $\mathcal{L}(\mathbf{d}|\boldsymbol{\theta})$. However, in estimating cosmological parameters, we are interested in the inverse relationship. We are interested in the value of the theoretical parameters given a data set, a quantity $P(\boldsymbol{\theta}|\mathbf{d})$ which is called *posterior* probability. To obtain the latter we can use Bayes' theorem

$$P(\boldsymbol{\theta}|\mathbf{d})P(\mathbf{d}) = P(\mathbf{d}|\boldsymbol{\theta})P(\boldsymbol{\theta}), \tag{2.6}$$

such that

$$P(\boldsymbol{\theta}|\mathbf{d}) = \frac{P(\mathbf{d}|\boldsymbol{\theta})P(\boldsymbol{\theta})}{P(\mathbf{d})}. \tag{2.7}$$

In the last expressions, $P(\mathbf{d}|\boldsymbol{\theta})$ is the likelihood function, as explained, which quantifies the extent to which the data set supports the parameter proposition. $P(\mathbf{d})$ is the probability of the data, it can be proved that it does not depend on the parameters ($\boldsymbol{\theta}$), so we can safely ignore it. $P(\boldsymbol{\theta})$ is the *prior* probability of the parameters, which represents one's beliefs about the theory, before data are taken into account. If we do not assume any prior information, we can consider it uniform, then

$$P(\boldsymbol{\theta}|\mathbf{d}) \propto \mathcal{L}(\mathbf{d}|\boldsymbol{\theta}). \tag{2.8}$$

The dependence on the prior can be problematic especially in cases where the data are not very discriminatory. Instead, if the data do have discriminatory power, the likelihood usually provides a good representation of the posterior probability. However, if the prior is strong, even with discriminatory data, the prior may still play a substantial role in the final estimation.

2.4.2 Likelihood Estimators

Returning to our problem of estimating cosmological parameters. Given some cosmological observations, we can determine the parameters by looking to those values with higher probability. Mathematically, we search for values that maximize the likelihood function in the parameter space. This statistical method is called *Maximum Likelihood Estimator* (MLE)

$$\bar{\boldsymbol{\theta}}_{MLE} = \arg\max_{\theta} \mathcal{L}(\mathbf{d}|\boldsymbol{\theta}). \tag{2.9}$$

Parameter estimation based on MLE has proven to be a powerful and indispensable tool. It not only provides an estimate of the parameter itself, but also its uncertainty. If we approach the problem analytically, the value that maximises the likelihood is that value for which the first derivative of the likelihood, with respect to the parameter itself, is zero

$$\left.\frac{\partial \log \mathcal{L}}{\partial \theta}\right|_{\theta=\bar{\theta}} = 0, \tag{2.10}$$

for simplicity we assume here that the likelihood only depends on one parameter θ and $\bar{\theta}$ is the value that maximises the likelihood. The second derivative of the likelihood with respect to the parameter

$$\mathcal{F} = -\left.\frac{\partial^2 \log \mathcal{L}}{\partial \theta^2}\right|_{\theta=\bar{\theta}} \tag{2.11}$$

represents the curvature of the likelihood function at its maximum value. It describes how rapidly the likelihood function falls away from the maximum. When the curvature is small, the likelihood changes slowly and the data are weakly constrained, resulting on large uncertainty on the parameter. In contrast, a large curvature results in small uncertainties.

The MLE uses a *Frequentist approach* because it estimates parameters purely based on data. From a probabilistic point of view, this means having not any prior information. However, in some cases of parameter estimation, we may already have a prior knowledge of the parameters we want to estimate. Following the notation introduced in the previous section, we have some belief distribution $P(\boldsymbol{\theta})$, or prior, and after observing data, we have a new belief distribution $P(\boldsymbol{\theta}|\mathbf{d})$, or posterior. We can then estimate the parameters by looking to those values that maximize the posterior distribution. This statistical method is called *Maximum A Posteriori* (MAP)

$$\bar{\boldsymbol{\theta}}_{MAP} = \arg\max_{\theta} P(\boldsymbol{\theta}|\mathbf{d}) = \arg\max_{\theta} \mathcal{L}(\mathbf{d}|\boldsymbol{\theta}) P(\boldsymbol{\theta}). \tag{2.12}$$

MAP reduces to an MLE in the case of uniform prior, in fact MAP is a generalisation of MLE.

The MAP uses a *Bayesian approach* because it incorporates prior knowledge into our estimate according to the Bayes' theorem. There exist several other methods of Bayesian estimation to select the central tendency from the posterior distribution apart from the maximum[1]. These estimation methods fall under the branch of statistics called *Bayesian Inference*. Without having a specific method of selecting the central tendency

[1]For example, the median of the posterior is also considered a robust estimator for one-dimensional problems.

of our estimate, we can still obtain a confidence interval for the estimated parameter. This is achieved by integrating the posterior

$$(\sigma_\theta)_{BI} = \int P(\boldsymbol{\theta}|\mathbf{d})\ d\boldsymbol{\theta} = \int \mathcal{L}(\mathbf{d}|\boldsymbol{\theta})P(\boldsymbol{\theta})\ d\boldsymbol{\theta} \tag{2.13}$$

where the extremes of integration determine the confidence interval.

2.4.3 Likelihood and CMB

In the context of CMB observations, given its very nature, we often have to deal with N-dimensional multivariate normal random vectors ($\mathbf{x}$). Thus, the likelihood takes the form

$$\mathcal{L}(\mathbf{x}) = \frac{1}{(2\pi)^{N/2}(\det \mathbf{C})^{1/2}} \exp\left(-\frac{1}{2}(\mathbf{x}-\boldsymbol{\mu})^T\mathbf{C}^{-1}(\mathbf{x}-\boldsymbol{\mu})\right) \tag{2.14}$$

where $\boldsymbol{\mu}$ is the mean vector and $\mathbf{C}$ is the covariance matrix. The observable $\mathbf{x}$ is the data we obtain from telescopes as sum of the CMB signal and noise[2]. It can be studied either in real space, as a pixelised map of the sky, or in spectral space through its power spectrum. Given its expression, far from the maximum, the likelihood $\mathcal{L}(\mathbf{x})$ typically becomes exponentially small. So it turns out to be much easier to deal with the logarithm of the likelihood ($-\log\mathcal{L}(\mathbf{x})$)[3], which reads

$$-\log\mathcal{L}(\mathbf{x}) = \frac{1}{2}(\mathbf{x}-\boldsymbol{\mu})^T\mathbf{C}^{-1}(\mathbf{x}-\boldsymbol{\mu}) + \frac{1}{2}\log(\det\mathbf{C}) + \text{const.} \tag{2.15}$$

Note that in a realistic scenario the likelihood is a complex object, and it is not always possible to find analytically the maximum from the equation 2.10. Then one must numerically evaluate the value of the likelihood for a reasonable range of values for the parameter θ and look for where the maximum lies.

The CMB we measure is only a statistical realisation obtainable from certain cosmological parameters. Apart from systematic errors and residual foregrounds, noise also has a statistical component. Thus, to assess the result obtained from the actual observation, we need to compare it with a large sample of data obtained with simulations[4]. Each simulation is the sum of signal and noise ($\mathbf{x}_i = \mathbf{s}_i + \mathbf{n}_i$), both of which are assumed to be drawn from some particular distributions. The MAP searches for the value $\{\theta_i\}$ that maximises the posterior (or likelihood in case of MLE) for each simulation $\{\mathbf{x}_i\}$. It thus provides a maxima distribution in parameter space, where each point represents the value that maximises the posterior, or likelihood, for a particular realisation of the signal plus noise. From this distribution it is possible to obtain the best estimate of cosmological parameters and their uncertainty. Those values can then be compared with the estimation found with the real observation of the sky.

[2]By noise we refer to that component of the observed signal that cannot be attributed to primordial processes. Thus it includes experimental noise, foreground residuals and any other effects that distort the primordial signal.

[3]We add the minus sign because numerically it is easier to look for a minimum, than a maximum. Thus, what an MLE usually does is to look for the minimum of the function ($-\log\mathcal{L}(\mathbf{x})$).

[4]Foregrounds as well as systematic errors do not cancel out when averaged over many simulations, so they must be taken into account in the likelihood itself.

An important quantity in cosmology is the *Fisher matrix*, computed as the average of the likelihood curvature over many realizations of signal and noise

$$F = \langle \mathcal{F} \rangle = - \left\langle \frac{\partial^2 \log \mathcal{L}}{\partial \theta^2} \right\rangle = \frac{1}{2} \left(\frac{\partial \mathbf{C}}{\partial \theta} \mathbf{C}^{-1} \frac{\partial \mathbf{C}}{\partial \theta} \mathbf{C}^{-1} \right). \tag{2.16}$$

If the data points are really distributed as a Gaussian, the expected errors on the parameters are $\sigma_\theta = 1/\sqrt{F}$ where F is evaluated at the likelihood true maximum. This is a simple and direct method of obtaining the achievable uncertainty for an estimated parameter. This is why it is widely used to generate forecasts for proposed experiments. Nevertheless, we emphasise that this method of estimating uncertainty is only accurate if the data are drawn from Gaussian distributions. Otherwise, this provides an approximated estimation, often optimistic, of the uncertainty.

2.4.4 Parameter Forecasting

A wide variety of ground-based and space-based experiments, that are currently under construction or in preparation, aim to measure the primordial tensor modes through the B-modes of the CMB. The parameter quantifying such primordial tensor perturbations is the tensor-to-scalar ratio (r). Thus, any experiment with this purpose, even before actual development begins, needs a prediction of the precision with which this parameter can be measured. This is generally referred to as *parameter forecasting*. The forecast is usually calculated using simulations and a parameter estimator.

Simulations play a key role in the forecast of an experiment. They must contain all experimental errors, including possible systematics and statistical noise. But also the contribution of Galactic and extra-galactic foregrounds. These simulations are usually generated from a sky model and a instrumental response model. Then the complete pipeline is applied to the simulated CMB, just as one would do with real data. The simulated CMB maps thus have the same characteristics that the data would have, including the noisy foreground residuals.

From the CMB simulations, we can then infer the values of the cosmological parameters, such as r, and their uncertainties. However, even before starting this inference process, non-trivial choices are required. The first choice is the observable, which can be directly the pixel values of the CMB sky map, or its power spectrum. The choice of sky region to be analysed is also an important choice. Once the observable is chosen, we need to define the likelihood function, such as the one in equation 2.14. This choice may depend on several factors, both mathematical and computational, and approximations are often necessary. Finally, we need to define which approach to use to estimate the parameters and their uncertainties. One can use a frequentist approach, such as the MLE, or a Bayesian approach, as MAP where a prior probability is required. Each of these individual choices can considerably influence the final result of the estimate.

In Chapter 5, we analyse the importance of these choices - observable, sky region, likelihood and statistical approach - in the estimation of the tensor-to-scalar ratio. Since we are mainly interested in the impact of such choices in estimating the uncertainty of r, we will use simple simulations of CMB and white noise, bypassing the difficulties in generating realistic simulations.

Chapter 3

Characterization of the polarized synchrotron emission from Planck and WMAP data

The purpose of this work is to characterize the diffuse Galactic polarized synchrotron, which is the dominant CMB foreground emission at low frequency. We present EE, BB, and EB power spectra estimated from polarization frequency maps at 23 and 30 GHz as observed respectively by the *WMAP* K-band and the *Planck* lowest frequency channel, for a set of six sky regions covering from 30% to 94% of the sky. We study the synchrotron polarization angular distribution and spectral energy distribution (SED) by means of the so-called pseudo-C_ℓ formalism, provided by the `NaMaster` package, in the multipole interval $30 \leq \ell \leq 300$. Best results are obtained cross-correlating *Planck* and *WMAP* data. The EE and BB angular power spectra show a steep decay of the spectral amplitude as a function of multipole, approximated by a power law $C^{EE,BB} \propto \ell^{\alpha_{EE,BB}}$, with $\alpha_{EE} = -2.95 \pm 0.04$ and $\alpha_{BB} = -2.85 \pm 0.14$. The B/E power asymmetry is proved with a B-to-E ratio, computed as the amplitude ratio at the pivot multipole $\ell = 80$, of 0.22±0.02. The EB cross-component is compatible with zero at 1σ, with an upper constraint on the EB/EE ratio of 1.2% at the 2σ level. We show that the EE and BB power-law model with null EB cross-correlation describes reasonably well the diffuse synchrotron polarization emission for the full sky if the bright Galactic center and point sources are masked. The recovered SED shows power-law spectral indices $\beta_{EE} = -3.00 \pm 0.10$ and $\beta_{BB} = -3.05 \pm 0.36$ compatible between themselves, in the frequency range 23–30 GHz. Results also seem to indicate that the SED gets steeper from low to high Galactic latitude.

3.1 Data and Simulations

3.1.1 Data

For our analysis, we will use *Planck* and *WMAP* data. *Planck* was a space-based experiment consisting of two instruments, the Low Frequency Instrument (LFI) and the High Frequency Instrument (HFI), observing both the total intensity and polarization of sky photons, and covering a wide frequency range from 30 to 857 GHz with 9 frequency

channels. In this work, we use the 2018 data release (PR3) [8], obtained from the full set of observations, focusing on the lowest channel at central frequency 28.4 GHz. In Appendix A.2.1, we use instead the 2020 *Planck* release (PR4), computed with the `NPIPE` processing pipeline [116], in order to test the consistency with our main results. *Planck* data were downloaded from the *Planck* Legacy Archive[1] (PLA) and then downgraded down to the pixel resolution corresponding to the $N_{side} = 512$ `Healpix` parameter. Note that the resolution of the PR3 (PR4) 30 GHz *Planck* map corresponds to an effective beam of FWHM = 32.39 (31.5) arcminutes.
WMAP was also a space-based experiment, which observed the total intensity and polarization of the sky, using a narrower frequency range, from 23 to 94 GHz, with five frequency bands. In our analysis, we include the lowest frequency channel of the *WMAP* dataset, namely the *K*-band centered at 23 GHz [117], obtained from the 9-yr data release. All *WMAP* products have been downloaded from LAMBDA[2] and have been analysed at their original resolution ($N_{side} = 512$, with an effective beam of FWHM=0.88°).

In order to estimate the power spectra from only *Planck* data, we cross-correlate the two half-ring 30 GHz maps, that are generated using only the first and the second halves of each pointing period, respectively. Using the cross-correlation of splits, rather than the auto-spectra from the full mission data, has the advantage of cancelling instrumental noise and reducing the effect of systematics. For the only-*WMAP* analysis, we follow an analogous procedure and use as splits the co-added maps from 1 to 4 years on one side, and from 5 to 9 years on the other. Power spectra results are also obtained from the cross-correlation of *WMAP* and *Planck* maps, using in this case the full-mission *Planck* and the co-added nine-year *WMAP* maps. By cross-correlating data from independent experiments, we can use directly the full data set rather than the splits, since the instrumental noise is uncorrelated and the effect of the systematics is also reduced. This also allows us to use the larger number of simulations which are available at the PLA for the *Planck* full mission case with respect to the half-ring splits. The full-mission *Planck* maps have significantly lower noise than the nine-year *WMAP* maps, however, the synchrotron brightness in the *Planck* lowest frequency, at 28 GHz, is around half that in the *WMAP* K-band, at 23 GHz, what ends up in very similar foreground signal-to-noise for both experiments. According to [60], at a scale of 1°, the median (mean) signal-to-noise for *WMAP* K-band is 2.47 (3.77) while for *Planck* 30 GHz we have 2.64 (3.72). Nevertheless, each map is better in some sky regions because of the different scan strategies. Maps are shown in Figure 3.1.

3.1.2 Simulations

In order to estimate the errors of our set of power spectra and evaluate the goodness of fit, we use simulations. The simulations for the two instruments, both splits and full-mission, contain the sum of CMB, foregrounds and noise. A foreground simulation is generated with the Python Sky Model package[3] (`PySM`) [98], currently used for the sky modeling of many CMB analysis, at *Planck* and *WMAP* frequencies with the considered

[1] pla.esac.esa.int
[2] lambda.gsfc.nasa.gov/product/map
[3] pysm3.readthedocs.io

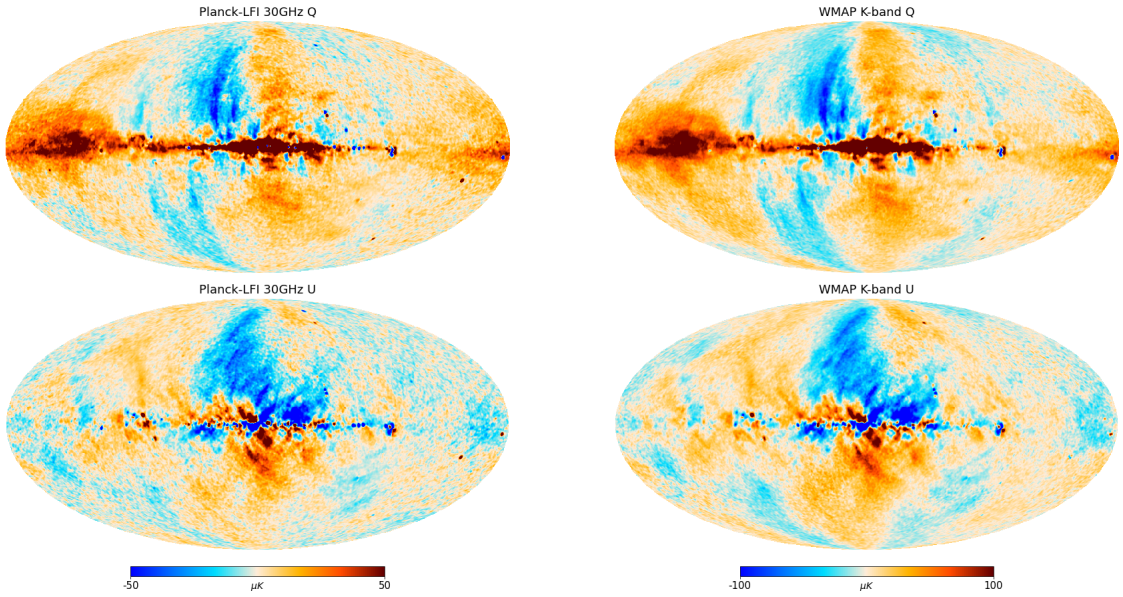

Figure 3.1: Left: Q (top) and U (bottom) polarization all-sky maps of the *Planck* 30 GHz frequency channel [8]. Right: Same maps for the *WMAP* K-band [117]. All maps have a resolution of 1°.

resolutions[4]. The chosen model includes two polarized components: thermal dust, modelled as a single-component modified black body (d1), and synchrotron emission, described as a power law scaling with a spatially varying spectral index (s1). AME and free-free emission are not included, since they are assumed to be unpolarised. We recall that the PySM synchrotron model was obtained combining the first *WMAP* polarization data with the Haslam total intensity map at 408 MHz [86], including a model for the Galactic magnetic field [118].

Note that we are always using the same foreground model for all simulations. This procedure has also been followed in previous analyses [51, 119] due to the fact that foregrounds are deterministic and also to the difficulty of producing different realistic foreground models. However, this procedure does not include the uncertainties associated to the knowledge of the foreground model, which are difficult to quantify, what could lead to a covariance matrix somewhat underestimated. In order to test the effect of the foreground model on our results, we repeated the analysis for our reference case using an alternative PySM model ("d2s2") finding fully compatible results.[5] We remark that it is very important to include an estimation of the foreground emission, even if fixed for all simulations, since this introduces significant variance in the power spectra due to the presence of chance correlations between the foregrounds and the other components.

For the *Planck* analysis, we use the CMB and noise PR3-2018 simulations (FFP10)

[4]Note that this applies to the analyses including WMAP and/or PR3. PR4, however, provides full simulations including foregrounds, that have been generated by evaluating the Commander sky model at the target frequency [116].

[5]Moreover, the analysis carried out using PR4 also considers a different (although again deterministic) foreground simulation, providing again consistent results (see Appendix A.2.1). This further confirms the stability of our conclusions versus the considered foreground model.

at the 30 GHz channel, generated using the end-to-end simulation pipeline [120], provided by the *Planck* Legacy Archive, which are also degraded to $N_{side} = 512$, the resolution considered in our analysis. In particular, we use 600 FFP10 lensed CMB maps [121], 300 full-mission LFI E2E simulations and 100 half-ring LFI E2E simulations per split, being the number of the noise simulations limited by the availability in the PLA. The LFI E2E simulations include noise and systematics due to realistic instrumental effects, which are then processed with the same algorithms as for the flight data. For a consistency test, we also use the new full-mission and A/B-splits *Planck* PR4 simulations, but further details are presented in Appendix A.2.1.

For the *WMAP* analysis, we generate 300 CMB Gaussian realizations using the power spectra from the *Planck* best-fit ΛCDM model [8] at the *WMAP* K-band channel resolution, using the `Healpy` package[6] [122, 123]. In addition, we generate a set of 600 noise simulations consistent with the full *WMAP* 9-yr and 2 sets of 300 noise simulations consistent with the split data sets. The full-data noise simulations are obtained from the full pixel by pixel covariance matrix, while those for the splits are generated combining the single-year covariance matrices from year 1 to 4 on one side and from year 5 to 9 on the other. The single-year and the full-mission covariance matrices are provided as LAMBDA Products.

[6] healpy.readthedocs.io

3.2 Masks

Although Galactic foregrounds studies usually focus on regions at high Galactic latitudes (since these are of greater interest for CMB analyses), these regions are very affected by noise in the *WMAP* 23 GHz and *Planck* 30 GHz polarised maps. Therefore, in order to have a higher signal-to-noise, our analysis will instead concentrate on low and intermediate latitudes, by constructing a set of customised masks with different sky fractions. For comparison, and in order to test the validity of our results also at high Galactic regions, the (almost) full-sky case will also be considered. In particular, our masks are constructed as a combination of a Galactic mask (that removes the brightest Galactic centre), a point source mask and a series of polarization masks constructed by thresholding the total polarised intensity ($P = \sqrt{Q^2 + U^2}$) of the *Planck* 30 GHz map. In this way, we end up with a set of five custom masks at intermediate and low Galactic latitude, which provide a useful sky fraction from 30 to 70%. For completeness, we also consider a 94% mask constructed simply combining the Galactic and the point sources masks.

3.2.1 Galactic Mask

The emission of the central part of the Galactic centre has a very complex behaviour and, therefore, can not be characterised with a simple power law model, as the one considered in this work. Therefore, it needs to be excluded from our analysis. For this we construct a customised Galactic mask in the following way.
First, as baseline, we exclude those pixels given by the 2015 Galactic plane mask (provided in the PLA) that leaves 97 per cent of the sky unmasked and that has been derived from *Planck* higher frequency channels. Second, in order to adapt better our customised mask to the considered data maps, we also exclude those pixels with $P > 70\ \mu K$ in the *Planck* 30 GHz channel and those with $P > 280\ \mu K$ in the *WMAP* 23 GHz map, both smoothed at 5°. The thresholds were set independently for each map in order to select the best region around the Galactic centre, such that the results of the analyses were robust while discarding only a small fraction of the sky.
In order to regularise the boundaries, the resulting mask is then smoothed with a Gaussian beam with FWHM=2°. All pixels with values ≤ 0.8 are considered for the mask and, therefore, discarded from the analysis. The final Galactic mask retains a sky fraction of $f_{sky} = 0.95$ (see grey Galactic region of Fig. 3.2).

3.2.2 Point Source Mask

The previous Galactic mask is not enough to ensure the exclusion of all regions with complex emission that do not follow a simple model for the power spectra. Indeed, we have seen that very bright point sources, both Galactic and extragalactic, can have a significant effect at the spectra at all scales. Therefore, we generate a point sources mask as a combination of *Planck* and *WMAP* polarization point source masks.
For *Planck*, we use the mask for the 30 GHz polarised map of the SEVEM pipeline (one of the four component separation methods used by the *Planck* Collaboration), which consists of 195 point sources that have polarization detection significance levels of 99% or more [63, 124, 125]. The *WMAP* point sources mask is generated from a

point source catalog [126] of 22 objects, where each source is detected in polarization with a significance level greater than 99.99% in at least one *WMAP* channel. After combining these two masks, we smooth it with a Gaussian beam with FWHM=30′ in order to enlarge the point source holes and, therefore, exclude from the analysis additional pixels that can still be affected by their emission. In particular, we mask only those pixels with values ≤ 0.8. The final point sources mask covers about 1% of the sky. The masked point sources can be seen in grey in Fig. 3.2.

3.2.3 Total Polarized Intensity Mask

The combination of the previous Galactic and point sources masks defines a preliminary region (of around 6 per cent of the sky) that will be excluded from all of our analysis. Once these pixels are removed, since for the characterization of the synchrotron emission one should consider regions with a sufficient signal-to-noise ratio, we construct a set of masks that select those areas with the largest polarization signal in the remaining 94 per cent of the sky. Thus, we mask those pixels below successively lower thresholds of P in the *Planck* 30 GHz polarization map, smoothed to a 5° resolution (Gaussian beam). The thresholds are chosen such that we select five regions that retain a f_{sky} from 0.3 to 0.7 in steps of 0.1, as shown in Figure 3.2. As one would expect, this procedure tends to mask mostly regions far from the Galactic plane, naturally excluding high latitudes, and leaving unmasked the central regions in both hemispheres. The mask selection process is described in more detail in Appendix A.1. In order to have masks with softer boundaries, we smooth them with a Gaussian beam of FWHM=3° and exclude all pixels ≤ 0.5. Furthermore, in the resulting masks, we remove small isolated "holes" and "islands" with radius smaller than 5°, which could otherwise complicate the spectra estimation. In this way, we have a set of 5 masks that, together with the near full sky mask (that removes only the Galactic and point source regions) constitute the basic set of masks for our analysis. Finally, before calculating the spectra and in order to reduce leakage effects in the power spectra, these six masks are apodized using the "C2" method of `NaMaster`[7] [127] with an apodization length of 3°, where pixels are multiplied by a cosine function of their distance to the nearest fully masked pixel.
For our main results, we pick as the reference mask the one with $f_{sky} = 0.5$, which is a good compromise between the considered sky fraction and the signal-to-noise ratio, as explained in Appendix A.1.

[7] namaster.readthedocs.io

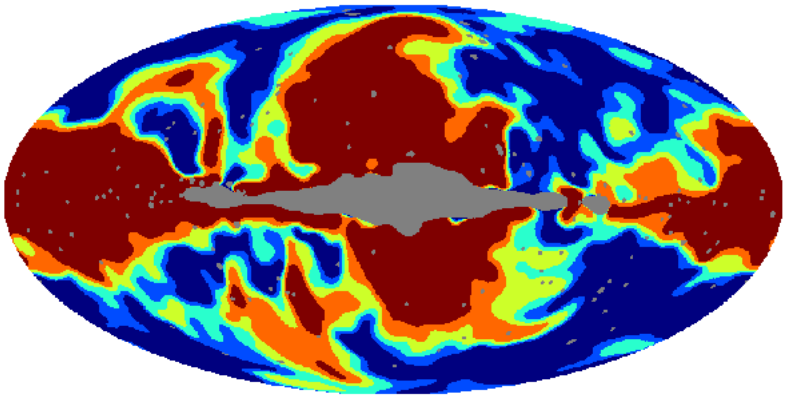

Figure 3.2: The different regions used to estimate the power spectra are shown. Note that the valid pixels of a given mask are also allowed in all the masks that leave a larger fraction unmasked. In this way, the sky fraction allowed by the 30% mask is showed in dark red, the valid pixels of the 40% mask are given by the combination of the dark red and orange regions, the 50% includes the dark red, orange and yellow areas, the 60% contains the same regions plus the turquoise one and, finally, the 70% also includes the light-blue pixels. The 94% mask only excludes from the analysis the grey region, which corresponds to the combination of the Galactic and point source masks.

3.3 Angular Power Spectra

In order to characterize the Galactic synchrotron polarization signal, we compute EE and BB auto-spectra and EB cross-spectra on the set of six masks described in the previous section. In particular, in order to deal with the presence of masks, which can induce mixing of power between multipoles and between polarization modes, we use the public code `NaMaster` [127], an advanced implementation of the pseudo-spectrum method to estimate the power spectra on an incomplete sky. Although this type of approach has been shown to be less optimal at large scales than Quadratic-Maximum Likelihood methods, they provide comparable results for the range of scales that we consider in this work, while being significantly faster (see [128]). `NaMaster` has already been successfully used in different cosmological applications [119, 129, 130].

Pseudo-C_ℓ^{EE} are estimated with the `NaMaster` E-purification method, where the so-called *pure* E mode is defined as the field that is orthogonal to all B modes. Similarly, pseudo-C_ℓ^{BB} are estimated with the `NaMaster` B-purification method. The pseudo-C_ℓ^{EB} are computed cross-correlating a *pure* E with a *pure* B field. Note that at large angular scales (low multipoles) diffuse synchrotron emission dominates, while at higher multipoles ($\ell > 250$) noise, and possibly extragalactic point sources, can play an important role. Taking this into account, we focus our main analyses in the multipole range $30 \leq \ell \leq 300$, binning with $\Delta\ell = 10$ for multipoles $30 \leq \ell \leq 200$ and with $\Delta\ell = 20$ for multipoles $\ell > 200$. We discard the lowest multipoles, since pseudo-spectra methods are suboptimal at very large scales on a masked sky. Consistency of the results versus a different choice of the multipole range ($10 \leq \ell \leq 400$) is discussed in Appendix A.2.2.

We model the EE and BB synchrotron power spectra as a power law parameterized by the index α and amplitude A evaluated on a pivot point $\ell = 80$

$$C_\ell^{XX} = A^{XX}\left(\frac{\ell}{80}\right)^{\alpha_{XX}} \tag{3.1}$$

with $XX = EE,\ BB$. The pivot point at $\ell = 80$ corresponds to the most important scale for measuring the synchrotron contamination to CMB because it is where the maximum of the contribution from cosmological gravitational waves is supposed to be located. We fit the EE and BB power spectrum estimated from the data to the previous model (with a total of 20 degrees of freedom) with a nonlinear least-squares algorithm provided by the `SciPy` [131] Python packages. Note that before performing the fit, the CMB contribution is subtracted from the data at the spectrum level and this is done by estimating the average CMB power spectra from CMB simulations using the same `NaMaster` procedure as for the data. With this procedure, we only subtract the average CMB signal, while the cosmic variance contribution is preserved in the covariance matrices.

The EB cross-spectra is simply modelled as a constant

$$C_\ell^{EB} = A^{EB}. \tag{3.2}$$

In this case we also perform a χ^2 fit, with a total of 21 degrees of freedom. In both fitting processes, we take into account the full covariance matrices computed with simulations. The effects of the instrumental beams and the pixel window function are also considered.

We first fit equations 3.1-3.2 independently to the power spectra estimated from *Planck* 30 GHz and from *WMAP* K-band data. Then we fit the EE, BB and EB models

to spectra obtained cross-correlating the *WMAP* K-band with the *Planck* 30 GHz maps. The results are presented in the following subsections. In order to test the robustness of the results, we also fit the same models to the power spectra estimated from the *Planck* PR4 30 GHz [116] data and to the spectra obtained cross-correlating *WMAP* and PR3 in a larger multipole range, results are presented in Appendix A.2.

3.3.1 Planck

We compute the EE, BB and EB power spectra cross-correlating the half-ring maps of the *Planck*-LFI 30 GHz maps. Covariance matrices are estimated from 100 half-ring simulations. We fit the model in equation 3.1 separately for E and B-modes, and for EB we fit a constant (equation 3.2). The power spectra and their corresponding fits are showed in Figure 3.3, each panel corresponding to a different mask. Both EE (red diamonds) and BB (blue squares) spectra show a steep decay of the synchrotron amplitude as a function of the scale. The goodness of the fit, reported in Table 3.1 in terms of χ^2, confirms that the simple power law model describes reasonably well the synchrotron polarization power spectra in most cases. Even so, there are a few χ^2 values, especially for EB, which slightly exceed the expectation for the considered distribution. This seems to be related to the limited number of simulations, which leads to a misestimation of the covariance matrix. Indeed, when repeating the same analysis using PR4 data, for which a larger number of simulations is available, the goodness of fit improves in most cases, especially for the EB fit (see Appendix A.2.1 for details). The effect of the number of simulations in also further considered in sections 3.3.2 and 3.3.3.

From Table 3.1, it is seen that, for all the considered masks, there is a systematic difference between the best-fit values for the indices α_{EE} and α_{BB}. In particular, for our reference mask ($f_{\rm sky} = 0.5$), we find -2.99±0.13 and -2.24±0.28, respectively, suggesting a steeper decay of the diffuse synchrotron E-component with respect to the B-component. By simply combining the errors quadratically, this implies that the two indices are inconsistent at the 2σ level. However, there may be correlations between both quantities that are not being taken into account, implying that the combined error may be somewhat underestimated. In addition, the analyses presented in the next sections do not show this behaviour. Therefore, this difference does not seem to be significant. The B-to-E ratio is computed as the amplitude ratio at the pivot multipole $\ell = 80$, and it turns out to be around 0.27 (slightly varying with the considered sky fraction). This amplitude asymmetry between the two polarization components is confirmed for all the masks, even in the 94% case, showing that it does not seem to be associated to specific regions but rather to be a feature of the diffusion synchrotron emission in almost the whole sky.
The EB cross-spectra is compatible with zero for the whole mask set within 1σ. We can put an upper constraint on the diffuse synchrotron polarization EB power spectrum, finding it to be smaller than 4.2% that of the EE spectrum. The constraint is computed from the 2σ error bar of the amplitude ratio A^{EB}/A^{EE} of the reference mask in Table 3.1, with the ratio evaluated at the pivot multipole $\ell = 80$. As far as we know, this is the first direct constraint on the EB cross-correlation of the diffuse synchrotron emission.

We can compare our results with those found by the *Planck* Collaboration in 2018

using the Commander and SMICA component separation methods [63]. They estimated the spectra from a different region, which considers intermediate and high Galactic latitudes, thus finding smaller amplitudes than in our analysis, $A^{EE} = 2.3 \pm 0.1$ (2.4 ± 0.1) μK^2 for Commander (SMICA), but very compatible[8] EE power spectrum index $\alpha_{EE} = -2.84 \pm 0.05$ (-2.88 ± 0.04). The value found with Commander (SMICA) for $\alpha_{BB} = -2.76 \pm 0.09$ (-2.75 ± 0.07) is slightly different from ours, even if compatible at 2σ. This apparent discrepancy can be explained by the very different procedure used in that work to extract the foreground signal (through a component separation method that takes into account all frequency channels), the use of different sky regions as well as a different power spectrum estimation method. Those differences are expected to have a larger impact on the BB spectrum, rather than EE, because of the lower signal-to-noise. The B-to-E ratio, around 0.34, is very compatible with the value we find for our 94% mask, that is 0.33±0.06, which is the most similar mask to that used in the *Planck* work. Nevertheless, the B-to-E ratio compatibility holds also for our 30% mask, that is 0.29±0.04, which instead left unmasked mostly low latitudes.
Comparing our results with the ones found in 2018 with *S-PASS* [81] at frequency 2.3 GHz, we see some differences. In particular, the BB synchrotron spectra is found to have a steeper decay, with α_{BB} around -3, and the B-to-E ratio is about 0.5 (although the specific values of these parameters vary strongly with the considered latitudes). These differences could be explained by the different frequency of observation of both experiments and, to a lesser extent, by the different regions considered for the analysis. Indeed, at low frequencies we expect other physical effects to take place, such as the Faraday rotation, depolarizing the synchrotron emission.

f_{sky}	**94%**	**70%**	**60%**	**50%**	**40%**	**30%**
α_{EE}	-3.09 ± 0.11	-2.82 ± 0.10	-2.84 ± 0.12	-2.99 ± 0.13	-2.87 ± 0.11	-2.87 ± 0.11
α_{BB}	-2.22 ± 0.28	-2.48 ± 0.24	-2.31 ± 0.22	-2.24 ± 0.28	-2.20 ± 0.33	-2.44 ± 0.35
A^{EE} $[10^{-3}\mu K]$	4.86 ± 0.28	7.69 ± 0.44	8.87 ± 0.52	10.01 ± 0.62	12.07 ± 0.61	14.4 ± 0.69
A^{BB} $[10^{-3}\mu K]$	1.62 ± 0.27	1.92 ± 0.29	2.61 ± 0.30	2.72 ± 0.37	3.04 ± 0.45	4.14 ± 0.59
A^{BB}/A^{EE}	0.33 ± 0.06	0.25 ± 0.04	0.29 ± 0.04	0.27 ± 0.04	0.25 ± 0.04	0.29 ± 0.04
χ^2_{EE} (20 dof)	19.3	22.0	25.6	29.8	21.9	19.5
χ^2_{BB} (20 dof)	35.3	20.3	20.6	22.1	21.7	25.2
A^{EB} $[10^{-3}\mu K]$	0.04 ± 0.12	0.08 ± 0.17	0.04 ± 0.16	-0.11 ± 0.21	0.04 ± 0.27	0.02 ± 0.35
A^{EB}/A^{EE}	0.008 ± 0.024	0.010 ± 0.022	0.005 ± 0.018	-0.011 ± 0.021	0.004 ± 0.022	0.002 ± 0.024
χ^2_{EB} (21 dof)	30.4	34.5	27.8	37.1	41.1	32.2

Table 3.1: *Planck* results. Best-fit parameters with 1σ errors and χ^2 of the power-law in equation 3.1 for EE and BB, and of the constant baseline in 3.2 for EB. Spectra are computed cross-correlating the *Planck* 30 GHz half-ring maps, for each of the six sky masks described in section 3.2.

[8]Along this work, when referring to compatibility between two values (either obtained here or in relation to previous results), unless otherwise stated, we mean that the difference of the two central values is less than 2σ. In this case we take $\sigma = \sqrt{\sigma_1^2 + \sigma_2^2}$ with σ_i the errors of the compared values. Note that this combined error is just an approximation, since it does not take into account possible correlations between the two considered quantities.

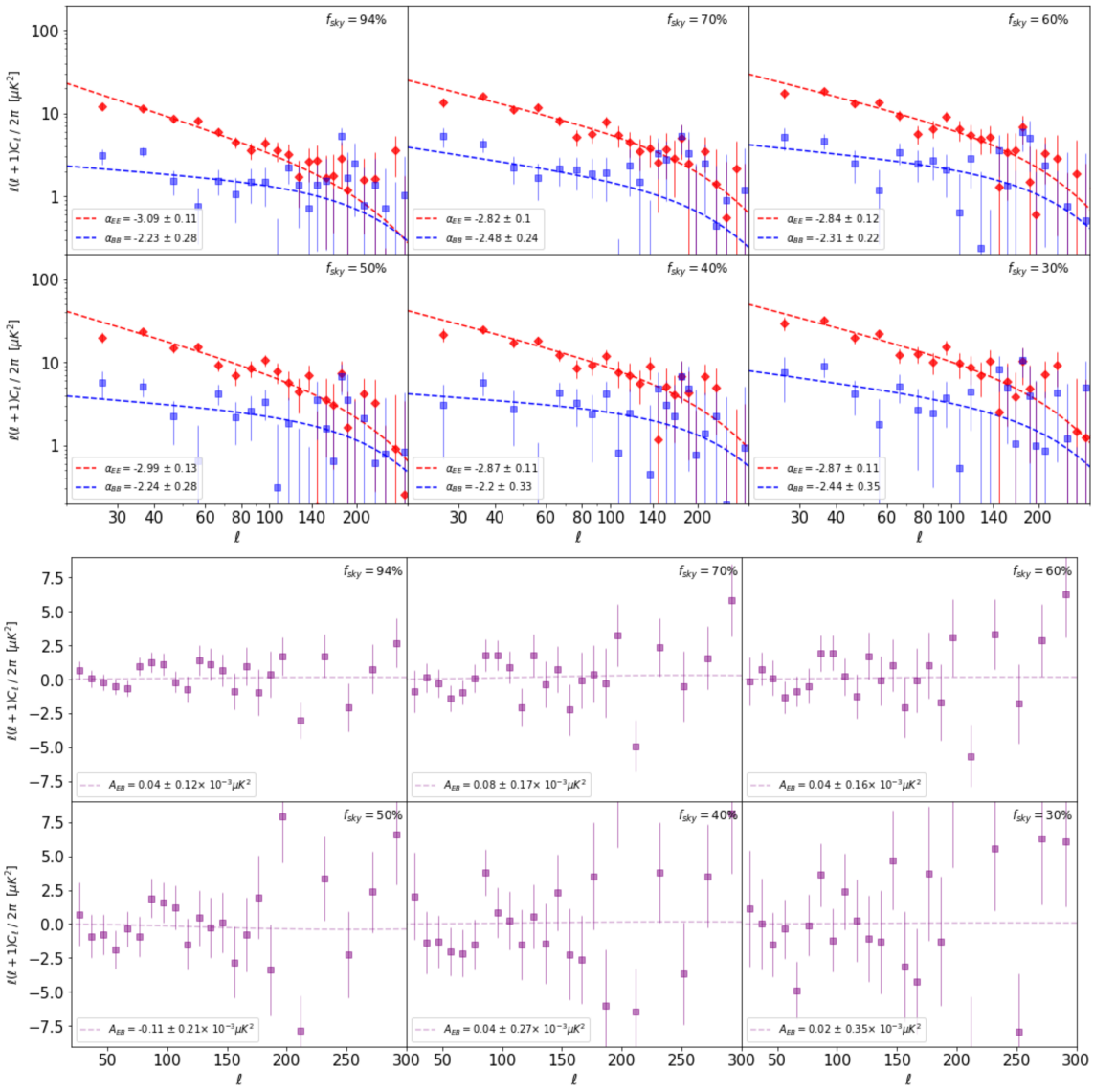

Figure 3.3: *Planck* results. Top panels: EE (red diamonds), BB (blue squares) pseudo-spectra, bottom panels: EB (purple squares) pseudo-spectra, at the nominal frequency 30 GHz. Spectra are computed cross-correlating the *Planck* 30 GHz half-ring maps, for each of the six sky masks, identified by the unmasked sky fraction. The dashed lines are the best fits to the data points. The indices α (top panels) are the exponent of the fitted power law 3.1 and the amplitudes A_{EB} (bottom pannels) are the constant fitted in equation 3.2.

3.3.2 WMAP

We compute the EE, BB and EB power spectra for the *WMAP* K-band cross-correlating the co-added year maps from 1 to 4 with the co-added year maps from 5 to 9. Covariance matrices are estimated from 300 simulations per year-split[9]. We fit the model in equation 3.1 separately for E and B-modes, and for EB we fit the model of equation 3.2. The power spectra and the corresponding fits are showed in Figure 3.4 while the best-fits parameters are given in Table 3.2.

As for *Planck*, EE and BB spectra show both a steep decay of the synchrotron amplitude as a function of scale. For the reference mask ($f_{sky} = 50\%$), we find $\alpha_{EE} = -2.92 \pm 0.07$ and $\alpha_{BB} = -2.84 \pm 0.29$, very compatible between them. This kind of consistency holds for most of the mask set, supporting the hypothesis that the two synchrotron polarization components decay as a function of multipoles with the same ratio. The estimated B-to-E ratio ranges from 0.23 ± 0.03 (for the 50 and 94% masks) to 0.17 ± 0.03 (when considering 40% of the sky). This amplitude ratio between the two polarization components suggests an even stronger asymmetry than the one found for the *Planck* 30 GHz channel.

The EB cross-correlation is compatible with zero at 1σ in the reference mask and within 2σ for the whole mask set. This is a further confirmation of the hypothesis of null cross-component in the diffuse synchrotron polarization. The EB/EE ratio evaluated at the pivot multipole $\ell = 80$, provides an upper limit to the EB amplitude $A_{EB} \leq 0.044\ A_{EE}$ at 2σ.

The model of the synchrotron polarization spectra derived from *WMAP*, for most of the masks, is consistent with the power law model with null EB cross-correlation that we obtained for *Planck*, as showed in Figure 3.5, as well as with the Commander and SMICA models [63]. However, *WMAP* data suggests a slightly smaller B-to-E ratio, where the E-component is about 4.3 times larger than the B-component. This is again also different from the *S-PASS* results [81], but, as previously mentioned, this could be explained by the different frequency and, to a lesser extent, by the different regions observed by both experiments.

3.3.3 WMAP-Planck cross spectra

From the previous *WMAP* and *Planck* individual analysis, we can conclude that our characterization of the synchrotron polarization power spectra, provided the Galactic centre and bright point sources are properly masked, holds reasonably well in the frequency range 23-30 GHz and is supported by two independent experiments. Therefore, we can improve the estimation of the model parameters by cross-correlating the data of the two experiments, increasing the signal-to-noise while reducing the effect of possible systematic errors. Differently from the previous analyses, we use the full-mission *Planck* 30 GHz and the co-added 9 years *WMAP* K-band maps instead of data splits. Since we are cross-correlating two independent experiments, instrumental noise will cancel and possible systematics will be reduced even when using the full data maps. In addition,

[9]Note that in the case of *Planck* half-ring maps, the number of simulations were limited to 100, as provided by the *Planck* collaboration. For *WMAP*, we tested the robustness of the results versus the number of simulations. We found that results were stable with 300 simulations, improving in particular the error in α_{EE} with respect to the use of a lower number of simulations.

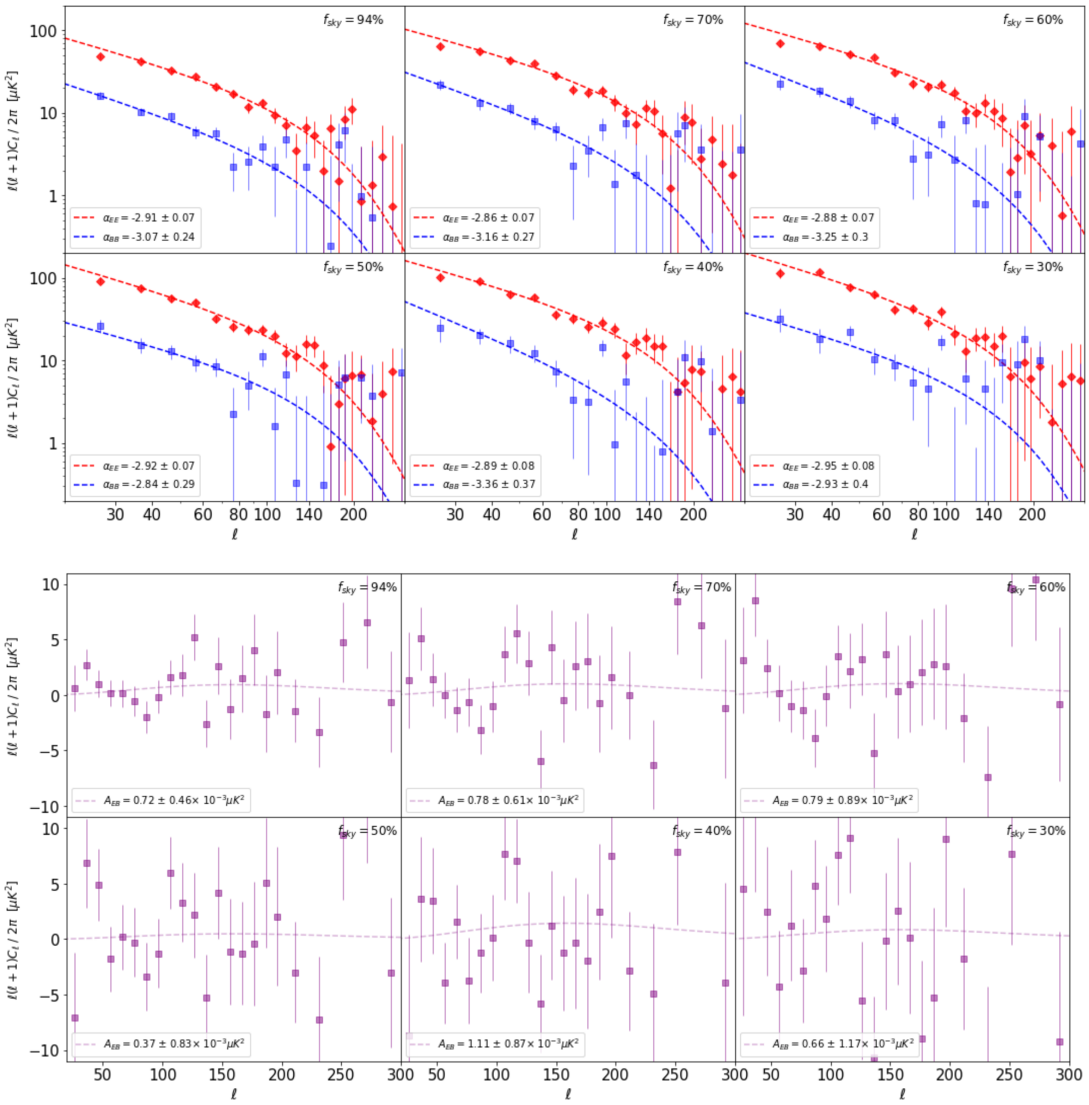

Figure 3.4: *WMAP* results. Top: EE (red diamonds), BB (blue squares) pseudo-spectra, bottom: EB (purple squares) pseudo-spectra, at the nominal frequency 23 GHz. Spectra are computed cross-correlating the co-added *WMAP* K-band year maps, for each of the six sky masks, identified by the unmasked sky fraction. The dashed lines are the best fits to the data points. The indices α (top) are the exponent of the fitted power law 3.1 and the amplitudes A_{EB} (bottom) are the constant fitted in equation 3.2.

f_{sky}	**94%**	**70%**	**60%**	**50%**	**40%**	**30%**
α_{EE}	-2.91 ± 0.07	-2.86 ± 0.07	-2.88 ± 0.07	-2.92 ± 0.07	-2.89 ± 0.08	-2.95 ± 0.08
α_{BB}	-3.07 ± 0.24	-3.16 ± 0.27	-3.25 ± 0.30	-2.84 ± 0.29	-3.36 ± 0.37	-2.93 ± 0.40
A^{EE} $[10^{-3}\mu K]$	21.83 ± 0.83	30.31 ± 1.02	34.87 ± 1.15	38.75 ± 1.29	45.45 ± 1.70	52.38 ± 1.99
A^{BB} $[10^{-3}\mu K]$	4.93 ± 0.66	6.03 ± 0.89	7.00 ± 1.09	8.73 ± 1.20	7.60 ± 1.43	10.16 ± 1.75
A^{BB}/A^{EE}	0.23 ± 0.03	0.20 ± 0.03	0.20 ± 0.03	0.23 ± 0.03	0.17 ± 0.03	0.19 ± 0.03
χ^2_{EE} (20 dof)	21.4	16.3	17.4	17.1	15.8	16.0
χ^2_{BB} (20 dof)	23.0	23.0	24.8	22.9	28.7	29.4
A^{EB} $[10^{-3}\mu K]$	0.72 ± 0.46	0.78 ± 0.61	0.79 ± 0.89	0.37 ± 0.83	1.11 ± 0.87	0.66 ± 1.17
A^{EB}/A^{EE}	0.033 ± 0.021	0.026 ± 0.020	0.023 ± 0.026	0.010 ± 0.022	0.024 ± 0.019	0.013 ± 0.022
χ^2_{EB} (21 dof)	23.0	24.6	35.6	27.3	22.9	31.3

Table 3.2: *WMAP* results. Best-fit parameters with 1σ errors and χ^2 of the power-law in equation 3.1 to EE and BB, and of the constant baseline in 3.2 to EB. Spectra are computed cross-correlating the co-added *WMAP* K-band years maps, for each of the six sky masks described in section 3.2.

we can benefit of the larger number of simulations available, that yields to smaller errors on the estimated parameters.

We generated 600 spectra cross-correlating Planck and WMAP simulations to estimate the covariance matrices. Being the *Planck* noise simulations limited to 300, we used each of these noise simulations twice[10]. Even if the simulations are not completely independent because of the limited number of the Planck noise simulations, the other two components (CMB and WMAP noise) are still fully independent, giving a better statistics which improves the estimation of the covariance matrix. Although for the sake of brevity we omit the results for the *Planck*-*WMAP* cross-spectra derived from the split data, they are fully compatible with the results presented in this section. Fig. 3.7 shows the EE, BB and EB power spectra and the best fits obtained from the *WMAP*-*Planck* cross-correlation analysis, Table 3.3 provides the best-fit parameters and the χ^2 values.

For our reference mask ($f_{sky} = 50\%$), the EE and BB power spectra of the diffuse synchrotron emission show a steep decay as a function of multipoles with consistent power spectrum indices $\alpha_{EE} = -2.95 \pm 0.04$ and $\alpha_{BB} = -2.85 \pm 0.14$. The goodness of the fits supports the validity of the power law model and the hypothesis of compatibility between the steepness of the two polarization components. Considering the results for the full set of masks shown in Figure 3.7, α_{EE} is very stable and compatible with the nearly-full sky case (94%). Instead, the BB power law shows a slight tendency to steeper values when including high latitudes. The B-to-E ratio for the reference mask is found to be 0.22 ± 0.02 and it ranges from 0.20 in the 94% mask to 0.25 for the 30% mask, which shows again how the foreground E-component dominates the polarization emission over the B-component at low frequency.
We find that the difference between the two polarization components, both in amplitude and steepness, is larger when considering the nearly full-sky case, whereas it tends to decrease when considering mainly regions closer to the Galactic plane (where the signal-to-noise is higher). In any case, the results computed for the complete set of masks are

[10] A similar procedure has been followed to increase the number of simulations in [132].

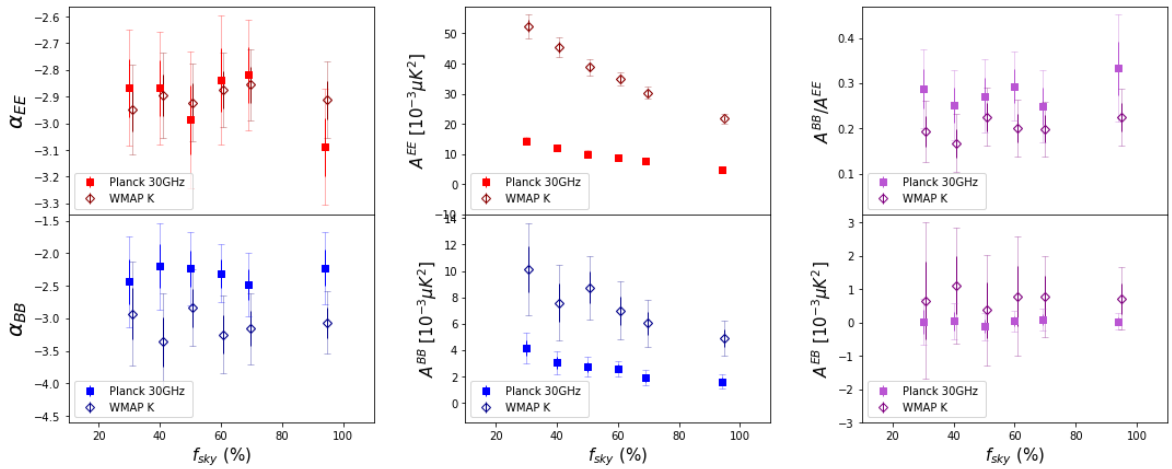

Figure 3.5: Comparison between the best-fit parameters found for *Planck* 30 GHz (filled squares) and *WMAP* K-band (blank diamonds) to the models of equations 3.1 and 3.2. 1σ and 2σ errors are showed with thick and thin lines, respectively. To allow for a better visualization, *WMAP* values are slightly shifted in the x-axis.

consistent at 2σ, except for the 94% mask (where consistency holds at 2.5σ). A more precise characterization of the EE and BB power spectra with latitude would require maps with better sensitivity in polarization.

The EB cross-spectra is consistent with zero at 1σ for the whole mask set, therefore, the hypothesis of null EB cross-correlation holds for the diffuse synchrotron emission even when considering the nearly full-sky case. The spectra provided by the cross-correlation of *Planck* and *WMAP* gives the most stringent upper limit to the EB amplitude, found to be $\leq$ 1.2% (2σ) of the EE amplitude, computed at multipole $\ell = 80$.
As anticipated in section 3.3.1, we point out that the covariance matrices used in the fit for EB could be underestimated because of the limited number of simulations, leading to some larger χ^2 values. We tested the dependency of χ^2 on the number of simulations using samples of different sizes, finding that a larger number of simulations lead to more stable results and to lower values of χ^2.

These results point out that the two most important polarised foregrounds, thermal dust and synchrotron, present some differences at spectra level. At high frequency the thermal dust emission shows a power law decay with power spectrum index $\alpha_d \approx$ -2.5 [51], less steep than the power spectrum index $\alpha_s \approx$ -2.9 that we find for synchrotron. Moreover, the B/E asymmetry for the synchrotron emission, around 0.22, is stronger than the asymmetry found for dust, around 0.5. The observed EB/EE power ratio, for both thermal dust and synchrotron, is smaller than about 0.03.

The results presented in this section for the cross-experiment analysis are, in general, compatible with the single-experiment analysis of *Planck* and *WMAP*. Moreover, the steepness of the power law model which describes the EE and BB power spectra are compatible with the *Planck* component separation results presented in 2018 [63]. Nevertheless, the B-to-E ratio we find in the nearly full sky case is slightly smaller than the ratio found by *Planck* in the intermediate and high latitudes. As discussed in the previous sections, several differences appear when comparing our results with the

model found with *S-PASS* [81], mainly due to the fact that they analyze maps at a lower frequency, that is 2.3 GHz, and only at high Galactic latitudes. In particular, we find a less steep and compatible decay for both EE and BB and a B-to-E ratio of about 0.22, where instead with *S-PASS* it is observed that at Galactic latitudes $|b| > 30°$ the mean value of the decay index is $\alpha \simeq -3.15$ and with a B-to-E ratio $\simeq 0.5$ for $|b| > 35°$.

From our analysis and the comparison with the two mentioned works, we can conclude that our characterization of the synchrotron polarization power spectra can be extended to high Galactic latitude, thus to the full sky after removing the brightest regions, in the frequency range 23-30 GHz. Instead, we cannot exclude that at different frequencies, in particular smaller, the synchrotron polarization power spectra could deviate from our characterization due to some physical effects.

In Appendix A.2 some robustness tests are presented, which confirm the results obtained in section 3.3. In particular, in section A.2.1 we repeat the same analysis cross-correlating the A/B detector splits of the 2020 *Planck* `NPIPE` release (PR4). In section A.2.2, we test the same power law model in a larger multipole range ($10 \leq \ell \leq 400$). Finally, in Appendix A.3, we also analyse and test the model independently in the Northern and Southern hemisphere, finding consistency with the results presented in this section.

f_{sky}	**94%**	**70%**	**60%**	**50%**	**40%**	**30%**
α_{EE}	-2.93 ± 0.05	-2.88 ± 0.05	-2.91 ± 0.05	-2.95 ± 0.04	-2.94 ± 0.05	-2.95 ± 0.07
α_{BB}	-3.26 ± 0.12	-3.11 ± 0.15	-3.04 ± 0.15	-2.85 ± 0.14	-2.97 ± 0.15	-2.79 ± 0.15
A^{EE} $[10^{-3}\mu K]$	10.26 ± 0.30	14.09 ± 0.33	16.02 ± 0.40	17.88 ± 0.39	21.02 ± 0.50	24.72 ± 0.83
A^{BB} $[10^{-3}\mu K]$	2.02 ± 0.14	2.92 ± 0.23	3.55 ± 0.26	3.99 ± 0.26	4.92 ± 0.32	6.06 ± 0.38
A^{BB}/A^{EE}	0.20 ± 0.01	0.21 ± 0.02	0.22 ± 0.02	0.22 ± 0.02	0.23 ± 0.02	0.25 ± 0.02
χ^2_{EE} (20 dof)	28.3	19.9	20.2	13.9	15.9	30.2
χ^2_{BB} (20 dof)	12.7	17.7	18.5	14.5	16.2	15.1
A^{EB} $[10^{-3}\mu K]$	0.02 ± 0.06	0.09 ± 0.10	0.05 ± 0.11	0.08 ± 0.11	0.08 ± 0.12	0.04 ± 0.14
A^{EB}/A^{EE}	0.002 ± 0.005	0.006 ± 0.007	0.003 ± 0.007	0.005 ± 0.006	0.004 ± 0.005	0.002 ± 0.006
χ^2_{EB} (21 dof)	23.0	37.1	36.4	29.5	24.6	23.6

Table 3.3: *Planck*-*WMAP* results. Best-fit parameters, 1σ errors and χ^2 values for the power-law in equation 3.1 for EE and BB, and for the constant baseline in 3.2 for EB. Power spectra are computed by cross-correlating the co-added 9 year *WMAP* K-band maps and the full-mission *Planck* 30 GHz maps, for each of the six sky masks described in section 3.2.

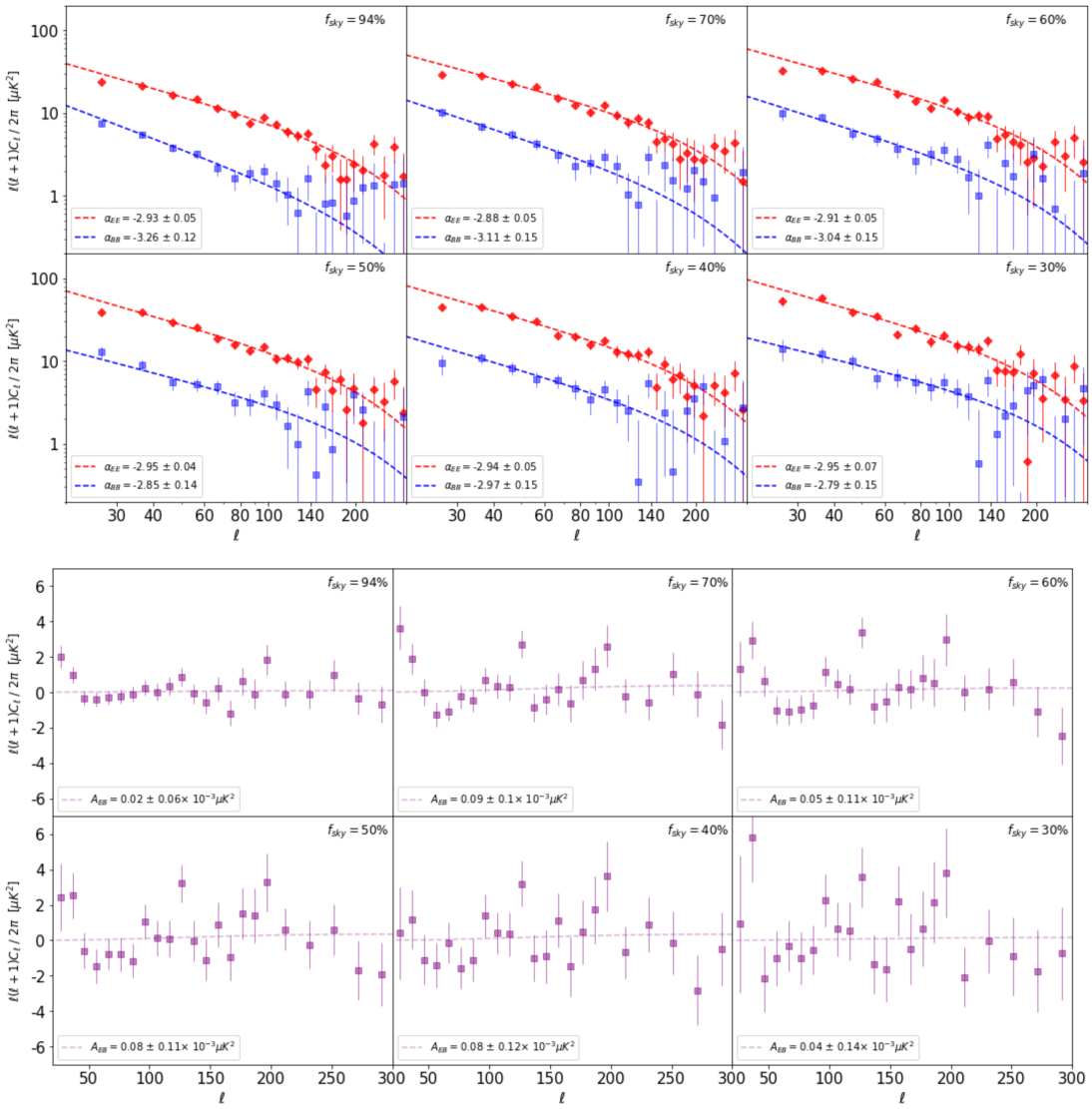

Figure 3.6: *Planck*-*WMAP* results. Top: EE (red diamonds), BB (blue squares) pseudo-spectra, bottom: EB (purple squares) pseudo-spectra. Spectra are computed cross-correlating the co-added 9 year *WMAP* K-band maps and the full-mission *Planck* 30GHz maps, for each of the six sky masks, identified by the unmasked sky fraction. The dashed lines are the best fits to the data points. The indices α (top) are the exponent of the fitted power law 3.1 and the amplitudes A_{EB} (bottom) are the constant fitted in equation 3.2.

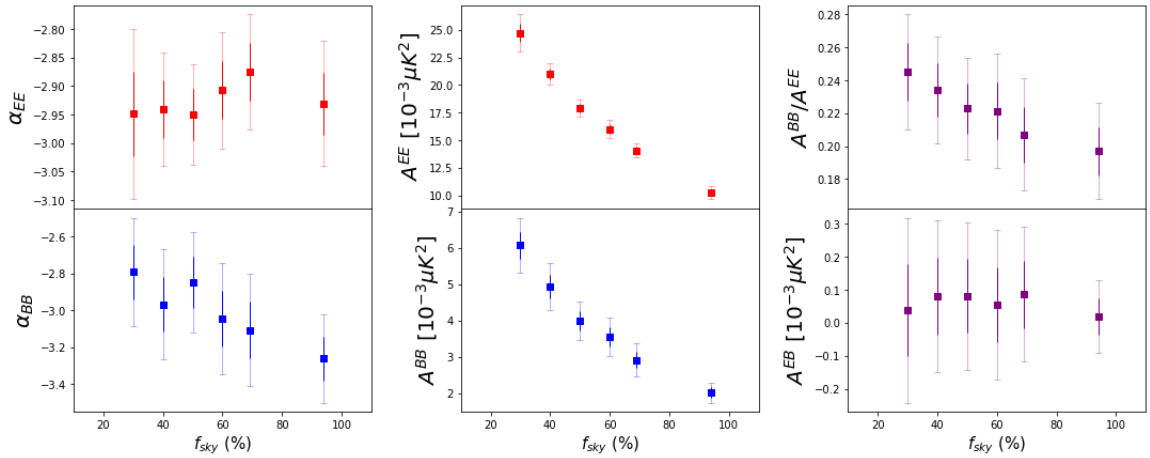

Figure 3.7: *Planck*-*WMAP* results. Best-fit parameters to the models of equations 3.1 and 3.2 computed on the cross-spectra of *WMAP* K-band and *Planck* 30GHz. 1σ and 2σ errors are showed with thick and thin lines, respectively.

3.4 Spectral Index

In the previous section we focused our analysis on the characterization of the polarization power spectra of *Planck* and *WMAP* at low frequency. However, since we have observations at different frequencies, nominally at 23 and 30 GHz, we can also get insights of the behaviour of the diffuse synchrotron polarization with frequency.

3.4.1 Methodology

The synchrotron spectral energy distribution (SED), both in temperature and polarization, is generally described for each pixel by a power law[11]

$$S = S_0 \left(\frac{\nu}{\nu_0}\right)^{\beta} \tag{3.3}$$

where S_0 is the foreground amplitude of a particular pixel at the pivot frequency ν_0 and β is the energy spectral index that we assume spatially constant for simplicity. The modelling of the synchrotron SED in polarization as well as the knowledge of the spectral index β, are essential to test and perform component separation in current and future CMB polarization studies.
From equation 3.3, we can get the relationship between the amplitudes of the power spectra of the *WMAP* K-band and the *Planck* 30 GHz maps for the two polarization components E and B

$$(A^{XX})^{WMAP} = (A^{XX})^{Planck} \left(\frac{\nu^{WMAP}}{\nu^{Planck}}\right)^{2\beta_{XX}} \tag{3.4}$$

with $\nu^{WMAP} = 23$ GHz, $\nu^{Planck} = 28.4$ GHz and $XX = EE,\ BB$.
Combining equations 3.4 and 3.1, we get a system of equations that relate the energy spectral index β and the power spectrum index α for each of the polarization components

$$\begin{cases} (C_\ell^{XX})^{Planck} = (A^{XX})^{Planck} \left(\frac{\ell}{80}\right)^{\alpha_{XX}} \\ (C_\ell^{XX})^{WMAP} = (A^{XX})^{Planck} \left(\frac{\ell}{80}\right)^{\alpha_{XX}} \left(\frac{\nu^{WMAP}}{\nu^{Planck}}\right)^{2\beta_{XX}} \end{cases} \tag{3.5}$$

with $XX = EE,\ BB$, and $(A^{XX})^{Planck}$ refers to the polarization power spectrum amplitude at $\ell = 80$ for the *Planck* lowest channel, centered at 28.4 GHz. Before performing the fit, in order to account for the effect introduced by the instrumental bandpasses, we corrected the amplitudes in equations 3.5 multiplying them by the colour correction coefficients, following the same procedure and using the same coefficients as those given in [51]. We perform a χ^2 fit to the system of equations 3.5 for the EE and BB auto-spectra with 41 degrees of freedom, keeping the amplitude A, the power spectrum index α and the energy spectral index β as free parameters. The first two parameters have been widely tested in the previous section, providing a robust test to validate the results presented in this section. In particular, for the analysis, we use the

[11] More complex models are also considered in the literature, such as the one including a curvature parameter. However, given the sensitivity of *Planck* and *WMAP* data, we restrict our analysis to the simple power law case. Future low frequency data, such as *QUIJOTE*, would help to discriminate between these two types of models.

EE and BB power spectra obtained in section 3.3.1 for *Planck* and section 3.3.2 for *WMAP*.

3.4.2 Results

Results are reported in Table 3.4. For our reference mask (50%), the spectral indices β_{EE} and β_{BB} are very consistent, with values of -3.00±0.10 and -3.05±0.36 respectively. These values are consistent with the spectral index found for intensity by previous *Planck*/*WMAP* analyses [59, 133], supporting the model of a steep decay due to radiative losses, which cause spectral ageing [134]. Moreover, our values are consistent with results found by *S-PASS* [81] in polarization and by the *Planck* component separation methods [63]. We note, however, that several χ^2 values corresponding to the B component exceed the expected values for the considered degrees of freedom. As already discussed in section 3.3, this seems to be related to the limited number of *Planck* simulations, having probably a larger impact on BB due to the smaller signal-to-noise.

Figure 3.8 shows the best-fit parameters for each of the considered masks for both the E- and B-mode components. It is interesting to point out that the power spectral indices tend to move towards steeper values when considering larger sky fractions, i.e., when including higher Galactic latitudes in the analysis. In particular, β_{EE} ranges from -2.98 to -3.22 while β_{BB} expands a wider range, from -2.39 to -3.48, but with larger uncertainties. This kind of steepening has been observed in other previous works [81, 62], showing that the spectral index gradually steepens from $\beta \simeq$ -2.8 to $\beta \simeq$ -3.3 when including higher Galactic latitudes.

We also note that the power spectrum indices α_{EE}, α_{BB} and the B-to-E ratio are compatible with the results presented in section 3.3.3, supporting the robustness of the analysis presented in this section.

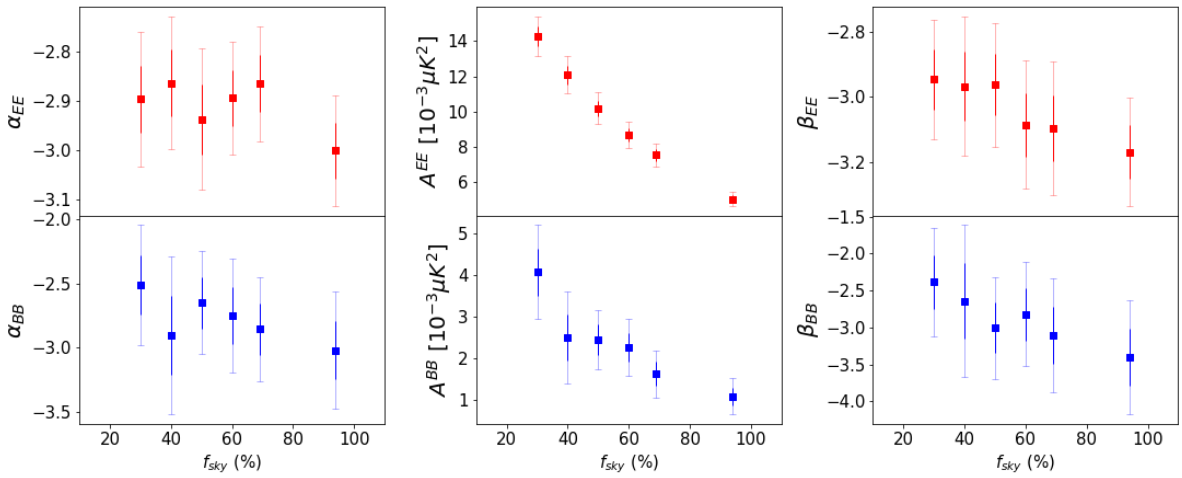

Figure 3.8: Best fit parameters to the system of equations of 3.5 computed from the *WMAP* K-band and *Planck* 30 GHz data. 1σ and 2σ errors are showed with thick and thin lines, respectively. A^{XX} refers to the polarization power spectrum amplitude at $\ell = 80$ for the *Planck* lowest channel.

f_{sky}	**94%**	**70%**	**60%**	**50%**	**40%**	**30%**
α_{EE}	-3.00 ± 0.06	-2.87 ± 0.06	-2.89 ± 0.06	-2.94 ± 0.07	-2.86 ± 0.07	-2.9 ± 0.07
α_{BB}	-3.02 ± 0.23	-2.85 ± 0.20	-2.75 ± 0.22	-2.65 ± 0.20	-2.90 ± 0.31	-2.51 ± 0.23
β_{EE}	-3.22 ± 0.09	-3.14 ± 0.11	-3.13 ± 0.10	-3.00 ± 0.10	-3.01 ± 0.11	-2.98 ± 0.10
β_{BB}	-3.48 ± 0.41	-3.15 ± 0.41	-2.85 ± 0.38	-3.05 ± 0.36	-2.66 ± 0.55	-2.39 ± 0.39
A^{EE} $[10^{-3}\mu K]$	4.55 ± 0.18	6.79 ± 0.30	7.82 ± 0.33	9.18 ± 0.40	10.88 ± 0.47	12.84 ± 0.50
A^{BB} $[10^{-3}\mu K]$	0.98 ± 0.20	1.47 ± 0.25	2.04 ± 0.31	2.21 ± 0.32	2.26 ± 0.50	3.67 ± 0.51
A^{BB}/A^{EE}	0.22 ± 0.04	0.22 ± 0.04	0.26 ± 0.04	0.24 ± 0.04	0.21 ± 0.05	0.29 ± 0.04
χ^2_{EE} (41 dof)	44.3	44.1	50.3	49.7	44.8	38.7
χ^2_{BB} (41 dof)	79.7	51.5	64.1	45.9	82.6	68.5

Table 3.4: *Planck*-*WMAP* results. Best-fit parameters (with 1σ errors) for the model given in equation 3.5 for the EE and BB power spectra, and their corresponding χ^2 values. *Planck* spectra are computed cross-correlating the half-ring maps, *WMAP* spectra are computed cross-correlating the co-added *WMAP* K-band years maps. The sky fractions are the ones retained by the six sky masks described in section 3.2.

3.5 Conclusions

We have analyzed the sky emission at 23 and 30 GHz with the *WMAP* K-band and the *Planck* lowest frequency channel data. The main target of our analysis has been the study of the angular and spectral distribution of the diffuse Galactic polarized synchrotron. We have constructed a set of six masks, five of them increasing from low to intermediate Galactic latitude (from 30 to 70 per cent of sky coverage), and a 94% mask which allows almost the full sky except for the Galactic center and some bright point sources. We have estimated EE, BB and EB power spectra from *Planck* and *WMAP* independently, as well as by cross-correlating the two experimental data. We have fitted the power law $C_\ell^{EE,BB} \propto \ell^{\alpha_{EE,BB}}$ independently for the EE and BB power spectra and the constant $C_\ell^{EB} = A^{EB}$ for the EB cross-spectrum, in the multipole range $30 \leq \ell \leq 300$ for each of the considered cases.

For the cross-correlation analysis and a mask that allows 50 per cent of the sky, we have found a steep decay for E and B-modes, with indices $\alpha_{EE} = -2.95 \pm 0.04$ and $\alpha_{BB} = -2.85 \pm 0.14$, consistent between both components, and an asymmetry between the two amplitude modes with a B-to-E ratio equal to 0.22±0.02, at the pivot multipole $\ell = 80$. The compatibility between the two polarization components is better, in general, when considering mainly regions with high signal-to-noise. For the cross-correlation analysis, we have also found that the EB cross-spectra is consistent with zero at 1σ for all the considered sky fractions, imposing a constraint on the EB amplitude to be $\leq 1.2\%$ (2σ) that of the EE amplitude for the 50% mask. We have also obtained, in general, consistent results from the *Planck* and *WMAP* independent analysis with respect to the ones found for the cross-correlation case. However, some small differences are present in the case of the best-fit parameters estimated only from the *Planck* 30 GHz map. In particular, we find a less steep BB spectra (α_{BB} around 2.24) and a slightly larger B/E ratio (around 0.27), even if consistency with the cross-correlation results holds at 2σ in both cases.

We have done some robustness tests which have confirmed the validity of our results. In particular, we have fitted our model to the frequency maps of the 2020 *Planck* `NPIPE` release (PR4), and in a larger multipole range ($10 \leq \ell \leq 400$). Moreover, we have estimated spectra independently for the two hemispheres finding a larger emission in the North in the case of the E mode. Apart from that, there are not significant differences in the model of the polarization power spectra between the two hemispheres and with the full sky.

We have fitted a simple power law to the synchrotron spectral energy distribution independently for the EE and BB spectra, considering both *Planck* and *WMAP* data. The recovered spectral indices β_{EE} and β_{BB}, with respective values -3.00±0.10 and -3.05±0.36 for the 50 per cent mask, are compatible. The results indicate a trend of the spectral indices towards steeper values when higher Galactic latitudes are included in the analysis.

Chapter 4

Morphological Analysis of the Polarized Synchrotron Emission with WMAP and Planck

The bright polarized synchrotron emission, away from the Galactic plane, originates mostly from filamentary structures. We implement a filament finder algorithm which allows the detection of bright elongated structures in polarized intensity maps. We analyse the sky at 23 and 30 GHz as observed respectively by *WMAP* and *Planck*. We identify 19 filaments, 13 of which have been previously observed. For each filament, we study the polarization fraction, finding values typically larger than for the areas outside the filaments, excluding the Galactic plane, and a fraction of about 30% is reached in two filaments. We study the polarization spectral indices of the filaments, and find a spectral index consistent with the values found in previous analysis (about –3.1) for more diffuse regions. Decomposing the polarization signals into the E and B families, we find that most of the filaments are detected in P_E, but not in P_B. We then focus on understanding the statistical properties of the diffuse regions of the synchrotron emission at 23 GHz. Using Minkowski functionals and tensors, we analyse the non-Gaussianity and statistical isotropy of the polarized intensity maps. For a sky coverage corresponding to 80% of the fainter emission, and on scales smaller than 6 degrees ($\ell > 30$), the deviations from Gaussianity and isotropy are significantly higher than 3σ. The level of deviation decreases for smaller scales, however, it remains significantly high for the lowest analised scale ($\sim 1.5^\circ$). When 60% sky coverage is analysed, we find that the deviations never exceed 3σ. Finally, we present a simple data-driven model to generate non-Gaussian and anisotropic simulations of the synchrotron polarized emission. The simulations are fitted in order to match the spectral and statistical properties of the faintest 80% sky coverage of the data maps.

4.1 Polarized Intensity

4.1.1 Data

For our analysis, we will make use of data taken by the *WMAP* and *Planck* satellites. We focus on the lowest frequency data from *WMAP*, specifically the 9-year *WMAP*

K-band (centered at 23 GHz) maps, provided in the `HEALPix`[1] pixelisation scheme with $N_{side} = 512$ and an effective Gaussian beam of 0.88° full-width-at-half-maximum (FWHM). The *WMAP* products have been downloaded from the Legacy Archive for Microwave Background Data Analysis (LAMBDA)[2]. For the *Planck* analysis, we use the 30 GHz frequency maps generated by the `NPIPE` processing pipeline (PR4). The `NPIPE` processing results in improved High Frequency Instrument (HFI) polarization data with reduced systematic artefacts and lower levels of noise. PR4 data from the Low Frequency Instrument (LFI) are also modified with respect to the 2018 *Planck* release. Further details are available in [116]. The frequency maps were downloaded from the *Planck* Legacy Archive[3] (PLA) at a pixel resolution corresponding to $N_{side} = 1024$ and an effective beam of FWHM = 31.5 arcminutes. Note that the polarization maps, and consequentially the analysis, follow the `HEALPix` convention.

As the synchrotron emission scales with frequency, the foreground signal is higher in the *WMAP* K-band compared to the *Planck* 30 GHz channel, however, the noise level of *Planck* is lower. As result, at a common resolution of 1°, the overall signal-to-noise ratio of the two experiments are similar [60], although one or other map may be better in some sky regions because of the different scanning strategies.

4.1.2 Smoothing

We smooth the *WMAP* and *Planck* maps to common resolutions of 1° and 3° FWHM. The 1° maps are downgraded to a `HEALPix` resolution of $N_{side} = 128$ (corresponding to a representative pixel size of ∼27 arcmin) that we will use for filament detection and statistical analysis, and the 3° maps to a resolution of $N_{side} = 64$ (a pixel size of ∼55 arcmin), that we will use for the filament analysis. The smoothing and downgrading are performed in harmonic space deconvolving the original effective beam and then convolving with a Gaussian beam[4]. The smoothing process helps to increase the signal-to-noise ratio of the maps and to minimise any effect due to beam-asymmetries in the two experiments.

We estimate the noise level of the data at the 1° and 3° resolutions, including uncertainties due to smoothing and pixel downgrading. For *WMAP*, we generate 600 Gaussian noise realisations based on the covariance matrices at full resolution. For *Planck*, we use the 600 noise simulations provided on the PLA [116]. We downgrade and smooth each simulation in the same way as the data. Finally, for each pixel we compute σ_Q^2, σ_U^2 and σ_{QU}^2 from the variance and covariance over all of the simulated Q and U maps.

4.1.3 Debiased Estimator

A morphological analysis is applied to the polarized intensity $P = \sqrt{(Q^2 + U^2)}$, which, given its positive nature, is subject to noise bias. In particular, in the low signal-to-

[1] https://healpix.sourceforge.io

[2] lambda.gsfc.nasa.gov/product/map

[3] pla.esac.esa.int

[4] We generate $a_{\ell m}$'s with the `map2alm healpy` routine from the Q, U maps. We convolve the maps with the new Gaussian beam and pixel window function following the method described in Appendix B.1. Finally, we regenerate the Q, U maps with the `alm2map` routine from the convolved $a_{\ell m}$'s.

noise regime, P will yield a positive estimate even if Q and U are zero. We use the modified asymptotic (MAS) estimator [135] in order to correct the polarized amplitude for the bias. We recall that the debiased polarized amplitude with the MAS estimator is computed as

$$P_{MAS} = P - \frac{1 - \exp(-P^2/b^2)}{2P} b^2 \tag{4.1}$$

where the noise bias b is function of the pixel variance and the polarization angle $\phi = \arctan(U/Q)$ given by

$$b^2 = \sigma_U^2 \cos^2(\phi - \theta) + \sigma_Q^2 \sin^2(\phi - \theta), \quad \theta = \frac{1}{2} \arctan\left(\frac{\sigma_{QU}}{\sigma_Q^2 - \sigma_U^2}\right). \tag{4.2}$$

The maps are showed in figure 4.1. [135] demonstrate that in the regime where the signal-to-noise ratio exceeds 2, the estimator is unbiased and essentially Gaussian. An estimate of the variance is then given by

$$\sigma_P^2 = \sigma_Q^2 \cos^2(\phi - \theta) + \sigma_U^2 \sin^2(\phi - \theta). \tag{4.3}$$

Note that the debiased polarized intensity and its variance are defined pixel by pixel. Thus, we do not take into account the correlation between pixels, which is introduced smoothing and downgrading of the maps. Although we use the MAS estimator in our analysis, several tests have been performed using the Wardle & Kronberg estimator [136, 66, 137] instead, finding consistent results.

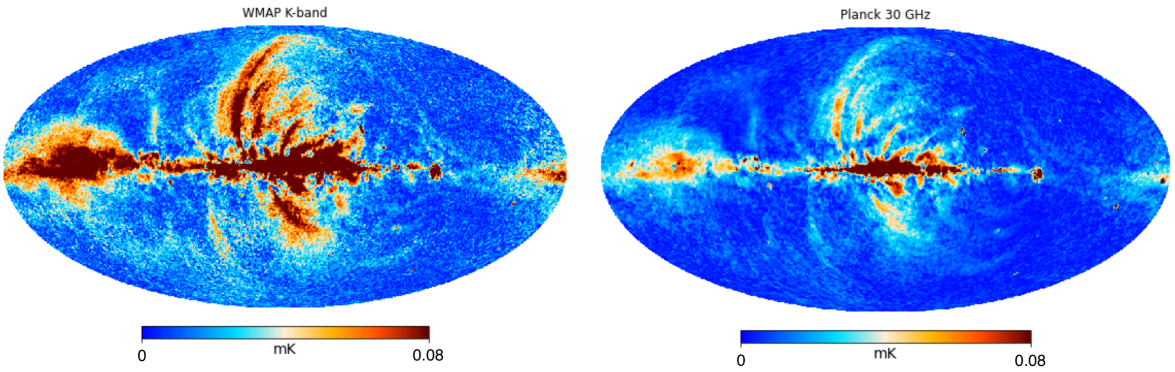

Figure 4.1: Debiased Polarized Intensity maps (1°) of the *WMAP* K-band at 23 GHz (left) and the 30 GHz channel of the *Planck* PR4 data set (right).

4.2 Filament Finder

4.2.1 Algorithm

We develop an algorithm in order to seek elongated structures in polarized intensity maps. The method resembles the two-dimensional version of the Smoothed Hessian Major Axis Filament Finder (`SHMAFF`) [138, 139]. The `SHMAFF` algorithm has previously been used to find filaments in the three-dimensional galaxy distribution and in the analysis of polarized dust structures in the *Planck* 353 GHz maps [84]. The main difference in our implementation is that, while the `SHMAFF` detection is based on the minimal eigenvalues of the Hessian matrix, our detection is based directly on the polarized intensity. This is because the Hessian matrix fails to find pixels with minimal eigenvalues in detecting the thick and diffuse filaments which we expect to be in the noisier area of the sky, that is outside the Galactic plane.

The algorithm works on a pixel by pixel basis, examining the orientation angle ψ defined in [84] and comparing the polarized intensity value P with respect to a threshold P_{th}. The orientation angle is determined from

$$\begin{aligned} \psi &= \arctan\left(-\frac{H_{\theta\theta} - H_{\phi\phi} + \alpha}{2H_{\theta\phi}}\right) \\ \text{with } \alpha &= \sqrt{(H_{\theta\theta} - H_{\phi\phi})^2 + 4H_{\theta\phi}^2}, \end{aligned} \tag{4.4}$$

where H is the Hessian matrix computed from the second-order covariant-derivatives with respect to the spherical coordinates (θ, ϕ) [140]. We compute the threshold values P_{th} from the P distribution. We cannot use the mean and the standard deviation because the distribution of P is not Gaussian and exhibits an extended tail, thus, we define the threshold from the median m_P and the median absolute deviation (MAD) σ_m [141, 142] as

$$P_{th} = m_P + \sigma_m = m_P + 1.4826 \cdot median(|P - m_P|). \tag{4.5}$$

The algorithm starts by identifying the brightest pixel P_0 and denoting its orientation angle ψ_0. It then considers its 8 (or 7) neighbouring pixels, identified with the `get_all_neighbours` routine of `HEALPix`. For each neighbour pixel, two conditions are checked: (i) if its polarized intensity is larger than the fixed threshold of equation 4.5, (ii) if its orientation angle is coherent with the initial pixel

$$\begin{aligned} &(i) \quad P_i > P_{th} \\ &(ii) \quad |\psi_i - \psi_0| < \Delta\psi, \end{aligned} \tag{4.6}$$

where we fix $\Delta\psi$ at 10° in order to detect the longest filaments. Nevertheless, we have checked that the results are robust for a reasonable range of $\Delta\psi$. If both conditions in equation 4.6 are satisfied, we accept the pixel as part of the same structure of the initial pixel. Then, we look for its neighbours which also satisfy the two conditions. We continue this friend-of-friend recursive algorithm until the conditions are no longer satisfied. Once a structure is defined, the pixels are masked from the map, the new brightest pixel is identified and the condition-based procedure is repeated.

We finally define a template, which includes all the pixels satisfying the previous conditions, with all the strongly polarized areas in the P map of arbitrary shapes and

sizes. We then smooth it with a 3° Gaussian beam, in order to soften the boundaries. In order to allow only elongated structures which can be identified as filaments, we apply one further criteria to the 3° smoothed map, i.e. we reject structures with length smaller than a threshold minimal length $L < L_{th}$, fixed at 10°. The length is defined as the maximum pixel-pair angular distance. The threshold length has been selected analysing simulations as discussed in appendix B.2.2.

4.2.2 Band-pass Filter

Different filaments have been observed in low frequency (¡ 1 GHz) radio continuum surveys, and more recently in the *WMAP* polarization data [66]. The filaments can be divided into two categories: bright and narrow, or weak and diffuse. In order to optimize the detection of these filaments, we filter the maps to focus on specific angular scales of interest before applying the filament finder algorithm. We compute the spherical harmonic coefficients a_{lm} by means of the `map2alm` routine of `HEALPix`, multiply by a band-pass filter of the following form

$$f(\ell) = \frac{1}{4}\left[1 + \tanh\left(\frac{\ell - \ell_{min}}{\Delta\ell}\right)\right]\left[1 - \tanh\left(\frac{\ell - \ell_{max}}{\Delta\ell}\right)\right] \tag{4.7}$$

then generate the filtered maps with the `alm2map` routine. The filter cuts off the amplitudes below a multipole scale ℓ_{min} and above ℓ_{max}. In order to detect the thinner filaments, we consider multipoles in the range 20-50, whereas for the diffuse filaments the multipoles are restricted to the range 15-20. The cuts are roughly in accordance with the widths of the filaments ($\ell \sim 180/\theta$). $\Delta\ell$ is set to 10, but the method is robust for a reasonable range of $\Delta\ell$.

The filters are shown in figure B.1 in appendix 4.1. By filtering out small-scale modes, we enhance the contrast of larger structures with respect to the diffuse foreground emission, and also reducing the instrumental noise. Moreover, we remove correlations on large scales which can negatively affect the detection. The application of the filter is critical to increase the accuracy of the estimation of the polarization orientations of the filaments, especially in areas where the signal-to-noise is low. A similar filter has been used in [93] for a statistical analysis of the 408 MHz Haslam data.

4.2.3 Results

Starting from the debiased polarized intensity maps obtained as described in section 4.1.3, we generate two bandpass-filtered maps $P^{20\text{-}50}$ and $P^{15\text{-}20}$, applying the filter in equation 4.7, where the superscripts correspond to the applied multipole ranges. We first mask the bright point sources, both Galactic and extragalactic, which could bias our algorithm. We use the mask derived for the *Planck* PR4 SEVEM component separation pipeline which includes all the point sources that have polarization detection significance levels of 99% or more in the 30 GHz polarized map [116, 124, 125]. The finder algorithm is based on the threshold condition in equation 4.6, where the threshold is computed from the P distribution (see equation 4.5). However, very bright areas such as the Galactic plane could bias the threshold value upwards, preventing filament detection. Therefore, when analysing the $P^{20\text{-}50}$ maps, we apply a Galactic mask excluding pixels at latitudes $|b| < 3°$. A similar argument applies to the $P^{15\text{-}20}$ analysis.

However, since we are looking for very faint filaments, the NPS and the Southern Fan regions are also excluded in addition to the Galactic plane. This can be achieved by simply masking the brightest 30% sky fraction. The specific choice of masks was tested on the simulations described in the appendix B.2.1.

After applying the filament finder algorithm to the two bandpass-filtered maps, we merge the two sets of results into one template, smooth it by 3° and apply the criteria of minimal length as described in section 4.2.1. The filament templates determined independently from the *WMAP* K-band and *Planck* 30 GHz data are shown in figure 4.2. The *WMAP* results reveal more compact and elongated structures than for *Planck*, indicating that the finder algorithm performs better when applied to the data with brighter synchrotron emission. However, several similar structures are detected in the same areas of the sky in both maps. The agreement between the independent results corroborates the validity of the algorithm and supports the existence of the filaments as real emission, and not due to noise or systematic effects. In appendix B.2.1, we explore the accuracy and limits of the filament finder algorithm, testing our method with toy filamentary foreground models.

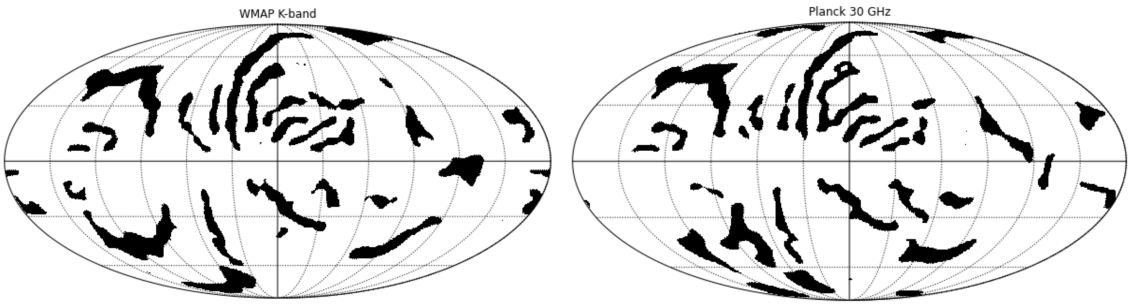

Figure 4.2: Filamentary structures detected in the debiased polarized intensity of the *WMAP* K-band at 23 GHz (left) and the *Planck* 30 GHz channel (right).

4.3 Filament analysis

4.3.1 Filaments

Combining the information obtained from *WMAP* and *Planck*, we get a final template of polarized filamentary structures detected in the frequency range 23-30 GHz, shown in figure 4.3. We use the *WMAP* detection as our benchmark, but only retain those structures which are detected, at least in part, in the *Planck* data. The one exception is filament XI, which is clearly detected in the *Planck* data, but only partially in *WMAP*. Its existence is supported by previous analysis performed on *WMAP* [66]. This method ensures that detected filaments are not due to noise or systematic residuals. Then, we remove those structures which do not show clear elongation, in particular in the Galactic plane, where the emission is more complex, and polar regions, where the signal-to-noise is low.

In order to specify the filaments, we use and expand the nomenclature used in [66]. Filaments I (NPS), IIIn, and IV have been recognised and studied for more than 60 years. These large structures have been observed in X-ray, gamma-ray and other microwave experiments [143, 90, 91]. Filament II (Cetus Arc) was previously detected in the radio sky [89], and found here for the first time in polarization despite its low emission. We detect ten further filaments reported in [66] (Is, GCS, IIIs, VII, IX, X, XI, XII, XIII, XIV) but not filament VIII. We also identify five new filaments (XV, XVI, XVII, XVIII, XIX) that are visible in both *WMAP* and *Planck*. Filament XV is a bright structure at the center of the Galactic Haze [144]. Filament XVI, because of the position and shape, seems to be related to Filament I. Filament XVIII is a bright structure of the Northern Fan region close to the Galactic plane. Finally, Filaments XVII and XIX are new detections in the region below the Galactic plane.

Most of the detected filaments have circular arc-like shapes, supporting the model of supernova remnants expanding into the Galactic magnetic field [92]. Several structures appear to be spatially correlated with each other, although most are stand-alone features. In the NPS, there are several elongated structures which do not resemble loop-like features. They were first identified in radio observations [91], but the NPS complexity is more evident in polarization. Because of their location, there are models which link these structures with the Fermi Bubbles (FB) detected in Fermi data at energies ∼10–500 GeV [145, 146].

4.3.2 Polarization Fractions

The polarization fraction is defined as the ratio of the polarization amplitude to total intensity

$$\Pi = \frac{P}{I}. \tag{4.8}$$

At the low frequencies of interest here, the synchrotron emission largely dominates the polarization signal, thus, we can neglect other physical emission mechanisms and consider directly the frequency data. However, this assumption does not apply in intensity where the CMB, free-free and AME also contribute to the total emission.

Most of the observations suggest that at frequencies above 20 GHz the spectral index of the synchrotron intensity spectrum is $\beta \approx -3$ [60]. However, according to some mod-

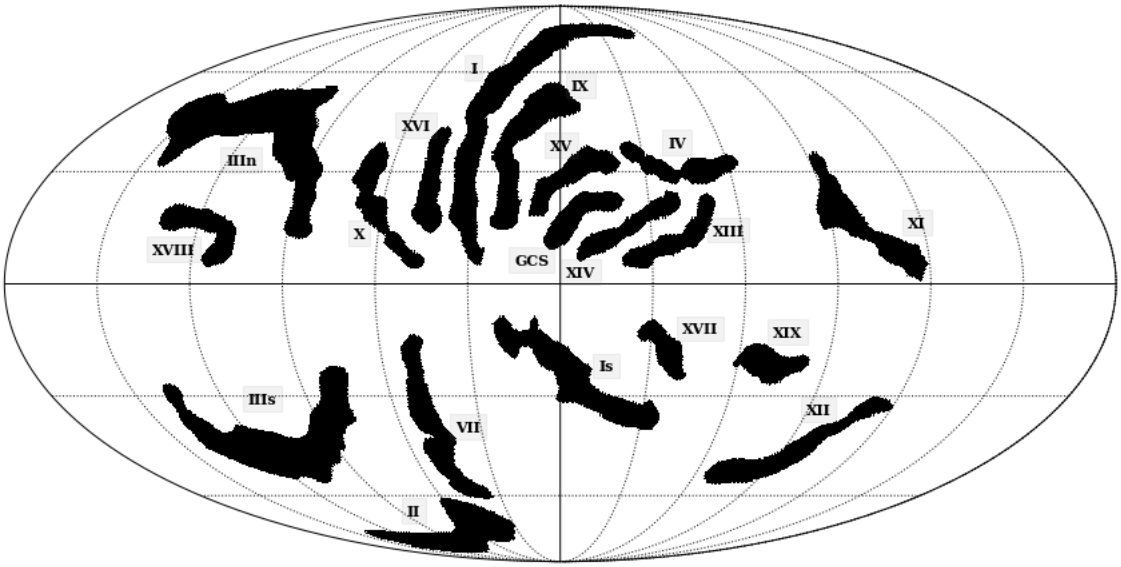

Figure 4.3: Template map showing the filaments of the polarized synchrotron emission detected by combining *WMAP* (23 GHz) and *Planck* (30 GHz) results.

els [147], it can get much flatter for frequencies below 10 GHz. Moreover, we expect it to exhibit significant spatial variations. In this analysis, we use the diffuse synchrotron intensity map provided in the Planck 2015 [148] release. The template has been generated at a reference frequency of 408 MHz by `Commander` (a parametric component separation method) applied to the *WMAP*, *Planck* and *Haslam* observations.

We estimate the synchrotron intensity extrapolating the 408 MHz map up to 23 GHz and 30 GHz adopting a fixed spectral index $\beta = -3.0$. The maps are analysed at 3° resolution and $N_{side} = 64$, masking the Galactic plane[5]. Pixels with a signal-to-noise ratio lower than 2.5 have been excluded.

The polarization fraction maps are showed in figure 4.4 (top panels). For each pixel, the polarization fraction error, σ_Π, is obtained propagating the errors in the polarization and intensity maps. The intensity uncertainty is, in turn, obtained propagating the uncertainty of the intensity spectral index. The weighted average of the polarization fractions over pixels for each filament are listed in Table 4.1. The largest source of uncertainty in σ_Π is due to the uncertainty in the intensity spectral index. We are aware that, locally, β can assume values over a very broad range. However, we compute the polarization fraction averaging over extended areas, so it is reasonable to assume that in these areas $\sigma_\beta = 0.1$ as found in previous works on partial-sky analysis [149, 1, 65]. We report good agreement between the *WMAP* and *Planck* results, the largest discrepancies arising for the more diffuse filaments, e.g., filament XII.

Assuming a uniform spectral index, we find that the polarization fraction of the filaments are typically larger than for external regions outside the filaments. The filaments with the highest polarization fractions, IX and XV, achieve values above 30%, and are both located in the NPS. Loop I has an average value of about 20%, slightly smaller

[5]In order to mask the bright pixels along the Galactic plane, we use a Galactic mask obtained combining the 2015 Galactic plane mask which allows the 90 per cent of the sky (provided in the PLA) and a Galactic latitude mask excluding pixels within ±5° of the Galactic plane.

than the value found at the center of the NPS. These results corroborate the results found in the previous analysis [66, 60]. We report a high polarization fraction also for filament XVIII, located in the Fan region. The lowest polarization fractions are found for filaments XI, XIII and XVII.

4.3.3 Spectral Index

The synchrotron spectral energy distribution (SED) is generally approximated by a power law[6] $S_\nu \propto \nu^\beta$ where β is the energy spectral index. Spatial variations of β have been reported in the literature [150, 64, 65]. In this section, we measure the spectral index of each filament described in 4.3.1 employing a method based on the Q and U Stokes parameters [151, 62].

Let us define the vector

$$d(\alpha) = Q\cos(2\alpha) + U\sin(2\alpha) \tag{4.9}$$

which represents, for each pixel, the projection of the Stokes parameters (Q, U) into a reference frame rotated by the angle α. We vary α over the range $(0°, 85°)$, in steps of 5°. For each filament, we compute a linear fit over all the internal pixels to the relation

$$d_{\rm P30}(\alpha) = m(\alpha)\cdot d_{\rm WK}(\alpha) + n(\alpha) \tag{4.10}$$

where $d_{\rm P30}(\alpha)$ and $d_{\rm WK}(\alpha)$ are computed respectively from the *Planck* and *WMAP* data. Adding the free parameter $n(\alpha)$ gives the advantage of removing any zero level due to possible systematics in the maps. The fit is performed with the orthogonal distance regression code `odr`[7] from `SciPy`, in order to account for the noise variance of both *WMAP* and *Planck*. A calibration error of 0.3% has been added in quadrature to both experiments [117, 116]. From the parameter $m(\alpha)$ and its uncertainty, we compute the spectral index for each α as

$$\beta(\alpha) = \frac{\log m(\alpha)}{\log(\nu_{\rm P30}/\nu_{\rm WK})} \quad \sigma_\beta(\alpha) = \frac{\sigma_m(\alpha)}{m(\alpha)}\frac{1}{\log(\nu_{\rm P30}/\nu_{\rm WK})} \tag{4.11}$$

where $\nu_{\rm P30}$ =28.4 GHz and $\nu_{\rm WK}$=22.8 GHz. The final value of the index is recovered from the weighted average

$$\beta = \frac{\sum_{\alpha=0}^{85}\beta(\alpha)\sigma_\beta^{-2}(\alpha)}{\sum_{\alpha=0}^{85}\sigma_\beta^{-2}(\alpha)}. \tag{4.12}$$

Since the $\beta(\alpha)$ values are strongly correlated, we take as the uncertainty on the final spectral index the minimum variance among the measurements $\sigma_\beta = \min(\sigma_\beta(\alpha))$. We checked that this uncertainty is always larger then the intrinsic uncertainty of $\beta(\alpha)$ given by the standard deviation estimated at different rotation angles.

As a consistency check, we also fitted the spectral index from the debiased polarized intensities with the T-T plot approach. We find consistent results with those determined with the method presented above. It has been shown that the synchrotron spectral index is not stable with respect to polarization orientation in the presence of systematics

[6] Given the sensitivity of *Planck* and *WMAP* data, we cannot explore more complex models.
[7] https://docs.scipy.org/doc/scipy/reference/odr

[152]. The (Q, U) method allows marginalization of the result over the polarization angle, making this approach more reliable.

The maps are analysed at 3° resolution and $N_{side} = 64$, masking the Galactic plane. Pixels with a signal-to-noise ratio lower than 2.5 have been excluded. The maps are converted to Rayleigh-Jeans temperature units and corrected by the colour correction using the coefficients given in [51].

In Table 4.1 the spectral indices determined for the different filaments are listed. For each filament, a mean χ^2 value is computed by averaging over all the values given at different rotation angles by the `odr` routine. Note that we do not take into account the presence of correlated noise between pixels, thus, leading to an underestimation of the uncertainties. This is one of the reasons which would explain some large χ^2 values. We find spectral index results, both inside and outside the filaments, consistent with the values found in previous analysis of about –3.1 [63, 81, 1]. As shown in figure 4.4 (bottom panel), the β values span a very broad range, from -3.59 (XVII) to -2.17 (VII). The value for loop I is consistent with the literature [66, 153]. Filaments IX and XV, the most polarized detections located at the NPS, show slightly flatter values ($\sim$ -2.5).

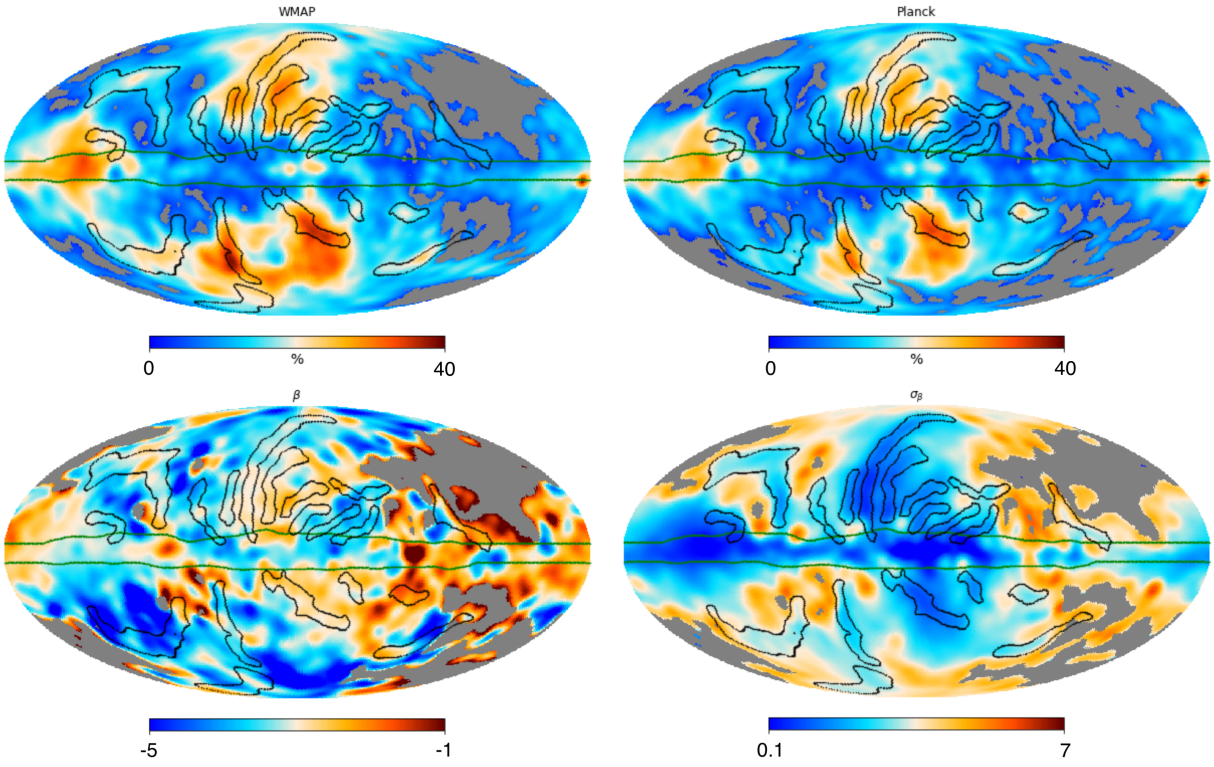

Figure 4.4: Top: polarization fraction of the *WMAP* K-band at 23 GHz (left) and the 30 GHz channel of the *Planck* PR4 (right). Bottom: spectral index β (left) with error σ_β (right). Outlines of the filaments (black) and the Galactic mask (green) used in the analysis are also shown. Pixels with a signal-to-noise ratio lower than 2.5 have been masked (grey). For illustrative purpose, the maps are smoothed to a resolution of 5°.

		polarization fraction				spectral index		
		WMAP		*Planck*				
filament	f_{sky} [%]	Π [%]	σ_Π [%]	Π [%]	σ_Π [%]	β	σ_β	χ^2_r
I	1.5	22.6	9.4	21.2	9.3	-3.06	0.01	1.92
Is	1.2	18.3	7.6	19.4	8.5	-2.80	0.03	1.87
II	0.8	24.5	10.4	20.4	9.2	-3.37	0.06	3.01
IIIn	2.1	18.9	8.0	17.4	7.7	-3.07	0.02	1.55
IIIs	1.8	19.8	8.4	15.5	7.1	-3.65	0.04	2.22
IV	0.5	18.1	7.6	15.1	6.8	-3.07	0.11	1.95
GCS	0.4	22.6	9.4	22.0	9.6	-2.80	0.03	2.35
VII	0.8	17.3	7.3	20.4	9.1	-2.17	0.09	1.97
IX	0.9	33.1	13.7	32.2	14.1	-2.64	0.02	1.90
X	0.6	17.1	7.2	14.2	6.3	-3.39	0.04	1.48
XI	0.8	13.2	5.7	13.3	6.0	-2.45	0.05	1.60
XII	0.7	20.6	9.0	13.9	6.5	-3.38	0.05	1.21
XIII	0.5	14.0	5.8	12.6	5.6	-3.28	0.03	2.42
XIV	0.5	17.6	7.3	14.5	6.4	-3.05	0.04	1.34
XV	0.5	33.8	14.0	34.8	15.3	-2.36	0.04	2.44
XVI	0.4	22.0	9.1	20.7	9.1	-3.39	0.11	1.51
XVII	0.3	14.6	6.1	15.7	6.9	-3.59	0.05	1.67
XVIII	0.5	30.1	12.5	26.4	11.6	-3.08	0.05	1.28
XIX	0.4	21.1	9.1	26.1	11.6	-2.28	0.09	0.91
inside filaments	15.2	19.0	8.0	17.2	7.7	-3.08	0.01	3.14
outside filaments	62.1	11.1	5.0	10.3	4.9	-3.15	0.01	3.34
combined	76.2	11.8	5.2	11.0	5.2	-3.10	0.01	3.29

Table 4.1: Polarization fractions and polarization spectral indices of the *WMAP* K-band and *Planck* 30 GHz channel. The synchrotron intensity map is extrapolated from the 408 MHz map up to 23 GHz and 30 GHz using a constant spectral index $\beta = -3.0$. The spectral index is computed over the 23-30 GHz frequency range.

4.3.4 E and B Modes

As described in appendix B.1, the polarized emission can be decomposed into E and B modes. The synchrotron polarized angular power spectra has been analysed in the frequency range 2-30 GHz, finding that: both E- and B- modes can be well described by a power law $C_\ell^{EE,BB} \propto \ell^{-2.9}$, the B-to-E ratio ranges between 0.2-0.5 and the EB correlation is compatible with zero [81, 1]. In this section we analyze how the filamentary structure relates to the two polarized components.

In [154] a method was proposed for decomposing the Q and U Stokes parameters into the so-called E- and B-mode families. Starting from the (Q, U) maps, we can compute the $a_{lm}^{E,B}$ coefficients using the `map2alm` routine of `HEALPix`. Setting $a_{lm}^B = 0$ and computing the Stokes parameters with the `alm2map` routine determines the contribution to Q and U from the E mode alone. Similarly, setting $a_{lm}^E = 0$, we get the contribution from the B mode. Therefore, we can compute the single-mode polarization intensities as

$$P_E = \sqrt{Q_E^2 + U_E^2} \quad P_B = \sqrt{Q_B^2 + U_B^2}. \tag{4.13}$$

For the sake of brevity, here we show an analysis performed on the *WMAP* K-band, however, the same conclusions can be obtained from the 30 GHz *Planck* data. We do not use any estimators to correct the polarized amplitude for the noise bias. This is because the estimator in equation 4.1 would require the decomposition of the variance into the E- and B families, which is not a straightforward operation. Nevertheless, we expect qualitatively correct results for the areas where the signal-to-noise is high, in which the bias is negligible.

Applying the filament finder algorithm to the decomposed maps, we find that nearly all of the filamentary structures are detected at least in part in the P_E, but not in the P_B map, as shown in figure 4.5. As expected, the algorithm fails to detect filaments II, IIIs and X, which are either diffuse or strongly affected by noise bias. The complex filamentary structure of the NPS emission is clearly visible in P_E, suggesting its E-nature. In the P_B maps, we detect parts of filaments I and IX (even if slightly shifted). Filament XIX is the only structure which is partially detected in B, but not in E.

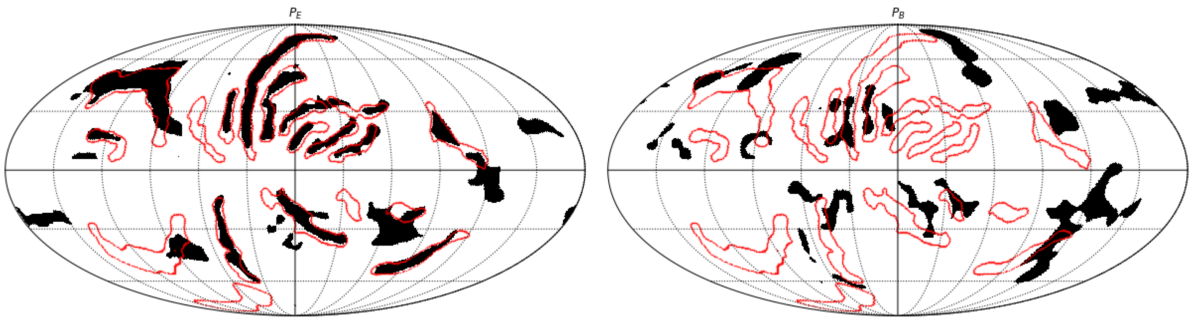

Figure 4.5: Filamentary structures detected in the decomposed polarized intensity P_E (left) and P_B (right) maps obtained with the *WMAP* K-band at 23 GHz. In red, the filaments detected from the polarized intensity P_{MAS} as described in section 4.3.

4.3.5 408 MHz Haslam Map

The current best full-sky map of the synchrotron intensity emission at 408 MHz is due to [86, 87]. A more recent version of the data that has been destriped and cleaned of bright point sources is described in [88]. We apply the filament finder algorithm to this map, provided as a LAMBDA product[8], to study the filamentary detection in intensity at low frequencies.

The map and the detected filaments are shown in figure 4.6. Filament I is the major structure in intensity as well as in polarization. Part of the detected structure is well matched by what is found at 23-30 GHz, but is more extended at the lower frequency. A similar observation holds for filament II. The majority of the structures in the NPS observed with *WMAP* are also visible, at least in part, in the *Haslam* map. However, in intensity the synchrotron emission is very diffuse, and the algorithm fails to detect the more diffuse filaments, such as III, XI, XII. An interesting result is that filaments IX and XVI, which are the two strong emission structures detected in polarization around Loop I, are not well detected in the 408 MHz map.

Note that the analysis presented in this section provides us with an additional robustness test for our algorithm. However, only a qualitative comparison between *Haslam* and *WMAP*/*Planck* maps is possible. This is because, in intensity, the synchrotron emission dominates at 408 MHz, but not at 23/30 GHz, where other components become important. On the other hand, the synchrotron emission dominates in polarization, but comprehensive data sets in polarization do not exist at 408 MHz. We hope that the results presented in this section will stimulate future analysis using new data at similar frequencies.

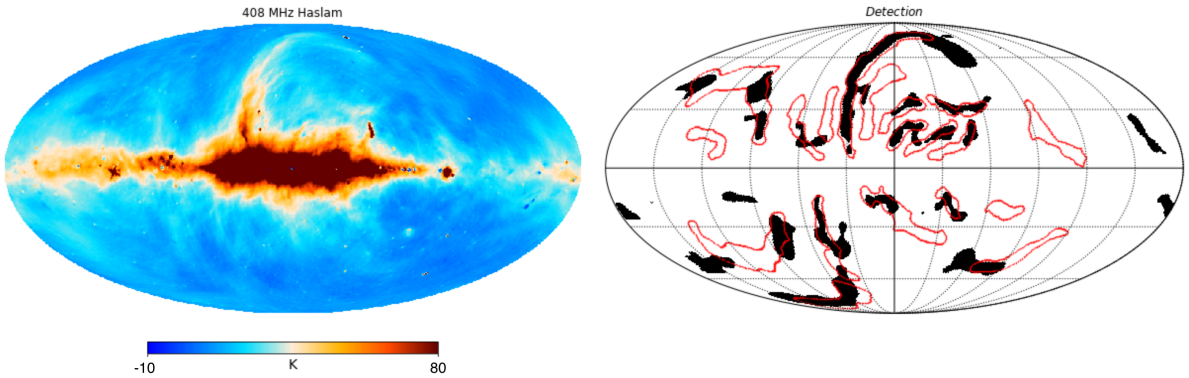

Figure 4.6: Left: full-sky 408 MHz map. Right: Structures detected in the data (black) compared to the filaments found in polarization at 23-30 GHz (red).

[8] https://lambda.gsfc.nasa.gov/product/foreground/fg_2014_haslam_408_info.html

4.4 Statistical Properties

4.4.1 Minkowski Formalism

According to Hadwinger's Theorem, any morphological property can be expressed as a linear combination of Minkowski Functionals (MFs). These are defined for any field not requiring any prior assumption, making them particularly advantageous for the analysis of fields for which a non-Gaussian nature is known. Several analyses have already been performed on CMB data using MFs to search for evidence of non-Gaussianity [155, 156, 157] and residual foreground contamination [158], or to characterize the properties of foregrounds [159, 93]. In this section, we will briefly review the method used for their numerical calculation, following the methodology developed by [160].

Given a map u on the sphere ($\mathbb{S}^2$) and a threshold v, there are 3 MFs which represent the area (V_0), the perimeter (V_1) and the integrated geodesic curvature (V_2) of an excursion set, that is the region where $u \geq v$, with boundaries defined by $u = v$. For a map in the `HEALPix` pixelization, we can numerically compute the MFs via a sum over all pixels

$$V_0(v) = \frac{1}{N_{pix}} \sum_{pixels} \mathcal{H}(u - v) \tag{4.14}$$

$$V_1(v) = \frac{1}{4} \frac{1}{N_{pix}} \sum_{pixels} \delta(u - v) \sqrt{u_{;\theta}^2 + u_{;\phi}^2} \tag{4.15}$$

$$V_2(v) = \frac{1}{2\pi} \frac{1}{N_{pix}} \sum_{pixels} \delta(u - v) \frac{u_{;\theta} u_{;\phi} u_{;\theta\phi} - u_{;\theta}^2 u_{;\phi\phi} - u_{;\phi}^2 u_{;\theta\theta}}{u_{;\theta}^2 + u_{;\phi}^2} \tag{4.16}$$

where $u_{;i}, u_{;ij}$ $(i, j \in (\theta, \phi))$ are the first and second partial derivatives in spherical harmonic space, $\mathcal{H}$ is the Heaviside step function and δ is the delta function. We rescale the field u to have zero mean and unit standard deviation. The δ-function is numerically approximated through a discretization

$$\delta(u - v) = \frac{1}{\Delta v} \left[\mathcal{H}\left(u + \frac{\Delta v}{2}\right) - \mathcal{H}\left(u - \frac{\Delta v}{2}\right) \right] \tag{4.17}$$

that is $\delta(u - v)$ is equal to $1/\Delta v$ if u is between $v - \Delta v/2$ and $v + \Delta v/2$, and zero elsewhere.

This pixelization method introduces systematic residuals. It has been shown that residuals scale as the square of the bin-size (Δv^2) [161]. However, if the bin-size is too small the results can be affected by map noise. We pick the value $\Delta v = 0.5$. We find that this bin-size minimizes the residual obtained comparing the numerical equations 4.15 and 4.16 with the MFs analytical equations valid for a perfect Gaussian field.

Minkowski Tensors (MTs) are tensorial quantities that generalize the scalar MFs. MTs have been already used in cosmology to study CMB [162] and foreground [93] anisotropies. There are three rank-two MTs on the sphere, usually denoted as W_k. The three scalar MFs, V_k, are then given by the traces of W_k. We are particularly interested in W_1, also called the Contour Minkowski Tensor (CMT), which encodes shape and alignment information for structures. It can be numerically computed as

$$W_1(v) = \frac{1}{4} \frac{1}{N_{pix}} \sum_{pixels} \delta(u - v) \frac{1}{|\nabla u|} M \tag{4.18}$$

where

$$M = \begin{pmatrix} u_{;\phi}^2 & -u_{;\phi}u_{;\theta} \\ -u_{;\phi}u_{;\theta} & u_{;\theta}^2 \end{pmatrix}. \tag{4.19}$$

W_1 is proportional to the identity matrix if the structures have no elongation in any particular direction. λ_+, λ_- are the two eigenvalues of W_1 such that λ_+ ¿ λ_-. We define α as

$$\alpha = \frac{\lambda_+}{\lambda_-}. \tag{4.20}$$

$\alpha = 1$ implies that the field preserves statistical isotropy (SI). In order to quantify the non-Gaussianity and anisotropy of data maps, we need to compare them with a set of suitable simulations. We then define, at each threshold v, the quantities

$$\chi_k = \frac{|\Delta V_k|}{\sigma_{V_k}}, \quad \Delta V_k(v) = V_k^{data}(v) - V_k^{sim}(v) \tag{4.21}$$

where V_k^{data} is the k-th MF computed from the data, V_k^{sim} and σ_{V_k} are the values obtained taking respectively the average and the standard deviation of the functionals determined from simulations. Analogously, we define at each threshold v the quantities

$$\chi_{(W_1)_{ii}} = \frac{|\Delta(W_1)_{ii}|}{\sigma_{(W_1)_{ii}}}, \quad \Delta(W_1)_{ii} = (W_1)_{ii}^{data} - (W_1)_{ii}^{sim} \tag{4.22}$$

where $(W_1)_{ii}$ stands for $(W_1)_{11}$ and $(W_1)_{22}$, which are the diagonal terms of the CMTs. The values $(W_1)_{ii}^{sim}$ and $\sigma_{(W_1)_{ii}}$ are computed from simulations. The same quantification could not be applied to α because its statistic follows the Beta probability distribution [93]. Thus we define the quantity

$$\chi_\alpha = \frac{\Delta\alpha}{\delta_1}\mathcal{H}(-\Delta\alpha) + \frac{\Delta\alpha}{\delta_2}\mathcal{H}(\Delta\alpha), \quad \Delta\alpha(v) = \alpha^{data}(v) - \alpha^{sim}(v) \tag{4.23}$$

where δ_1 and δ_2 denote the 95% confidence interval and $\mathcal{H}$ is the Heaviside step function. Note that a value $|\chi_\alpha| > 1$ implies a deviation from the simulations outside the 95% confidence interval. In this and the following sections we will focus on the analysis and results obtained from the *WMAP* K-band polarization maps at resolution 1° and $N_{side} = 128$. The same analysis has been performed with 30 GHz *Planck* maps and the results presented in appendix B.3.

4.4.2 Masking and Filtering

It is well known that the synchrotron emission is non-Gaussian and anisotropic on the full sky. In this analysis, we are mainly interested in understanding if this behaviour holds in regions of the sky where the emission is more diffuse, that is when the brightest areas (Galactic plane, the Spur and Fan regions) are masked.

We define two different masks for the analysis of the faintest 80% and 60% of the sky. To avoid possible leakage of power which can arise when computing power spectra in the presence of sharp boundaries between the masked and the unmasked regions, we apodize the masks with the `mask_apodization` ("C2") routine of `NaMaster`[9] with

[9] `NaMaster` is a public software package providing a general framework to estimate pseudo-C_ℓ angular power spectra. [127] namaster.readthedocs.io

apodization scale of 5°. We also take into account a point source mask, as used in the filament finder analysis in section 4.2.3, apodized at 1°. To minimize the effects of the mask boundary in the sum in equations 4.14-4.18, we only include those pixels such that the smoothed mask value is larger than 0.9. For the two masks adopted here, this corresponds to sky fractions of 76.4% and 57.1%. The threshold has been conservatively chosen in order to maximize the statistical significance of our results. Note that we do not construct a specific filament mask, because from prior tests we have noticed that the Minkowski method is more reliable when we use a compact mask rather than a complex mask with many holes and islands.

Besides the region-dependency, in this analysis we want to test the statistical behavior on different scales. The maps are therefore filtered using the band-pass filter presented in section 4.2.2. We analyze different scale ranges varying ℓ_{min} in equation 4.7. We do not study the maps for multipoles smaller than $\ell_{min} = 30$ because the anisotropic nature of the emission at such large scale is well known, so we will only focus on $\ell_{min} \geq 30$. We fix $\ell_{max} = 180$, in accordance with the map resolution at 1°. In figure 4.7 the *WMAP* polarized intensity maps, filtered with the ($\ell_{min} = 30$, $\ell_{max} = 180$) band-pass, are shown. The region in grey corresponds to the pixels masked in the Minkowski analysis. We finally subtract the mean and then rescale with the standard deviation, where mean and standard deviation are computed from the data in the unmasked area of the maps.

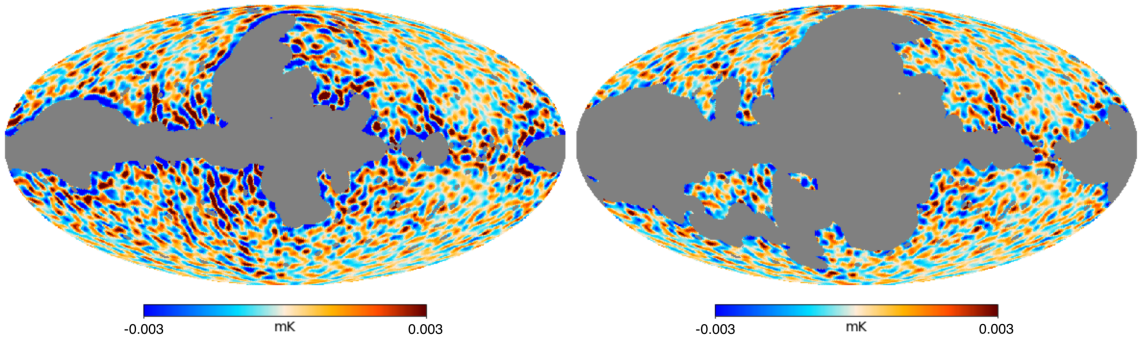

Figure 4.7: Debiased *WMAP* K-band polarized intensity maps at 1° resolution, after band-pass filtering as defined in equation 4.7 with $\ell_{min} = 30$ and $\ell_{max} = 180$. The grey regions correspond to the missing pixels for the 80% (left) and 60% (right) masks.

4.4.3 Gaussian Simulations

In order to quantify the non-Gaussianity and anisotropy of the polarized synchrotron emission, we need to compare the polarization data with a set of suitable simulations. To generate simulations, we first compute with `NaMaster` the polarization power spectra of the data maps in the unmasked areas. In fact, we compute the cross-spectra between the co-added *WMAP* 1 to 4 year sky maps and 5 to 9 year data. In this way, we reduce the effects of instrumental noise and systematics. Based on this spectrum, we then generate Gaussian and isotropic simulations of full-sky Q and U Stokes parameter maps at the data resolution using the `HEALPix synfast` routine. We add noise and compute the debiased polarized intensity of the simulations as described in section 4.1.3. We obtain

600 total polarization simulations which have a mean power spectrum compatible with the data, but are isotropic and generated from Gaussian-distributed Q and U. Note that the variance of the simulations includes both sample variance and noise. Finally, we compute the MFs and MTs for the simulations using the same band-pass filter and masks as used for the data.

4.4.4 Results

The results for the MFs and the CMT, derived from band-pass filtered data are shown in figure 4.8. We find that the non-Gaussian and anisotropic deviations are much lower when bright regions are masked. For the larger sky fraction ($f_{sky} = 80\%$), we find that the first MF (V_0) shows the largest deviation from Gaussianity. For most thresholds, the deviation is higher than 3σ and several values exceed 5σ. The deviations of the other two MFs and the CMT diagonal terms exceed 3σ for several thresholds, few exceed 5σ. $|\chi_\alpha|$ is lower than one except for one threshold, implying a weak deviation from isotropy. For the smaller sky fraction ($f_{sky} = 60\%$), for all the thresholds we find that the deviations of the three MFs and the CMT diagonal terms never exceed 3σ, with average values (over all thresholds) lower than 1.2σ. The value of α never exceeds the 95% interval.

In figure 4.9 we show results for different values of ℓ_{min}. For the larger sky fraction ($f_{sky} = 80\%$), we find that the deviation decreases as ℓ_{min} increases, however, the MF deviation for some thresholds remains significantly high ($>3\sigma$), even at the smallest scales considered ($\ell_{min} = 130$). For the smaller sky fraction ($f_{sky} = 60\%$), the deviations remain almost constant with ℓ_{min}, indicating consistency between the data and simulations for all thresholds and multipoles at the 3σ level.

Referring back to figure 4.7, we see that the areas where several filaments (IIIn, IIIs, IV, VII, X, XVI, XVII) have been detected are masked by the 60% mask and not the 80% mask. This suggests that the contribution of the sky regions where these large complex structures are present affects the emission on scales smaller than $\sim 6^\circ$.

The non-Gaussian deviation decreases for smaller scales, corroborating the hypothesis that at small scales the emission tends to be more Gaussian. However, the effect of bright local structures is still not negligible on a scale of $\sim 1.5^\circ$. From this analysis we also learn that the non-Gaussian nature is mainly of the kurtosis type, since V_0 shows the largest deviations from simulations, as explained in [93]. These results at 23 GHz are in good agreement with those from the *Planck* 30 GHz polarization maps. More details can be found in appendix B.3.1. Moreover, very similar conclusions are obtained for intensity in the analysis of the 408 MHz maps by [93].

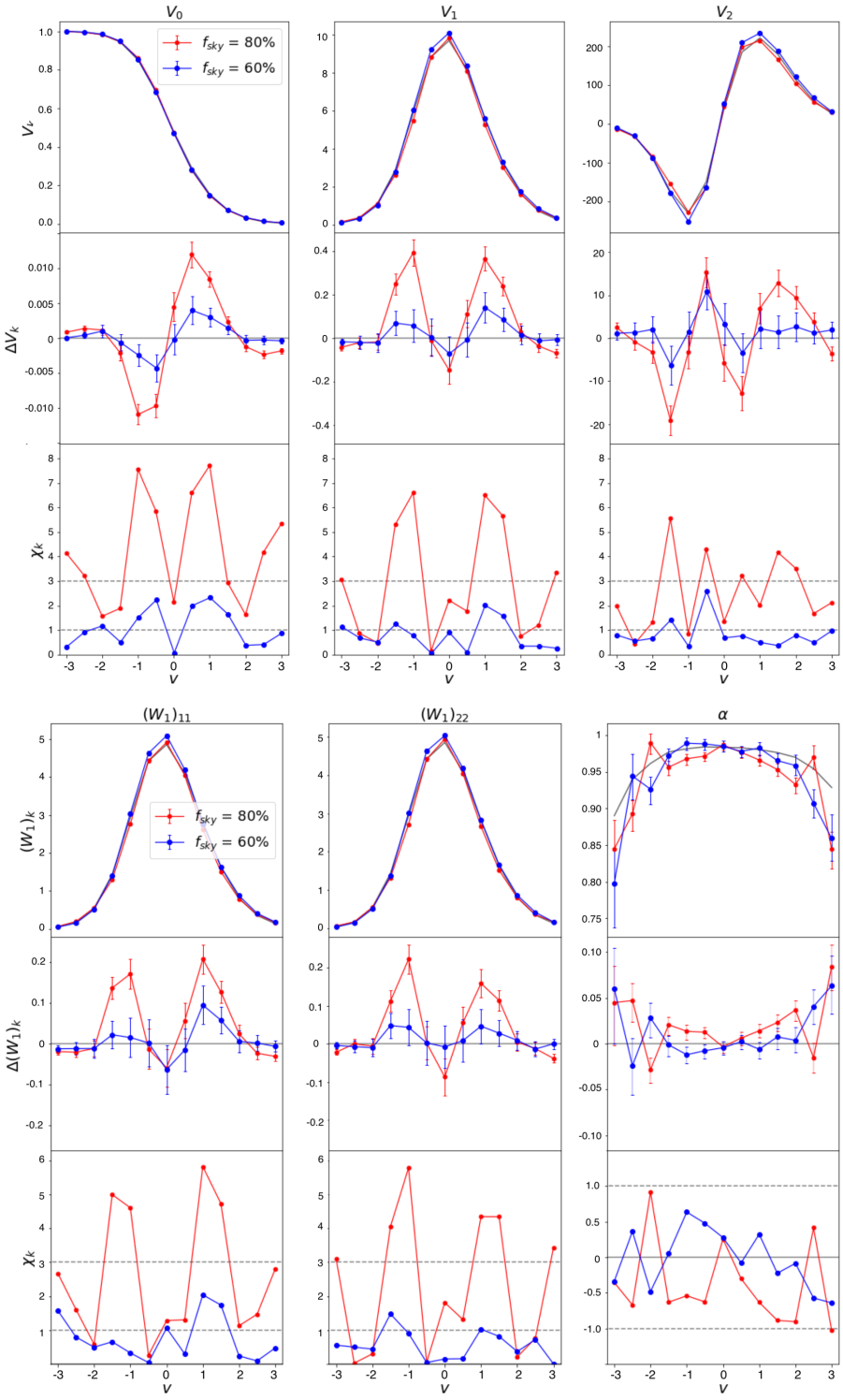

Figure 4.8: Upper panel: MFs (top), difference between data and Gaussian simulations (middle) and χ_k (bottom) as a function of threshold. Lower panel: CMT diagonal terms and α (top), difference between data and Gaussian simulations (middle) and χ_k (bottom) as a function of threshold. The maps are previously filtered with a band-pass ($\ell = 30 - 180$), error bars are computed from simulations.

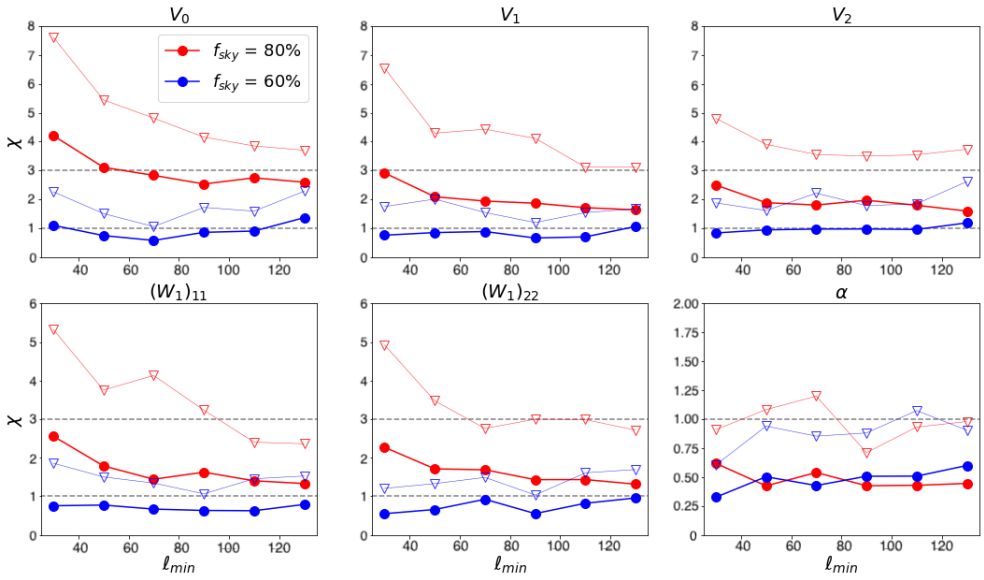

Figure 4.9: The three MFs (top), the CMT diagonal terms and α (bottom) deviations as a function of the lower multipole cut, ℓ_{min}, of the applied band-pass filter. The dots and the triangles represent respectively the average and 95% percentile values computed over all threshold values.

4.5 Non-Gaussian Simulations

4.5.1 A model for non-Gaussian emission

Using MFs and MTs, we have determined clear statistical differences between the real synchrotron polarized emission and an isotropic and Gaussian-distributed model, even at small scales. In this section, we propose a simple way to generate polarized synchrotron maps which can better resemble the real statistical properties of the emission in the fainter regions of the sky on scales smaller than about 6°, which corresponds to multipoles $\ell > 30$.

From our statistical analysis, it is impossible to disentangle non-Gaussianity from anisotropy. That is, we are unable to determine whether the measured non-Gaussianity is an intrinsic feature of the synchrotron emission, or is due to an underlying anisotropic pattern of emission on small scales. However, even if we assume the latter case, because of the lack of information about the small scale distribution of the emission, we need a mechanism to simulate the non-Gaussianity.

We generate the simulations as follows. We start with three complex vectors, ζ^T, ζ^E, ζ^B, generated from a Gaussian random distribution with zero mean and unit variance. The ζ^E and ζ^B coefficients are then transformed according to the *sinh-arcsinh* transformation [163]

$$\tilde{\zeta^E} = \sinh(\delta \ \mathrm{arcsinh}(\zeta^E) - \epsilon) \tag{4.24}$$

$$\tilde{\zeta^B} = \sinh(\delta \ \mathrm{arcsinh}(\zeta^B) - \epsilon) \tag{4.25}$$

where ζ^E and ζ^B are the initial Gaussian-distributed vectors and $\tilde{\zeta^E}$ and $\tilde{\zeta^B}$ are the transformed ones. The use of this transformation is motivated by the fact that it allows one to control the level of non-Gaussianities with two parameters, ϵ and δ, whose effects have a simple statistical interpretation. The parameter δ introduces symmetrically both positive and negative tails to the statistical distribution, which increases the excess kurtosis. The parameter ϵ controls the level of skewness. We find that the Gaussian case is correctly recovered with $(\epsilon, \delta) \to (0, 1)$, when performing simple consistency tests.

We assume, for the sake of simplicity, that the level of non-Gaussianity is the same for E and B in the part uncorrelated to T. This explains why we use the same parameters (ϵ, δ) for both transformations in equations 4.24-4.25 and we do not transform ζ^T. We are aware that in a more realistic context this could not be the case, but this goes beyond the scope of this analysis. The values used for (ϵ, δ) are discussed in section 4.5.3. We then generate the spherical harmonic coefficients as follows

$$a_j^T = \sqrt{C_\ell^{TT}}\zeta^T \tag{4.26}$$

$$\tilde{a}_j^E = \frac{C_\ell^{TE}}{\sqrt{C_\ell^{TT}}}\zeta^T + \sqrt{C_\ell^{EE} - \frac{(C_\ell^{TE})^2}{C_\ell^{TT}}}\tilde{\zeta^E} \tag{4.27}$$

$$\tilde{a}_j^B = \frac{C_\ell^{TB}}{\sqrt{C_\ell^{TT}}}\zeta^T + \sqrt{C_\ell^{BB} - \frac{(C_\ell^{TB})^2}{C_\ell^{TT}}}\tilde{\zeta^B} \tag{4.28}$$

where the index j refers to the (ℓ, m) pair. The C_ℓ values are computed from the *WMAP* yearly maps as described in section 4.4.3. Note that after rescaling, the $\tilde{a}_{lm}$-distributions are different from the $\tilde{\zeta}$-distributions, but still non-Gaussian. We generate the $(I,\ \tilde{Q},\ \tilde{U})$ maps, which represent our small-scale template, from the $\tilde{a}_{lm}$ using the `alm2map` routine of `HEALPix`.

4.5.2 Model for anisotropic modulation of the emission

Besides the non-Gaussian nature, we have shown that at high multipoles the synchrotron emission is not isotropic. We simply assume that this is due only to a modulation caused by the large bright structures which are also visible at large scales. To simulate the effect, we divide the polarization *WMAP* map into 3 patches (p_i) according to the application of thresholds on P. We divide the unmasked 80% of the sky into two patches of 20%, p_1: 80-60%, p_2: 60-40%, and one of 40%, p_3: 40-0%, according to the sky brightness. For each patch, we smooth the boundaries with a 5° Gaussian and compute the polarization spectra $C_\ell^P(p_i)$. Then we define a spatially varying normalization factor

$$N_i = \sqrt{\left\langle \frac{C_\ell^P(p_i)}{C_\ell^P} \right\rangle} \tag{4.29}$$

where the C_ℓ^P is computed from 80% of the sky and the average is computed over the multipoles $\ell \in [30, 180]$. N is then smoothed with a 10° beam. As shown in figure 4.10 (top left), this method naturally introduces the effect at low-scales of most of the filamentary structures presented in section 4.3. We multiply the non-Gaussian $\tilde{Q}$ and $\tilde{U}$ maps, computed in the previous section, by the normalization factor

$$Q = N\tilde{Q}, \quad U = N\tilde{U}. \tag{4.30}$$

The resulting Q and U maps form the final set of anisotropic and non-Gaussian simulations.

To our small-scale model, we add a large-scale template generated directly from the *WMAP* data. In order to match the maps, we smooth the small-scale and the large-scale templates with respectively the functions $W(\ell)$ and $(1 - W(\ell))$, where

$$W(\ell) = \frac{1}{2}\left(1 - \tanh\left(\frac{\ell - \ell_0}{\Delta\ell_0}\right)\right), \tag{4.31}$$

with $\ell_0 = 20$ and $\Delta\ell = 5$, chosen such that at the scales of interest in this work, that is smaller than 6°, the simulations are mainly driven by our small-scale model. Finally, in order to compare simulations with data, we add noise and compute the debiased polarized intensity with the MAS estimator.

4.5.3 Tuning and Results

We have described above the method we use to generate polarized synchrotron simulations on scales below 6°. The level of non-Gaussianity of the simulations is controlled by the two parameters (ϵ, δ) in equation 4.24-4.25, which are related respectively to the skewness S and kurtosis K of the maps.

Similarly to equation 4.21, we define the quantities which measure the deviation between data and simulations as

$$\chi_\mu = \sum_{k=2}^{4} \frac{\Delta\mu_k}{\sigma_{\mu_k}}, \quad \Delta\mu_k = |\mu_k^{data} - \mu_k^{sim}| \tag{4.32}$$

where $\mu_2 = \sigma_P = \sqrt{\langle (p - \langle p \rangle)^2 \rangle}$ is the standard deviation, $\mu_3 = S = \langle (p - \langle p \rangle)^3 / \sigma_P^3 \rangle$ is the skewness and $\mu_4 = K = \langle (p - \langle p \rangle)^4 / \sigma_P^4 \rangle$ is the kurtosis. The values μ_k^{sim} and σ_{μ_k} are computed taking respectively the average and standard deviation over the simulations. Moreover, we define a variable which quantifies the spectral deviations as

$$\chi_{sp} = \sum_{\ell=30}^{180} \frac{\Delta C_\ell}{\sigma_\ell}, \quad \Delta C_\ell = |C_\ell^{data} - C_\ell^{sim}| \tag{4.33}$$

where C_ℓ^{sim} and σ_ℓ are computed taking respectively the average and standard deviation over the simulations. Note that the C_ℓ are binned with a range $\Delta\ell = 10$. We vary ϵ and δ over the ranges $(-1,\ 1)$ and $(0.3,\ 1.5)$, respectively. For each pair of values, we generate 100 total polarization simulations, smoothing them with the band-pass filter ($\ell_{min} = 30$, $\ell_{min} = 180$). We find that the quantity $\chi_\mu + \chi_{sp}$ is minimised for $\epsilon = -0.46$ and $\delta = 0.78$, as shown in figure 4.10 (top right). These define the values to generate a set of reference simulations. An example of a simulated sky, and the comparison between the simulated and real power spectra are shown in figure 4.10 (bottom).

The deviation in the MF and CMT measures between data and simulations, when the band-pass ($\ell_{min} = 30$, $\ell_{min} = 180$) filter is applied, are shown in figure 4.11. In figure 4.12, we show the deviations for different ℓ_{min}. The simulations agree with the data at the 3σ level for both the 80% and 60% masks. This suggests that the non-Gaussianity introduced with the *sinh-arcsinh* transformation (equations 4.24-4.25) is more relevant in the bright regions, instead is mitigated in the more faint sky emission. As noted in section 4.5.1, we do not know if the non-Gaussianity we introduce is related to the intrinsic nature of the synchrotron emission, or due to an underlying anisotropic emission at small scales. However, the mechanism to produce this non-Gaussianity provides a simple method to tune our simulations by means of two simple parameters (ϵ, δ). Overall, the non-Gaussian and anisotropic simulations seem to reproduce the statistical properties of the polarized synchrotron emission well.

In appendix B.3.2, we test how our method performs simulating the synchrotron emission at 30 GHz, as observed by *Planck*. We keep the parameters ϵ, δ and N as fitted from *WMAP*. We observe that the method performs well at small scales (>2.5°), but under-performs for larger scales.

The goal of this section is to show a simple data-driven way to generate more realistic simulations. There are several assumptions and limitations which are negligible at the current data sensitivity, but will not be the case for future experiments. For example, we assume that the E and B modes are equally non-Gaussian, even if we do not have evidence of it. We do not take into account the correlation of the non-Gaussianity between intensity and polarization. We consider ϵ and δ as fixed values, but in a more realistic context, they could vary with scale and space. Moreover, a frequency dependence in our model (ϵ, δ, N), for example due to a possible decorrelation between frequencies as observed in the dust emission [51], could not be excluded. Such effects could explain the poor performance at 30 GHz for the large scales.

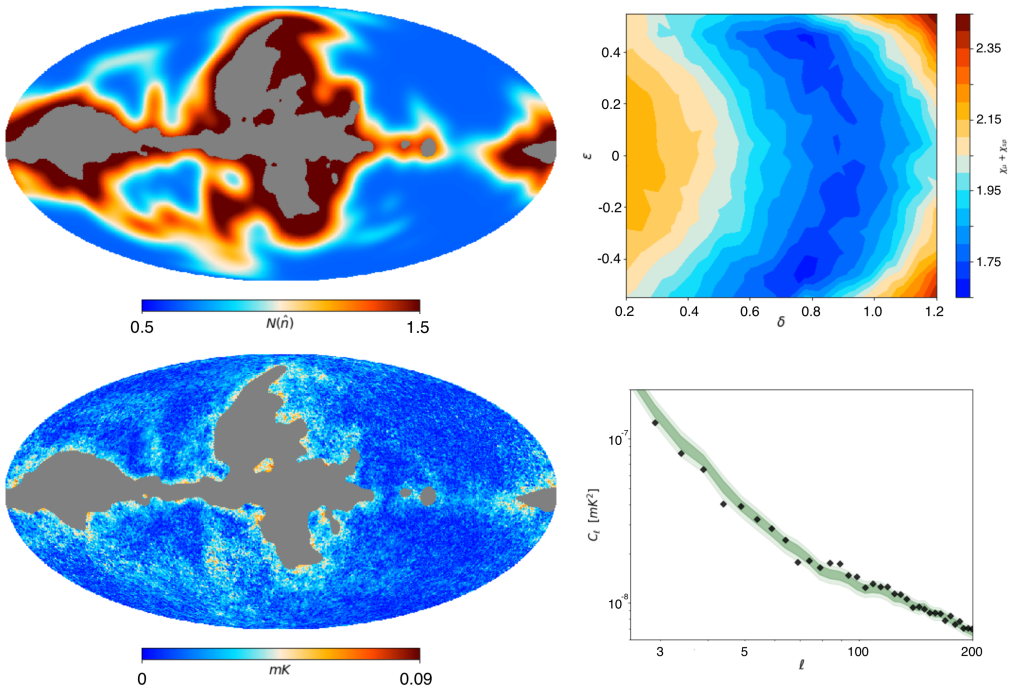

Figure 4.10: Top Left: Spatially varying normalization factor used to modulate the simulations in real space. Top Right: $\chi_{sp} + \chi_{\mu}$ as function of the parameters ϵ and δ, on logarithmic scale. Bottom Left: Simulation of the *WMAP* polarized intensity map. Bottom Right: Total polarization power spectrum of the *WMAP* K-band (black dots) compared to the 1σ (dark green) and 2σ (light green) intervals obtained from the variance of the simulations.

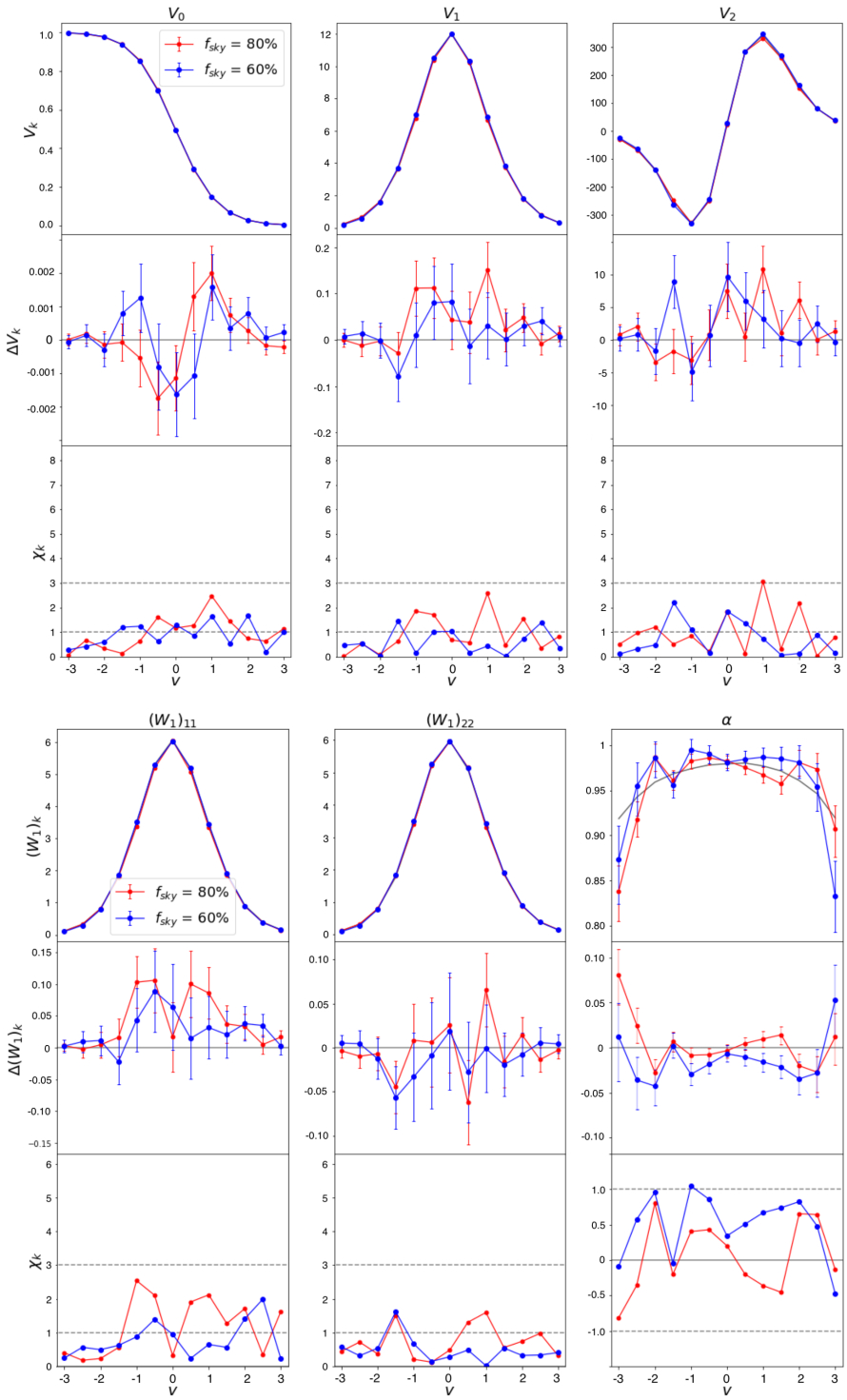

Figure 4.11: Upper panel: MFs (top), the difference between data and *non-Gaussian* simulations (middle) and χ_k (bottom) as a function of threshold. Lower panel: CMT diagonal terms and α (top), difference between data and *non-Gaussian* simulations (middle) and χ_k (bottom) as a function of threshold. The maps are previously filter with a band-pass ($\ell = 30 - 180$), error bars are computed from the standard deviation of the simulations. For the bottom panels, we use the same axis ranges as in figure 4.8 to allow a direct comparison.

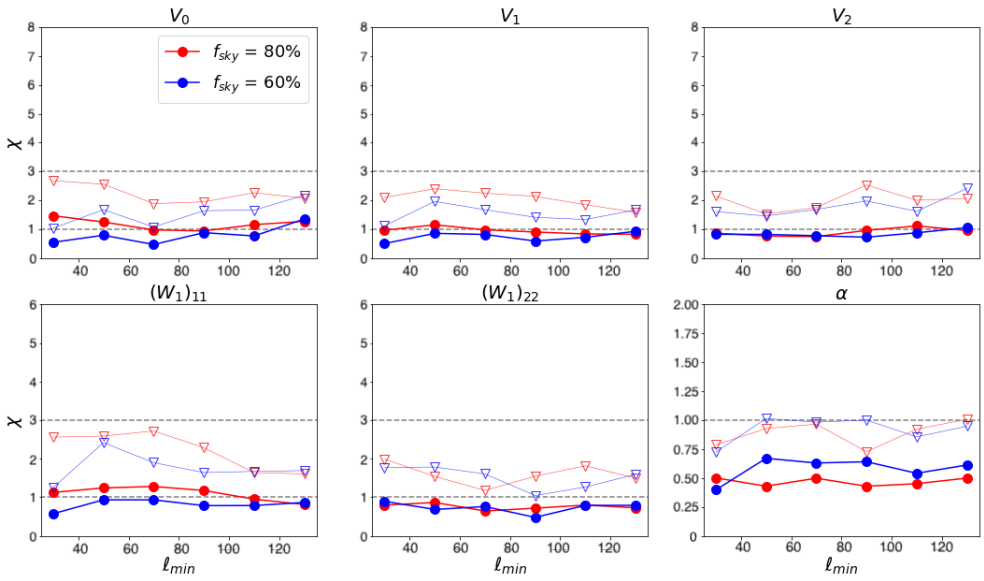

Figure 4.12: The three MFs (top), the CMT diagonal terms and α (bottom) deviations from the *non-Gaussian* simulations as function of the lower multipole cut, ℓ_{min}, of the applied band-pass filter. The dots and the triangles represent respectively the average and 95% percentile computed over all threshold values. For comparison purposes, we use the same axes as in figure 4.9.

4.6 Summary and Conclusions

In the analysis we have covered two important aspects of the polarized synchrotron emission: the presence of large filamentary structures outside the Galactic plane, and its statistical proprieties at small scales. The analysis has been performed on the debiased polarized amplitude maps at 23 and 30 GHz as observed respectively by *WMAP* and *Planck*. We developed a filament finder routine based on a friend-of-friend recursive algorithm, which detects elongated coherent emission in the sky. The method has been tested with foreground simulations including a toy model of filamentary structure. We identify 19 filaments which are detected, at least in part, in both *Planck* and *WMAP*. Some of the filaments have been already reported in the literature as observed in radio sky or in previous *WMAP* analysis. Five of them are reported for the first time in this work. We analysed some properties of the detected filaments.

- We compute the polarization fraction as the ratio of the *WMAP* and *Planck* data maps with respect to a `Commander` intensity template rescaled with a spectral index $\beta_I = -3$. Typically, we find that the polarization fractions of the filaments are larger than for the areas outside the filaments, excluding the Galactic plane. For two filaments, both located in the NPS, we find values of about 30%.

- We study the polarization spectral indices of the filaments from the Q, U maps. We find consistent spectral indices of about -3.1 inside and outside the filaments. However, the β values span a very broad range, from -3.59 to -2.17.

- Applying the filament finder algorithm to the P_E and P_B maps, we find that most of the filaments, especially in the NPS, are clearly visible in E, but not in B.

- Applying the finder method to the Haslam map, we observe that for some bright filaments in polarization we do not detect bright counterparts in intensity.

Using Minkowski functionals and tensors, we have analysed the non-Gaussianity and statistical isotropy of the polarised *WMAP* and *Planck* maps. We focused on the the faintest 80% and 60% of the sky. We compared the results obtained from data with a set of Gaussian and isotropic simulations. We summarize our findings.

- Analysing the 80% sky fraction, we see large deviations ($> 3\sigma$) from Gaussianity and isotropy at 6° scale. The deviations decrease towards smaller scales, even if they remain significantly high down to 1.5°.

- Analysing the 60% sky fraction, we obtain consistent results between data and simulations for all the considered thresholds and multipole ranges at the 3σ level.

- These results suggest that the large filaments are the main source of non-Gaussianity, even at small scales. When those filamentary structures are masked, the Gaussian and isotropic simulations resemble well the diffuse emission at the *WMAP* and *Planck* resolution.

Finally, we present a simple data-driven method used to generate non-Gaussian and anisotropic simulations. We generate non-Gaussian harmonic coefficients by mean of a simple transformation. We account for the anisotropies with a normalization template

that resemble the diffuse filamentary structures. The simulations are then fitted in order to match the spectral and statistical properties of the 80% sky coverage of the data maps.

Chapter 5

Tensor-to-scalar ratio Estimation

The purpose of this study is to analyse different likelihood estimators and statistical approaches used to estimate a cosmological parameter, the tensor-to-scalar ratio (r). The specific study case is the estimation of the uncertainty, or upper-bound, of r from partial sky maps, in the particular case of null CMB tensor modes ($r = 0$). The work is a methodological analysis, that considers only simulations containing CMB and white noise. We present four likelihood estimators, three of which operate in the spectral domain and one in real space, explaining for each one the approximations made and the difficulties in implementation. We test them using three statistical approaches: Maximum Likelihood Estimation (MLE), Maximum A Posteriori Estimation (MAP) and Bayesian Inference (BI). We show how each method produces different estimates depending on the fraction of sky observed. Best results are obtained using the pixel-based estimator and Bayesian approach thus considered as a reference. We show that spectral estimators that neglects the correlation between different multipoles, approximating the presence of the mask with the term $(f_{sky})^{-1}$, provide an underestimate of the uncertainty. More sophisticated spectral estimators that take this correlation into account, however, produce overestimates of the uncertainties compared to the pixel-based. These considerations apply particularly to the case $r = 0$. For positive tensor-to-scalar ratios, the spectral methods become more reliable and converge to similar estimates.

5.1 Likelihood Estimators

In this work we compare different Likelihood Estimators known in the literature to be useful for estimating a cosmological parameter from CMB maps. In particular, we focus in the different approaches useful for estimating the tensor-to-scalar ratio when only a portion of the sky is available. We focus on the case of $r = 0$, because it is a case of great interest especially in the context of experiment forecasts. In the regime of zero, or very small, tensor modes, most of the information needed to estimate r is encapsulated in the large and intermediate scales. We will show that this aspect has a strong impact on the different methods used to estimate the amplitude of tensor modes.

The work presented here is designed as a methodological study, so we limit the analysis to an ideal case where the signal consists only of CMB and white noise. The analysis is based only on polarization Q and U maps, and the corresponding E- and B-modes in spectral space. Temperature is not considered because it plays a negligible

role in estimating r.

In the following sections, we present four different estimators used to fit the tensor-to-scalar ratio r and its uncertainty σ_r:

- *Gaussian* estimator
- *Fisher* estimator
- *Hamimeche & Lewis* estimator
- *Pixel-based* estimator.

None of the methods used are new, they are well known methods used in the literature. However, the names used were chosen by us for the sake of clarity; in literature they may be called differently [164].

5.1.1 Simulations and Power Spectra

For all methods employed to estimate the tensor-to-scalar ratio, we use 2000 simulations. Simulations are generated with the `synfast` routine of `Healpy` [122] from a fiducial spectrum

$$C_\ell^{fid} = C_\ell^{lens} + N_\ell \tag{5.1}$$

where C_ℓ^{lens} and N_ℓ are respectively the lensing and the noise power spectra. The CMB lensing spectrum is produced with `CAMB`[1], setting the tensor contribution to zero. The noise is white and uncorrelated, thus N_ℓ is constant and independent on the multipoles

$$N_\ell = 4\pi \, \frac{\sigma_{pix}^2}{N_{pix}} \tag{5.2}$$

where N_{pix} is the number of pixels in the map, and σ_{pix}^2 is the noise variance in each pixel. For our case study we use a noise of 10 μK-arcmin. This noise is high compared to the noise expected to be achieved by future and current experiments. However, it could be in accordance with the level of uncertainty that foreground residuals might add to the maps. Certainly, the contribution of foreground residuals is much more complex, because it is not Gaussian and is correlated. However, the value of 10 μK-arcmin could mimic the residuals effect at least at the amplitude level.

Once the simulations have been obtained, we mask them and calculate the spectra. We use the *Planck* galactic masks [8], provided by the Planck Legacy Archive[2] (PLA). In particular, we use the masks that allow portions of the sky approximately between 60% and 90%. The choice is due to the fact that in estimating parameters from real observations, it is required to mask the galactic center, because it is strongly affected by residual foregrounds, despite component separation methods. We calculate the spectra of the masked simulations with `ECLIPSE` [128], an optimized Quadratic Maximum Likelihood (QML) estimator. `ECLIPSE` enables spectrum calculation at large and medium scales, optimally reducing E-to-B leakage due to the mask. For notation sake, in the

[1] `CAMB` (Code for Anisotropies in the Microwave Background), is a python code which allows to calculate CMB spectra from cosmological parameters [165]

[2] https://pla.esac.esa.int/pla

following sections we denote the "experimental" spectra, i.e. obtained from simulations with ECLIPSE, with $\hat{C}_\ell$.

In a nutshell, the process of estimating the tensor-to-scalar ratio consists of comparing spectra (or maps in the pixel-based case) with a model. We use a simplified model where the tensor-to-scalar ratio enters linearly as

$$C_\ell = r\, C_\ell^{tens} + C_\ell^{lens} + N_\ell, \tag{5.3}$$

where C_ℓ^{tens} is the tensor contribution to the spectra produced with CAMB setting $r = 1$ and $n_t = 0$[3]. The linear dependence of the spectrum on r is an approximation. The actual relationship depends on the inflationary theory used, e.g. for the *single-field slow-roll* model the consistency condition $r = -8n_t$ would compromise the linear model. However, the linear model is well suited to our case study because of its simplicity and because it allows us to simplify many calculations. The lensing and noise power spectra are showed in figure 5.1 compared to the tensor spectra obtained for different values of the tensor-to-scalar ratio.

For the three spectral-based estimators: *Gaussian*, *Fisher* and *Hamimeche & Lewis*, simulations and masks are generated at $N_{side} = 64$ with an 80 arcmin FWHM Gaussian beam. In the r estimation we only take into account the BB-spectrum in the range of multipoles between $\ell_{min} = 2$ and $\ell_{max} = 128$. We neglect the EE and EB spectra for simplicity, also since these provide little information concerning tensor modes. For the *Pixel-based* estimator, we use simulations and masks at $N_{side} = 4$ and multipoles between $\ell_{min} = 2$ and $\ell_{max} = 12$, without beam. This difference in resolution is due to the fact that the *Pixel-based* estimator is computationally much more expensive than spectral-based methods. Possible effects of resolution and beam are discussed in the following sections.

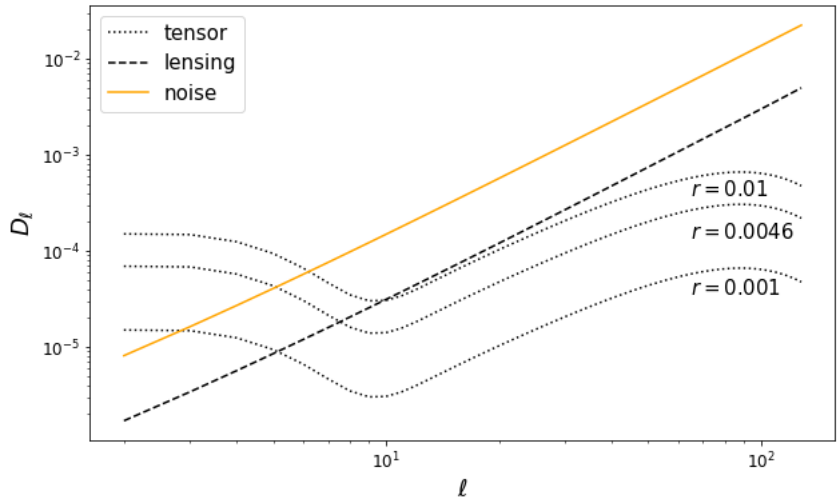

Figure 5.1: BB power spectra of the different components, where $D_\ell = \ell(\ell+1)C_\ell/2\pi$. The tensor spectra are computed multiplying the spectrum obtained with CAMB (setting $r = 1$ and $n_t = 0$) by the value of r showed near the corresponding line.

[3] n_t is the tensor spectral index (or tensor tilt), which quantifies the scale dependence of the tensor spectrum.

5.1.2 Gaussian estimator

Most of the power spectra approaches used for the parameter estimation usually relies on the maximum likelihood estimator of an approximate multivariate normal distribution

$$\log \mathcal{L} = -\frac{1}{2}(\hat{C}_\ell - C_\ell)^T \mathbf{C}^{-1}_{\ell\ell'}(\hat{C}_{\ell'} - C_{\ell'}) - \log\left((2\pi)^{1-\ell_{max}}|\mathbf{C}|^{1/2}\right). \tag{5.4}$$

It is well known that for the full sky the C_ℓ's follow a χ^2 distribution with $2\ell+1$ degrees of freedom. However, the Gaussian approximation becomes reasonably good when ℓ increases, making this approach sufficient to estimate parameters in many cases. The covariance matrix $\mathbf{C}$ is theoretically defined as

$$\mathbf{C}_{\ell\ell'} = \langle(\hat{C}_\ell - C_\ell)(\hat{C}_{\ell'} - C_{\ell'})^T\rangle, \tag{5.5}$$

where C_ℓ depend in principle on the tensor-to-scalar ratio, making the covariance $\mathbf{C}$ also dependent on r. However, this dependency is very weak and can be neglected. This leads to a great computational advantage, because we can calculate the matrix only once from simulations, setting $C_\ell = \langle\hat{C}_\ell\rangle$. This choice is supported by the fact that the `ECLIPSE` estimator is unbiased, thus it is equivalent to have in the covariance $\langle\hat{C}_\ell\rangle = {C_\ell}^{fid}$, which represents the maximum of the likelihood by definition. Under this condition, the likelihood maximization reduces to the minimization of the quantity

$$-2\log\mathcal{L} = (\hat{C}_\ell - C_\ell)^T\mathbf{C}^{-1}(\hat{C}_{\ell'} - C_{\ell'}). \tag{5.6}$$

Knowing that the model is a simple linear function in r, see equation 5.3, we can find an analytical form to compute the tensor-to-scalar ratio. We calculate the minimum of the function in equation 5.6 by setting the partial derivative with respect to r equal to zero, obtaining

$$\frac{\partial\log\mathcal{L}}{\partial r} = 0 \;\Leftrightarrow\; r = \frac{1}{({C_\ell}^{tens})^T\mathbf{C}^{-1}{C_\ell}^{tens}}\,({C_\ell}^{tens})^T\mathbf{C}^{-1}(\hat{C}_\ell - {C_\ell}^{lens} - N_\ell). \tag{5.7}$$

We have verified that the numerical minimisation of equation 5.6 or the direct calculation of r from equation 5.7 provide the same results. We use 1500 simulations to estimate the covariance matrix $\mathbf{C}$ and the remaining 500 to estimate the tensor-to-scalar ratio. The choice is due to the fact that the covariance matrix requires more simulations to converge to a stable solution, whereas the process of estimating the posterior distribution of r does not require a large number of simulations. These observations resulted from preliminary tests carried out with different sets of simulations. Note that it is possible to analytically compute the uncertainty of the tensor-to-scalar ratio directly from the second derivative of the likelihood in equation 5.6

$$\sigma_r^2 = -\left[\frac{\partial^2\log\mathcal{L}}{\partial r^2}\right]^{-1}_{r=0} = [(C_\ell^{tens})^T\mathbf{C}^{-1}C_\ell^{tens}]^{-1}. \tag{5.8}$$

However, we do not use this analytical equation for σ_r, but we compute it from the distribution of maxima of r. This allows us to use a method that can be applied to all estimators.

Finally, we want to emphasize that this estimator is based on two approximations: C_ℓ's are considered Gaussian distributed, and the dependence of the covariance matrix on r is negligible. The first approximation, which is indeed the most important, becomes more reliable at large multipoles. Thus, the accuracy of this approximation depends on how the different multipoles contribute to estimating r.

5.1.3 Fisher estimator

The *Fisher* estimator is a semi-analytical approach to compute the tensor-to-scalar ratio and its uncertainty from power spectra. We define the likelihood [164]

$$\log \mathcal{L} = -\frac{1}{2}\, \hat{\mathbf{a}}_{\ell m}^T \mathbf{C}_\ell^{-1} \hat{\mathbf{a}}_{\ell m} - \log |2\pi \mathbf{C}_\ell| \tag{5.9}$$

where $\hat{\mathbf{a}}_{\ell m}$ are the harmonic coefficient of the simulations in Fourier space. For a full sky map, CMB and white noise are assumed Gaussian and isotropic. Thus, the corresponding harmonic coefficients $\hat{\mathbf{a}}_{\ell m}$ are Gaussian variables with zero correlation between different multipoles. Under these conditions, the likelihood in equation 5.9 is exact. The model covariance matrix is $\mathbf{C}_\ell = \langle \mathbf{a}_{\ell m}^T \mathbf{a}_{\ell m} \rangle$. If we define the observed covariance matrix as $\hat{\mathbf{C}}_\ell = \langle \hat{\mathbf{a}}_{\ell m}^T \hat{\mathbf{a}}_{\ell m} \rangle$, the likelihood reduces to

$$\log \mathcal{L} = -\frac{(2\ell+1)}{2} (tr \hat{\mathbf{C}}_\ell \mathbf{C}_\ell^{-1} + \log |\mathbf{C}_\ell|) + \text{const.} \tag{5.10}$$

Note that the matrix notation for $\mathbf{a}_{\ell m}$, $\mathbf{C}_\ell$ and $\hat{\mathbf{C}}_\ell$ is used because, in principle, they take into account self and cross-correlation between different modes (T, E and B). However, it is important to emphasize that the covariance matrices have zero correlation between different multipoles.

In our analysis we only take into account the BB spectrum, thus the likelihood in equation 5.10 reads

$$\log \mathcal{L} = -\sum_\ell \frac{2\ell+1}{2} \left[\frac{\hat{C}_\ell}{C_\ell} + \log C_\ell - \frac{2\ell-1}{2\ell+1} \log \hat{C}_\ell \right] \tag{5.11}$$

a (reduced) χ-squared of C_ℓ's with $(2\ell+1)$ degrees of freedom. The likelihood showed in equation 5.11 is well-defined and exact when analyzing full-sky maps. The presence of the mask results in a loss of information, coming from the masked area. For partial sky, a common procedure is to adapt the likelihood by multiplying by the observed sky fraction, f_{sky}, to reflect the overall loss of the independent modes in the available data [166, 167]. For simplicity we will call this procedure the f_{sky}*-approximation*

$$\log \mathcal{L}^{\text{partial}} = f_{sky}\ \log \mathcal{L}^{\text{full-sky}}. \tag{5.12}$$

In terms of the uncertainty of the tensor-to-scalar ratio, f_{sky}-approximation is equivalent to writing

$$\sigma_r^{\text{partial}} = \frac{1}{\sqrt{f_{sky}}} \sigma_r^{\text{full-sky}}. \tag{5.13}$$

For each simulation, we numerically obtain the best-fit value of the tensor-to-scalar ratio maximizing the likelihood. Then, we compute σ_r from the maxima distribution.

The one shown so far is a numerical estimator that is based on maximising the likelihood, which is exact for full-sky and approximated for partial-skies. However, there is also an analytical derivation to obtain the uncertainty of the tensor-to-scalar ratio, taking the second derivative of the likelihood with respect to r

$$\sigma_r = 1/\sqrt{F} \quad \text{with} \quad F = -\left\langle \frac{\partial^2 \log \mathcal{L}}{\partial r^2} \right\rangle_{r=0} \tag{5.14}$$

where F is the *Fisher variance*, from which the estimator is named [167]. By definition, the Fisher variance is the second partial derivative of the likelihood with respect to r, when the C_ℓ's correspond to the true model, that in our case is $r = 0$. Under this approximation, and recalling the dependency of the model spectra with respect to r, see equation 5.3, we find an analytical equation for the Fisher variance

$$F = f_{sky} \sum_\ell \frac{2\ell+1}{2} \left[2 \frac{\langle \hat{C}_\ell \rangle}{(C_\ell{}^{lens} + N_\ell)^3} (C_\ell{}^{tens})^2 - \frac{1}{(C_\ell{}^{lens} + N_\ell)^2} (C_\ell{}^{tens})^2 \right]. \tag{5.15}$$

where $\langle \hat{C}_\ell \rangle$ is the average over simulations of the spectra obtained with simulations.

Mathematically speaking, the Fisher variance is the curvature of the likelihood at the maximum point. Calculating σ_r by this analytical method is totally equivalent to calculating σ_r by the maxima distribution only in the case where the data points, in our case the $\hat{C}_\ell$'s, are drawn from Gaussian distributions. However, this is not our case, so the analytical method based on the Fisher variance is an approximation. In the next sections, we will show the results obtained from numerical derivation, i.e. maximising the likelihood. However, we presented also this approximate method because it is widely used in the literature.

Finally, we want to emphasize that both the numerical and the analytical *Fisher* estimators are based on the approximation that the presence of the mask is accounted by the f_{sky}-approximation. This approximation is equivalent to saying that the $a_{\ell m}$ at different multipoles are statistically uncorrelated. In our case of CMB and white noise, this assumption is only correct at full-sky. In case of partial sky, the presence of the mask affects the correlation structure of the $a_{\ell m}$'s coefficients, introducing correlations between different multipoles. Furthermore, the analytical derivation inherently makes a second approximation which is equivalent to the approximation described in the *Gaussian* estimator, that is C_ℓ's are considered Gaussian distributed. Both the f_{sky}-approximation and Gaussianity approximation are reliable for large multipoles, but can fail for small multipoles. The f_{sky}-approximation fails because it does not correctly take into account the presence of the mask. The analytical derivation fails because the low multipoles are less Gaussian.

5.1.4 Hamimeche & Lewis estimator

Hamimeche & Lewis [164] proposed a likelihood approximation that can be used with Gaussian correlated fields, which is applicable in the presence of partial sky. It involves a fiducial model, but, it is weakly dependent on it. It also assumes that the spectra covariance matrix is positive definite. This assumption breaks down when the covariance is computed from simulations, especially for low multipoles. To overcome this problem, we use the offset-modification proposed by [168]. The likelihood has the following form

$$-2 \log \mathcal{L} = \sum_{\ell,\ell'} X_\ell^T \mathbf{M}^{-1}_{\ell,\ell'} X_{\ell'} \tag{5.16}$$

with the variable X_ℓ defined as

$$X_\ell = \sqrt{C_\ell{}^{fid} + O_\ell}\; g\left(\frac{\hat{C}_\ell + O_\ell}{C_\ell + O_\ell} \right) \sqrt{C_\ell{}^{fid} + O_\ell} \tag{5.17}$$

where $g(x) = sign(x)\sqrt{2(|x| - \log x - 1)}$. We compute the covariance matrix making use of the fiducial model

$$\mathbf{M}_{\ell,\ell'} = \frac{1}{N-1}\sum_{i=1}^{N}(\hat{C}_{i,\ell} - {C_\ell}^{fid})(\hat{C}_{i,\ell'} - {C_{\ell'}}^{fid}) \tag{5.18}$$

where N is the number of independent simulations. We estimate the offsets in equation 5.17 recursively, the i-th iteration is calculated as

$$O_\ell^i = \sqrt{\Delta\hat{C}_\ell - \frac{2{C_\ell}^{fid}}{f_{sky}(2\ell+1)}({C_\ell}^{fid} + 2O_\ell^{(i-1)})} \tag{5.19}$$

where $\Delta\hat{C}_\ell$ is the standard deviation of the spectrum, corresponding to the diagonal terms of the covariance $\mathbf{M}_{\ell,\ell'}$. At the first iteration we set $O_\ell^0 = 0$. The final offset is obtained after 10 iterations. This operation ensures that the matrix $\mathbf{P} = \mathbf{C}^{-1/2}\hat{\mathbf{C}}\mathbf{C}^{-1/2}$ is positive-definite for at least 99% of our simulations. From equation 5.19, note that the offset depends on the noise amplitude, on the mask used and weakly on the fiducial model. For more details, please refer to the original articles [164, 168].

When the covariance matrix is estimated from simulations, it has some intrinsic uncertainty itself [169]. Thus, we need to infer parameters by marginalizing over the true covariance matrix, conditioned on its estimated value. Considering this issue, we decide to use a modified *Hamimeche & Lewis* likelihood[4], referred in literature as *Sellentin & Heavens* likelihood [170], of the following form

$$\mathcal{L} = \frac{1}{\sqrt{2\pi\det\mathbf{M}}}\left(1 + \sum_{\ell,\ell'}\frac{X_\ell^T\mathbf{M}_{\ell,\ell'}^{-1}X_{\ell'}}{N-1}\right)^{-N/2}. \tag{5.20}$$

Unlike previous methods, this method does not have a simple analytical solution, so we directly maximize the likelihood numerically. Thus, for each simulation we obtain the best-fit value of r and, then, calculate σ_r from the maxima distribution. As for the *Gaussian* estimator, we use 1500 simulations to estimate the covariance matrix $\mathbf{M}$ and the remaining 500 to estimate the tensor-to-scalar ratio.

The *Hamimeche & Lewis* estimator is a more sophisticated method than those described above, where no strong approximations are made. However, increasing complexity also leads to increasing operations and small assumptions. In fact, the method itself depends on few factors that can have an impact on the final results. For example, the need to regularize the covariance matrix could lead to results which depends on the offset, making the results less robust.

5.1.5 Pixel-based estimator

The *Pixel-based* estimator is an exact and mathematically rigorous approach for partial-sky analysis, it relies only on quantities defined in pixel space. The full pixel-based likelihood reads

$$\mathcal{L} = \frac{1}{2\pi|\mathbf{M}|^{1/2}}\ \exp\left(-\frac{1}{2}\hat{\mathbf{p}}^T\mathbf{M}^{-1}\hat{\mathbf{p}}\right) \tag{5.21}$$

[4]Although the one used in this analysis is not exactly the likelihood proposed by Hamimeche & Lewis, we will continue to call it the *Hamimeche & Lewis* estimator in order to still refer to the original work, where this parametrization was first presented.

or in its simpler logarithmic form

$$-2\log\mathcal{L} = \mathbf{p}^T\mathbf{M}^{-1}\mathbf{p} + \log|\mathbf{M}| + \text{const.} \tag{5.22}$$

The quantity $\hat{\mathbf{p}}$ is a vector of pixel values of the simulated Q and U maps, and $\mathbf{M}$ is the pixel-pixel covariance. The latter is a matrix of shape

$$\mathbf{M} = \begin{pmatrix} \langle QQ\rangle & \langle QU\rangle \\ \langle QU\rangle & \langle UU\rangle \end{pmatrix}. \tag{5.23}$$

In our case study where both CMB and noise are Gaussian and isotropic, the four blocks of the covariance matrix can be calculated exactly from the model power spectra $(C_\ell^{EE},\ C_\ell^{BB}, C_\ell^{EB})$ [171], as

$$\begin{aligned} \langle QQ\rangle &= \sum_\ell \left(\frac{2\ell+1}{4\pi}\right)(F^{12}C_\ell^{EE} - F^{22}C_\ell^{BB}) \\ \langle UU\rangle &= \sum_\ell \left(\frac{2\ell+1}{4\pi}\right)(F^{12}C_\ell^{BB} - F^{22}C_\ell^{EE}) \\ \langle QU\rangle &= \sum_\ell \left(\frac{2\ell+1}{4\pi}\right)(F^{12} + F^{22})C_\ell^{EB} \end{aligned} \tag{5.24}$$

where $F^{12} = F^{12}(\hat{z})$ and $F^{22} = F^{22}(\hat{z})$ are functions of the cosine of the angle $\hat{z}$ between the two pixels under consideration. As for the power spectra in equation 5.3, the covariarce matrix can be decomposed in

$$\mathbf{M} = r\mathbf{M}^{tensor} + \mathbf{M}^{scalar} + \mathbf{M}^{noise} \tag{5.25}$$

where $\mathbf{M}^{tensor}$ is the tensor contribution to the spectra for $r = 1$ and $n_t = 0$, and $\mathbf{M}^{scalar}$ is the CMB scalar contribution which includes lensing effects for the B-mode. $\mathbf{M}^{noise}$ is the noise pixel covariance, that in the case of white noise reduces to a diagonal matrix

$$\mathbf{M}^{noise} = \mathbf{I}\ \frac{N_{pixel}}{4\pi} N_\ell = \mathbf{I}\ \sigma^2_{noise} \tag{5.26}$$

where $\mathbf{I}$ is the identity matrix, and σ^2_{noise} is the noise variance at each pixel. In the case of partial sky, $\hat{\mathbf{p}}$ in equation 5.22 is a vector of size $N_p = (2f_{sky}N_{pixel})$ containing only pixels which are allowed by the mask. Likewise, the covariance is an $(N_p \times N_p)$-matrix, containing the same pixels. Since the likelihood is evaluated pixel by pixel, we do not make any approximation in the likelihood or defining the covariance, unlike the other estimators. However, although on the mathematical side the method is exact and well-defined, on the implementation side it is very challenging.

The first challenge is the computational cost. Through the linear dependence of the tensor-to-scalar ratio in equation 5.25, we have the advantage of calculating the individual matrices ($\mathbf{M}^{tensor}$, $\mathbf{M}^{scalar}$, $\mathbf{M}^{noise}$) only once, and the computation of the total covariance reduces to a sum. However, for each value of r to be evaluated, we always need to compute the inverse matrix ($\mathbf{M}^{-1}$) which enters in the likelihood. This step has no loopholes and must be calculated exactly, making it the bottleneck of the estimation process. The second challenge is numerical. When working with large covariances, it is

easy to fall into problems of ill-conditioned matrices, making it impossible to calculate the inverse of the covariance. Most of the time these issues are purely numerical, related to the way the inverse is computed or to limits in computer precision. To address both problems, computational and numerical, we adopt a resolution of $N_{side} = 4$, which has $N_{pixel} = 192$ per map, and take into account multipoles up to $\ell_{max} = 3N_{side} = 12$. On the one hand, the low resolution allows us to work with matrices that can be handled with an ordinary laptop. On the other hand, it is proved that for $N_{side} \leq 4$ (`HEALPix` scheme) the covariance matrix always achieve the maximum possible rank [172]. Nevertheless, even at such low resolution we still have numerical issues that need to be addressed and solved with a regularization method. An example of regularization process is showed in section 5.2.1.

5.1.6 Contribution from Different Scales

The maps we use for the spectral estimators are at $N_{side} = 64$ with an 80 arcmin Gaussian beam. This resolution is high enough to allow us to access multipoles up to $\ell_{max} = 128$ without concern. The FWHM value of the beam is kept small in order to affect only the very large multipoles. The maps used for the *Pixel-Based* estimator are generated at $N_{side} = 4$ without beam. The choice of low resolution is due to computational cost and numerical reasons, as discussed in more detail in the previous section. The choice not to use the beam is due to the fact that we would not want to lose important signal by smoothing the maps, plus the maps are analysed directly in real space, without going through spectral transformations. However, one could argue that generating the maps at low resolution could affect the results.

In this section we apply the procedure described in section 8 of [173] to show how the different scales, in terms of multipoles, affect the estimation of σ_r. Recalling the linear approximation $C_\ell^{tens}(r) = r\ C_\ell^{tens}(r = 1)$, for each multipole moments the estimator for the tensor-to-scalar ratio can be summarised as

$$r_\ell = \frac{\hat{C}_\ell - C_\ell^{lens} - N_\ell}{C_\ell^{tens}(r = 1)}. \tag{5.27}$$

The variance, for each multipole moment, of r_ℓ is then

$$(\sigma_r)^2_\ell = \frac{(\Delta\hat{C}_\ell)^2}{[C_\ell^{tens}(r = 1)]^2} = \frac{2}{2\ell + 1}\frac{(C_\ell^{tens} + C_\ell^{lens} + N_\ell)^2}{[C_\ell^{tens}(r = 1)]^2}. \tag{5.28}$$

The estimators obtained from each multipole can be added with inverse-variance weighting to obtain the minimum-variance estimator for r. The standard deviation of the final estimator is

$$\sigma_r = \left[\sum_{\ell=2}^{\ell_{max}} \frac{2\ell + 1}{2}\left(\frac{C_\ell^{tens}(r = 1)}{C_\ell^{tens} + C_\ell^{lens} + N_\ell}\right)^2\right]^{-1/2}. \tag{5.29}$$

See section 8 of [173] for more details on computation steps not directly explained. This analysis refers to the full-sky case, where no approximation is applied and the angular power spectrum contains all the information. In the case of greatest interest for this work, i.e. $r = 0$, the term C_ℓ^{tens} in the denominator is zero.

Equation 5.29 gives us an analytical relationship between the estimation error of the tensor-to-scalar ratio and the maximum value of multipoles involved, parameterized by

ℓ_{max}. In Figure 5.2 it is showed the value of σ_r obtained adding only the contributions from multipoles between 2 and ℓ_{max} on the x-axis for the $r = 0$ case. The plot shows how σ_r decreases significantly including multipoles up to $\ell = 12$. The uncertainty remains roughly constant if multipoles $12 \leq \ell < 30$ are included. Finally, σ_r slightly decreases by including multipoles larger than 30. This suggests that most of the information useful for estimating the uncertainty of r comes from the reionization bump at low multipoles. The recombination bump, at higher multipoles, has a significantly lower weighting in the estimation. Numerically, the difference in σ_r calculated with $\ell_{max} = 12$ and $\ell_{max} = 128$ is about 2%.

This analysis shows us how most of the information useful for estimating the tensor-to-scalar ratio uncertainty is in the large scales. Thus, using a lower resolution for the *Pixel-based* estimator has a very small impact. In other words, this result allows us to safely compare the results of the spectral estimators with the *Pixel-based* estimator.

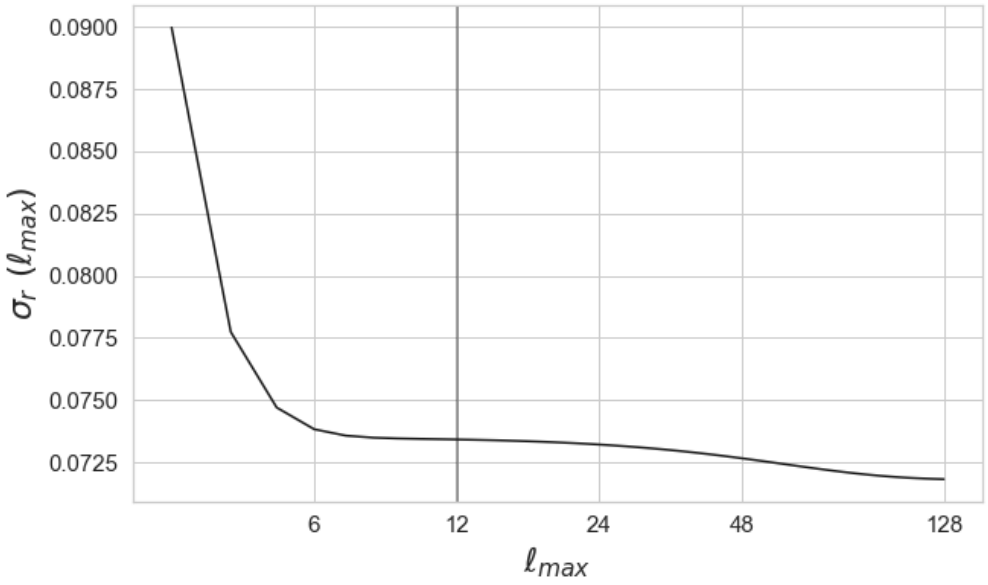

Figure 5.2: Uncertainty in the estimation of r, under the hypothesis $r = 0$, as function of the largest multipole taken in the sum in equation 5.29.

5.2 Maximum Likelihood Estimation

In the following sections, we will show the results in the estimation of r and its uncertainty when it is assumed null, obtained using the different estimation methods presented in the previous sections. We show the results for two different approaches: a Frequentist approach (MLE) without constraint, and a Bayesian approach (MAP and Bayesian Inference) with constraint $r \geq 0$. In this specific section we focus on the Frequentist approach, using a Maximum Likelihood Estimator (MLE) process without constraint, where we evaluate all values of r both positive and negative. This is equivalent to assume a uniform prior probability for all values of the tensor-to-scalar ratio. We are aware that negative values have no physical meaning. Nevertheless, ours is a methodological study, and having the full distributions of maxima of r for the different estimators allows us to explore some statistical features of these.

5.2.1 Pixel-Based Regularization

The *Pixel-Based* estimator is the exact and optimal method for estimating cosmological parameters. It becomes crucial when information contained at large scales dominates the estimation. Exactly as in our case where the estimated parameter, the tensor-to-scalar ratio, is very small. Nevertheless, the problem with using the likelihood function in real space is that the computational cost is driven by the covariance inversion operation, which scales like N_{pixel}^3. This has two negative implications. On the computation side, one has to repeat this calculation for a large number of simulations and for many values of r, to profile correctly the likelihood. On the numerical side, with the succession of many operations, the sum of small errors due to the precision of the computer can lead to an ill-conditioned covariance.

Estimating the tensor-to-scalar ratio with the MLE, we need to assess likelihood even for negative values. If a simulation fits a negative value of r, it means that it has less signal than the expected fiducial. On a statistical level, this is either due to cosmic variance or simply due to an unfortunate realisation of the noise. However, at particular negative values of r the covariance matrix may become not positive-definite. In figure 5.3 (top left) we show the eigenvalues of the covariance matrix for $r = -0.002$[5]. The eigenvalues are almost all positive, except for a few (less than 5%) that take negative values[6]. A non positive-definite covariance matrix has no physical meaning, and creates numerical problems at the time of inversion. This is clearly visible in Figure 5.3 (top right), where the likelihood becomes numerically unstable for negative r. This instability affects the search for the $(-\log \mathcal{L})$ minimum, even though for that particular value of r the matrix is positive-definite.

In order to solve this numerical issue and allow the minimisation algorithm to find the best fit, we use a regularization process[7] as follows. First we calculate the covariance for a given r, and check whether the matrix is positive-defined. For negative outcome,

[5]Note that the value $r = -0.002$ is a borderline case. We will show that it is equivalent to 5 (2.5) times the uncertainty of r for the full-sky (60% sky) case.

[6]A matrix is positive-definite only if all its eigenvalues Λ are positive.

[7]We tested the standard procedure of adding an uncorrelated regularization noise, i.e. adding a constant to the diagonal of the covariance, however, it did not help solve the problem. So we employ a different method of regularization.

we calculate the eigenvalues and eigenvectors of the matrix. We fix the negative eigenvalues to a slightly positive value ($\Lambda_{reg} = 0.01 \cdot |\Lambda_-|$) and recalculate the regularised matrix using the same eigenvectors. An example of regularization and how this affects the likelihood are shown in the figure 5.3 (red lines in top panels). Regularization corrects the numerical instability for negative r, allowing the search for the minimum. In figure 5.3 (bottom) we show the covariance matrix for $r = -0.002$ before (left) and after (middle) the regularization process. The difference is very small and cannot be appreciated visually. But if we plot the relative difference (right), we observe that the regularization acts mainly on the off-diagonal terms, leaving the diagonal almost unchanged. This suggests how numerical problems arise from the fluctuations around zero of the off-diagonal terms, which are more sensitive to negative values of r.

Finally, we would like to emphasise that this regularisation is only necessary for profiling the left tail of the likelihood, allowing the function for finding the maximum likelihood to converge numerically to an estimation of r. It was necessary for about 25% of the simulations. For all those simulations, the estimated value, corresponding to the maximum likelihood, was in the safe range zone, where the covariance matrix was positive-definite.

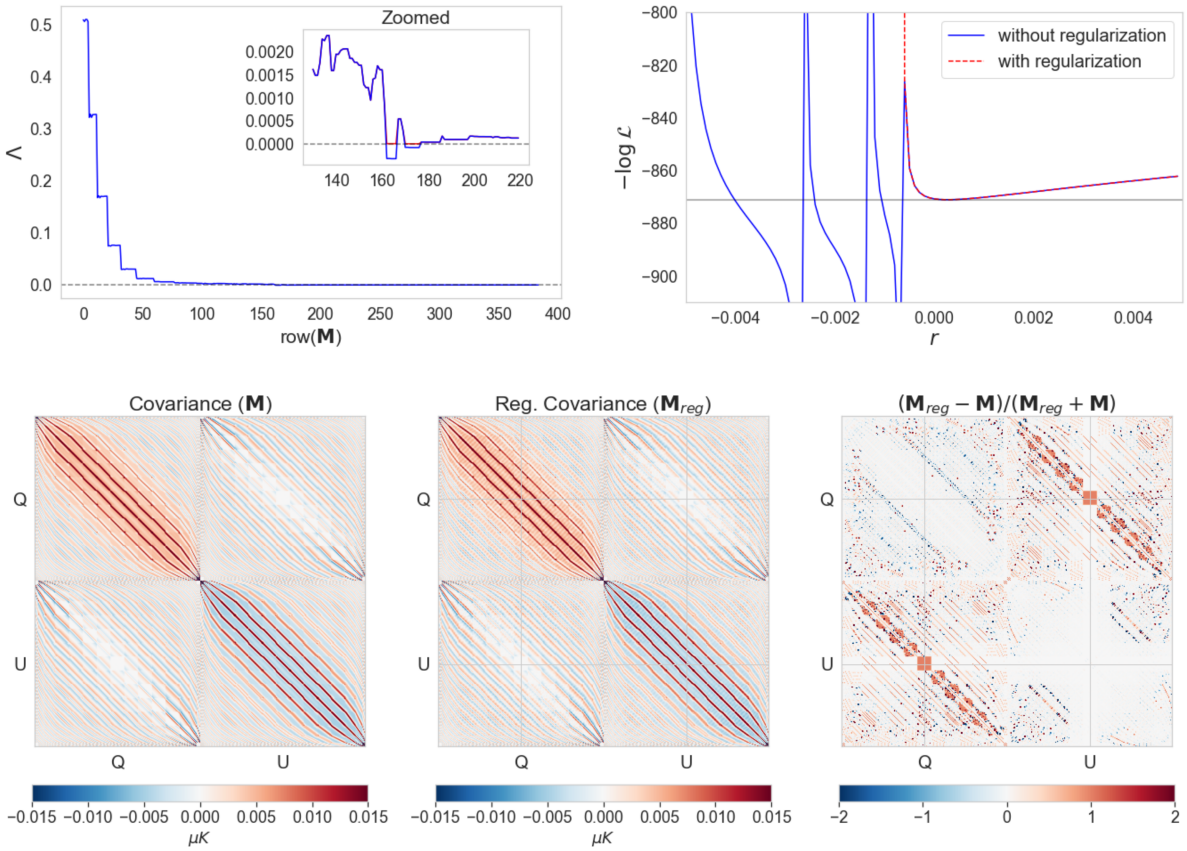

Figure 5.3: Top Left: Eigenvalues of the covariance matrix for $r = -0.002$. Top Right: Likelihood (full-sky) as function of r before and after regularization. Bottom: Covariance matrix for $r = -0.002$ before (left) and after (middle) regularization. On the right, the relative difference between the two matrices.

5.2.2 Results

Using the four estimators presented in the previous sections, we estimate the value of the tensor-to-scalar ratio for each simulation, finding the value of r which maximizes the likelihood for each simulation. In particular, the *Gaussian* estimator has an analytical solution obtained imposing the derivative of the likelihood with respect to r equal to zero. Instead, for the *Fisher*, *Hamimeche & Lewis* and *Pixel-based* approaches, we find the minimum of the quantity $(-\log \mathcal{L})$ by means of the `iminuit` routine[8] [174] in the range $[-0.01,\ 0.01]$ of r. The resulting estimations are showed in figure 5.4. The figure on the left shows the maxima distributions of r for the full sky analysis. A simple visual analysis shows how the distributions are not symmetrical, but have a longer tail toward positive values of r. This behaviour also happens when masks are applied, resulting in non-symmetric error bars, especially for the *Hamimeche & Lewis* and *Pixel-based* approaches. The figure on the right shows the expected value of the tensor-to-scalar ratio for each method, obtained averaging the values of r over simulations. For all sky fractions and for all methods we observe values consistent with the true value ($r = 0$) within the 68% confidence interval.

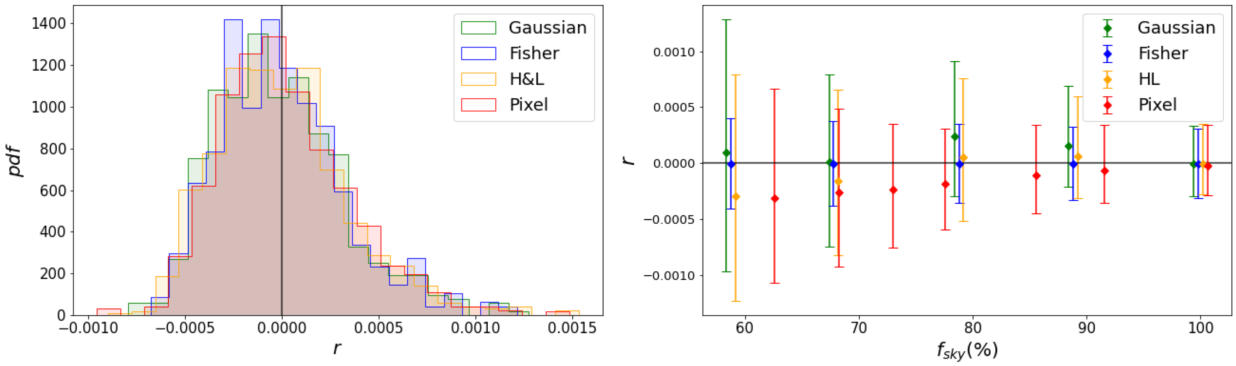

Figure 5.4: Tensor-to-scalar ratio estimation with the MLE for the four methods. Left: maxima distributions of r for the case of full-sky. Right: estimation of r for different sky fractions, with error bars showing the 68% confidence intervals. The solid black line represents the theoretical value $r = 0$. The different values of f_{sky} for the *Pixel-based* estimator are due to the mask downgrading from $N_{side} = 64$ to $N_{side} = 4$.

All methods thus appear to recover the true value of the tensor-to-scalar ratio. What particularly differentiates them is the value of the uncertainty of r. To allow a simple comparison between the methods, and give a simple numerical value, we define the uncertainty of r as

$$\sigma_r = \frac{1}{3.92}\,(r_{0.975} - r_{0.025}) \tag{5.30}$$

where $r_{0.975}$ and $r_{0.025}$ represent the value of r at which 0.975 and 0.025 percentage of estimations lie respectively above and below those values. The choice is made because the 95% confidence interval bounded by the 0.975 and 0.025 percentiles approximates the value of 3.92σ for a Gaussian distribution. This definition has the advantage of

[8] https://iminuit.readthedocs.io/en/stable/about.html

considering almost the entire distribution, giving more weight to the tails. Results are showed in figure 5.5. Note that for the *Pixel-based* approach, the value of σ_r is computed for two extra masks in order to better show the shape of the curve[9].

Fisher, *Hamimeche & Lewis* and *Pixel-based* methods provide compatible estimations of the uncertainty of the tensor-to-scalar ratio when the full-sky maps are analysed. This is expected because those estimators are exact for full-sky. Whereas the *Gaussian* estimator provides slightly sub-optimal results because of the approximation. For partial sky instead, each method results in a different estimation of this uncertainty. The *Fisher* estimator gives the smallest estimations of σ_r for all sky fractions. The *Gaussian* and *Hamimeche & Lewis* estimators provide similar large values of σ_r for partial skies. The two methods start to diverge for sky fraction smaller than 70%. The *Pixel-based* estimator provides values smaller than the *Gaussian* and *Hamimeche & Lewis*, but larger than the *Fisher* estimator.

The comparison of spectral methods therefore suggests that different estimators produce different uncertainties. These mismatches become increasingly important for smaller sky fractions. The results seem to suggest that the *Fisher* estimator underestimates the true value of uncertainty when considering the optimal *Pixel-based* estimator. However, the comparison with the *Pixel-based* is only possible if we use the regularisation process. One could argue that this process may affect the estimation of the tensor-to-scalar ratio in some way. For this reason, we take the comparison between spectral and *Pixel-based* estimators as qualitative. In the next section we will show the results we obtain when the prior $r > 0$ is applied, where no regularisation process is needed and the *Pixel-based* method is exact. That will then give us a quantitative comparison, allowing us to draw conclusions on the estimators.

5.2.3 Robustness Tests

In this section we present two tests we perform in order to check the robustness of our results. First, we repeated the same analysis for $r = 0$, but including different amplitudes for the white noise, in particular 2.5, 5, 10 and 15 μK-arcmin. Second, we perform the r-estimation for simulations with different values of tensor-to-scalar ratio, keeping the 10 μK-arcmin noise. We test two cases: $r = 0.01$, which is slightly below the actual experimental constraint, and $r = 0.00461$, corresponding to the Starobinsky model [175]. We restrict the analysis to the mask that allows about 60% sky fraction, because this is the case where the differences among the estimators are larger. In figure 5.6 the values and the uncertainties of the tensor-to-scalar ratio are showed.

The noise amplitude affects all estimators as one would expect, higher noise leads to a higher uncertainty of r. However, it can be seen that the relative ratio between the values of σ_r obtained with the different estimators is rather constant. Nevertheless, with higher amplitudes of noise, the *Hamimeche & Lewis* estimator provides a lower uncertainty than the *Gaussian* one, thus proving to be more efficient.

The analysis performed for different values of the input tensor-to-scalar ratio brings us interesting insights about the different estimators. The *Pixel-based* method provides a slightly biased estimation of the r-value towards lower values, with large uncertainties.

[9]The new masks are generated from the 77% *Planck* mask (downgraded to $N_{side} = 4$). We smooth it with a Gaussian beam of 10° and 12°, then we apply a threshold of 0.8. The results obtained with the new masks are plotted with empty diamond markers.

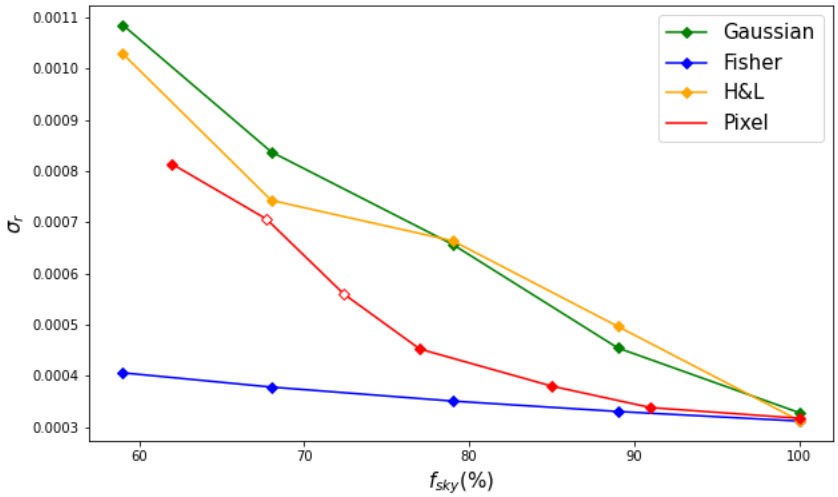

Figure 5.5: Uncertainty of the tensor-to-scalar ratio estimated with the MLE for the four methods, with different sky fractions. The value of σ_r is computed from the 95% confidence interval, see equation 5.30.

This is because the *Pixel-based* has access to multipoles $\ell_{max} \leq 12$, lacking the information from the recombination bump, useful for estimating r-values comparatively not so close to zero ($r > 10^{-3}$). Another important result is that for r greater than zero, in particular for $r = 0.01$, the three spectral estimators converge towards the same uncertainty estimation. This result corroborates the thesis that for a larger tensor-to-scalar ratio, high multipoles play a more important role in the estimation, so the f_{sky}-approximation and the Gaussian approximation become more reliable.

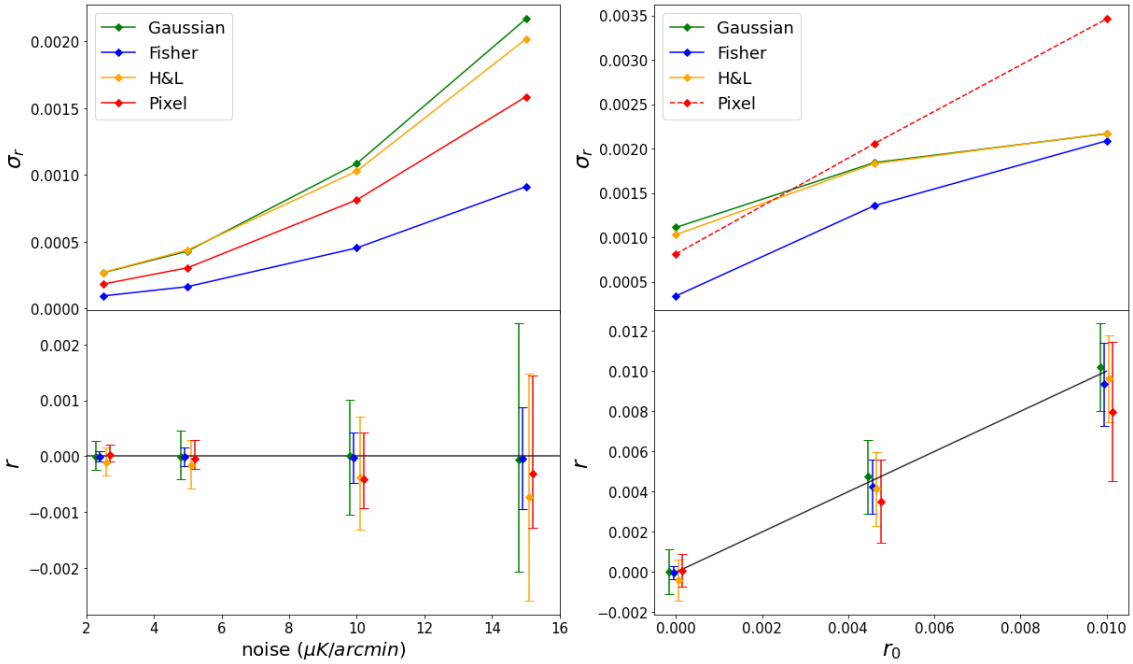

Figure 5.6: Left: Estimated tensor-to-scalar ratio (bottom) and uncertainty (top) for $r = 0$ as function of the noise amplitude. Right: Estimated tensor-to-scalar ratio (bottom) and uncertainty (top) for a 10 μK-arcmin noise as function of the input (true) tensor-to-scalar ratio r_0. The solid black line represents the true value of r. The line standing for σ_r obtained with the *Pixel-based* approach is dashed because it is strongly affected by the low resolution, $N_{side} = 4$, used for this method. The analysis is performed with the mask that allows about 60% sky fraction.

5.3 Bayesian Approach

Admitting both positive and negative values in the estimation of the tensor-to-scalar ratio is interesting from the methodological point of view in order to evaluate the performance of the different considered estimators. However, from a physical point of view, we know that the value of r can only be equal to or greater than zero. In statistical terms, this means having a prior probability of r, which can be represented by a step function, where $P(r) = 0$ for $r < 0$, and $P(r) =$ constant for $r \geq 0$. In addition, we have showed that when trying to estimate the value of r by admitting negative values, the *Pixel-based* estimator shows numerical problems. This issue is completely removed by excluding negative values a priori. We will estimate the uncertainty of r using a Bayesian approach in two different ways, which are: the Maximum A Posteriori Estimation (MAP) and Bayesian Inference. We will explore these two methods in the following sections.

5.3.1 Maximum A Posteriori Estimation

The Maximum A Posteriori Estimation (MAP) is a estimator based on frequentist statistics in a Bayesian context. This is because we perform a likelihood maximisation, as a MLE, but including a prior, in our case $r \geq 0$. Operationally we maximise the likelihood in the constrained range $[0, 0.01]$. The use of the prior $r \geq 0$ for null tensor-to-scalar ratio leads to a different interpretation of the results with respect to the MLE. In the latter, we obtain an average of the estimates of the tensor-to-scalar ratio and an uncertainty interval. The MAP remains an estimator, where a value of r can be inferred. However in our case of null tensor-to-scalar ratio, due to the different shape of the distribution of the maxima estimates, it is more appropriate to provide an upper-bound to the estimator, under the null hypothesis $r = 0$. In our calculation we fix the boundary at the 95% percentile of the maxima distribution, in order to give more weight to the differences between the estimation methods in the tails of the distributions.

Results are showed in figure 5.7. All the estimators provide very similar results for full-sky, then split into two branches. On the one hand, *Gaussian* and *Hamimeche & Lewis* estimators both show a strong dependence on the sky fraction. However, for fractions smaller than 80%, *Hamimeche & Lewis* reduces the slope. On the other hand, *Pixel-based* and *Fisher* estimators show a weaker dependence with the sky fraction. However, for fractions smaller than 80%, *Pixel-based* increases the slope. This result seems to suggest that the *Pixel-based* is compatible with the *Fisher* estimations for large sky fractions ($> 80\%$), whereas it becomes more compatible with the *Hamimeche & Lewis* estimations for smaller fractions ($< 60\%$). However, this approach somehow forces the estimation of r to zero for all those simulations that would fit a negative value as likelihood maximum. So one could argue that the distribution of the maxima estimates is in this case very asymmetric with a high peak near zero and therefore hard to determine with good accuracy which makes setting the upper-bound somewhat unstable. Thus, we refer the final conclusions to the next section.

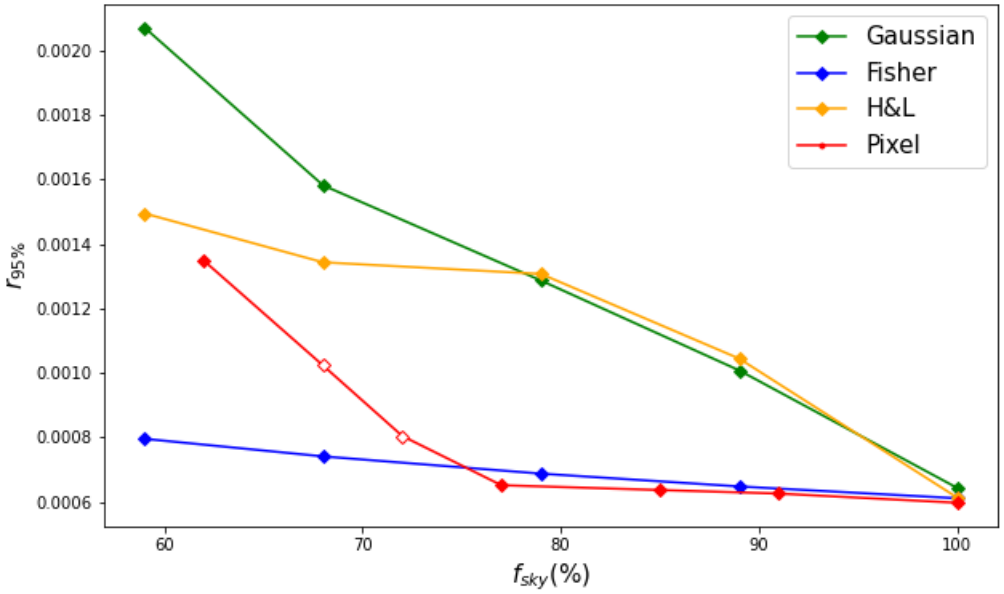

Figure 5.7: Upper-bound of the tensor-to-scalar ratio estimated with the four estimators. The estimations are obtained with MAP, setting the prior $r > 0$. This is equivalent to perform a MLE in the constrained range $r \in [0, 0.01]$.

5.3.2 Bayesian Inference

Bayesian inference is a fully Bayesian approach in which the parameter estimates with their uncertainties are derived directly from the posterior distribution without any maximisation process. The posterior distribution is the product of the likelihood by the prior. In our case the prior function is zero for $r < 0$, and constant for $r \geq 0$. Therefore, the posterior for each simulation is simply the likelihood evaluated for positive values of r. We compute the mean posterior averaging over all the simulations and integrate it in order to get the upper-bound as the 95% percentile. The Bayesian Inference allows us to tie a probability (in the statistical sense) to the values that r can take. This bound tells us at which confidence level a possible estimation of r is compatible with zero.

Results are showed in figure 5.8. The *Fisher*, *Hamimeche & Lewis* and *Pixel-based* methods agree for full-sky. The *Gaussian* method provides lower values (of about 20%). The relationship between the estimated values and the sky fraction is very similar to that found in the previous analysis. Considering the *Pixel-based* method as a reference, we can conclude that the *Gaussian* and *Fisher* methods underestimate and the *Hamimeche & Lewis* method overestimates the uncertainty of the tensor-to-scalar ratio. Quantitatively, the *Gaussian* method performs worse for large sky fractions ($f_{sky} \geq 90$) and the *Fisher* method performs worse for sky fractions of 80% down. The *Hamimeche & Lewis* is the only reliable spectral method although it is sub-optimal since provides less constrained upper bounds. The discussion and interpretation of these results are presented in the next section.

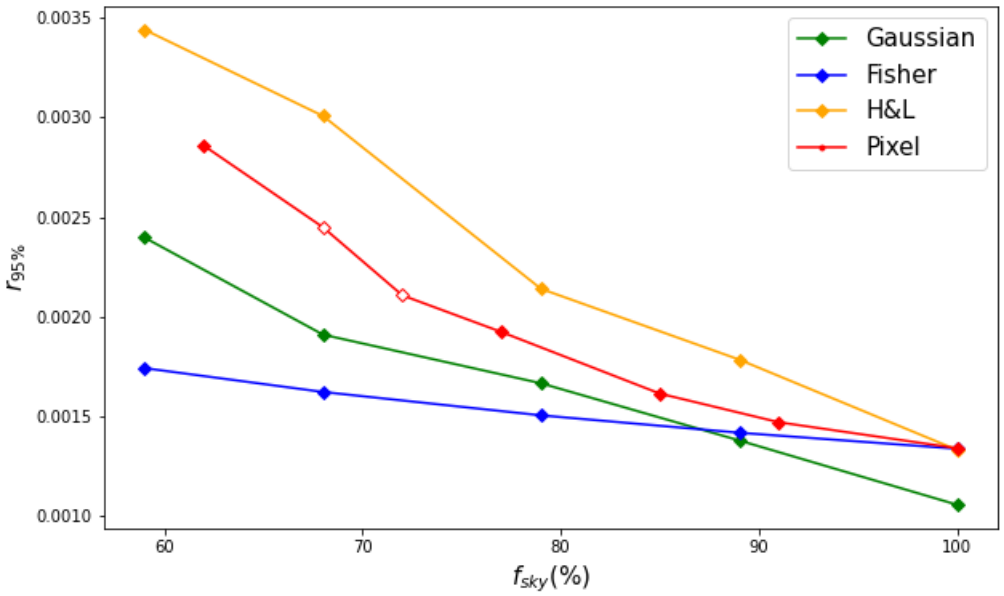

Figure 5.8: Upper-bound of the tensor-to-scalar ratio estimated with the four methods. The estimations are obtained integrating the mean posterior, which in turn is computed averaging over the simulations' posteriors.

5.3.3 Discussion

In this section, we discuss the four methods, their characteristics and implementations, and try to give meaning to the obtained results. We refer to all tested approaches, however we use as a reference the Bayesian Inference. This is because the *Pixel-based* does not require any regularisation. In addition, unlike the MAP, we maintain the real posterior distribution of r, without forcing values to zero.

The first case analysed is the *Gaussian* method. It is based on the very simple approximation that C_ℓ's are Gaussian distributed. This is a reasonable approximation for large multipoles, but it is less appropriate for low multipoles. The impact of this approximation can be quantified by comparing the upper-bound obtained from the posterior distribution at full-sky obtained with the *Gaussian* method with respect to the other methods, as showed in Figure 5.8. When considering the maxima distribution of r, as in the MLE and MAP, this effect is mitigated, as showed in Figure 5.5 and 5.7. From this we deduce that the Gaussian approximation strongly affects the shape of the posterior, but slightly the position of its maximum.

The relationship between the uncertainty of r and the sky fraction is explained by the following. In a nutshell, the presence of the mask reduces the number of pixels, thus the information, from which the spectrum is calculated. Plus, it generates cross-correlation between different multipoles. Therefore, the mask increases the covariance, which in turn increases the value of uncertainty of the tensor-to-scalar ratio, as shown in equation 5.8. In our case, the effect is exacerbated because most of the information for estimating r is contained in the low multipoles, as showed in section 5.1.6, which are the ones most affected by the presence of the mask.

The *Hamimeche & Lewis* is a parameter estimator used in the presence of correlated fields. It started out as a method with the aim of overcoming the approximations of the *Gaussian* estimator. Indeed, it does not assume C_ℓ's Gaussianity, so it is exact for complete sky, and the entire covariance matrix is considered in the estimation. Looking at the results in figures 5.5 and 5.7, we deduce that the estimator is quite compatible with the *Gaussian* estimator for large ($> 70\%$) fractions of the sky. For smaller fractions, when the correlation between different multipoles increases, *Hamimeche & Lewis* returns better results. When we estimate using Bayesian Inference, we still see a similar trend to the *Gaussian* estimator, but the latter is heavily biased by the Gaussian approximation. Even the *Hamimeche & Lewis* method has caveats. For example, it requires additional information such as a fiducial model and an offset, obtained from the simulations themselves. The result can therefore be affected by a limited number of simulations.

The *Fisher* estimator is an exact method for complete sky, but for partial skies it makes an approximation, which we refer as f_{sky}-approximation. This is equivalent to replacing equation 5.8, with

$$\sigma_r^2 = -\frac{1}{f_{sky}}\left[\frac{\partial^2 \log \mathcal{L}^{\text{full-sky}}}{\partial r^2}\right]^{-1}_{r=0} = \frac{1}{\sqrt{f_{sky}}}[(C_\ell^{tens})^T(\mathbf{C}^{\text{full-sky}})^{-1}C_\ell^{tens}]^{-1}. \tag{5.31}$$

Since both CMB and noise are Gaussian and uncorrelated, the full-sky covariance is diagonal $\mathbf{C}^{\text{full-sky}} = (C_\ell^{lens} + N_\ell)$. The approximation therefore consists of estimating the effect of the mask by the factor $(f_{sky})^{-1/2}$. Nevertheless, our analysis shows that this f_{sky}-approximation underestimates the uncertainty of r. The reason lies in the fact that the f_{sky}-term quantifies the loss of information due to fewer pixels, but does not quantify the presence of correlation between different multipoles, generated by the presence of the mask. This correlation is especially relevant for small multipoles. The f_{sky}-approximation is then only reliable for large multipoles as seen in section 5.2.3, when estimating the tensor-to-scalar ratio for values greater than zero.

Note that in equation 5.31 we have used the analytical derivation of σ_r because it is easy to interpret, but the argument also applies if we maximise the likelihood numerically. The difference between numerical and analytical calculation affects the estimation of the uncertainty of r independently of the mask. Recall that the analytical equation underlies an approximation, namely that the C_ℓ's are Gaussian distributed, exactly as the *Gaussian* estimator does.

The *Pixel-based* estimator is the only one based on an exact and optimal method. On a theoretical level, it does not require any approximation, or the introduction of additional information such as offsets or fiducials. However, we have already explained in section 5.1.5 how it has several computational and numerical complexities. The main problems occur when trying to estimate r with the MLE. For some simulations and some negative values of r, the pixel-pixel covariance may become not positive-definite. However, it becomes reliable, without the use of numerical regularization, simply by setting the prior $r \geq 0$.

To summarise, the results show us that all methods succeed in recovering the true value of the tensor-to-scalar ratio on average. However, the uncertainty on this estimate is different depending on the estimator. The *Pixel-based* estimator is the optimal method, which returns the most reliable uncertainty value. The *Hamimeche & Lewis*

estimator overestimates this uncertainty, especially for large fractions ($> 70\%$) of sky. Although it tends to become more reliable for smaller sky fractions. The *Gaussian* method makes a very strong approximation that leads to overestimates or underestimates depending on the approach used. The *Fisher* method always underestimates the uncertainty of r for partial skies. The f_{sky}-approximation may be reasonable for large sky fractions ($> 80\%$), but it is not reliable for smaller fractions.

5.3.4 Pixel-Based Resolution

The maps used for the *Pixel-Based* method are generated at $N_{side} = 4$ without beam. This resolution was chosen to significantly reduce computing costs, allowing us to test the different approaches and methods presented in this analysis. Instead, the choice not to use a beam lies in the fact that it makes the analysis much simpler and easier to interpret. This will be clarified later in the text. However, what we use is an ideal study case, not applicable in real data analysis.

In a real context, parameter estimations are done using the highest possible resolution, within computational limits. In addition, maps and simulations require a beam to avoid problems such as aliasing. In our analysis, we know from theory that when analysing full-sky maps, resolution and beam do not matter much. To demonstrate it numerically, we show the 68% and 95% upper-bounds found for different resolutions in Table 5.1. For each simulation, we apply a Gaussian beam with FWHM that is 2.4 times the pixel size. Taking the 68% upper-bound, we obtain very compatible values. The difference between the lowest and the highest analyzed resolutions, respectively $N_{side} = 4$ and $N_{side} = 16$, is about 3%. It is similar to the difference in the standard deviations, of about 2%, found theoretically in section 5.1.6. For the 95% bound, the differences are slightly more pronounced. This suggests that a higher resolution could still help to better track the right tail of the likelihood[10].

f_{sky} (%)	N_{side}	FWHM ($'$)	$r_{68\%}$	$r_{95\%}$
100	4	2110	6.1×10^{-4}	1.49×10^{-3}
100	8	1055	6.1×10^{-4}	1.47×10^{-3}
100	16	528	5.9×10^{-4}	1.38×10^{-3}

Table 5.1: Upper-bounds of the tensor-to-scalar ratio estimated with the *Pixel-Based* method from full-sky simulations. The FWHM of the beams used are approximately 2.4 times the pixel size at each resolutions. The bounds are obtained with the Bayesian Inference approach.

If full-sky analysis is straightforward, partial-sky analysis is much more complex. When we apply the beam to the full map, it creates correlations between pixels, even if they are far apart. So when we then apply the mask, part of the information of the masked region of the sky is shared with the unmasked pixels[11]. The larger the beam,

[10] This can be explained by the large difference in the number of pixels used to fit the likelihood, exactly 384 for $N_{side} = 4$ and 6144 for $N_{side} = 16$, considering both Q and U.

[11] Some might think that by increasing the mask, applying for example the same beam and a threshold, this correlation can be eliminated. We have seen from preliminary tests that the Gaussian beam has a very diffuse effect, affecting very distant pixels. In addition, the choice of threshold is not trivial and remains an arbitrary parameter that strongly affects the final estimation.

the greater the mixing of information between the pixels inside and outside the mask. If, on the other hand, we apply the beam after masking, we would have major problems with pixels bordering the mask. So when masks and beams are involved, there is not a straightforward way to compare results at different resolutions.

In any case, the most important result obtained in this chapter by comparing different likelihood estimators was to show that the f_{sky}-approximation is not reliable in the case of $r = 0$ and partial sky. However, this was demonstrated by referring to a low-resolution *Pixel-Based* likelihood without beam. Here we show how the approximation behaves with respect to a more realistic case, using the maximum resolution we can achieve with its proper beam. Results obtained with the Bayesian Inference are showed in Figure 5.9. Once again we see how the f_{sky}-approximation for partial sky, used by the *Fisher* estimator, leads to an underestimation of the uncertainty of r.

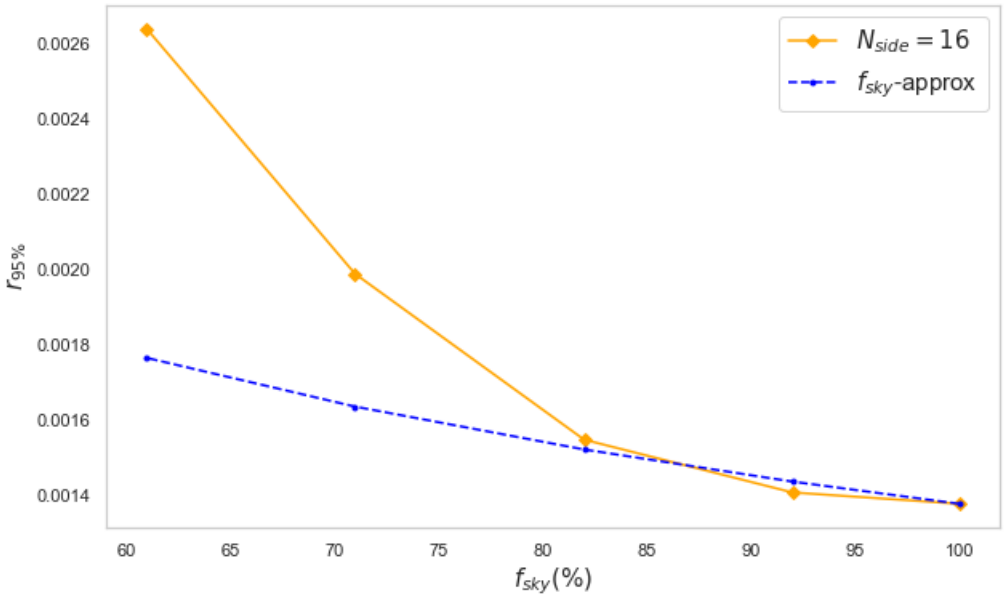

Figure 5.9: Upper-bound of the tensor-to-scalar ratio estimated with the *Pixel-Based* method using Bayesian Inference. Results obtained with the resolution $N_{side} = 16$. In blue the values we would have obtained if we had used the f_{sky}-approximation as in the *Fisher* estimator.

5.4 Conclusions

The work presented in this chapter is a methodological study of the techniques used for estimating the uncertainty of the tensor-to-scalar ratio (r). In particular, we focused on the concrete case of $r = 0$, which is of great interest because, as demonstrated analytically and numerically, most of the information resides in large scales. This generates a number of complications when estimating this cosmological quantity if only a portion of the sky is available.

We analysed four likelihood estimators, three acting in spectral space and one in real space. The first method, which we called *Gaussian* estimator, is based on the approximation that C_ℓ's are Gaussian distributed. The second, called *Fisher* estimator, is an exact method for full sky, but makes an approximation for partial skies, i.e. the multipoles are statistically independent and the presence of the mask is taken into account through the factor $(f_{sky})^{-1}$. The third spectral method, called *Hamimeche & Lewis*, is more sophisticated than the previous ones, it does not make major approximations, but requires a number of additional operations and parameters. The last method, called *Pixel-based* estimator, as the name suggests operates in real space so it is exact, but the implementation has computational complications.

We compared the four estimators using three different statistical approaches. The first is totally frequentist, the *Maximum Likelihood* estimation, where we estimate the value of r maximizing the likelihood by imposing no initial constraints. The second is the *Maximum A Posteriori* estimation, which is a hybrid approach because we estimate the value of r by maximising the likelihood at which we impose the prior $r > 0$. The third approach is the *Bayesian Inference*, where the uncertainty of r is obtained integrating the mean posterior, without a maximisation process.

Our reference results are those obtained with the *Pixel-based* method and the Bayesian approach, since this method is the most reliable and can be potentially optimal. The study tells us that the *Gaussian* estimator leads to unreliable results, even for full sky, due to the strong approximation that falls for large scales. The *Hamimeche & Lewis*, although more reliable, produces an overestimation of the uncertainty of r when compared to the method in real space. Finally, the most important lesson we learn is that the *Fisher* method produces an underestimation of the uncertainty of r when calculated from partial regions of the sky. This is because the $(f_{sky})^{-1}$ approximation does not take into account the correlation between multipoles, induced by the mask. The results obtained with the other statistical approaches, MLE and MAP, confirm the main findings, i.e. a tendency for the *Fisher* and the *Hamimeche & Lewis* methods to respectively underestimate and overestimate the uncertainty of r.

What has been said so far concerns to the case of $r = 0$. For positive values of the tensor-to-scalar ratio, the different approximations made by the spectral estimators become more reliable, with all methods converging to compatible results. Therefore, considering the different limitations of each method, the best method to estimate r in the general case of any value of r would consist of an appropriate combination of the pixel-based estimator for low multipoles and a spectral one for the high multipoles.

Several combinations of estimators and statistical approaches were tested in this work. However, all results are obtained under simpler conditions than real observations, i.e. maps consisting simply of CMB and white noise. For cases of estimates applicable to experimental observations, the picture is much more complicated. Nevertheless, this

methodological study shows the importance of a careful choice of methods for parameter forecasts of future experiments.

Chapter 6

Conclusions

The Cosmic Microwave Background radiation has provided profound insights into the origin and evolution of the universe. However, much remains to be discovered. Its polarised B-mode conceals key information for understanding the very early universe. However, a large number of challenges are around the corner. One of the biggest challenges is the decoupling of the CMB from other astrophysical radiation, which involves a detailed study of such emissions. In this thesis, we have dedicated two chapters to the spectral and morphological analysis of one important astrophysical emission, the polarized synchrotron radiation.

Even in the ideal case of having a deep knowledge of these contaminants as well as of the instrumental uncertainties, we still need a method to estimate faithfully the cosmological parameters. The last chapter of the thesis is then devoted to the study of techniques useful for obtaining precise cosmological estimates, in particular of the tensor-to-scalar ratio.

6.1 Synchrotron Spectral Analysis

In the work presented in Chapter 3 [1], we have analyzed the sky emission observed by *WMAP* and *Planck* respectively at 23 and 30 GHz. We have created a set of six masks: a 94% mask that enables nearly the entire sky except for the Galactic centre and a few brilliant point sources, and five masks that increase from low to moderate Galactic latitude (from 70 to 30 per cent of sky coverage). From the region of sky allowed by each mask we estimated EE, BB and EB power spectra. We fitted a power law $C_\ell^{EE,BB} \propto \ell^{\alpha_{EE,BB}}$ for the EE and BB power spectra independently, and a constant $C_\ell^{EB} = A^{EB}$ for the EB cross-spectrum. The analysis was made considering only the multipoles $30 \leq \ell \leq 300$, from *Planck* and *WMAP* maps independently, as well as by cross-correlating the two experimental data.

Reference results are given for the mask that allows 50 per cent of the sky, using cross-experiments analysis. We found a steep decay for E and B-modes, with indices $\alpha_{EE} = -2.95 \pm 0.04$ and $\alpha_{BB} = -2.85 \pm 0.14$, and an asymmetry between the two modes with a B-to-E ratio equal to 0.22 ± 0.02, at the pivot multipole $\ell = 80$. When focusing mostly on areas with a high signal-to-noise ratio, the indices obtained for the two polarisation components are generally more compatible. We found that the EB cross-spectra is consistent with zero at 1σ for all the considered sky fractions,

imposing a constraint on the EB amplitude to be $\leq 1.2\%$ (2σ) that of the EE amplitude. In addition, we have obtained results from the independent analyses of *Planck* and *WMAP* that are generally consistent with those obtained for the cross-correlation case. Nevertheless, there are a few minor variations when using best-fit parameters that are solely derived from the *Planck* 30 GHz map. Specifically, we find slightly larger B/E ratio (around 0.27), and less steep BB spectra (α_{BB} around 2.24) even though consistency with the cross-correlation results holds at 2σ in both cases.

A series of robustness tests that we conducted validated the accuracy of our findings. Specifically, we have fitted our model in a larger multipole range ($10 \leq \ell \leq 400$) and to the frequency maps of the 2020 *Planck* `NPIPE` release (PR4). Furthermore, we have separately estimated the spectra for the two hemispheres and discovered that, in the case of the E mode, there is more emission in the north. Other than that, the model of the polarisation power spectrum with the full sky and between the two hemispheres does not significantly differ.

To conclude the work, using both *Planck* and *WMAP* data, we have fitted a straightforward power law to the synchrotron spectral energy distribution separately for the EE and BB spectra. The recovered spectral indices β_{EE} and β_{BB} are compatible with the 50% mask; their respective values are -3.00±0.10 and -3.05±0.36. The findings show that adding higher Galactic latitudes to the analysis causes the spectral indices to tend towards steeper values.

6.2 Synchrotron Morphological Analysis

In the work presented in Chapter 4 [2] we have covered two aspects of the polarized synchrotron emission: the existence of substantial filamentary structures outside the Galactic plane and the statistical characteristics at small scales. The debiased polarised amplitude maps observed at 23 and 30 GHz, respectively by *WMAP* and *Planck*, have been analysed.

We designed a filament finder routine that looks for elongated coherent emission in the sky. It is based on a friend-of-friend recursive algorithm. Foreground simulations, which included a toy model of filamentary structure, were used to test the method. We find 19 filaments that are detected in both *Planck* and *WMAP*, at least partially. A few of the filaments have already been documented in the literature as findings from earlier *WMAP* analyses or observations in radio sky. Five of them are reported for the first time. We examined a few characteristics of the filaments from which we outline some considerations below. The polarization fraction of the filaments are larger than for the areas outside the filaments, excluding the Galactic plane, with values up to 30%. The polarization spectral indices of the filaments are about -3.1, consistent with the diffuse area. Most filaments have a strong polarisation E-component, but not B, moreover, some of them have not a bright counterpart in intensity.

We then have examined the statistical isotropy and non-Gaussianity of the polarised *WMAP* and *Planck* maps using Minkowski functionals and tensors. Our interest went to the faintest 80% and 60% of the sky. Results obtained from data were compared to results obtained from a set of Gaussian and isotropic simulations. We found large deviations ($> 3\sigma$) from Gaussianity and isotropy at 6° scale for the 80% sky fraction. Even though the deviations are still noticeably high at 1.5°, they become smaller as

one moves towards smaller scales. Analysing the 60% sky fraction, we found consistent results between simulations and data at the 3σ level. Our findings suggest that, even at small scales, the large filaments are the primary source of non-Gaussianity. The Gaussian and isotropic simulations at the *WMAP* and *Planck* resolution closely mimic the diffuse emission when those filamentary structures are masked.

Finally, we introduce a data-driven technique that produces anisotropic and non-Gaussian simulations. We employ a mathematical transformation to produce non-Gaussian harmonic coefficients. We account for the anisotropies with a normalization template resembling the diffuse filamentary structures. The simulations are fitted to match the statistical and spectral characteristics of the data for the 80% sky coverage.

6.3 Estimating the Tensor-to-scalar ratio

The last work presented in the thesis, Chapter 5, is a methodological study of the statistical approaches and likelihood methods used for estimating the uncertainty of the tensor-to-scalar ratio (r). We focus on the particular case of $r = 0$, which is very interesting since the majority of the information is found in large scales, as demonstrated both analytically and numerically. If only a portion of the sky is available, this leads to several complications in estimating this cosmological quantity.

We analysed three spectral estimators. The first, which we called *Gaussian* estimator, makes the approximation that C_ℓ's are Gaussian distributed. The second, called *Fisher* estimator, approximates the presence of the mask with the factor $(f_{sky})^{-1}$ for partial sky. The third spectral method, called *Hamimeche & Lewis*, does not make major approximations, but requires a number of additional precisely adjusted parameters. We also analyse a method, called the *Pixel-based* estimator, which operates in real space, so it is exact, but has several computational complications. The four estimators are implemented and compared by applying three different statistical approaches: *Maximum Likelihood*, *Maximum A Posteriori* and *Bayesian Inference*.

Most reliable results are obtained with the *Pixel-based* method and the Bayesian approach, thus used as a reference. Results obtained with the *Gaussian* estimator are the least reliable, even for full sky, due to the strong approximation that falls for large scales. The *Hamimeche & Lewis*, although more reliable, produces an overestimated uncertainty of r, compared with that obtained in real space. Finally, when calculating the uncertainty of r from partial regions of the sky, the *Fisher* method underestimates the uncertainty. This is due to the fact that the $(f_{sky})^{-1}$ approximation ignores the mask-induced correlation between multipoles. These considerations were confirmed using all three statistical approaches.

For positive values of the tensor-to-scalar ratio, the various approximations made by the spectral estimators become more reliable, and all methods converge to results that are compatible.

In this work, various combinations of estimators and statistical techniques were tested. All results, however, are obtained with less complex conditions than actual observations, i.e., with maps that only contain white noise and CMB. The situation becomes considerably more complicated when the estimates are obtained from experimental observations. However, even from this simplified case, the key takeaway is that an inaccurate choice of method can lead to an over- or an under-estimation of the

capabilities of a given experiment to estimate the tensor-to-scalar ratio. These considerations should be kept in mind especially when making forecasts of future experiments.

Appendix A

Synchrotron Spectral Analysis

The following appendix is a faithful excerpt from the appendix of the article "*Characterization of the polarized synchrotron emission from Planck and WMAP data*".

A.1 Mask Selection

In this section, we present the procedure used to construct a reliable set of masks by imposing different threshold levels in polarization, such that the selected regions correlate well with those where the synchrotron emission has a higher signal-to-noise ratio. For this task, we consider two types of simulations: (i) only-foregrounds simulation at frequency 30 GHz, computed with the PySM model ("d1","s1"), (ii) simulation of *Planck* data, as described in section 3.1, adding the PySM foreground map, a CMB realization and a *Planck* noise simulation. From both simulated maps, once smoothed to 5° resolution and after excluding the emission from the Galactic center and from point sources (as described in section 3.2.3), we mask the total polarized intensity map below successively higher thresholds of P, selecting eight regions with f_{sky} from 0.9 to 0.2 in steps of 0.1. We repeat the procedure with 5 different noise and CMB realizations.

By comparing the masks constructed in this way from the only-foregrounds (that would provide the *ideal* mask) and the complete simulations, we can see when the presence of other components is starting to affect the constructed mask and, therefore, at which threshold the selected regions do not correlate so well with the synchrotron amplitude. For each realization we compute the cross-correlation coefficient ρ between the only-foregrounds mask and the full-components mask. Moreover, we compute the foregrounds signal-to-noise ratio as the dispersion of the PySM foreground maps over the one of the CMB plus noise map, at scale of 1°, when the full-components mask is applied. The average values over the different realizations are reported in Table A.1. Comparing the regions allowed from the two mask sets shown in Figure A.1, we see that the masks constructed from the full simulated data start to be quite affected by noise for large sky fractions, deviating significantly from the masks constructed from the only-foregrounds simulation. The discrepancy is quantified by the cross-correlation and S/N values which, as expected, decrease with the sky fraction.

From this insight, we decided not to consider in the analysis those masks with an average signal-to-noise ratio smaller than 2.5, to prevent the inclusion of too noisy regions. Moreover, we do not consider masks that retain a too small sky fraction, in

order to limit the effect of the mask in the spectra estimation. Therefore, we pick the most reliable mask set as the one which retain a sky fraction ranging from 0.7 to 0.3. We select the mask with $f_{sky} = 50\%$ as the reference case for our main results, because it represents the best compromise of sky fraction, signal-to-noise ratio and cross-correlation between the ideal and realistic mask.

The $f_{sky} = 0.94$ mask that we use in the analysis, but not directly considered in this test, has the lowest signal-to-noise ratio and in some regions can be even dominated by noise, therefore, some considerations can be less reliable than for the other mask cases. However, we decided to show results also for the $f_{sky} = 0.94$ mask in order to check if the characterization of the diffuse synchrotron features can be extended to the full sky, when the Galactic plane and bright point sources are properly masked.

f_{sky} [%]	ρ	S/N
90	0.82	2.37
80	0.83	2.48
70	0.88	2.60
60	0.91	2.74
50	0.92	2.88
40	0.93	3.06
30	0.93	3.27
20	0.95	3.61

Table A.1: Cross-correlation and signal-to-noise values, corresponding to the different masks, estimated averaging over five only-foregrounds and all-components simulations (see text for details). The S/N value reported is the average between the Q and U signal-to-noise ratio. Note that differently to the masks used in the spectra estimation (see section 3.2.3), these masks were not apodized and their boundaries were not regularized.

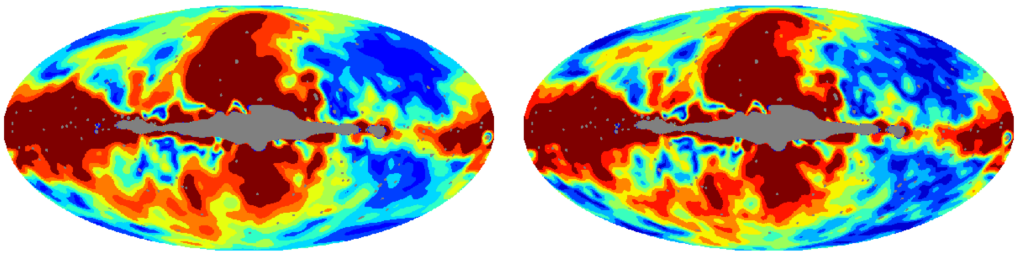

Figure A.1: Left: All-sky map showing the sky regions computed with the successive thresholds applied to the PySM foregrounds simulation. Right: same regions for one simulation including the PySM foregrounds, CMB and noise. The unmasked regions by the eight masks are showed from the smallest sky fraction mask (20%) in dark-red, and by adding the regions in red, orange, yellow, green, turquoise, light-blue and blue, up to the one allowing the largest sky fraction (94%) which leaves unmasked the full sky except for the grey region. This excluded region corresponds to the combination of the Galactic center mask and the point source mask.

A.2 Robustness test

In order to test the robustness of our results we have carried out the following analyses. First, following a similar procedure presented in section 3.3.2, we test the power-law model cross-correlating the A/B detector splits of the new 2020 *Planck* `NPIPE` release (PR4) maps at 30 GHz, in order to check the robustness of the results versus the considered 2018 *Planck* release, which uses a different pipeline. Second, we fit the model to the same data set as in section 3.3.3, but to a larger multipole range $10 \leq \ell \leq 400$, in order to check if the model holds when smaller and larger scales are included.

A.2.1 Planck Release 4

In 2020 the *Planck* Collaboration has released new frequency maps in temperature and polarization using the `NPIPE` processing pipeline [116]. `NPIPE` introduces several improvements which lead to lower systematics as well as lower levels of noise, being the changes more significant for polarization data and for HFI channels. Nevertheless, low frequency channels are also affected by the new pipeline and, therefore, it is worth checking the consistency of the results between the PR3 and PR4 releases.
The PR4 provides full-mission and A/B splits for data maps and simulations (for details see [116]). In particular, for the 30 GHz channel, the A subset is obtained combining maps of the years 1 and 3 and the B subset combining years 2, 4 and start of 5. In this section, we present the analysis performed cross-correlating the A/B splits of the `NPIPE` 30 GHz maps, degraded at the pixel resolution corresponding to $N_{side} = 512$.

We estimate the covariance matrices cross-correlating 300 A-split simulations with 300 B-split simulations provided by the *Planck* Legacy Archive[1] (PLA). Table A.2 shows the best-fit parameters and the χ^2 values for this case. These results are consistent within the errors with those found in section 3.3.1 using *Planck* release 3, as shown in Figure A.2 (left panel) for the reference mask. As for PR3, spectra estimated from PR4 shows in general a less steep decay for both components, most notably for the B-mode, compared to the result found in 3.3.3 with the cross-analysis. However, the spectral indices α_{EE} and α_{BB} are, in general, more consistent between them for PR4 than for PR3. The EB cross-term is also consistent with zero at 1σ for the whole mask set. It is interesting to point out that the values found for the χ^2 tend to be smaller when using PR4 data with respect to PR3, which is especially notable for the EB fit. This improvement is likely due to the larger number of simulations used in the PR4 analysis.

A.2.2 Large Multipole Range

In the main analysis we have considered the multipole range $30 \leq \ell \leq 300$. The upper limit is chosen because at higher multipoles both noise and possible emission of extra-Galactic compact sources can be important and then can strongly contaminate the foreground emission. The lower limit is chosen because pseudo-spectra methods (as `NaMaster`) are expected to be less reliable at small multipoles for masked sky regions. However, it makes sense to wonder if our results are robust when considering a larger

[1] pla.esac.esa.int

f_{sky}	**94%**	**70%**	**60%**	**50%**	**40%**	**30%**
α_{EE}	-2.86 ± 0.11	-2.82 ± 0.12	-2.81 ± 0.11	-2.84 ± 0.11	-2.87 ± 0.12	-2.96 ± 0.13
α_{BB}	-2.41 ± 0.23	-2.61 ± 0.19	-2.52 ± 0.17	-2.53 ± 0.24	-2.47 ± 0.28	-2.44 ± 0.35
A^{EE} $[10^{-3}\mu K]$	5.63 ± 0.31	8.0 ± 0.42	9.14 ± 0.47	10.34 ± 0.54	11.74 ± 0.62	14.37 ± 0.84
A^{BB} $[10^{-3}\mu K]$	1.74 ± 0.22	2.16 ± 0.2	2.36 ± 0.19	2.52 ± 0.27	2.94 ± 0.39	3.55 ± 0.54
A^{BB}/A^{EE}	0.31 ± 0.04	0.27 ± 0.03	0.26 ± 0.02	0.24 ± 0.03	0.25 ± 0.04	0.25 ± 0.04
χ^2_{EE} (20 dof)	23.8	22.2	21.9	25.7	21.6	20.7
χ^2_{BB} (20 dof)	24.6	18.3	19.0	20.4	19.3	22.7
A^{EB} $[10^{-3}\mu K]$	0.04 ± 0.08	-0.02 ± 0.10	0.01 ± 0.11	-0.05 ± 0.1	-0.01 ± 0.12	0.0 ± 0.15
A^{EB}/A^{EE}	0.007 ± 0.014	-0.002 ± 0.012	0.001 ± 0.012	-0.005 ± 0.009	-0.001 ± 0.010	0.0 ± 0.010
χ^2_{EB} (21 dof)	25.2	20.5	20.4	23.9	25.3	24.8

Table A.2: *Planck* PR4 results. Best-fit parameters, 1σ errors and χ^2 values for the power-law in equation 3.1 for EE and BB, and for the constant baseline in 3.2 for EB. Power spectra are computed by cross-correlating A/B detector split of the *Planck* `NPIPE` (PR4) 30 GHz maps, for each of the six sky masks described in section 3.2.

range. Therefore, in this section we show the best parameters we find fitting equations 3.1-3.2 in the multipole range $10 \leq \ell \leq 400$ to the pseudo-C_ℓ computed cross-correlating the co-added 9 year *WMAP* K-band maps and the full-mission *Planck* (PR3) 30 GHz data, with exactly the same procedure described in section 3.3.3. The fit parameters and χ^2 values are reported in table A.3.

When working with the larger multipole range, we find in general slightly flatter values for both EE and BB for the different considered sky fractions, although this is not the case for the reference mask (see Fig. A.2, right panel) where α_{BB} is actually slightly steeper. Nevertheless, for the whole mask set the results are still quite compatible with those found in the main analysis. This indicates that the model is also valid at the larger scale range considered in this extended analysis.

f_{sky}	**94%**	**70%**	**60%**	**50%**	**40%**	**30%**
α_{EE}	-2.81 ± 0.04	-2.76 ± 0.04	-2.78 ± 0.05	-2.84 ± 0.04	-2.85 ± 0.05	-2.82 ± 0.06
α_{BB}	-3.12 ± 0.07	-3.05 ± 0.09	-2.96 ± 0.09	-2.96 ± 0.09	-2.85 ± 0.11	-2.87 ± 0.12
A^{EE} $[10^{-3}\mu K]$	10.39 ± 0.32	14.15 ± 0.38	16.05 ± 0.49	17.79 ± 0.5	20.78 ± 0.6	24.52 ± 0.87
A^{BB} $[10^{-3}\mu K]$	2.13 ± 0.13	2.97 ± 0.19	3.61 ± 0.22	3.94 ± 0.24	4.92 ± 0.33	5.95 ± 0.39
A^{BB}/A^{EE}	0.20 ± 0.01	0.21 ± 0.01	0.23 ± 0.02	0.22 ± 0.02	0.24 ± 0.02	0.24 ± 0.02
χ^2_{EE} (27 dof)	44.9	31.7	38.1	34.3	31.2	48.1
χ^2_{BB} (27 dof)	19.1	18.7	20.0	17.4	23.6	21.2
A^{EB} $[10^{-3}\mu K]$	0.01 ± 0.07	0.12 ± 0.10	0.03 ± 0.10	0.02 ± 0.12	0.04 ± 0.11	0.01 ± 0.13
A^{EB}/A^{EE}	0.001 ± 0.007	0.008 ± 0.007	0.002 ± 0.006	0.001 ± 0.007	0.002 ± 0.005	0.001 ± 0.005
χ^2_{EB} (28 dof)	60.1	70.6	52.5	53.9	37.1	30.4

Table A.3: *Planck*-*WMAP* results. Best-fit parameters, 1σ errors and χ^2 values for the power-law in equation 3.1 for EE and BB, and for the constant baseline in 3.2 for EB. Power spectra is computed by cross-correlating the co-added 9 year *WMAP* K-band maps and the full-mission *Planck* 30 GHz maps, for each of the six sky masks described in section 3.2. Fits are performed on the multipole range $10 \leq \ell \leq 400$.

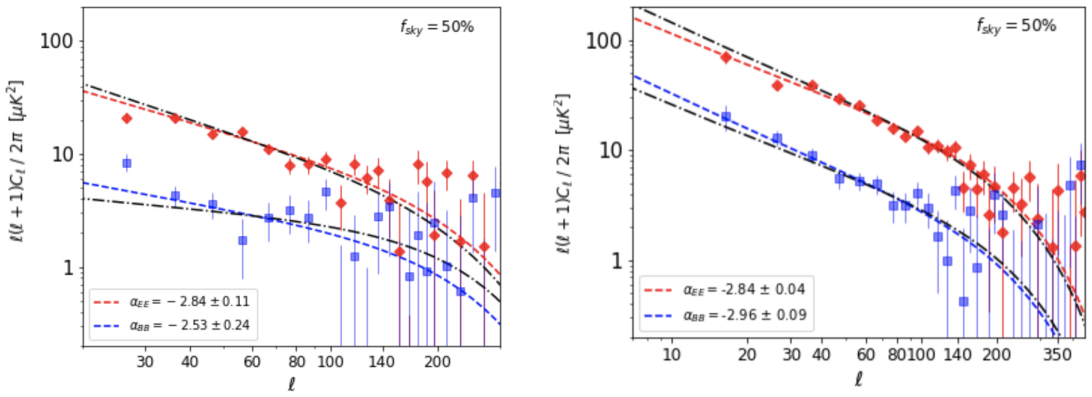

Figure A.2: Best fit (dashed line) to the EE (red diamonds) and BB (blue squares) pseudo-spectra for the reference mask ($f_{sky} = 50\%$). Left: spectra are computed cross-correlating A/B splits of the *Planck* `NPIPE` (PR4) 30 GHz maps. The fit with PR3 data presented in section 3.3.1 (black dash-dotted line) is given for comparison. Right: spectra are computed cross-correlating *WMAP* K-band and the *Planck* (PR3) 30 GHz maps and the fit is performed considering the large multipole range $10 \leq \ell \leq 400$. The best cross-analysis fit presented in section 3.3.3 (black dash-dotted line) is given for comparison.

A.3 Hemisphere analysis

In this appendix, we repeat the same analysis as in section 3.3.3 but independently for the Northern and Southern hemispheres. The mask set is the one presented in section 3.2, where we simply separate regions from the two celestial hemispheres. We do not include the two most stringent masks in the analysis because they retain too small sky fractions which can negatively affect the spectra computation at low multipoles, where the diffuse synchrotron signal is important. We still keep the same multipole range ($30 \leq \ell \leq 300$) and binning of the main analysis. Table A.4 shows the best-fit parameters (with 1σ errors) and χ^2 values for both hemispheres while Figure A.3 shows the power spectra and best-fit models for each case. For comparison, the best-fit model (black dot-dashed line) obtained from the full analysis is also shown, which tends to fall between the two hemisphere fits, showing a good level of consistency.

It is interesting to note that there are some differences between both hemispheres, as shown in Figure A.4, where the best-fit parameters for each hemisphere are compared. The synchrotron polarized emission in the Northern hemisphere is brighter than in the Southern hemisphere, with a factor around 1.4 larger for the amplitude of the EE spectra (slightly lower factor for BB). We also find a steeper decay of the synchrotron amplitude in the Southern hemisphere with respect to the Northern one. Nevertheless, the B-to-E ratio is quite consistent for the two hemispheres. The EB cross-term is compatible with zero at the 2σ level for the whole mask set, even if the estimated EB/EE amplitude is smaller for the Southern hemisphere. The goodness of the fits, in terms of the χ^2 value, points out that the EE and BB power-law model with null EB term describes better the synchrotron polarization emission in the Southern hemisphere than in the Northern one. This discrepancy could be hinting that the mask procedure might be working better in the Southern than in the Northern hemisphere, where instead

some complex structures, such as point sources or very bright Galactic plane emission, may remain unmasked. Nevertheless, the simple model considered in this analysis still seems to provide a reasonable good fit for both hemispheres.

f^N_{sky}	**47%**	**36%**	**30%**	**26%**
α_{EE}	-2.87 ± 0.10	-2.83 ± 0.09	-2.87 ± 0.09	-2.83 ± 0.09
α_{BB}	-3.17 ± 0.20	-3.04 ± 0.25	-2.87 ± 0.22	-2.67 ± 0.21
A^{EE} $[10^{-3}\mu K]$	11.74 ± 0.52	16.01 ± 0.58	18.36 ± 0.74	20.80 ± 0.74
A^{BB} $[10^{-3}\mu K]$	2.31 ± 0.23	3.34 ± 0.34	3.95 ± 0.37	4.70 ± 0.40
A^{BB}/A^{EE}	0.20 ± 0.02	0.21 ± 0.02	0.22 ± 0.02	0.23 ± 0.02
χ^2_{EE} (20 dof)	45.0	33.9	37.9	30.9
χ^2_{BB} (20 dof)	18.0	23.1	19.8	20.9
A^{EB} $[10^{-3}\mu K]$	0.06 ± 0.10	0.20 ± 0.14	0.22 ± 0.14	0.16 ± 0.17
A^{EB}/A^{EE}	0.007 ± 0.011	0.017 ± 0.012	0.018 ± 0.011	0.012 ± 0.012
χ^2_{EB} (21 dof)	31.4	40.4	30.5	35.5

f^S_{sky}	**47%**	**35%**	**30%**	**25%**
α_{EE}	-3.02 ± 0.08	-3.26 ± 0.1	-3.17 ± 0.11	-3.06 ± 0.11
α_{BB}	-3.55 ± 0.32	-3.17 ± 0.33	-3.12 ± 0.33	-3.23 ± 0.33
A^{EE} $[10^{-3}\mu K]$	8.51 ± 0.31	11.48 ± 0.52	12.55 ± 0.55	13.77 ± 0.57
A^{BB} $[10^{-3}\mu K]$	1.57 ± 0.24	2.64 ± 0.35	3.22 ± 0.43	3.51 ± 0.51
A^{BB}/A^{EE}	0.18 ± 0.03	0.23 ± 0.03	0.26 ± 0.04	0.25 ± 0.04
χ^2_{EE} (20 dof)	14.7	19.1	17.8	16.3
χ^2_{BB} (20 dof)	16.0	21.4	21.0	18.5
A^{EB} $[10^{-3}\mu K]$	-0.04 ± 0.08	-0.10 ± 0.13	0.04 ± 0.13	0.08 ± 0.12
A^{EB}/A^{EE}	-0.005 ± 0.009	-0.009 ± 0.011	0.003 ± 0.010	0.006 ± 0.009
χ^2_{EB} (21 dof)	18.9	35.0	28.7	21.2

Table A.4: *Planck*-*WMAP* results. Top: Northern hemisphere, bottom: Southern hemisphere. Best-fit parameters with 1σ errors and χ^2 values of the power-law in equation 3.1 for EE and BB, and of the constant baseline in 3.2 for EB, computed cross-correlating the co-added 9 year *WMAP* K-band maps and the full-mission *Planck* 30 GHz maps. The masks used are constructed isolating Northern and Southern regions for the four masks (from 0.94 to 0.5) described in section 3.2.

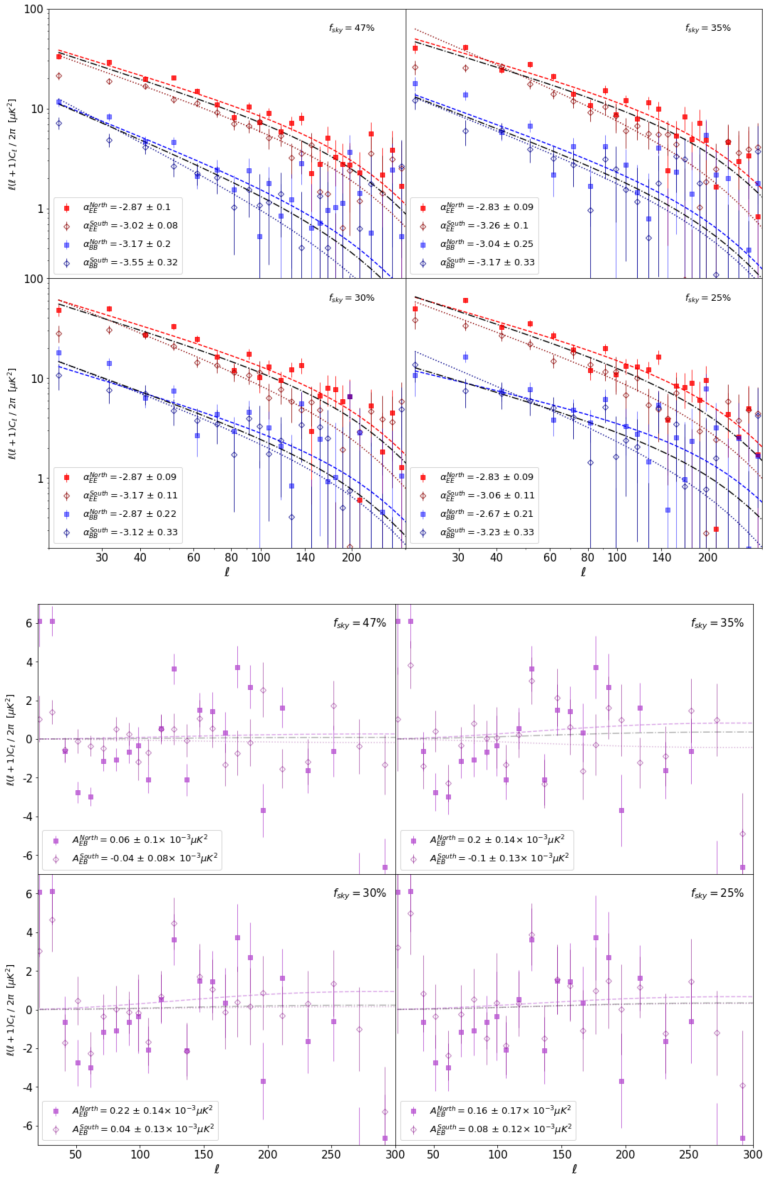

Figure A.3: *Planck*-*WMAP* results. Top: Northern EE (red squares), Southern EE (red diamonds), Northern BB (blue squares) and Southern BB (blue diamonds) pseudo-spectra. Bottom: Northern EB (purple squares) and Southern EB (purple diamonds) pseudo-spectra. Spectra are computed cross-correlating the co-added 9 year *WMAP* K-band maps and the full-mission *Planck* PR3 30 GHz maps, for the northern and southern parts of each of the four masks allowing the largest sky fractions. The f^S_{sky} label of each panel indicates the area of the southern region allowed by the corresponding mask. The dashed and dotted lines are, respectively, the Northern and Southern best fits to the hemisphere spectra and the black dash-dotted line is the best fit presented in section 3.3.3.

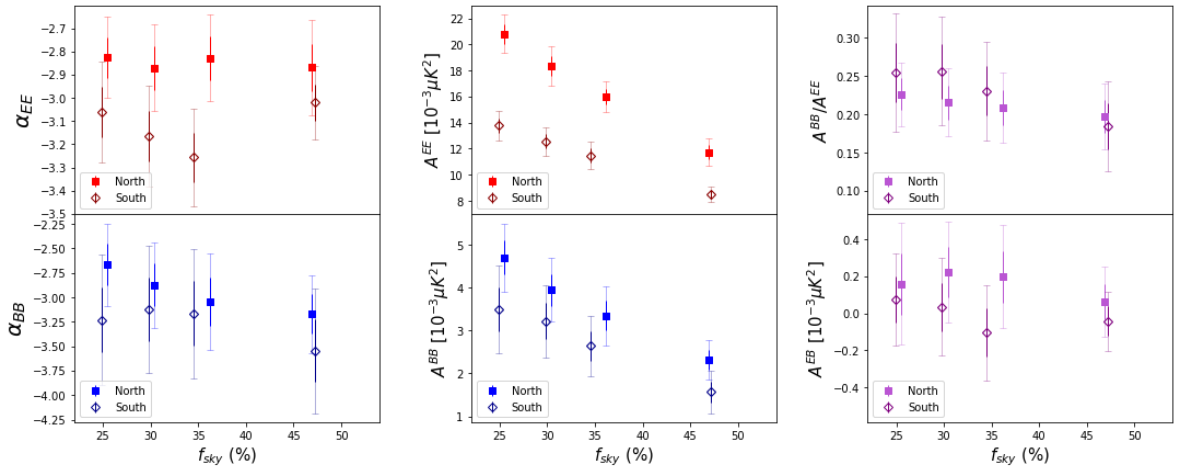

Figure A.4: Comparison between the best-fit parameters found in the Northern hemisphere (squares) and in the Southern hemisphere (diamonds) to the models of equations 3.1-3.2. 1σ and 2σ errors are showed, respectively, with thicker and thinner lines.

Appendix B

Synchrotron Morphological Analysis

The following appendix is a faithful excerpt from the appendix of the article "*Morphological Analysis of the Polarized Synchrotron Emission with WMAP and Planck*".

B.1 Power Spectra

In this section, we give a very brief review of the statistical quantities we use in this work, motivated by standard cosmological practises. CMB experiments usually produce data in the form of three pixelized maps, T for intensity and Q and U Stokes parameters for polarization. On the sky, these fields are usually expanded in terms of spherical harmonics

$$T = \sum_{\ell m} a_{\ell m} Y_{\ell m} \tag{B.1}$$

$$(Q \pm iU) = \sum_{\ell m} a_{\pm 2,\ell m}\ {}_{\pm 2}Y_{\ell m} \tag{B.2}$$

where $Y_{\ell m}$ and ${}_{\pm 2}Y_{\ell m}$ are respectively the standard and tensor (spin-2) spherical harmonics on a 2-sphere. The quantities $a_{\ell m}$ are the so-called spherical harmonic coefficients. Details of the mathematical formalism can be found in [44, 45].

If we define the linear combinations

$$a_{E,\ell m} = -\frac{1}{2}(a_{2,\ell m}\ + a_{-2,\ell m}\ ) \quad a_{B,\ell m} = -\frac{1}{2i}(a_{2,\ell m}\ - a_{-2,\ell m}\ ) \tag{B.3}$$

we can decompose the polarization emission into two scalar fields, the gradient-like E mode and the curl-like B mode

$$E = \sum_{\ell m} a_{E,\ell m} Y_{\ell m} \quad B = \sum_{\ell m} a_{B,\ell m} Y_{\ell m}. \tag{B.4}$$

The harmonic coefficients may be combined into the angular power spectrum

$$C_\ell^{XY} = \frac{1}{2\ell + 1} \sum_m \langle a^*_{X,\ell m} a_{Y,\ell m} \rangle, \quad X, Y = T, E, B \tag{B.5}$$

which represent: the auto-correlations of temperature and polarization modes denoted by TT, EE, and BB, the cross-correlation between temperature and polarization denoted by TE and TB, and the cross-correlation between polarization modes denoted by EB. For a Gaussian and isotropic field, all the statistical properties are captured by these two-point statistics.

Experimental observations are affected by the instrumental (beam) response and the pixelization process. The observed maps can then be written as the convolution of the actual sky signal with the instrumental beam (B) and the pixel window function (W). The latter is a function of the resolution at which the maps are produced. In harmonic space, it implies that

$$a_{\ell m}^{obs} = a_{\ell m} B_\ell \, W_\ell \tag{B.6}$$
$$C_\ell^{obs} = C_\ell \, B_\ell^2 \, W_\ell^2 \tag{B.7}$$

where B_ℓ and W_ℓ are respectively the harmonic transformations of the instrumental beam and the pixel window function. When analyzing maps produced by different experiments at resolution different from the one in which the original maps are produced, as discussed in this work, it is appropriate to smooth the maps to a common resolution. This can be achieved in harmonic space by

$$a_{\ell m}^{out} = a_{\ell m}^{in} \, \frac{B_\ell^{out}}{B_\ell^{in}} \, \frac{W_\ell^{out}}{W_\ell^{in}} \tag{B.8}$$

where B_ℓ^{in} and B_ℓ^{out} are respectively the instrumental and the required beams, W_ℓ^{out} and W_ℓ^{in} are the pixel window functions at the final and initial resolutions.

B.2 Finder Algorithm

B.2.1 Toy model for filaments

In this section, we test the performance of the filament finder algorithm using foreground simulations including a toy model of filamentary structure. Each simulation is computed as the sum of different independent components

$$S = S_{Gal} + S_{dif} + S_{Loops} + S_{noise}, \tag{B.9}$$

where:

- S_{Gal} is a Galactic plane simulation. The template is generated from the *WMAP* K-band P map, smoothed to a resolution of 5° and filtered with a low-pass filter $f(\ell) = [1 - \tanh((\ell - 10)/10)]/2$. In this way we preserve the Galactic morphology on large scales ($\ell < 10$) whilst removing the small scales corresponding to the real filaments.

- S_{dif} is a diffuse Gaussian template created with the `synfast` routine using the power spectra model: $C_\ell \propto (\ell/80)^{-2.9}$ [1]. The simulated map is filtered with a high-pass filter $f(\ell) = [1 - \tanh((\ell + 10)/10)]/2$, which only allows multipoles $\ell > 10$.

- S_{Loops} is a template where different loops are projected onto the sphere. The loops are based on filaments observed in *WMAP* [66]. Each loop has been generated with a width in the range 2–4°. In order to simulate both thin and diffuse filaments, we smooth the loops with a 1.5° or a 3° Gaussian beam. The loops are shown in figure B.2 (top right).

- S_{noise} is a noise simulation with properties estimated from the *WMAP* noise covariance matrices.

The simulation S is produced at $N_{side} = 128$ and a resolution of 1°, as used for the data. The Galactic and diffuse templates have been re-scaled in order to match the data signal-to-noise ratio. We tested different amplitudes, locations and radii for the loops, although in the following we will only refer to the case including Loops I, III, GCS, VII and XI, at a signal-to-noise ratio of 5, as shown in figure B.2. We filter the maps with the filters in figure B.1 and apply the friends-of-friends algorithm to 100 simulations. Note that each simulation has the same S_{Gal} and S_{Loop}, but different realization of S_{dif} and S_{noise}. Figure B.2 presents an example of a simulation (top left), and the corresponding detected structures before (bottom left) and after (bottom right) the minimal length criteria is applied, as described in section 4.2.1.

For each simulation, we recover on average 71.0% (±1.4%) of the original filaments. However, we also assign a detection of filamentary structure to around 7.2% (±0.7%) of the sky which is not associated with any input loops. From figure B.2, we observe that the filament finder mostly fails to detect parts of filaments close or tangential to the Galactic plane, where the strong Galactic emission dominates. We also point out that the detection can fail in those areas where two or more loops overlap, because the orientation angle in those pixels is the result of the average over different loops. The detections that are not associated with any input loop mainly arise in the regions with the lowest signal-to-noise ratio, suggesting that the noise is the cause. However, we note that it is possible to identify most of these spurious detections by comparing two simulations with different noise realisations. In practice, in our main analysis with real data, this is achieved by comparing the results of two independent maps, from *WMAP* and *Planck*, which allows us to reduce the number of spurious detections.

Note that the quantitative results presented in this appendix are obtained with reference to the *WMAP* data. However, all qualitative considerations also apply to the *Planck* data. Possible differences in the performance of the algorithm are mainly attributable to the fact that the difference of the filament brightness to the diffuse background is greater in the *WMAP* map than in the *Planck* map. In addition, the different distributions of noise for the two experiments could also have an impact on the performance of the algorithm, although we expect it to be subdominant.

B.2.2 Minimal length criteria

The filament finder method presented in section 4.2.1 is a simple friends-of-friends recursive algorithm based on the properties of single pixels. When a group of coherent and bright pixels is identified, it is not obvious if it is part of a filamentary structure or not. Considering the positive nature of the polarization intensity, regions where the noise is strong can confuse the detection. Moreover, the synchrotron diffuse background can also have a detrimental effect. In order to reduce spurious detections, we reject

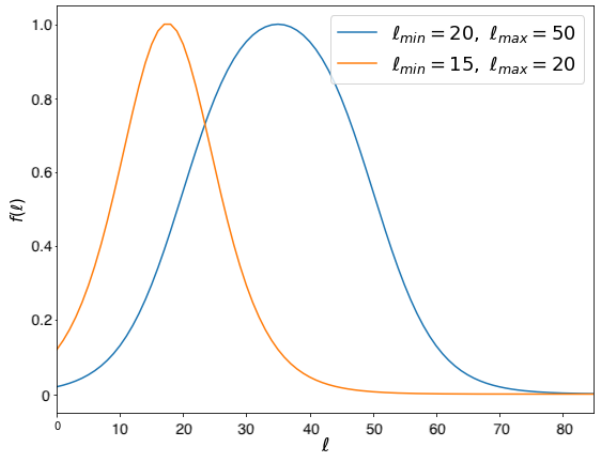

Figure B.1: Band-pass filters defined in equation 4.7 used for the detection of the bright (blue) and the weak (orange) filaments.

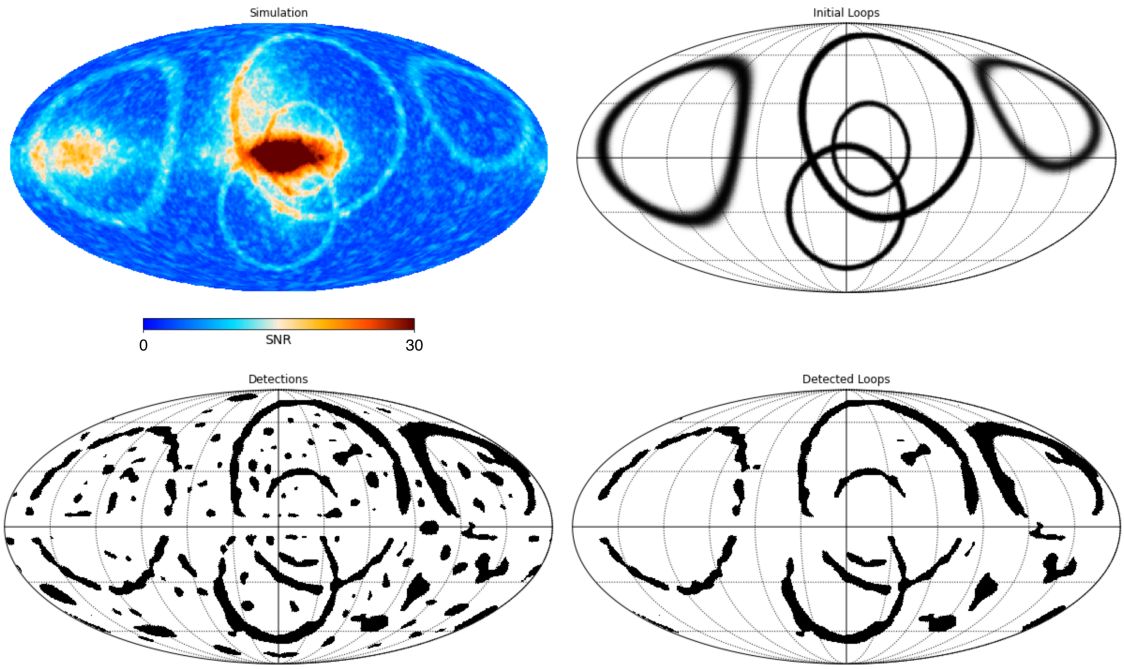

Figure B.2: Top Left: Toy filamentary foreground simulation. Top Right: Loop template used in the simulation. Bottom Left: All the detections found with the friends-of-friends recursive algorithm. Bottom Right: final result of the filament finder algorithm.

structures where the maximum pixel-pair angular distance is smaller than a threshold value L_{th}.

We find the best value for L_{th} by analysing simulations that do not contain loop structures. As in section B.2.1, we generate 100 diffuse synchrotron simulations from $S = S_{Gal} + S_{dif} + S_{noise}$, where the single components are described in the previous section. Note that in this case the simulations do not include the S_{Loops} term.

We apply the finder algorithm to each simulation which now can only detect spurious signals due to noise and the diffuse emission. Figure B.3 shows an example of a detection (left) and the distribution of the lengths determined from the simulations (right). We find that 68% of detections have a length smaller than roughly 3.1°, 95% smaller than 10.2° and 99% smaller than 17.5°. From this result, we pick the threshold value $L_{th} = 10°$. Note that this estimate holds for the pessimistic scenario of a loop-less foreground. In a more realistic case, i.e. including bright filaments, the algorithm would rely on a larger P_{th}, so a part of the noise detection would not exceed the threshold, and we would get less spurious detections.

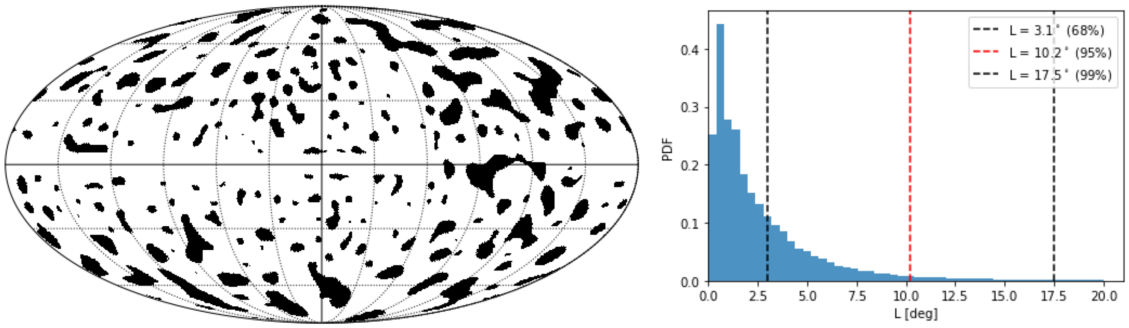

Figure B.3: Left: All the detections found with the friends-of-friends recursive algorithm from a loop-less simulation. Right: Distribution of the maximum angular lengths obtained from 100 loop-less simulations.

B.3 *Planck* Statistical Properties

B.3.1 Gaussian Simulations

In the main text, we analyse the statistical properties of the *WMAP* K-band maps. The choice is motivated by the fact that at 23 GHz the synchrotron emission is much stronger than at the 30 GHz *Planck* frequency channel. However, as a consistency check, in this section we present the results obtained when analysing the *Planck* data. We use the same masks and filters presented in section 4.4.2.

In order to quantify the non-Gaussianity and anisotropy of the synchrotron emission observed by *Planck*, we need to compare data with a set of suitable simulations. We compute pseudo-spectra in the unmasked regions cross-correlating A/B split maps[1].

[1]The PR4 provides A/B splits for data maps and simulations [116]. For the 30 GHz frequency channel, the A and B subsets are obtained respectively combining maps from years 1 and 3, and years 2 and 4.

From the spectra, we generate 600 Gaussian and isotropic simulations of Q and U, add noise, then compute the debiased polarized intensity.

Results are shown in figure B.4. For the larger sky fraction ($f_{sky} = 80\%$), we find that for the cases with $\ell_{min} < 80$, even averaging over the thresholds, the deviation exceeds 3σ. The deviation decreases when ℓ_{min} increases, however, for all the quantities (except $(W_1)_{22}$), some thresholds remain significantly higher than 3σ. For the smaller sky fraction ($f_{sky} = 60\%$), we generally find consistency between the data and simulations. These results are in substantial agreement with those determined with *WMAP* at 23 GHz, corroborating the discussion in section 4.4.4.

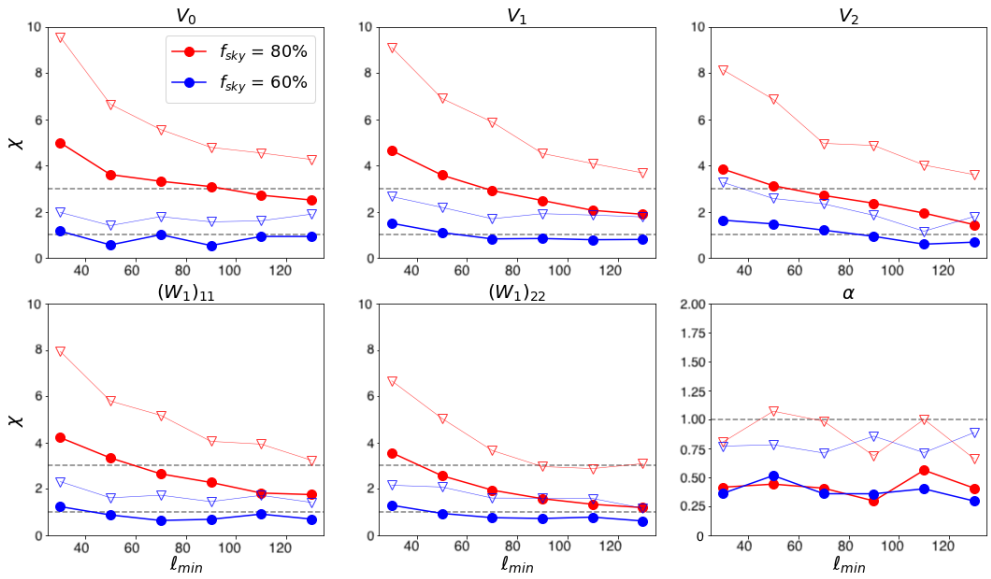

Figure B.4: Top: The three MFs, and bottom: the CMT diagonal terms and the α deviations from the Gaussian simulations, computed with *Planck* data, as a function of the low multipole cut ℓ_{min} from the applied band-pass filter. The dots and the triangles represent respectively the average and 95% percentile values computed over all threshold values.

B.3.2 Non-Gaussian Simulations

In section 4.5, we present a data-driven method to simulate the polarized synchrotron emission at 23 GHz. In this section, we show how the model performs in reproducing the emission at 30 GHz. We use the same spatially varying normalization factor (see figure 4.10) and (ϵ, δ) parameters to introduce anisotropies and non-Guassianities as for *WMAP*. The results are shown in figure B.5.

The simulations agree with the data at the 3σ level for the 80% mask for those cases with $\ell_{min} > 70$, and for all the considered multipole ranges for the 60% mask. The model seems to under-perform for the cases with $\ell_{min} \leq 70$ when considering the 80% mask, although the deviations from the data are clearly not so pronounced as when using Gaussian simulations. Considering that the largest deviation comes from $(W_1)_{11}$, it is reasonable to think that we are not correctly taking into account the anisotropy of the field.

It has been shown, even in this work, that the polarization spectral index shows spatial variations, and bright structures at 23 GHz are less detectable at 30 GHz. This suggests that the spatially varying normalization factor computed only from the *WMAP* data, could also depend on frequency. In addition, given that the V_1 and V_2 values computed with simulations deviate from the data when considering multipoles $\ell < 60$, we can not exclude the possibility that the non-Gaussianity level could also depend on frequency, which in our model translates into $\epsilon = \epsilon(\nu)$ and $\delta = \delta(\nu)$.

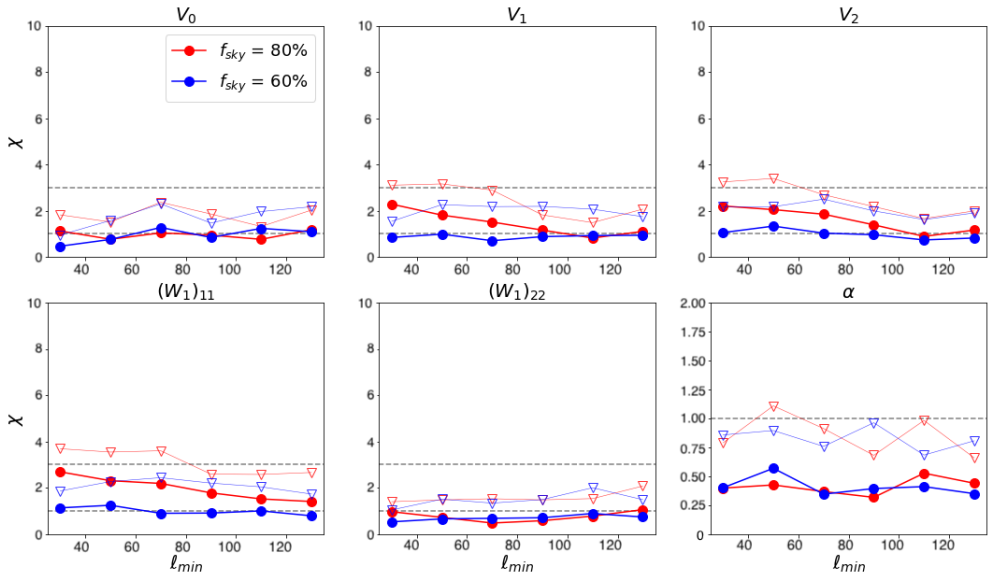

Figure B.5: Top: The three MFs, and bottom: the CMT diagonal terms and α deviations from the *non-Gaussian* simulations, computed with *Planck* data, as a function of the low multipole cut ℓ_{min} from the applied band-pass filter. The dots and the triangles represent respectively the average and 95% percentile computed over all threshold values. For comparison purposes, we use the same ranges as in figure B.4.

Bibliography

[1] F. Martire, R. Barreiro, and E. Martínez-González, "Characterization of the polarized synchrotron emission from Planck and WMAP data," *Journal of Cosmology and Astroparticle Physics*, vol. 2022, p. 003, apr 2022.

[2] F. A. Martire, A. J. Banday, E. Martínez-González, and R. B. Barreiro, "Morphological analysis of the polarized synchrotron emission with WMAP and Planck," *Journal of Cosmology and Astroparticle Physics*, vol. 2023, p. 049, Apr. 2023.

[3] E. P. Hubble, "Extragalactic nebulae.," *The Astrophysical Journal*, vol. 64, pp. 321–369, Dec. 1926.

[4] A. Einstein, "Die Grundlage der allgemeinen Relativitätstheorie," *Annalen der Physik*, vol. 354, pp. 769–822, Jan. 1916.

[5] M. Viel, G. D. Becker, J. S. Bolton, and M. G. Haehnelt, "Warm dark matter as a solution to the small scale crisis: New constraints from high redshift lyman-α forest data," *Phys. Rev. D*, vol. 88, p. 043502, Aug 2013.

[6] A. H. G. Peter, "Dark Matter: A Brief Review," *arXiv e-prints*, p. arXiv:1201.3942, Jan. 2012.

[7] DESI Collaboration, "DESI 2024 III: Baryon Acoustic Oscillations from Galaxies and Quasars," *arXiv e-prints*, p. arXiv:2404.03000, Apr. 2024.

[8] Planck Collaboration, "Planck 2018 results. I. Overview and the cosmological legacy of Planck," *Astronomy & Astrophysics*, vol. 641, p. A1, Sept. 2020.

[9] S. Dodelson, *Modern Cosmology*. Academic Press., 2003.

[10] M. Colless, "First results from the 2dF Galaxy Redshift Survey," *Philosophical Transactions of the Royal Society of London Series A*, vol. 357, p. 105, Jan. 1999.

[11] S. Shen, H. J. Mo, S. D. M. White, M. R. Blanton, G. Kauffmann, W. Voges, J. Brinkmann, and I. Csabai, "The size distribution of galaxies in the Sloan Digital Sky Survey," *MNRAS*, vol. 343, pp. 978–994, Aug. 2003.

[12] D. J. Eisenstein, I. Zehavi, D. W. Hogg, and S. et al., "Detection of the Baryon Acoustic Peak in the Large-Scale Correlation Function of SDSS Luminous Red Galaxies," *The Astrophysical Journal*, vol. 633, pp. 560–574, Nov. 2005.

[13] A. Refregier, "Weak Gravitational Lensing by Large-Scale Structure," *Annual Review of Astronomy & Astrophysics*, vol. 41, pp. 645–668, Jan. 2003.

[14] S. Burles and D. Tytler, "The Deuterium Abundance toward Q1937-1009," *The Astrophysical Journal*, vol. 499, pp. 699–712, May 1998.

[15] R. J. Cooke, M. Pettini, and C. C. Steidel, "One Percent Determination of the Primordial Deuterium Abundance," *The Astrophysical Journal*, vol. 855, p. 102, Mar. 2018.

[16] D. M. Scolnic, D. O. Jones, A. Rest, and P. et al., "The Complete Light-curve Sample of Spectroscopically Confirmed SNe Ia from Pan-STARRS1 and Cosmological Constraints from the Combined Pantheon Sample," *The Astrophysical Journal*, vol. 859, p. 101, June 2018.

[17] S. C. LIGO and C. Virgo, "Tests of general relativity with binary black holes from the second ligo-virgo gravitational-wave transient catalog," *Phys. Rev. D*, vol. 103, p. 122002, Jun 2021.

[18] C. Dvorkin, M. Gerbino, D. Alonso, N. Battaglia, S. Bird, A. Diaz Rivero, A. Font-Ribera, G. Fuller, M. Lattanzi, M. Loverde, J. B. Muñoz, B. Sherwin, A. Slosar, and F. Villaescusa-Navarro, "Neutrino Mass from Cosmology: Probing Physics Beyond the Standard Model," *Astro2020*, vol. 51, p. 64, May 2019.

[19] B. Ryden, *Introduction to cosmology*. Cambridge University Press, 1970.

[20] D. Baumann, "TASI Lectures on Inflation," *arXiv e-prints*, p. arXiv:0907.5424, July 2009.

[21] A. H. Guth, "Inflationary universe: A possible solution to the horizon and flatness problems," *Phys. Rev. D*, vol. 23, pp. 347–356, Jan 1981.

[22] A. R. Liddle and D. H. Lyth, *Cosmological Inflation and Large-Scale Structure*. Cambridge University Press, 2000.

[23] A. A. Penzias and R. W. Wilson, "A Measurement of Excess Antenna Temperature at 4080 Mc/s.," *The Astrophysical Journal*, vol. 142, pp. 419–421, July 1965.

[24] R. H. Dicke, P. J. E. Peebles, P. G. Roll, and D. T. Wilkinson, "Cosmic Black-Body Radiation.," *The Astrophysical Journal*, vol. 142, pp. 414–419, July 1965.

[25] J. C. Mather, E. S. Cheng, D. A. Cottingham, and e. a. Eplee, "Measurement of the Cosmic Microwave Background Spectrum by the COBE FIRAS Instrument," *The Astrophysical Journal*, vol. 420, p. 439, Jan. 1994.

[26] S. Masi, "The BOOMERanG experiment and the curvature of the universe," *Progress in Particle and Nuclear Physics*, vol. 48, pp. 243–261, Jan. 2002.

[27] A. T. Lee, P. Ade, A. Balbi, J. Bock, J. Borrill, A. Boscaleri, P. de Bernardis, P. G. Ferreira, S. Hanany, V. V. Hristov, A. H. Jaffe, P. D. Mauskopf, C. B. Netterfield, E. Pascale, B. Rabii, P. L. Richards, G. F. Smoot, R. Stompor, C. D. Winant, and J. H. P. Wu, "A High Spatial Resolution Analysis of the MAXIMA-1 Cosmic Microwave Background Anisotropy Data," *The Astrophysical Journal*, vol. 561, pp. L1–L5, Nov. 2001.

[28] A. Benoît, P. Ade, A. Amblard, R. Ansari, É. Aubourg, S. Bargot, J. G. Bartlett, J. P. Bernard, R. S. Bhatia, A. Blanchard, J. J. Bock, A. Boscaleri, F. R. Bouchet, A. Bourrachot, P. Camus, F. Couchot, P. de Bernardis, J. Delabrouille, F. X. Désert, O. Doré, M. Douspis, L. Dumoulin, X. Dupac, P. Filliatre, P. Fosalba, K. Ganga, F. Gannaway, B. Gautier, M. Giard, Y. Giraud-Héraud, R. Gispert, L. Guglielmi, J. C. Hamilton, S. Hanany, S. Henrot-Versillé, J. Kaplan, G. Lagache, J. M. Lamarre, A. E. Lange, J. F. Macías-Pérez, K. Madet, B. Maffei, C. Magneville, D. P. Marrone, S. Masi, F. Mayet, A. Murphy, F. Naraghi, F. Nati, G. Patanchon, G. Perrin, M. Piat, N. Ponthieu, S. Prunet, J. L. Puget, C. Renault, C. Rosset, D. Santos, A. Starobinsky, I. Strukov, R. V. Sudiwala, R. Teyssier, M. Tristram, C. Tucker, J. C. Vanel, D. Vibert, E. Wakui, and D. Yvon, "The cosmic microwave background anisotropy power spectrum measured by Archeops," *Astronomy and Astrophysics*, vol. 399, pp. L19–L23, Mar. 2003.

[29] N. W. Halverson, E. M. Leitch, C. Pryke, J. Kovac, J. E. Carlstrom, W. L. Holzapfel, M. Dragovan, J. K. Cartwright, B. S. Mason, S. Padin, T. J. Pearson, A. C. S. Readhead, and M. C. Shepherd, "Degree Angular Scale Interferometer First Results: A Measurement of the Cosmic Microwave Background Angular Power Spectrum," *The Astrophysical Journal*, vol. 568, pp. 38–45, Mar. 2002.

[30] J. L. Sievers, J. R. Bond, J. K. Cartwright, C. R. Contaldi, B. S. Mason, S. T. Myers, S. Padin, T. J. Pearson, U. L. Pen, D. Pogosyan, S. Prunet, A. C. S. Readhead, M. C. Shepherd, P. S. Udomprasert, L. Bronfman, W. L. Holzapfel, and J. May, "Cosmological Parameters from Cosmic Background Imager Observations and Comparisons with BOOMERANG, DASI, and MAXIMA," *The Astrophysical Journal*, vol. 591, pp. 599–622, July 2003.

[31] A. Slosar and C. Dickinson, "The Very Small Array: Observations and Latest Results," in *Maps of the Cosmos* (M. Colless, L. Staveley-Smith, and R. A. Stathakis, eds.), vol. 216 of *IAU Symposium*, p. 67, Jan. 2005.

[32] M. C. Runyan, P. A. R. Ade, R. S. Bhatia, J. J. Bock, M. D. Daub, J. H. Goldstein, C. V. Haynes, W. L. Holzapfel, C. L. Kuo, A. E. Lange, J. Leong, M. Lueker, M. Newcomb, J. B. Peterson, C. Reichardt, J. Ruhl, G. Sirbi, E. Torbet, C. Tucker, A. D. Turner, and D. Woolsey, "ACBAR: The Arcminute Cosmology Bolometer Array Receiver," *The Astrophysical Journal Supplement Series*, vol. 149, pp. 265–287, Dec. 2003.

[33] E. M. Leitch, J. M. Kovac, C. Pryke, J. E. Carlstrom, N. W. Halverson, W. L. Holzapfel, M. Dragovan, B. Reddall, and E. S. Sandberg, "Measurement of polarization with the Degree Angular Scale Interferometer," *Nature*, vol. 420, pp. 763–771, Dec. 2002.

[34] G. Hinshaw, D. Larson, E. Komatsu, D. N. Spergel, C. L. Bennett, J. Dunkley, M. R. Nolta, M. Halpern, R. S. Hill, N. Odegard, L. Page, K. M. Smith, J. L. Weiland, B. Gold, N. Jarosik, A. Kogut, M. Limon, S. S. Meyer, G. S. Tucker, E. Wollack, and E. L. Wright, "Nine-year Wilkinson Microwave Anisotropy Probe (WMAP) Observations: Cosmological Parameter Results," *ApJ Supp.*, vol. 208, p. 19, Oct. 2013.

[35] SO Collaboration, "The Simons Observatory: science goals and forecasts," *Journal of Cosmology and Astroparticle Physics*, vol. 2019, p. 056, Feb. 2019.

[36] BICEP/Keck Collaboration, "Bicep/*keck* xiv: Improved constraints on axionlike polarization oscillations in the cosmic microwave background," *Phys. Rev. D*, vol. 105, p. 022006, Jan 2022.

[37] J. A. Sobrin, A. J. Anderson, A. N. Bender, B. A. Benson, D. Dutcher, A. Foster, N. Goeckner-Wald, J. Montgomery, A. Nadolski, A. Rahlin, P. A. R. Ade, Z. Ahmed, E. Anderes, M. Archipley, J. E. Austermann, J. S. Avva, and et al., "The Design and Integrated Performance of SPT-3G," *ApJ Supp.*, vol. 258, p. 42, Feb. 2022.

[38] K. N. Abazajian, P. Adshead, Z. Ahmed, and e. a. Allen, "CMB-S4 Science Book, First Edition," *arXiv e-prints*, p. arXiv:1610.02743, Oct. 2016.

[39] LiteBIRD Collaboration, "Probing cosmic inflation with the LiteBIRD cosmic microwave background polarization survey," *Progress of Theoretical and Experimental Physics*, vol. 2023, p. 042F01, Apr. 2023.

[40] S. Hanany, M. Alvarez, E. Artis, and e. a. Ashton, "PICO: Probe of Inflation and Cosmic Origins," in *Bulletin of the American Astronomical Society*, vol. 51, p. 194, Sept. 2019.

[41] W. Hu and N. Sugiyama, "Anisotropies in the Cosmic Microwave Background: an Analytic Approach," *The Astrophysical Journal*, vol. 444, p. 489, May 1995.

[42] M. Tristram, A. J. Banday, K. M. Górski, and e. a. Keskitalo, "Improved limits on the tensor-to-scalar ratio using bicep and *planck* data," *Phys. Rev. D*, vol. 105, p. 083524, Apr 2022.

[43] W. Hu and M. White, "CMB anisotropies: Total angular momentum method," *Physical Review D*, vol. 56, pp. 596–615, July 1997.

[44] M. Kamionkowski, A. Kosowsky, and A. Stebbins, "A probe of primordial gravity waves and vorticity," *Phys. Rev. Lett.*, vol. 78, pp. 2058–2061, Mar 1997.

[45] M. Zaldarriaga and U. Seljak, "All-sky analysis of polarization in the microwave background," *Physical Review D*, vol. 55, pp. 1830–1840, Feb. 1997.

[46] W. Hu and M. White, "A CMB polarization primer," *New Astronomy*, vol. 2, pp. 323–344, Oct. 1997.

[47] Planck Collaboration, "Planck intermediate results. L. Evidence of spatial variation of the polarized thermal dust spectral energy distribution and implications for CMB B-mode analysis," *Astronomy & Astrophysics*, vol. 599, p. A51, Mar. 2017.

[48] Planck Collaboration, "Planck early results. XIX. All-sky temperature and dust optical depth from Planck and IRAS. Constraints on the "dark gas" in our Galaxy," *Astronomy & Astrophysics*, vol. 536, p. A19, Dec. 2011.

[49] Planck Collaboration, "Planck intermediate results. XLVIII. Disentangling Galactic dust emission and cosmic infrared background anisotropies," *Astronomy & Astrophysics*, vol. 596, p. A109, Dec. 2016.

[50] A. M. Meisner and D. P. Finkbeiner, "Modeling Thermal Dust Emission with Two Components: Application to the Planck High Frequency Instrument Maps," *The Astrophysical Journal*, vol. 798, p. 88, Jan. 2015.

[51] Planck Collaboration, "Planck 2018 results. XI. Polarized dust foregrounds," *Astronomy & Astrophysics*, vol. 641, p. A11, Sept. 2020.

[52] B. S. Hensley and P. Bull, "Mitigating complex dust foregrounds in future cosmic microwave background polarization experiments," *The Astrophysical Journal*, vol. 853, p. 127, jan 2018.

[53] V. Pelgrims, S. E. Clark, B. S. Hensley, G. V. Panopoulou, V. Pavlidou, K. Tassis, H. K. Eriksen, and I. K. Wehus, "Evidence for line-of-sight frequency decorrelation of polarized dust emission in Planck data," *Astronomy & Astrophysics*, vol. 647, p. A16, Mar. 2021.

[54] BICEP2 Collaboration, P. A. R. Ade, R. W. Aikin, D. Barkats, S. J. Benton, C. A. Bischoff, J. J. Bock, J. A. Brevik, I. Buder, E. Bullock, C. D. Dowell, L. Duband, J. P. Filippini, S. Fliescher, S. R. Golwala, M. Halpern, M. Hasselfield, S. R. Hildebrandt, G. C. Hilton, V. V. Hristov, K. D. Irwin, K. S. Karkare, J. P. Kaufman, B. G. Keating, S. A. Kernasovskiy, J. M. Kovac, C. L. Kuo, E. M. Leitch, M. Lueker, P. Mason, C. B. Netterfield, H. T. Nguyen, R. O'Brient, R. W. Ogburn, A. Orlando, C. Pryke, C. D. Reintsema, S. Richter, R. Schwarz, C. D. Sheehy, Z. K. Staniszewski, R. V. Sudiwala, G. P. Teply, J. E. Tolan, A. D. Turner, A. G. Vieregg, C. L. Wong, and K. W. Yoon, "Detection of B-Mode Polarization at Degree Angular Scales by BICEP2," *Physical Review Letters*, vol. 112, p. 241101, June 2014.

[55] M. Remazeilles, C. Dickinson, H. K. K. Eriksen, and I. K. Wehus, "Sensitivity and foreground modelling for large-scale cosmic microwave background B-mode polarization satellite missions," *MNRAS*, vol. 458, pp. 2032–2050, May 2016.

[56] O. Adriani, G. C. Barbarino, G. A. Bazilevskaya, R. Bellotti, and e. a. Boezio, "Cosmic-ray electron flux measured by the pamela experiment between 1 and 625 gev," *Phys. Rev. Lett.*, vol. 106, p. 201101, May 2011.

[57] Fermi LAT Collaboration, "Fermi lat observations of cosmic-ray electrons from 7 gev to 1 tev," *Phys. Rev. D*, vol. 82, p. 092004, Nov 2010.

[58] G. B. Rybicki and A. P. Lightman, *Radiative processes in astrophysics*. A Wiley-Interscience Publication, 1979.

[59] R. D. Davies, C. Dickinson, A. J. Banday, T. R. Jaffe, K. M. Górski, and R. J. Davis, "A determination of the spectra of Galactic components observed by the Wilkinson Microwave Anisotropy Probe," *Monthly Notices of the Royal Astronomical Society*, vol. 370, pp. 1125–1139, 07 2006.

[60] Planck Collaboration, "Planck 2015 results. XXV. Diffuse low-frequency Galactic foregrounds," *Astronomy & Astrophysics*, vol. 594, p. A25, Sept. 2016.

[61] K. Ferrière, J. L. West, and T. R. Jaffe, "The correct sense of Faraday rotation," *MNRAS*, vol. 507, pp. 4968–4982, Nov. 2021.

[62] U. Fuskeland, K. J. Andersen, R. Aurlien, R. Banerji, M. Brilenkov, H. K. Eriksen, M. Galloway, E. Gjerløw, S. K. Næss, T. L. Svalheim, and I. K. Wehus, "Constraints on the spectral index of polarized synchrotron emission from WMAP and Faraday-corrected S-PASS data," *Astronomy & Astrophysics*, vol. 646, p. A69, Feb. 2021.

[63] Planck Collaboration, "Planck 2018 results. IV. Diffuse component separation," *Astronomy & Astrophysics*, vol. 641, p. A4, Sept. 2020.

[64] R. de Belsunce, S. Gratton, and G. Efstathiou, "Testing for spectral index variations in polarized CMB foregrounds," *MNRAS*, vol. 517, pp. 2855–2866, Dec. 2022.

[65] E. de la Hoz, R. B. Barreiro, P. Vielva, E. Martínez-González, J. A. Rubiño-Martín, B. Casaponsa, F. Guidi, M. Ashdown, R. T. Génova-Santos, E. Artal, F. J. Casas, R. Fernández-Cobos, M. Fernández-Torreiro, D. Herranz, R. J. Hoyland, A. N. Lasenby, M. López-Caniego, C. H. López-Caraballo, M. W. Peel, L. Piccirillo, F. Poidevin, R. Rebolo, B. Ruiz-Granados, D. Tramonte, F. Vansyngel, and R. A. Watson, "QUIJOTE scientific results - VIII. Diffuse polarized foregrounds from component separation with QUIJOTE-MFI," *MNRAS*, vol. 519, pp. 3504–3525, Mar. 2023.

[66] M. Vidal, C. Dickinson, R. D. Davies, and J. P. Leahy, "Polarized radio filaments outside the Galactic plane," *MNRAS*, vol. 452, pp. 656–675, Sept. 2015.

[67] C. Dickinson, R. D. Davies, and R. J. Davis, "Towards a free-free template for CMB foregrounds," *MNRAS*, vol. 341, pp. 369–384, May 2003.

[68] C. Dickinson, Y. Ali-Haimoud, R. J. Beswick, S. Casassus, K. Cleary, B. Draine, R. Genova-Santos, K. Grainge, T. C. Hoang, A. Lazarian, E. Murphy, R. Paladini, M. W. Peel, Y. Perrott, J. A. Rubino-Martin, A. Scaife, C. Tibbs, L. Verstraete, M. Vidal, R. A. Watson, and N. Ysard, "Studies of Anomalous Microwave Emission (AME) with the SKA," in *Advancing Astrophysics with the Square Kilometre Array (AASKA14)*, p. 124, Apr. 2015.

[69] B. T. Draine and A. Lazarian, "Magnetic Dipole Microwave Emission from Dust Grains," *The Astrophysical Journal*, vol. 512, pp. 740–754, Feb. 1999.

[70] R. Génova-Santos, J. A. Rubiño-Martín, A. Peláez-Santos, F. Poidevin, R. Rebolo, R. Vignaga, E. Artal, S. Harper, R. Hoyland, A. Lasenby, E. Martínez-González, L. Piccirillo, D. Tramonte, and R. A. Watson, "QUIJOTE scientific results - II. Polarisation measurements of the microwave emission in the Galactic molecular complexes W43 and W47 and supernova remnant W44," *MNRAS*, vol. 464, pp. 4107–4132, Feb. 2017.

[71] F. Poidevin, J. A. Rubiño-Martín, C. Dickinson, R. Génova-Santos, S. Harper, R. Rebolo, B. Casaponsa, A. Peláez-Santos, R. Vignaga, F. Guidi, B. Ruiz-Granados, D. Tramonte, F. Vansyngel, M. Ashdown, D. Herranz, R. Hoyland, A. Lasenby, E. Martínez-González, L. Piccirillo, and R. A. Watson, "QUIJOTE scientific results - III. Microwave spectrum of intensity and polarization in the Taurus Molecular Cloud complex and L1527," *Monthly Notices of the Royal Astronomical Society*, vol. 486, pp. 462–485, June 2019.

[72] D. Tramonte, R. T. Génova-Santos, J. A. Rubiño-Martín, P. Vielva, F. Poidevin, C. H. López-Caraballo, M. W. Peel, M. Ashdown, E. Artal, R. B. Barreiro, F. J. Casas, E. de la Hoz, M. Fernández-Torreiro, F. Guidi, D. Herranz, R. J. Hoyland, A. N. Lasenby, E. Martinez-Gonzalez, L. Piccirillo, R. Rebolo, B. Ruiz-Granados, F. Vansyngel, and R. A. Watson, "QUIJOTE scientific results - V. The microwave intensity and polarization spectra of the Galactic regions W49, W51 and IC443," *Monthly Notices of the Royal Astronomical Society*, vol. 519, pp. 3432–3459, Mar. 2023.

[73] C. H. López-Caraballo, B. Ruiz-Granados, R. T. Génova-Santos, M. Fernández-Torreiro, J. A. Rubiño-Martín, M. W. Peel, F. Poidevin, E. Artal, M. Ashdown, R. B. Barreiro, F. J. Casas, E. de la Hoz, R. González-González, F. Guidi, D. Herranz, R. Hoyland, A. Lasenby, E. Martínez-González, L. Piccirillo, R. Rebolo, D. Tramonte, F. Vansyngel, P. Vielva, and R. A. Watson, "QUIJOTE scientific results - XIII. Intensity and polarization study of the microwave spectra of supernova remnants in the QUIJOTE-MFI wide survey: CTB 80, Cygnus Loop, HB 21, CTA 1, Tycho, and HB 9," *Monthly Notices of the Royal Astronomical Society*, vol. 527, pp. 171–204, Jan. 2024.

[74] Planck Collaboration, "Planck early results. XX. New light on anomalous microwave emission from spinning dust grains," *Astronomy & Astrophysics*, vol. 536, p. A20, Dec. 2011.

[75] G. Puglisi, V. Galluzzi, L. Bonavera, J. Gonzalez-Nuevo, A. Lapi, M. Massardi, F. Perrotta, C. Baccigalupi, A. Celotti, and L. Danese, "Forecasting the Contribution of Polarized Extragalactic Radio Sources in CMB Observations," *The Astrophysical Journal*, vol. 858, p. 85, May 2018.

[76] R. A. Sunyaev and Y. B. Zeldovich, "The Observations of Relic Radiation as a Test of the Nature of X-Ray Radiation from the Clusters of Galaxies," *Comments on Astrophysics and Space Physics*, vol. 4, p. 173, Nov. 1972.

[77] Planck Collaboration, "Planck intermediate results. XLVIII. Disentangling Galactic dust emission and cosmic infrared background anisotropies," *Astronomy & Astrophysics*, vol. 596, p. A109, Dec. 2016.

[78] M. Righi, C. Hernández-Monteagudo, and R. A. Sunyaev, "Carbon monoxide line emission as a CMB foreground: tomography of the star-forming universe with different spectral resolutions," *Astronomy & Astrophysics*, vol. 489, pp. 489–504, Oct. 2008.

[79] Y. Minami, H. Ochi, K. Ichiki, N. Katayama, E. Komatsu, and T. Matsumura, "Simultaneous determination of the cosmic birefringence and miscalibrated polarisation angles from CMB experiments," *arXiv e-prints*, p. arXiv:1904.12440, Apr. 2019.

[80] P. Diego-Palazuelos, J. R. Eskilt, Y. Minami, M. Tristram, R. M. Sullivan, A. J. Banday, R. B. Barreiro, H. K. Eriksen, K. M. Górski, R. Keskitalo, E. Komatsu, E. Martínez-González, D. Scott, P. Vielva, and I. K. Wehus, "Cosmic Birefringence from the Planck Data Release 4," *Physical Review Letters*, vol. 128, p. 091302, Mar. 2022.

[81] N. Krachmalnicoff, E. Carretti, C. Baccigalupi, G. Bernardi, S. Brown, B. M. Gaensler, M. Haverkorn, M. Kesteven, F. Perrotta, S. Poppi, and L. Staveley-Smith, "S-PASS view of polarized Galactic synchrotron at 2.3 GHz as a contaminant to CMB observations," *Astronomy & Astrophysics*, vol. 618, p. A166, Oct. 2018.

[82] A. Ritacco, F. Boulanger, V. Guillet, J.-M. Delouis, J.-L. Puget, J. Aumont, and L. Vacher, "Dust polarization spectral dependence from Planck HFI data. Turning point for cosmic microwave background polarization-foreground modeling," *Astronomy & Astrophysics*, vol. 670, p. A163, Feb. 2023.

[83] Planck Collaboration, "Planck intermediate results. XXXII. The relative orientation between the magnetic field and structures traced by interstellar dust," *Astronomy & Astrophysics*, vol. 586, p. A135, Feb. 2016.

[84] Planck Collaboration, "Planck intermediate results. XXXVIII. E- and B-modes of dust polarization from the magnetized filamentary structure of the interstellar medium," *Astronomy & Astrophysics*, vol. 586, p. A141, Feb. 2016.

[85] S. E. Clark, C.-G. Kim, J. C. Hill, and B. S. Hensley, "The Origin of Parity Violation in Polarized Dust Emission and Implications for Cosmic Birefringence," *The Astrophysical Journal*, vol. 919, p. 53, Sept. 2021.

[86] C. Haslam, U. Klein, C. Salter, H. Stoffel, W. Wilson, M. Cleary, D. Cooke, and P. Thomasson, "A 408 MHz all-sky continuum survey. I-observations at southern declinations and for the north polar region," *Astronomy and Astrophysics*, vol. 100, pp. 209–219, 1981.

[87] C. Haslam, C. Salter, H. Stoffel, and W. Wilson, "A 408 MHz all-sky continuum survey. II-the atlas of contour maps," *Astronomy and Astrophysics Supplement Series*, vol. 47, p. 1, 1982.

[88] M. Remazeilles, C. Dickinson, A. Banday, M.-A. Bigot-Sazy, and T. Ghosh, "An improved source-subtracted and destriped 408-MHz all-sky map," *Monthly Notices of the Royal Astronomical Society*, vol. 451, no. 4, pp. 4311–4327, 2015.

[89] M. I. Large, M. J. S. Quigley, and C. G. T. Haslam, "A new feature of the radio sky," *Monthly Notices of the Royal Astronomical Society*, vol. 124, p. 405, Jan. 1962.

[90] M. J. S. Quigley and C. G. T. Haslam, "Structure of the Radio Continuum Background at High Galactic Latitudes," *Nature*, vol. 208, pp. 741–743, Nov. 1965.

[91] M. I. Large, M. F. S. Quigley, and C. G. T. Haslam, "A radio study of the north polar spur. II, A survey at low declinations," *Monthly Notices of the Royal Astronomical Society*, vol. 131, p. 335, Jan. 1966.

[92] T. A. T. Spoelstra, "Galactic Loops as Supernova Remnants in the Local Galactic Magnetic Field," *Astronomy & Astrophysics*, vol. 24, p. 149, Apr. 1973.

[93] F. Rahman, P. Chingangbam, and T. Ghosh, "The nature of non-Gaussianity and statistical isotropy of the 408 MHz Haslam synchrotron map," *Journal of Cosmology and Astroparticle Physics*, vol. 2021, p. 026, July 2021.

[94] F. Rahman, P. Chingangbam, and T. Ghosh, "Statistical properties of Galactic synchrotron temperature and polarization maps – a multi-frequency comparison," *arXiv e-prints*, p. arXiv:2212.06076, Dec. 2022.

[95] M. Tegmark, D. J. Eisenstein, W. Hu, and A. de Oliveira-Costa, "Foregrounds and forecasts for the cosmic microwave background," *The Astrophysical Journal*, vol. 530, p. 133, feb 2000.

[96] V. Jelić, S. Zaroubi, P. Labropoulos, R. M. Thomas, G. Bernardi, M. A. Brentjens, A. G. De Bruyn, B. Ciardi, G. Harker, L. V. E. Koopmans, V. N. Pandey, J. Schaye, and S. Yatawatta, "Foreground simulations for the LOFAR–epoch of reionization experiment," *Monthly Notices of the Royal Astronomical Society*, vol. 389, pp. 1319–1335, 09 2008.

[97] A. Waelkens, T. Jaffe, M. Reinecke, F. Kitaura, and T. Enßlin, "Simulating polarized galactic synchrotron emission at all frequencies - The Hammurabi code," *Astronomy & Astrophysics*, vol. 495, no. 2, pp. 697–706, 2009.

[98] B. Thorne, J. Dunkley, D. Alonso, and S. Næss, "The python sky model: software for simulating the galactic microwave sky," *Monthly Notices of the Royal Astronomical Society*, vol. 469, p. 2821–2833, May 2017.

[99] C. L. Bennett, R. S. Hill, G. Hinshaw, M. R. Nolta, N. Odegard, L. Page, D. N. Spergel, J. L. Weiland, E. L. Wright, M. Halpern, N. Jarosik, A. Kogut, M. Limon, S. S. Meyer, G. S. Tucker, and E. Wollack, "First-Year Wilkinson Microwave Anisotropy Probe (WMAP) Observations: Foreground Emission," *The Astrophysical Journal Supplement Series*, vol. 148, pp. 97–117, Sept. 2003.

[100] J. Delabrouille, J. F. Cardoso, M. Le Jeune, M. Betoule, G. Fay, and F. Guilloux, "A full sky, low foreground, high resolution CMB map from WMAP," *Astronomy & Astrophysics*, vol. 493, pp. 835–857, Jan. 2009.

[101] M. Remazeilles, J. Delabrouille, and J.-F. Cardoso, "Foreground component separation with generalized Internal Linear Combination," *Monthly Notices of the Royal Astronomical Society*, vol. 418, pp. 467–476, Nov. 2011.

[102] M. Remazeilles, A. Rotti, and J. Chluba, "Peeling off foregrounds with the constrained moment ILC method to unveil primordial CMB B modes," *Monthly Notices of the Royal Astronomical Society*, vol. 503, pp. 2478–2498, May 2021.

[103] J.-F. Cardoso, M. Le Jeune, J. Delabrouille, M. Betoule, and G. Patanchon, "Component Separation With Flexible Models—Application to Multichannel Astrophysical Observations," *IEEE Journal of Selected Topics in Signal Processing*, vol. 2, pp. 735–746, Nov. 2008.

[104] R. Fernández-Cobos, P. Vielva, R. B. Barreiro, and E. Martínez-González, "Multiresolution internal template cleaning: an application to the Wilkinson Microwave Anisotropy Probe 7-yr polarization data," *MNRAS*, vol. 420, pp. 2162–2169, Mar. 2012.

[105] H. K. Eriksen, I. J. O'Dwyer, J. B. Jewell, B. D. Wandelt, D. L. Larson, K. M. Górski, S. Levin, A. J. Banday, and P. B. Lilje, "Power Spectrum Estimation from High-Resolution Maps by Gibbs Sampling," *ApJ Supp.*, vol. 155, pp. 227–241, Dec. 2004.

[106] J. Delabrouille, J. F. Cardoso, and G. Patanchon, "Multidetector multicomponent spectral matching and applications for cosmic microwave background data analysis," *MNRAS*, vol. 346, pp. 1089–1102, Dec. 2003.

[107] E. de la Hoz, "Diffuse polarized foregrounds from component separation with QUIJOTE-MFI," *arXiv e-prints*, p. arXiv:2203.04861, Mar. 2022.

[108] A. Carones, M. Migliaccio, G. Puglisi, C. Baccigalupi, D. Marinucci, N. Vittorio, D. Poletti, and LiteBIRD collaboration, "Multiclustering needlet ILC for CMB B-mode component separation," *Monthly Notices of the Royal Astronomical Society*, vol. 525, pp. 3117–3135, Oct. 2023.

[109] G. Puglisi, G. Mihaylov, G. V. Panopoulou, D. Poletti, J. Errard, P. A. Puglisi, and G. Vianello, "Improved galactic foreground removal for B-mode detection with clustering methods," *MNRAS*, vol. 511, pp. 2052–2074, Apr. 2022.

[110] J. M. Casas, L. Bonavera, J. González-Nuevo, C. Baccigalupi, M. M. Cueli, D. Crespo, E. Goitia, J. D. Santos, M. L. Sánchez, and F. J. de Cos, "CENN: A fully convolutional neural network for CMB recovery in realistic microwave sky simulations," *Astronomy & Astrophysics*, vol. 666, p. A89, Oct. 2022.

[111] P. Diego-Palazuelos, E. Martínez-González, P. Vielva, R. B. Barreiro, M. Tristram, E. de la Hoz, J. R. Eskilt, Y. Minami, R. M. Sullivan, A. J. Banday, K. M. Górski, R. Keskitalo, E. Komatsu, and D. Scott, "Robustness of cosmic birefringence measurement against Galactic foreground emission and instrumental systematics," *Journal of Cosmology and Astroparticle Physics*, vol. 2023, p. 044, Jan. 2023.

[112] J. A. Rubiño-Martín, R. Rebolo, M. Tucci, R. Génova-Santos, S. R. Hildebrandt, R. Hoyland, J. M. Herreros, F. Gómez-Reñasco, C. L. Caraballo, E. Martínez-González, P. Vielva, D. Herranz, F. J. Casas, E. Artal, B. Aja, L. d. Fuente, J. L.

Cano, E. Villa, A. Mediavilla, J. P. Pascual, L. Piccirillo, B. Maffei, G. Pisano, R. A. Watson, R. Davis, R. Davies, R. Battye, R. Saunders, K. Grainge, P. Scott, M. Hobson, A. Lasenby, G. Murga, C. Gómez, A. Gómez, J. Ariño, R. Sanquirce, J. Pan, A. Vizcargüenaga, and B. Etxeita, "The QUIJOTE CMB Experiment," in *Highlights of Spanish Astrophysics V*, vol. 14 of *Astrophysics and Space Science Proceedings*, p. 127, Jan. 2010.

[113] E. Carretti, M. Haverkorn, L. Staveley-Smith, G. Bernardi, B. M. Gaensler, M. J. Kesteven, S. Poppi, S. Brown, R. M. Crocker, C. Purcell, D. H. F. M. Schnitzeler, and X. Sun, "S-band Polarization All-Sky Survey (S-PASS): survey description and maps," *MNRAS*, vol. 489, pp. 2330–2354, Oct. 2019.

[114] M. E. Jones, A. C. Taylor, M. Aich, C. J. Copley, H. C. Chiang, R. J. Davis, C. Dickinson, R. D. P. Grumitt, Y. Hafez, H. M. Heilgendorff, C. M. Holler, M. O. Irfan, L. R. P. Jew, J. J. John, J. Jonas, O. G. King, J. P. Leahy, J. Leech, E. M. Leitch, S. J. C. Muchovej, T. J. Pearson, M. W. Peel, A. C. S. Readhead, J. Sievers, M. A. Stevenson, and J. Zuntz, "The C-Band All-Sky Survey (C-BASS): design and capabilities," *MNRAS*, vol. 480, pp. 3224–3242, Nov. 2018.

[115] J. L. May, A. E. Adler, J. E. Austermann, S. J. Benton, R. Bihary, M. Durkin, S. M. Duff, J. P. Filippini, A. A. Fraisse, T. J. L. J. Gascard, S. M. Gibbs, S. Gourapura, J. E. Gudmundsson, J. W. Hartley, J. Hubmayr, W. C. Jones, S. Li, J. M. Nagy, K. Okun, I. L. Padilla, L. J. Romualdez, S. Tartakovsky, and M. R. Vissers, "Instrument Overview of Taurus: A Balloon-borne CMB and Dust Polarization Experiment," *arXiv e-prints*, p. arXiv:2407.01438, July 2024.

[116] Planck Collaboration, "Planck intermediate results. LVII. Joint Planck LFI and HFI data processing," *Astronomy & Astrophysics*, vol. 643, p. A42, Nov. 2020.

[117] C. L. Bennett, D. Larson, J. L. Weiland, N. Jarosik, G. Hinshaw, N. Odegard, K. M. Smith, R. S. Hill, B. Gold, M. Halpern, and et al., "Nine-year wilkinson microwave anisotropy probe (wmap) observations: Final maps and results," *The Astrophysical Journal Supplement Series*, vol. 208, p. 20, Sep 2013.

[118] M.-A. Miville-Deschenes, N. Ysard, A. Lavabre, N. Ponthieu, J. Macías-Pérez, J. Aumont, and J. Bernard, "Separation of anomalous and synchrotron emissions using wmap polarization data," *åp*, vol. 490, pp. 1093–1102, 11 2008.

[119] Y. Minami, "Determination of miscalibrated polarization angles from observed cosmic microwave background and foreground eb power spectra: Application to partial-sky observation," *Progress of Theoretical and Experimental Physics*, vol. 2020, Jun 2020.

[120] Planck Collaboration, "Planck 2018 results. III. High Frequency Instrument data processing and frequency maps," *Astronomy & Astrophysics*, vol. 641, p. A3, Sept. 2020.

[121] Planck Collaboration, "Planck 2015 results. XII. Full focal plane simulations," *Astronomy & Astrophysics*, vol. 594, p. A12, Sept. 2016.

[122] K. M. Gorski, E. Hivon, A. J. Banday, B. D. Wandelt, F. K. Hansen, M. Reinecke, and M. Bartelmann, "Healpix: A framework for high-resolution discretization and fast analysis of data distributed on the sphere," *The Astrophysical Journal*, vol. 622, p. 759–771, Apr 2005.

[123] A. Zonca, L. Singer, D. Lenz, M. Reinecke, C. Rosset, E. Hivon, and K. Gorski, "healpy: equal area pixelization and spherical harmonics transforms for data on the sphere in python," *Journal of Open Source Software*, vol. 4, p. 1298, Mar. 2019.

[124] F. Argüeso, J. L. Sanz, D. Herranz, M. López-Caniego, and J. González-Nuevo, "Detection/estimation of the modulus of a vector. Application to point-source detection in polarization data," *Monthly Notices of the Royal Astronomical Society*, vol. 395, pp. 649–656, May 2009.

[125] M. López-Caniego, D. Herranz, J. González-Nuevo, J. L. Sanz, R. B. Barreiro, P. Vielva, F. Argüeso, and L. Toffolatti, "Comparison of filters for the detection of point sources in Planck simulations," *Monthly Notices of the Royal Astronomical Society*, vol. 370, pp. 2047–2063, Aug. 2006.

[126] M. López-Caniego, M. Massardi, J. González-Nuevo, L. Lanz, D. Herranz, G. De Zotti, J. L. Sanz, and F. Argüeso, "Polarization of the wmap point sources," *The Astrophysical Journal*, vol. 705, p. 868–876, Oct 2009.

[127] D. Alonso, J. Sanchez, and A. Slosar, "A unified pseudo-c_ℓ framework," *Monthly Notices of the Royal Astronomical Society*, vol. 484, pp. 4127–4151, 04 2019.

[128] J. Bilbao-Ahedo, R. Barreiro, P. Vielva, E. Martínez-González, and D. Herranz, "Eclipse: a fast quadratic maximum likelihood estimator for cmb intensity and polarization power spectra," *Journal of Cosmology and Astroparticle Physics*, vol. 2021, p. 034, Jul 2021.

[129] R. E. Upham, M. L. Brown, and L. Whittaker, "Sufficiency of a gaussian power spectrum likelihood for accurate cosmology from upcoming weak lensing surveys," *Monthly Notices of the Royal Astronomical Society*, vol. 503, p. 1999–2013, Feb 2021.

[130] S. Azzoni, M. Abitbol, D. Alonso, A. Gough, N. Katayama, and T. Matsumura, "A minimal power-spectrum-based moment expansion for cmb b-mode searches," *Journal of Cosmology and Astroparticle Physics*, vol. 2021, p. 047, May 2021.

[131] P. Virtanen, R. Gommers, T. E. Oliphant, M. Haberland, T. Reddy, D. Cournapeau, E. Burovski, P. Peterson, W. Weckesser, J. Bright, S. J. van der Walt, M. Brett, J. Wilson, K. J. Millman, N. Mayorov, A. R. J. Nelson, E. Jones, R. Kern, E. Larson, C. J. Carey, İ. Polat, Y. Feng, E. W. Moore, J. VanderPlas, D. Laxalde, J. Perktold, R. Cimrman, I. Henriksen, E. A. Quintero, C. R. Harris, A. M. Archibald, A. H. Ribeiro, F. Pedregosa, P. van Mulbregt, and SciPy 1.0 Contributors, "SciPy 1.0: Fundamental Algorithms for Scientific Computing in Python," *Nature Methods*, vol. 17, pp. 261–272, 2020.

[132] Planck Collaboration, "Planck 2018 results. VII. Isotropy and statistics of the CMB," *Astronomy & Astrophysics*, vol. 641, p. A7, Sept. 2020.

[133] P. Ade, N. Aghanim, Z. Ahmed, R. Aikin, K. Alexander, M. Arnaud, J. Aumont, C. Baccigalupi, A. Banday, D. Barkats, and et al., "Joint analysis of bicep2/keck array and planck data," *Physical Review Letters*, vol. 114, Mar 2015.

[134] C. Dickinson, "Cmb foregrounds - a brief review," 2016.

[135] S. Plaszczynski, L. Montier, F. Levrier, and M. Tristram, "A novel estimator of the polarization amplitude from normally distributed stokes parameters," *Monthly Notices of the Royal Astronomical Society*, vol. 439, pp. 4048–4056, feb 2014.

[136] J. Wardle and P. Kronberg, "The linear polarization of quasi-stellar radio sources at 371 and 111 centimeters," *Astrophysical Journal*, vol. 194, pp. 249–255, dec 1974.

[137] M. Vidal, J. P. Leahy, and C. Dickinson, "A new polarization amplitude bias reduction method," *Monthly Notices of the Royal Astronomical Society*, vol. 461, pp. 698–709, jun 2016.

[138] N. A. Bond, M. A. Strauss, and R. Cen, "Crawling the cosmic network: identifying and quantifying filamentary structure," *Monthly Notices of the Royal Astronomical Society*, vol. 409, no. 1, pp. 156–168, 2010.

[139] N. A. Bond, M. A. Strauss, and R. Cen, "Crawling the cosmic network: exploring the morphology of structure in the galaxy distribution," *Monthly Notices of the Royal Astronomical Society*, vol. 406, no. 3, pp. 1609–1628, 2010.

[140] C. Monteserín, R. B. Barreiro, J. L. Sanz, and E. Martínez-González, "Scalar statistics on the sphere: application to the cosmic microwave background," *Monthly Notices of the Royal Astronomical Society*, vol. 360, pp. 9–26, jun 2005.

[141] F. R. Hampel, "The influence curve and its role in robust estimation," *Journal of the american statistical association*, vol. 69, no. 346, pp. 383–393, 1974.

[142] R. Komm, Y. Gu, F. Hill, P. Stark, and I. Fodor, "Multitaper spectral analysis and wavelet denoising applied to helioseismic data," *The Astrophysical Journal*, vol. 519, no. 1, p. 407, 1999.

[143] R. Hanbury Brown, R. D. Davies, and C. Hazard, "A curious feature of the radio sky," *The Observatory*, vol. 80, pp. 191–198, Oct. 1960.

[144] C. Dickinson, "Large-scale features of the radio sky and a model for loop I," *Galaxies*, vol. 6, p. 56, 05 2018.

[145] G. Dobler, D. P. Finkbeiner, I. Cholis, T. Slatyer, and N. Weiner, "The Fermi haze: a gamma-ray counterpart to the microwave haze," *The Astrophysical Journal*, vol. 717, no. 2, p. 825, 2010.

[146] M. Su, T. R. Slatyer, and D. P. Finkbeiner, "Giant gamma-ray bubbles from Fermi-LAT: Agn activity or bipolar galactic wind?," *The Astrophysical Journal*, vol. 724, pp. 1044–1082, nov 2010.

[147] E. Orlando and A. Strong, "Galactic synchrotron emission with cosmic ray propagation models," *Monthly Notices of the Royal Astronomical Society*, vol. 436, pp. 2127–2142, oct 2013.

[148] Planck Collaboration, "Planck 2015 results. X. Diffuse component separation: Foreground maps," *Astronomy & Astrophysics*, vol. 594, p. A10, Sept. 2016.

[149] Planck Collaboration, "Planck 2015 results. XXVI. The Second Planck Catalogue of Compact Sources," *Astronomy & Astrophysics*, vol. 594, p. A26, Sept. 2016.

[150] T. L. Svalheim, K. J. Andersen, R. Aurlien, R. Banerji, M. Bersanelli, S. Bertocco, M. Brilenkov, M. Carbone, L. P. L. Colombo, H. K. Eriksen, M. K. Foss, C. Franceschet, U. Fuskeland, S. Galeotta, M. N. Galloway, S. Gerakakis, E. Gjerløw, B. S. Hensley, D. Herman, M. Iacobellis, M. Ieronymaki, H. T. Ihle, J. B. Jewell, A. Karakci, E. Keihänen, R. Keskitalo, G. Maggio, D. Maino, M. Maris, S. Paradiso, B. Partridge, M. Reinecke, A.-S. Suur-Uski, D. Tavagnacco, H. Thommesen, D. J. Watts, I. K. Wehus, and A. Zacchei, "BeyondPlanck XIV. polarized foreground emission between 30 and 70 GHz," *arXiv: Cosmology and Nongalactic Astrophysics*, 2020.

[151] U. Fuskeland, I. K. Wehus, H. K. Eriksen, and S. K. Næss, "Spatial Variations in the Spectral Index of Polarized Synchrotron Emission in the 9 yr WMAP Sky Maps," *The Astrophysical Journal,*, vol. 790, p. 104, Aug. 2014.

[152] I. K. Wehus, U. Fuskeland, and H. K. Eriksen, "The Effect of Systematics on Polarized Spectral Indices," *he Astrophysical Journal*, vol. 763, p. 138, Feb. 2013.

[153] F. Guidi *et al.*, "QUIJOTE scientific results VI. The Haze as seen by QUIJOTE," *Mon. Not. Roy. Astron. Soc.*, vol. 519, no. 3, pp. 3460–3480, 2023.

[154] H. Liu, J. Creswell, and P. Naselsky, "E and B families of the stokes parameters in the polarized synchrotron and thermal dust foregrounds," *Journal of Cosmology and Astroparticle Physics*, vol. 2018, pp. 059–059, may 2018.

[155] J. Schmalzing and K. M. Gorski, "Minkowski functionals used in the morphological analysis of cosmic microwave background anisotropy maps," *Monthly Notices of the Royal Astronomical Society*, vol. 297, pp. 355–365, jun 1998.

[156] P. Chingangbam, V. Ganesan, K. Yogendran, and C. Park, "On minkowski functionals of CMB polarization," *Physics Letters B*, vol. 771, pp. 67–73, aug 2017.

[157] A. Carones, J. C. Duque, D. Marinucci, M. Migliaccio, and N. Vittorio, "Minkowski functionals of CMB polarisation intensity with pynkowski: theory and application to planck data," 2022.

[158] P. Chingangbam and C. Park, "Residual foreground contamination in the WMAP data and bias in non-gaussianity estimation," *Journal of Cosmology and Astroparticle Physics*, vol. 2013, pp. 031–031, feb 2013.

[159] S. Rana, T. Ghosh, J. S. Bagla, and P. Chingangbam, "Non-gaussianity of diffuse galactic synchrotron emission at 408 MHz," *Monthly Notices of the Royal Astronomical Society*, vol. 481, pp. 970–980, aug 2018.

[160] P. Chingangbam, K. Yogendran, P. Joby, V. Ganesan, S. Appleby, and C. Park, "Tensor minkowski functionals for random fields on the sphere," *Journal of Cosmology and Astroparticle Physics*, vol. 2017, pp. 023–023, dec 2017.

[161] E. A. Lim and D. Simon, "Can we detect hot/cold spots in the CMB with minkowski functionals?," *Journal of Cosmology and Astroparticle Physics*, vol. 2012, pp. 048–048, jan 2012.

[162] P. Joby, P. Chingangbam, T. Ghosh, V. Ganesan, and C. Ravikumar, "Search for anomalous alignments of structures in Planck data using minkowski tensors," *Journal of Cosmology and Astroparticle Physics*, vol. 2019, pp. 009–009, jan 2019.

[163] A. Pewsey, "Sinh-arcsinh distributions," *Biometrika*, vol. 96, 11 2009.

[164] S. Hamimeche and A. Lewis, "Likelihood analysis of CMB temperature and polarization power spectra," *Physical Review D*, vol. 77, p. 103013, May 2008.

[165] A. Lewis and A. Challinor, "CAMB: Code for Anisotropies in the Microwave Background." Astrophysics Source Code Library, record ascl:1102.026, Feb. 2011.

[166] R. Stompor, J. Errard, and D. Poletti, "Forecasting performance of CMB experiments in the presence of complex foreground contaminations," *Physical Review D*, vol. 94, p. 083526, Oct. 2016.

[167] J. Errard, S. M. Feeney, H. V. Peiris, and A. H. Jaffe, "Robust forecasts on fundamental physics from the foreground-obscured, gravitationally-lensed CMB polarization," *Journal of Cosmology and Astroparticle Physics*, vol. 2016, p. 052, Mar. 2016.

[168] A. Mangilli, S. Plaszczynski, and M. Tristram, "Large-scale cosmic microwave background temperature and polarization cross-spectra likelihoods," *MNRAS*, vol. 453, pp. 3174–3189, Nov. 2015.

[169] E. Sellentin and A. F. Heavens, "Parameter inference with estimated covariance matrices," *MNRAS*, vol. 456, pp. L132–L136, Feb. 2016.

[170] D. Beck, A. Cukierman, and W. L. K. Wu, "Bias on tensor-to-scalar ratio inference with estimated covariance matrices," *MNRAS*, vol. 515, pp. 229–236, Sept. 2022.

[171] M. Tegmark and A. de Oliveira-Costa, "How to measure CMB polarization power spectra without losing information," *Physical Review D*, vol. 64, p. 063001, Sept. 2001.

[172] J. D. Bilbao-Ahedo, R. B. Barreiro, D. Herranz, P. Vielva, and E. Martínez-González, "On the regularity of the covariance matrix of a discretized scalar field on the sphere," *Journal of Cosmology and Astroparticle Physics*, vol. 2017, p. 022, Feb. 2017.

[173] M. Kamionkowski and E. D. Kovetz, "The Quest for B Modes from Inflationary Gravitational Waves," *Annual Review of Astronomy & Astrophysics*, vol. 54, pp. 227–269, Sept. 2016.

[174] H. Dembinski and P. O. et al., "scikit-hep/iminuit," Dec 2020.

[175] A. A. Starobinskiĭ, "Spectrum of relict gravitational radiation and the early state of the universe," *Soviet Journal of Experimental and Theoretical Physics Letters*, vol. 30, p. 682, Dec. 1979.